The chemical evolution of galaxies explored through multi-object integral field spectroscopy

Connor James Hayden-Pawson

Department of Physics
University of Cambridge

This thesis is submitted for the degree of
Doctor of Philosophy

Jesus College   September 2022

Declaration

I hereby declare that this thesis is the result of my own work and includes nothing which is the outcome of work done in collaboration except as declared in the preface and specified in the text. It is not substantially the same as any work that has already been submitted before for any degree or other qualification except as declared in the preface and specified in the text. It does not exceed the prescribed word limit of 60,000 words for the Faculty of Physics and Chemistry Degree Committee.

Connor James Hayden-Pawson
September 2022

Acknowledgements

I cannot emphasise enough how grateful I am to each and every person that contributed to the completion of this thesis. First, I would like to thank the UK taxpayers who funded my PhD. It has been an immense privilege to spend the past four years studying the nature of the Universe, and I hope to pay this generosity forward unto others in the future. I thank my brilliant supervisor Roberto Maiolino for his guidance, enthusiasm, and patience throughout the many ups and downs we have faced over the course of the PhD. I also extend my gratitude to Mirko Curti for supporting me extensively throughout all aspects of my PhD: from providing feedback on my work to being my tag-team partner in presenting the results of the KLEVER survey at conferences far and wide, it truly has been a pleasure to work alongside you. I thank all of the members of Roberto's group, both past and present, who have helped make Cambridge a warm, friendly and pleasant place to work. I extend thanks to the administrator of the Kavli, Steve Brereton, for being a constant source of kindness and assisting in all matters, including but not limited to supplying the Kavli Christmas party with snowball cocktails.

The work presented in this thesis would not have been possible without the KLEVER survey, and I thank the many members of the KLEVER collaboration for their support over the course of the reduction, analysis and interpretation of the data. In particular I would like to thank Alice Concas for her contribution to refining the KLEVER data products, which undoubtedly helped to improve the quality of the survey. I would also like to thank Michele Cirasuolo for hosting me at the European Southern Observatory during the second year of my PhD. Although the experience was cut short by the outbreak of coronavirus, I truly enjoyed the time I did spend at ESO, and Munich will always hold a special place in my heart. Thanks go out to my ESO amigos Vanessa, Caz, Jon, Gabriella, Anežka and José for all of the weird and wonderful adventures we shared.

Over the duration of my time in Cambridge I have shared many great experiences with many great friends. I thank all of my fellow students across the Kavli, IoA and Cavendish for their good nature and companionship. To my fellow Jesuans Henry, Joe, Rhys, Orla and Chris, among others, I thank you for the many pub trips, formals and all the fun times that we shared. To my friends beyond Cambridge, who need not be named, I thank you for always

being there when needed. The unprecedented circumstances of the past few years have meant that much of the work in this thesis was performed from home. In this way, bedrooms were transformed into offices, and housemates into office mates. I am therefore truly blessed that my housemates happened to feel so much like family. To Jasper, Jack, Friede and Giulia, I will forever cherish the many movies, boardgames, meals and lockdown celebrations that we shared. I could not have chosen a better group of people to be trapped in a house with, and I look forward to making more memories with you all in the future.

Finally, I would like to thank my family, who ask for so little but to whom I owe so much. Particular thanks go to Beth and Joe for housing me at a moment's notice during the first months of lockdown. Our family has grown since I started this PhD, and I look forward to spending more time with my niece Ella and nephew Albie, who knows more about space at age 3 than I did at 23 and will undoubtedly put this thesis to shame in the future. I love you all dearly.

Abstract

Galaxies are expected to grow and evolve via a series of physical processes relating to gas flows into and out of the galaxy. Inflows of gas from the surrounding cosmic web provide fuel for star formation, which subsequently causes an enrichment of the interstellar medium (ISM) with the metals produced within stars, whilst supernovae-driven outflows drive gas out of the galaxy, re-distributing metals in the process. In this way, measurements of chemical abundances within galaxies can provide insight into the different physical processes that drive galaxy evolution. The interplay between these different processes has been well studied in the local Universe by large spectroscopic surveys that have established a number of scaling relations between stellar mass, star formation rate and gas-phase metallicity. However, the existence of such relations at earlier times in the Universe is less well studied. The aim of this thesis is to investigate the evolution of chemical abundances within galaxies across cosmic time, making use of integral field spectroscopic data obtained through the KLEVER survey.

In the first part of this thesis, I compare the galaxy-integrated properties of galaxies at $z \sim 2$ to those found in local galaxies, with a particular focus of the abundance of nitrogen relative to oxygen (N/O). I find that high redshift galaxies have similar N/O values to local galaxies at a fixed metallicity, but much lower N/O values than local galaxies at a fixed stellar mass. I then demonstrate that an anti-correlation exists locally between N/O and star formation rate, such that at a fixed stellar mass galaxies with higher star formation rates have lower N/O values. In light of this, I parameterise a three-dimensional relationship between stellar mass, star formation rate and N/O abundance, before demonstrating that this relationship accurately predicts the N/O ratios of galaxies at $z \sim 2$ as well as those observed locally. As such, I name this relationship the fundamental nitrogen relation (FNR), in analogy to the fundamental metallicity relation (FMR). Furthermore, I show that the measured FNR is well described by a simple combination of the FMR and a non-evolving relationship between N/O and metallicity. These results suggest that the physical processes that govern the FMR must be sensitive not only to the metallicity, but also the N/O abundance.

In the second part of this thesis I extend my analysis to the spatially resolved scale, studying the spatial distribution of N/O in galaxies at $z \sim 2$. I present some of the first measurements of N/O gradients at $z \sim 2$, finding they are generally flatter than those found locally. This is contrary to inside-out growth models, which predict steeper gradients at earlier times, however this difference may be reconciled by invoking star-formation driven feedback mechanisms that effectively mix metals within the ISM. I present observations of inverted N/O gradients, which I suggest may be a consequence of the inverted metallicity gradients also observed at high redshift. I also present evidence for negative Balmer decrement gradients within $z \sim 2$ galaxies, consistent with high levels of star formation in the galaxy centre that may be associated with early bulge formation. I note that the slope of the N/O gradients is dependent on the choice of diagnostic used to determine the N/O, suggesting this may be driven by differences in the ionisation properties of sulphur relative to oxygen.

Finally, in the third part of this thesis I present preliminary work analysing the scatter in the relationship between N/O and O/H for local galaxies. I present observations of a population of galaxies with low metallicities that have enhanced N/O abundances. I show that the galaxies with the highest N/O values also have higher stellar masses and star formation rates. I then investigate the possibility that these galaxies have undergone recent gas accretion, driving changes in their metallicities and N/O values whilst boosting their star formation. I compare to a simple gas mixing model, finding that the deviations of galaxies from their expected metallicities and N/O values can be well modelled by the accretion of metal rich gas with a metallicity equal to 55% of that of the galaxy. However, the models also predict that the gas fraction within the galaxy is expected to increase by between 0.64–1 dex during the accretion event, much larger than the changes in gas fraction inferred from the observed deviations from the star forming main sequence for local galaxies. I demonstrate that the expected changes in gas fraction are better matched by accretion of lower metallicity gas, however such models are unable to reproduce the observed decrease in N/O from the expected values. I conclude that improved models are needed that include prescriptions for star formation, chemical enrichment and gas outflows in order to better constrain the impact of dilution events on the N/O values and metallicities within galaxies.

Table of contents

List of figures

List of tables

Chapter 1

Introduction

On those fortunate nights where the clouds that usually hang stagnant above British skies part, an upward glance towards the heavens will be greeted by a plethora of light sources piercing through the darkness of space. The longer we look, the more light sources emerge as our eyes adjust to the darkness and allow for the observation of increasingly faint objects. If we extend our capabilities beyond the limitations of the human eye and confines of Earth's atmosphere, we begin to obtain images such as Figure 1.1 that unveil the true beauty and complexity of the night sky. Taken by the James Webb Space Telescope, this image captures only a small fragment of the sky equivalent in size to a grain of sand held at an arm's length. Yet, despite covering such a small region of space, it contains numerous objects with stunning diversity: from red to blue, large to small, disc-like to elliptical, even objects that appear stretched and distorted due to the effects of gravitational lensing (discussed further in Section 1.5.1). However, even with the evident diversity, the majority of these objects are in fact very similar in that they are all galaxies: collections of planets, stars and gas much like our own Milky Way.

To look at an image such as Figure 1.1 is to look back across the history of the Universe, as such we are able to investigate how galaxy populations differ across cosmic time. The oldest, faintest, most distant galaxies appear clumpy and irregular in their morphology. More recent, nearby galaxies can generally be categorised into one of two categories: blue spiral galaxies which are highly structured, gas-rich and are actively forming stars, or red diffuse, elliptical galaxies that have smooth structures and form very few stars. Understanding what physical processes drive galaxies to look so different to one another at different cosmic times, as well as discerning how these galaxies may be connected evolutionarily, are key questions within modern astrophysics.

Within this chapter, I provide a brief overview of our current understanding of the processes that govern the formation and evolution of galaxies. In particular, I introduce how

Fig. 1.1 The first Deep Field image taken by James Webb Space telescope, centred around the SMACS 0723 galaxy cluster. The image captures an area of the sky similar in size to a grain of sand held at an arm's length, yet contains thousands of galaxies of different shapes, sizes and colours, including some of the oldest and most faint structures ever observed. Credit: NASA, ESA, CSA, and STScI.

observations of the chemical content of galaxies can provide insight into their evolutionary history. In Section 1.1 I provide an introduction to the growth of structure within the Universe and early galaxy formation. In Section 1.2 I discuss how gas is converted into stars within galaxies. Section 1.3 introduces the nucleosynthetic origin of different chemical elements, with Section 1.4 discussing how these chemicals enrich the gas within galaxies and can subsequently provide and insight into galaxy evolution. Finally, in Section 1.5 I discuss how integral field spectroscopy is exploited to investigate star formation and chemical abundances within galaxies across cosmic time, before outlining the motivations for this thesis in Section 1.6.

1.1 Structure formation in the early Universe

1.1.1 Cosmological framework

Galaxies represent the visible end products of cosmic structure formation and must therefore be understood within the context of the formation and evolution of the Universe itself. Within our current understanding, spacetime as we know it began with the Big Bang. At extremely early times, the entire Universe was small enough to be in causal contact, allowing all regions of space to equilibrate to a common temperature. A fraction of a second after the Big Bang, the Universe rapidly expanded in a process called inflation. The result of this brief inflationary epoch was a larger Universe that remained generally homogeneous, with the exception of some residual inhomogeneities in the distributions of matter. The expansion of the Universe then continued, albeit at a slower rate, cooling as it did so and allowing nucleosynthesis to occur. However, the photons, ions and electrons that existed at early times remained coupled together in a dense cosmic plasma from which visible light was unable to escape. It wasn't until $\sim$380,000 years after the Big Bang that the Universe became cool enough for electrons to recombine with ions to form neutral hydrogen and helium. At this point, the Universe became optically thin, and for the first time photons were able to travel freely into space from the surface of their last scattering event. We observe these photons in the present day as the cosmic microwave background (CMB) - the earliest possible image of the Universe.

In an increasingly expanding Universe, it is the attractive force of gravity that drives the growth of structures. Our best understanding of gravity is given by Einstein's theory of general relativity (Einstein, 1916), which specifies how spacetime is curved in the presence of matter. The growth of structures within the Universe is therefore governed by its geometrical curvature, the mass and energy content and their distributions. These parameters have been inferred from precise studies of the CMB (Planck Collaboration et al., 2020) in conjunction with the current ‘standard model’ for cosmology, referred to as Lambda Cold Dark Matter (ΛCDM). Within our current understanding, the Universe is flat, isotropic and homogeneous on large scales. Indeed, observations of the CMB show that it is almost perfectly isotropic, with small temperature perturbations at the scale $\delta T/T \sim 10^{-5}$, with corrresponding density perturbations of a similar size. The exact origins of these perturbations are beyond the scope of ΛCDM, as they are expected to arise at early times in the Universe when general relativity breaks down and quantum effects become dominant.

Within ΛCDM, the energy density of the Universe is dominated by three main components: dark energy, dark matter and baryonic matter. Dark energy, believed to be the energy density of the vacuum, drives the accelerated expansion of spacetime and accounts for $\sim$70% of the total energy density of the Universe. Dark matter dominates the mass component of the Universe, making up $\sim$25% of the total energy density, with the remaining 5% being made up of baryonic matter. Within astronomy, baryonic matter constitutes all visible matter within the Universe, including leptons.

1.1.2 Dark matter haloes

Due to its abundance relative to baryonic matter, dark matter plays a pivotal role in the formation of structures in the early Universe. Unlike baryonic matter, which can interact with and emit electromagnetic radiation, dark matter is believed to interact only gravitationally. As such, dark matter could decouple from the cosmic plasma prior to recombination and begin to undergo gravitational collapse due to the lack of pressure support provided by radiation. This caused primordial fluctuations in the distribution of dark matter to grow, amplified by gravity, forming both overdense regions and empty voids. These overdense regions go on to form gravitationally bound structures, known as dark matter haloes. These haloes then grow through the accretion of additional dark matter as well as through mergers with other dark matter haloes. The result of this hierarchical growth is a large-scale structure known as the cosmic web: a complex network of haloes connected via elongated filaments intertwined with vast empty voids.

As the name suggests, dark matter is ‘dark’ by nature, with its inability to emit electromagnetic radiation meaning there is no current direct evidence for its existence. As such, the exact nature of dark matter is unknown. However, the existence of dark matter is strongly supported via indirect evidence based on its gravitational influence on visible matter. Zwicky (1933) observed that galaxies in clusters have larger velocity dispersions than would be expected from virial theorem when accounting only for the luminous, baryonic matter. Similarly, observations of spiral galaxies have found rotation curves that flatten at large galactocentric radii, in conflict with the fall expected from the mass distribution of gas and stars (Rubin et al., 1978, 1980). Without invoking alternative theories of gravity, the flattening at large radii can be explained by the presence of a dark matter halo, with a density profile proportional to the inverse square of the radius. Furthermore, measurements of the mass of galaxy clusters determined from gravitational lensing provide mass estimates well in excess of the observed baryonic mass (Taylor et al., 1998).

1.1.3 Cosmic accretion and galaxy formation

In contrast to dark matter, which has no pressure support, baryonic matter can interact with and emit electromagnetic radiation. Therefore, visible matter was initially unable to collapse into gravitationally supported structures, and instead oscillated in space scattering off of photons until the Universe was cool enough for recombination to occur. Due to this, the growth of baryonic structures within the Universe lags behind the growth of dark matter structures, tracing the structure formation that has already occurred. In this way, dark matter haloes within the cosmic web serve as sites for galaxy formation.

The collisional nature of baryonic matter means that as it undergoes gravitational collapse, falling towards the centre of a dark matter halo, it is shock heated to the halo's virial temperature. This heating results in the formation of a hot halo of baryonic gas that is stabilised against further collapse by thermal pressure support. Further collapse of the gas halo is then strongly reliant on the ability of the gas to dissipate energy via radiative cooling mechanisms. By comparing the cooling timescale, t_{cool}, to the dynamical timescale, t_{dyn}, we can define two distinct cooling regimes: the hot mode and the cool mode. In the hot regime, where $t_{cool} > t_{dyn}$, cooling is inefficient and the gas persists as a hot halo that is stable against gravitational collapse, slowly cooling over time. This cooling mode is typical of more massive haloes, with the central parts of the haloes forming more massive galaxies at later times. In the cold mode, where $t_{cool} < t_{dyn}$, the gas loses pressure support and efficiently collapses onto the centre of the dark matter halo. As the gas falls into the potential well of the halo, it maintains its specific angular momentum whilst radiating away potential energy. Since a circular orbit has the lowest energy at a fixed angular momentum, the gas infall will result in the formation of a rotation supported gas disk. However, even within the cold mode structure formation is not so simple. For example, feedback from massive black holes can drive powerful outflows that can eject gas from a galaxy and/or heat the surrounding halo, resulting in diminished accretion of cold gas from the intergalactic medium (IGM) and the circumgalactic medium (CGM) (Fabian, 2012; Cicone et al., 2014; Fluetsch et al., 2019).

In this way, the seed formation of galaxies is relatively well understood, however how these gaseous disks begin to form stars and evolve into galaxies remains a complex issue with many different physical processes to consider. As sketched in Figure 1.2, galaxies at the

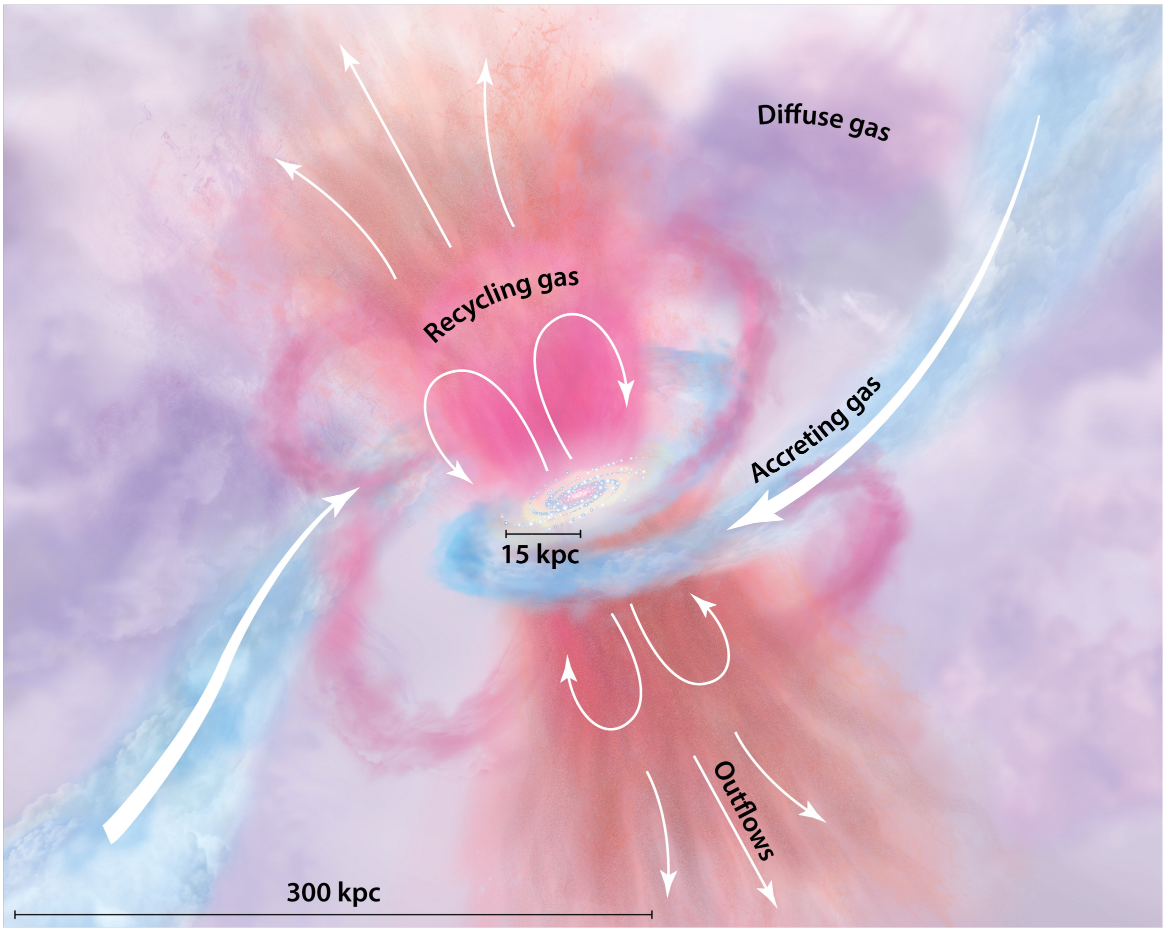

Fig. 1.2 Diagram of the baryon cycle in galaxies. The central galaxy accretes fresh gas from the intergalactic medium. This cold, dense gas gravitationally collapses to form stars. Outflows then drive gas out of the galaxy. Credit: Tumlinson et al. (2017).

centre of dark matter haloes are expected to accrete fresh gas along cold, dense filamentary structures within the cosmic web, with an accretion rate that is expected to be greater at earlier times (Dekel et al. 2013;Bennett & Sijacki 2020). This gas is expected to drive fresh star formation (as explained in further detail in the following sections) which will then cause enrichment of the surrounding interstellar medium (ISM) with heavy elements. This star formation can also cause outflows, driven by stellar winds or supernovae explosions, notwithstanding any outflows driven by the accreting central supermassive black hole at the heart of the galaxy. Such outflows can redistribute elements within a galaxy as well as expel chemically enriched gas into the surrounding IGM, which may itself be reaccreted onto the galaxy at a later time.

1.2 Galactic star formation

In order for a cloud of gas to produce stars it must first undergo gravitational collapse. Jeans (1902) demonstrated that the stability of a gas cloud is dependent on the ratio of the gravity and pressure support. Perturbations that exceed the size of the Jeans' length, $\lambda_J = \sqrt{\pi c_s^2 / G\rho}$, will become unstable as the internal pressure support becomes insufficient relative to the gravitational attraction. It then follows that we can define a critical mass, M_J, above which a spherically symmetric gas cloud is unstable against collapse. This mass scales as

$$M_J \propto \frac{c_s^3}{\sqrt{\rho}} \propto \sqrt{\frac{T^3}{\rho}}, \tag{1.1}$$

where c_s, T and ρ are the sound speed, temperature and density of the system respectively. From Equation 1.1 it is clear that the mass threshold necessary for gravitational collapse is relatively low when gas has a low temperature and a high density. The ISM within galaxies is a multiphase medium made up of gas at different densities, temperatures and ionisation states. As such, conditions within much of the ISM are unsuitable for star formation to occur. In fact, star formation is only found to occur within the coldest ($\sim$10 K) and most dense ($\sim 10^4 - 10^6$ cm^{-3}) regions of molecular gas clouds. However, direct observations of this molecular gas remain difficult, particularly at high redshift. We therefore tend to trace the star formation rate (SFR) within galaxies using empirical scaling relations between different ISM properties that are derived by studying phases of the ISM which are more readily observable.

1.2.1 Initial mass function

Of key importance in the process of star formation is the mass of a star at birth, as this property governs much of its subsequent evolution. As giant molecular clouds undergo gravitational collapse they fragment, forming groups of coeval stars that can be born with a range of different stellar masses. The probability of forming a star of a given mass can then be described by an Initial Mass Function (IMF). The functional form of the IMF has been determined by multiple authors based on stellar counts within the Milky Way. Salpeter (1955) found that, for stars with masses > 0.4 M$_\odot$, the IMF follows a power law of the form

$$\mathrm{d}N/\mathrm{d}M = \phi_{IMF}(M) \propto M^{-\alpha}, \tag{1.2}$$

where dN/dM indicates the number of stars formed per unit mass and $\alpha = 2.35$. More recent studies have similarly observed a power-law decrease towards high masses, however by probing a wider range of stellar masses they have also revealed a 'bimodal' form for the

IMF, with a tapering towards low stellar masses below a characteristic turnover mass. As shown in Figure 1.3, some parameterisations of the IMF, such as those from Kroupa (2001) and Chabrier (2003), are ‘top-heavy’, exhibiting an excess of high mass stars relative to the Salpeter (1955) IMF, whereas others such as Kroupa et al. (1993) are more ‘bottom-heavy’, with a higher fraction of stars formed at solar (and slightly sub-solar) masses with respect to the Salpeter IMF.

Observations within the Milky Way suggest that the IMF is universal across the Galaxy, regardless of the physical conditions of the ISM. However, questions remain regarding the universality of the IMF when applied to extragalactic studies. Indeed, studies of nearby elliptical galaxies have found IMFs with an excess of low-mass stars relative to the Milky Way, suggesting that the IMFs of star forming galaxies in the early Universe may be more bottom-heavy (Van Dokkum & Conroy, 2010; Sarzi et al., 2018). Similarly, changes in the characteristic turnover mass of the IMF (Elmegreen et al., 2008) at high-redshifts could have a large impact on chemical yields obtained from stellar modelling (Vincenzo et al., 2016a). As such, the uncertainty surrounding the universality of the IMF presents a limitation to extragalactic studies that involve the modelling of stellar populations.

1.2.2 Empirical star formation relations

The observed nature of the IMF, with a decreasing power law towards high stellar masses, means that massive stars are rarer than their low mass counterparts. Since the luminosity of main sequence stars scales with mass as $L \propto M^4$, and stellar lifetimes scale as $t \propto M^{-3}$ (assuming a linear relation between stellar mass and fuel available for nuclear fusion), then massive stars are also brighter and more short-lived than low mass stars. Massive stars therefore dominate the light spectra of young stellar populations, meaning the star formation rate can be estimated by measuring the amount of radiation produced by these stars.

Massive O- and B- type stars emit large amounts of UV radiation that ionises the surrounding ISM, forming H II regions. Electrons and protons within this ionised medium will subsequently recombine to form neutral hydrogen, and in doing so will radiate strongly in various hydrogen recombination lines, such as the Balmer series. The observed luminosity of Hα then acts as a tracer for the number of young massive stars, which can then be used to estimate the star formation rate. The common functional form for the relationship between Hα luminosity and star formation rate, reported by Kennicutt & Evans (2012), is given by

$$\log(\mathrm{SFR}) = \log(\mathrm{H}\alpha) - 41.27, \tag{1.3}$$

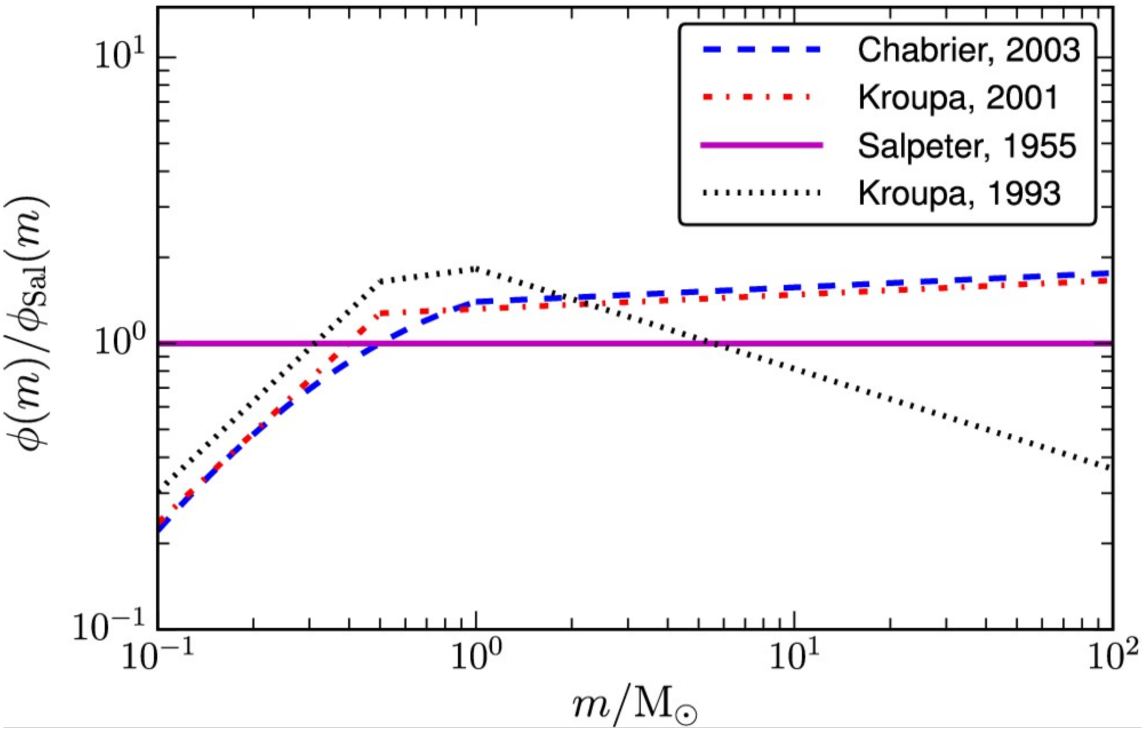

Fig. 1.3 The number of stars formed at different masses, normalised to the Salpeter (1955) IMF. The Kroupa (2001) and Chabrier (2003) IMFs exhibit an excess of massive stars relative to the Salpeter (1955) IMF and are thus ‘top-heavy’, whilst in comparison the IMF from Kroupa et al. (1993) exhibits a lower fraction of massive stars. Credit: Vincenzo et al. (2016a).

where the Hα luminosity is dust-corrected and measured in erg s^{-1}, SFR is expressed in units of M$_{\odot}$yr^{-1} and an underlying Kroupa (2001) IMF is assumed. Alternative tracers of the SFR include the UV continuum itself and far-infrared emission, which traces dust grains heated by the UV continuum (see Kennicutt & Evans (2012) for more details).

Given the understanding that star formation is fuelled by gas, Schmidt (1959) suggested that the star formation rate surface density, Σ_{SFR}, may be related to the gas mass surface density, Σ_{gas}, as a power law. This relationship, now known as the Schmidt-Kennicutt relation (S-K law), was confirmed by Kennicutt (1998) using observations of star forming galaxies, as shown in the left panel of Figure 1.4. The S-K law is parameterised as

$$\log(\Sigma_{\mathrm{SFR}}) = \alpha + \beta \log(\Sigma_{\mathrm{gas}}), \tag{1.4}$$

where β is the slope, determined observationally to be 1.4 (Kennicutt, 1998). This value is incredibly close to the value of 1.5 that is expected from star formation that is controlled by the self-gravity of gas. In this scenario, the SFR can be approximated by the ratio of available gas mass relative to the time taken for the gas cloud to collapse, multiplied by an efficiency factor that controls the fraction of gas which is converted into stars. For a uniform sphere, the free-fall time is proportional to $1/\sqrt{\rho}$, meaning that $\rho_{\mathrm{SFR}} = \varepsilon_{SF}(\rho_{\mathrm{gas}}/\tau_{\mathrm{free}}) \propto \rho_{\mathrm{gas}}^{1.5}$. However, in reality the processes that govern gravitational collapse and star formation and are more complex than this simple prescription, with the lifetimes of some giant molecular clouds observed to far exceed the free-fall time associated with their densities (Blitz & Rosolowsky, 2006), suggesting the existence of processes that support against gravitational collapse.

In the local Universe, if we focus on those galaxies that are actively forming stars we also observe a tight correlation between the star formation rate and galaxy stellar mass. This relationship is referred to as the star formation main sequence (SFMS), and is parameterised as

$$\log(\mathrm{SFR}) = \alpha + \beta \log(\mathrm{M}_{\star}). \tag{1.5}$$

This relationship is incredibly tight, with a typical scatter of just 0.2–0.3 dex. This suggests that the relationship between the star formation rate, which traces the recent star formation within the galaxy, and the stellar mass, which encodes all previous star formation, is secular and smooth. Stochastic events that may drive deviations from the SFMS, such as merger-driven starbursts, therefore do not play a significant role in galaxy evolution. Nevertheless, it can be useful to define an additional quantity, the specific star formation rate, sSFR = SFR/M$_{\star}$, to quantify the level of recent star formation with respect to the historic, integrated star formation within a galaxy. Observations in the local Universe have shown that the sSFR decreases with increasing stellar mass, suggesting that more massive galaxies evolved first,

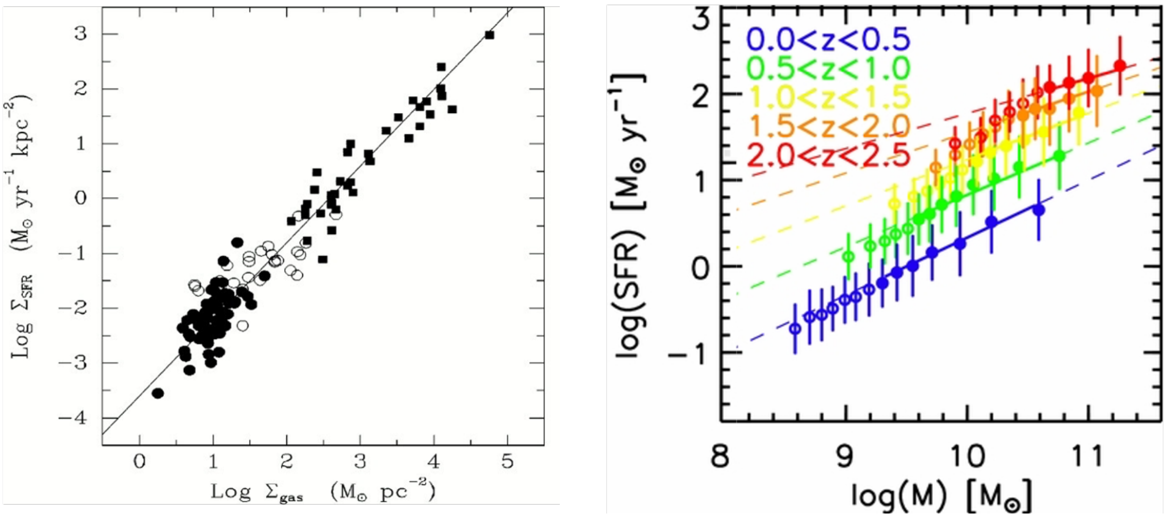

(a) (b)

Fig. 1.4 Empirical star formation laws for star forming galaxies. (a) The Schmidt-Kennicutt law demonstrating the correlation between gas mass surface density and star formation rate surface density. (b) The star forming main sequence across different comsic epochs. Adapted from (a) Kennicutt (1998) and (b) Whitaker et al. (2012).

forming the majority of their stars at early times, in contrast to less massive galaxies that are still in an earlier stage of their evolution and are more actively forming new stars.

As well as being observed in local galaxies, the existence of the SFMS has been confirmed across several epochs up to $z \sim 6$, albeit with an evolving normalisation and slope. As demonstrated in the right panel of Figure 1.4, the normalisation is found to increase up to $z \sim 2$, such that the typical SFR of a galaxy has decreased by a factor of ∼30 between $z \sim 2$ and the present day. Indeed, as shown in Figure 1.5, the star formation rate density is observed to reach an absolute peak near to $z \sim 2$. The high levels of star formation around $z \sim 2$ make that epoch a prime time for the formation of the most massive objects observed in the local Universe. Galaxies in this epoch are expected to have large gas reservoirs, fuelled through accretion from the cosmic web. This fresh cold gas can go on to fuel increased levels of star formation. Observations have shown that these galaxies were not only more gas-rich, but also more efficient at converting that gas into stars.

1.3 The nucleosynthetic origin of elements

The origin of different chemical elements within stars is a complex topic at the intersection between nuclear physics and astrophysics. Within minutes of the Big Bang, nuclear reactions

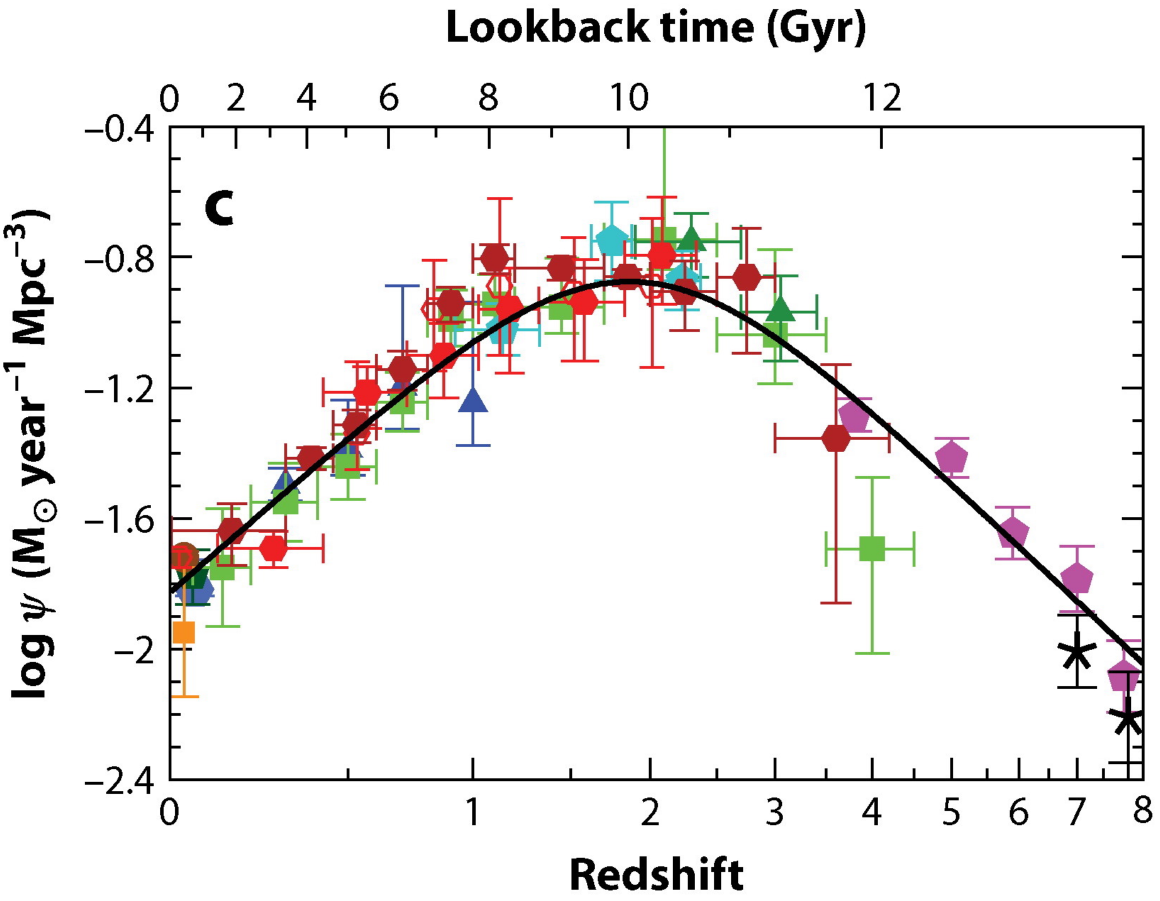

Fig. 1.5 The history of cosmic star formation rate density. Red and orange points correspond to SFR estimated from infrared emission, whilst all other colours indicate estimates made using UV luminosity measurements. Credit: Madau & Dickinson (2014).

were able to produce hydrogen, helium, and small amounts of lithium. All heavier elements, referred to within astronomy as metals, are produced from a range of different astronomical sources including nuclear reactions within stars, supernovae explosions and mergers of binary systems. These heavier elements are expelled from stars and released into the ISM via stellar winds and supernovae explosions, enriching the gas within galaxies. In this section, we discuss the mechanisms for the production of elements within stars of different masses, highlighting in particular the production mechanisms for nitrogen, an element central to this thesis.

1.3.1 Fusion mechanisms within stars

Several different nucleosynthetic production processes are understood to exist within stars (for extensive reviews on this topic, see Burbidge et al. 1957; Matteucci 2012; Nomoto et al. 2013). In short, the majority of energy production within stars on the stellar main sequence is driven by hydrogen burning, wherein ^{4}He is produced via either proton-proton nuclear reactions or the carbon-nitrogen-oxygen (CNO) cycle. Within the CNO cycle, which dominates in stars with $M_\star > 1.3\ M_\odot$, four protons fuse to create ^{4}He by using carbon, nitrogen and oxygen as catalysts, with each of these elements being consumed at one step of the cycle and produced as a product at another. Crucially, the step at which ^{14}N captures a proton to become ^{15}O has a relatively low cross section, meaning that over time nitrogen accumulates at the expense of carbon and oxygen. After the hydrogen-burning within the core of the star has been exhausted, helium-burning takes over in the core. This process is facilitated by the conversion of gravitational potential energy within the star into thermal energy, increasing the core temperature and allowing helium-burning to occur. The advent of helium-burning enables the triple-α reaction to occur, wherein three ^{4}He nuclei (α particles) combine to form ^{12}C. The production of further α-process elements such as ^{16}C and ^{32}S is then possible through additional α-capture reactions. After the helium-burning stage has begun, the life, death and subsequent chemical production of stars is mainly determined by their initial stellar mass. This is discussed in further detail in Sections 1.3.2 and 1.3.3.

In the context of stellar nucleosynthesis, an element can be considered to have either ‘primary’ or ‘secondary’ origin. Primary production occurs when an element is produced from the hydrogen and helium present within a star at birth. Since the abundance of heavy elements within a star is determined by the chemical abundance of the gas cloud from which it was birthed, the yields of primary nucleosynthetic products are largely independent of the chemical enrichment of the gas within galaxies, exhibiting only a minor dependence on stellar metallicity (Vincenzo et al., 2016a). In contrast, a secondary nucleosynthetic product forms from heavy elements that are already present within the star at its birth. For example, within the CNO cycle, the yield of ^{14}N will increase if ^{12}C and ^{16}O are more abundant. In this way, secondary nucleosynthetic products have yields that increase as the abundance of heavy metals within their galaxy increases.

1.3.2 Low- and intermediate-mass stars

Low- and intermediate-mass stars (hereafter LIMS) are typically designated as those having stellar masses within the range $0.8\ \mathrm{M}_\odot < \mathrm{M}_\star < 8\ \mathrm{M}_\odot$. Once LIMS have exhausted helium burning within their cores, they enter the asymptotic giant branch (AGB) phase. This phase is characterised by the star increasing in luminosity and decreasing in temperature, whilst simultaneously burning both hydrogen and helium in independent shells. Of particular importance in the evolution of LIMS are so-called 'dredge-up' episodes, wherein convection zones from the surface extend deep into the star. In doing so, these episodes are capable of transferring the products of fusion from the inner burning zones up towards the outer envelope of the star, enriching the surface of the star with heavy elements such as ^{12}C. Most important is the third dredge-up, which is driven by thermal instabilities in the helium-burning shell and occurs once the star has entered the AGB phase. In the AGB phase, the base of the convective envelope of the star overlaps with the hydrogen-burning shell. As such, the base of the convective envelope itself becomes hot enough to sustain proton-capture nucleosynthesis in a phenomenon known as hot-bottom burning. In conjunction with the third dredge-up enriching the surface of the star with heavy elements, this allows the CNO cycle to operate near the outer surface of the star, further enriching the surface with ^{14}N. The thermal instabilities of the helium shell that drive the dredge-up episodes also cause intense stellar winds as well as increases in mass-loss. As a consequence, low and intermediate mass stars are largely responsible for the enrichment of the ISM with elements such as carbon and nitrogen.

The ^{14}N produced as a consequence of hot bottom burning is still considered to be a primary nucleosynthetic product as it forms from the initial hydrogen and helium within the star, albeit in a non-trivial sequence. First, ^{12}C must be synthesised from the triple-α process in a helium-burning region, before a dredge-up must occur to transport the ^{12}C into a hydrogen-burning region, where the CNO cycle can then convert it into ^{14}N. In this sense, primary nitrogen can form in any star with both helium- and CNO- burning shells, provided there is some mechanism enabling mixing between these two regions. Indeed, stellar yield models from Ventura et al. (2013) predict that the majority of primary nitrogen is produced by stars with masses between $3\ \mathrm{M}_\odot < \mathrm{M}_\star < 6\ \mathrm{M}_\odot$. Nevertheless, nitrogen production by LIMS is still dominated by secondary nucleosynthetic pathways, since any carbon and oxygen present at the birth of the star will act to increase the yield of nitrogen. With the combination of primary and secondary nitrogen production mechanisms within LIMS, galactic chemical

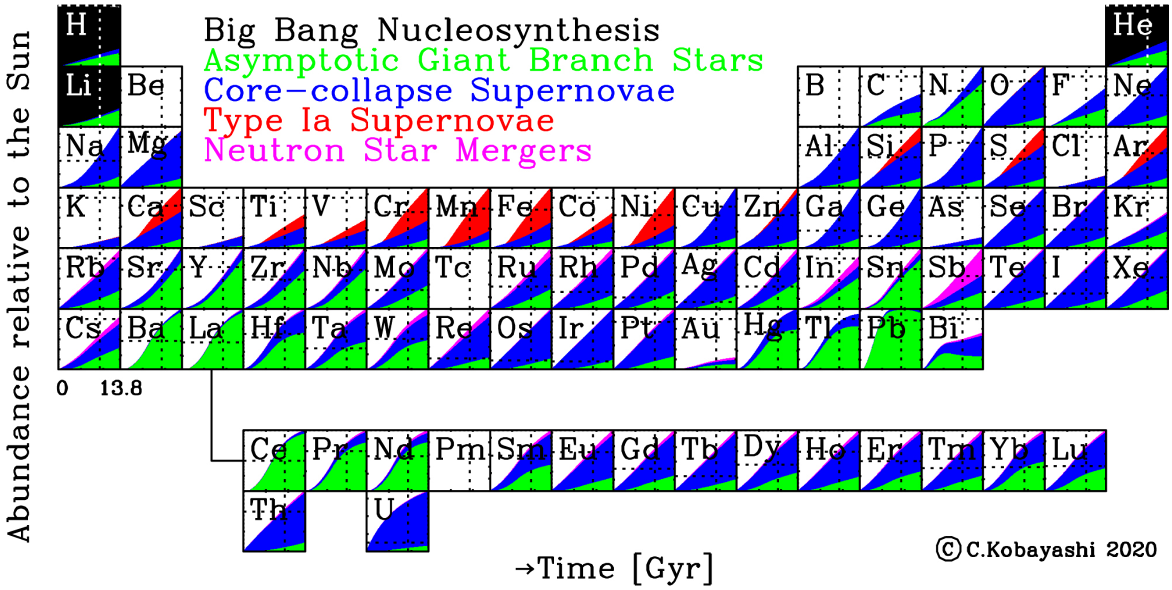

Fig. 1.6 Periodic table of elements, with colours highlighting the different astrophysical origins of elements over time. Credit: Kobayashi et al. (2020).

evolution models predict these stars may produce up to 74% of nitrogen within the ISM (Kobayashi et al., 2020). This is highlighted in Figure 1.6, which shows how different nucleosynthetic sources contribute to the production of different elements across cosmic time, as predicted from galactic chemical evolution models (Kobayashi et al., 2020).

1.3.3 Massive stars

Despite being more rare and short-lived than their low-mass counterparts, massive stars ($M_\star > 8\ M_\odot$) are the most important metal producers within the Universe. Unlike in lower mass stars, where no additional core-burning stages take place beyond helium burning until after the death of the star, massive stars are capable of increasing their core temperatures enough to burn heavier elements such as carbon, oxygen and silicon. This process of burning increasingly heavier metals continues until the core is primarily composed of iron, at which point massive stars die as core-collapse supernovae, leaving behind a remnant black hole or neutron star. At this stage, all elements produced within the star, as well as those synthesised during the supernovae, are released into the surrounding ISM. In this way, massive stars are responsible for the production of the bulk of α-elements, such as oxygen, present in the ISM.

A similar effect to the dredge-up episodes in LIMS can be achieved in massive stars by invoking stellar rotation, which can cause heavy elements such as carbon and oxygen to diffuse out of helium-burning regions and into hydrogen-burning shells. As with LIMS, the CNO cycle can then convert these heavy elements into primary nitrogen that resides in the convective envelope of the star (Meynet & Maeder, 2002). Similarly, the most massive stars ($M_\star > 25\ M_\odot$) are expected to have intense stellar winds that remove external hydrogen-rich envelopes, forming Wolf-Rayet (W-R) stars. These stars have helium-rich outer envelopes that can be converted into nitrogen via the CNO cycle leading to the enrichment of ISM with nitrogen on short timescales, and thus increasing the N/O ratio (Pagel et al., 1986; Brinchmann et al., 2008).

1.4 Chemical enrichment of the ISM

In the previous sections we have highlighted how galaxy formation and evolution is governed by a complex interplay of many different physical processes. As gas within galaxies is converted into stars, elements heavier than hydrogen and helium are produced within those stars and released into the surrounding interstellar medium via stellar winds and supernova explosions. In this context, the current level of chemical enrichment within the ISM acts as a fossil record for a given galaxy, tracing its star formation history. Furthermore, beyond direct enrichment from stellar nucleosynthesis, the level of enrichment can be impacted by gas flows, part of the baryon cycle. Accretion of fresh gas onto the galaxy can cause a dilution effect, increasing the abundance of hydrogen relative to heavier elements already present in the galaxy whilst fuelling fresh star formation episodes. Similarly, outflows can drive heavy elements out of a galaxy, redistributing the chemical content of the ISM in the process. The chemical enrichment of a galaxy therefore acts as a useful probe of galaxy evolutionary processes.

In general, the chemical enrichment of a system is traced by the 'metallicity' (generally indicated with Z), a quantity defined as the mass fraction of metals relative to the total baryonic mass. Since oxygen is the most abundant heavy element by mass, and the baryonic mass is dominated by hydrogen, it is common to provide a proxy of the metallicity with the quantity $12 + \log(\mathrm{O/H})$, where O/H is the abundance of oxygen atoms relative to hydrogen, and the additional value of 12 is introduced so that all elements have positive Solar values.

In this section, we discuss the structure of H II regions, explaining how their emission can be used to determine chemical abundances within the ISM, before describing how various abundance scaling relations can then be used to gain an insight into physical processes relevant to galaxy evolution.

1.4.1 The structure of H II regions

As introduced in Section 1.2.2, H II regions are photoionised nebulae surrounding massive O- and B-type stars. The proximity of H II regions to young, massive stars means that these nebular regions act as tracers of the recent star formation within galaxies, with a Hα luminosity that is proportional to the amount of ionising radiation. The ionised gas within these regions is primarily probed through observations of recombination and collisionally excited emission lines.

Recombination of hydrogen

Recombination lines are produced as electrons bind to ions, forming a recombined species in an excited state. This species then decays into lower energy states via a cascade of radiative transitions until the ground state is reached. Since hydrogen is the most abundant element within the ISM, it emits the strongest recombination lines. The recombination of hydrogen is readily observed via the Balmer series in the rest-frame optical wavelength range. Knowledge of the recombination cross section and relative transition probabilities allows the relative ratios of the different emission lines produced in the recombination spectrum of hydrogen to be modelled. In particular, the ratios of the recombination lines are sensitive to the optical thickness of the nebula to Lyman series radiation. Two extreme cases for the recombination of hydrogen can then be considered: Case A, which assumes the nebula is optically thin to all Lyman series radiation, and case B, which assumes the nebula is optically thick to Lyman series radiation. In the latter scenario, Lyman photons resonantly scatter within the nebula, and are rapidly re-absorbed and re-emitted by the gas. This scenario is favoured by typical H II regions, as Lyman series lines tend to have high optical depths.

Collisionally excited lines

Collisions of ions and thermal electrons can excite electrons in the low-lying, fine structure energy levels of heavy elements. In the optical, these collisionally-driven transitions typically correspond to energies of a few eV, and produce a number of rest-frame optical emission lines including [O II]$\lambda\lambda3727,29$, [O III]$\lambda\lambda4959,5007$, [N II]$\lambda\lambda6548,6584$ and [S II]$\lambda\lambda6716,6732$. Most of these collisionally excited transitions are described as 'forbidden', as they have no associated electric dipole transition, meaning they have an extremely low probability of spontaneously decaying. In this way, the label of 'forbidden' is somewhat misleading, and these transitions may better be understood as 'highly improbable'. Indeed, in the low density environment of the ISM, these species remain undisturbed for a long enough

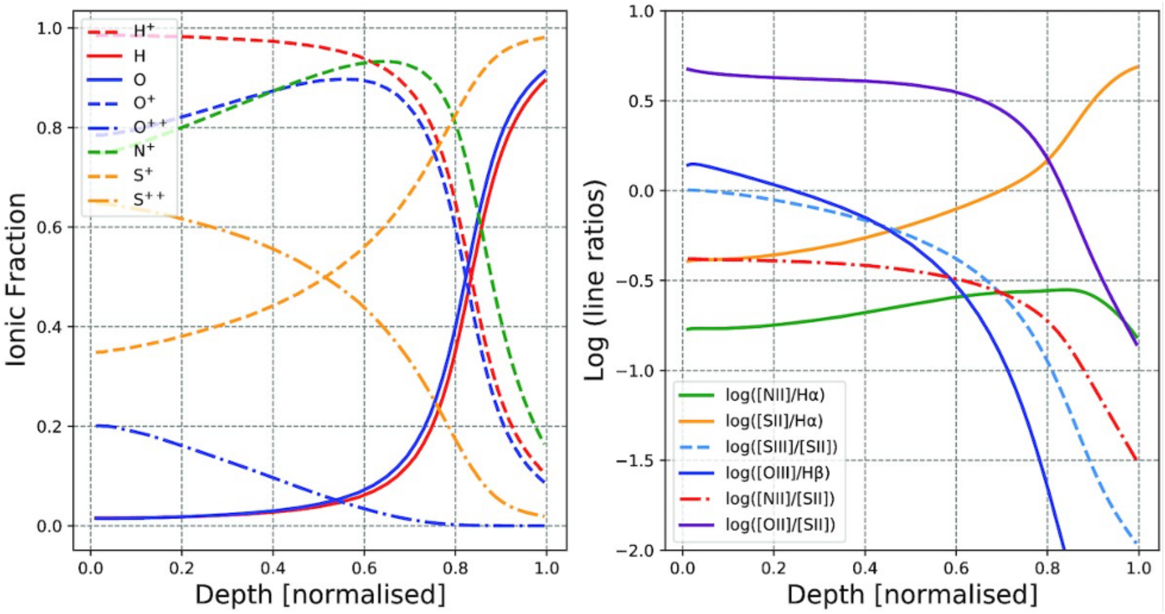

Fig. 1.7 The expected ionisation structure (left) and consequent emission line flux ratios (right) calculated using the photoionisation code CLOUDY. The model assumes a spherically symmetric H II region with a 2 Myr-old simple stellar population, density of $10^2\mathrm{cm}^{-3}$, metallicity [Fe/H]=-0.2 and an ionisation parameter log(U)=-3.5. Credit: Mannucci et al. (2021).

time for the spontaneous decay and subsequent emission of a photon to occur. Similarly, the probability of the photon emitted from a forbidden line being re-absorbed within the nebula is low. As such the photons from collisionally excited species escape from H II regions, providing some of the dominant mechanisms for the cooling of the ionised ISM.

Ionisation structure

The ionisation structure of a H II region is governed by the metallicity of the gas, the ionising stellar spectrum and the ionisation parameter, U, which is defined as the number of ionising photons per hydrogen atom and is parameterised as

$$\mathrm{U}(r) = Q/(4\pi r^2 n_e c), \tag{1.6}$$

where Q is the number of ionising photons per second emitted by the central source, n_e is the electron density and r is the distance between the gas and the source. Using these parameters as inputs, photoionisation models such as that CLOUDY (Ferland et al., 2013) can model the resulting ionisation structures of nebular regions. This can be useful for shedding light on how different ionisation species inhabit different regions of H II regions. Figure 1.7 shows one such example of the ionisation structure of a nebular emission region derived from photoionisation models. Species that are doubly-ionised, such as [O III] and [S III], tend to dominate in the central regions of nebulae relative to their lower ionisation, singly-ionised counterparts ([O II] and [S II] respectively). The opposing scenario can also be seen to exist, with low ionisation species dominating the outer regions of nebulae. Even amongst ions that are all singly-ionised such as [S II], [O II] and [N II], all of which have similar first ionisation energies (10.36, 13.6 and 14.5 eV, respectively), stark differences in the ionisation structures exist. As shown in the right hand panel of Figure 1.7, the varying ionisation structures of different species has a direct impact on the ratios of emission lines observed at different depths of the H II regions. Observations that encompass only the central regions of H II nebulae may therefore be biased towards line ratio values that are not representative of the full emission region.

The impact of dust

Dust within the ISM exists mostly as grains of graphite and silicate with typical sizes on the order of a few microns. Dust plays an important role in the evolution of galaxies, depleting the ISM of chemicals, catalysing the formation of molecular hydrogen and acting as an important coolant via absorption of UV radiation and subsequent emission in the far-infrared, impacting the ionisation structure of nebular regions. Dust grains cause an obscuring effect that can complicate observations of rest-frame optical emission line spectra. Within the optical wavelength range, dust not only attenuates light , but also changes the shape of the emitted spectrum, absorbing light at shorter, bluer wavelengths more than light at longer, redder wavelengths. We refer to these two effects as extinction and reddening respectively. The extinction at a given wavelength, λ, can be expressed as

$$\mathrm{A}_\lambda = 2.5\log(\mathrm{F}^0_\lambda/\mathrm{F}_\lambda), \tag{1.7}$$

where F_λ is the observed flux and F^0_λ is the intrinsic, unattenuated flux. The wavelength dependence of the extinction is then generally expressed in terms of an extinction curve, parameterised as $\mathrm{k}_\lambda = \mathrm{A}_\lambda/\mathrm{E(B-V)}$, where E(B-V) is the colour excess defined by the difference in the B- and V-band magnitudes of the background sources relative to the unattenuated magnitudes.

For a given extinction curve, we can measure the reddening of emission line fluxes by comparing the observed ratio of two Balmer lines (typically Hα and Hβ, i.e. the Balmer decrement) with the intrinsic value predicted theoretically, which corresponds to Hα/Hβ = 2.87 for case B recombination at a temperature of 10^4 K. By combining Equation 1.7 with the parameterisation of the extinction curve and inputting the expected Balmer decrement value, $E(B\text{-}V)_{gas}$ can then be estimated as

$$E(B\text{-}V)_{gas} = \frac{-2.5}{(k_{H\beta} - k_{H\alpha})} \log\left(\frac{F_{H\alpha}/F_{H\beta}}{2.87}\right), \tag{1.8}$$

where $F_{H\beta}$ and $F_{H\alpha}$ are the observed fluxes of Hβ and Hα, respectively. Once $E(B\text{-}V)_{gas}$ has been determined for a given source, a reddening correction can be applied to all observed emission lines.

Extinction curves apply to the simple case of a dusty screen in front of a background source, depending only on the properties of the dust within the screen, and have been determined within the Milky Way through comparisons of attenuated and un-attenuated stellar populations (Cardelli et al., 1989). For a more complex scenario where the emitting source is mixed within the dusty medium, as expected for extragalactic sources, the extinction will depend on both the dust properties and the relative geometry of the emitting source and the dusty medium, described by an attenuation curve (Calzetti et al., 2000). Recent efforts have been made to calibrate attenuation curves out to high redshifts, with observations of galaxies at $z \sim 2$ by Reddy et al. (2015) finding an attenuation curve identical to that of Calzetti et al. (2000), albeit with a lower normalisation.

1.4.2 Determination of chemical abundances

Direct method

In Section 1.4.1 we highlighted how H II regions within galaxies are rich in collisionally excited emission lines. The flux of these emission lines is proportional to the abundance of the emitting ionic species, multiplied by some emissivity factor, $\varepsilon_\lambda(T_e, n_e)$. It therefore follows that if the emissivity can be determined, then the chemical abundances can be derived. Since the emissivity is a function of the electron temperature, T_e, and density, n_e, measurements of these quantities are central to this method of abundance determination. For this reason, the direct method is also commonly referred to as the T_e, or electron-temperature method.

The electron density can be derived from the intensity ratios of emission line doublets, which have similar excitation energies, but different critical densities for collisional de-excitation (Osterbrock & Ferland, 2006). Collisionally excited doublets such as [O II]$\lambda\lambda$3727, 29 and [S II]$\lambda\lambda$6716, 32 are particularly useful for measuring densities in the range typical of H II regions (i.e. $n_e \sim 10^2 – 10^4$ cm^{-3}). Meanwhile, the electron temperature can be determined through the ratios of weak auroral emission lines to strong nebular emission lines, i.e. [O III]λ4363/[O III]λ5007, with the former being emitted from higher energy excited

Notation	Line Ratio
R2	[O II]$\lambda\lambda$3727,29 / Hβ
R3	[O III]λ5007 / Hβ
N2	[N II]λ6584 / Hα
S2	[S II]$\lambda\lambda$6717,31 / Hα
R23	([O II]$\lambda\lambda$3727,29 + [O III]$\lambda\lambda$4959, 5007) / Hβ
O32	[O III]λ5007 / [O II]$\lambda\lambda$3727,29
N2O2	[N II]λ6584 / [O II]$\lambda\lambda$3727,29
N2S2	[N II]λ6584 / [S II]$\lambda\lambda$6717,31

Table 1.1 Definitions of line ratios commonly adopted as strong line diagnostics for determining chemical abundances.

states than the latter. A more comprehensive list of available line ratios is provided by Pérez-Montero (2017). Practical use of this method is limited by the intrinsic faintness of the auroral lines, which are often 10-1000 times fainter than the Balmer lines. Indeed, at high redshifts, only a limited number of direct auroral line detections exist.

Strong line calibrations: O/H

The impracticality of observing weak auroral lines for large samples of galaxies means that it is often necessary to rely on indirect methods of chemical abundance determination. In particular, the ratios of strong nebular emission lines, which are readily observable in large samples of galaxies across different cosmic epochs, have been calibrated to serve as tracers of the gas-phase metallicity.

Several different nebular line ratios have been calibrated via the direct method to act as tracers of the gas-phase metallicity, with definitions of the diagnostics used throughout this thesis quoted in Table 1.1. Within these definitions, all emission lines used are expected to have been corrected for extinction from dust (see Section 1.4.1). Each choice of diagnostic has its own advantages and disadvantages when being used to determine the metallicity of gas, with dependencies on other quantities such as ionisation parameter or the nitrogen abundance being common. An example of calibrations for several strong line diagnostics is presented in Figure 1.8, taken from Curti et al. (2020a), which are calibrated using a sample of individual H II galaxies and stacked spectra taken from the Sloan Digital Sky Survey (SDSS). This combined sample allows for use of several nebular diagnostics over the metallicity range 12+log(O/H) $\in$ [7.6,8.9] that is typical of H II regions within galaxies.

One of the most popular diagnostics is the R23 index, first introduced by Pagel et al. (1979). Since this diagnostic includes both of the main ionisation species of oxygen, O^+

and O^{++}, it is relatively unaffected by the underlying ionisation structure of the H II regions. Nevertheless, the index remains dependent on the ionisation parameter, which can be probed through the O32 index. O32 is strongly sensitive to the ionisation state, as it probes the ratio of doubly-ionised species relative to singly-ionised species. In this way, it can be used in isolation as an indirect tracer of the metallicity, reliant on the anti-correlation that exists between the ionisation parameter and metallicity. Moreover, O32 can be used in combination with R23 to account for the dependency on the ionisation parameter in order to better constrain the metallicity (McGaugh, 1991; Nagao et al., 2006).

Beyond the dependence on ionisation parameter, it is often necessary to adopt a second diagnostic alongside R23 as the latter is doubly-branched, meaning a single R23 value can correspond to two metallicity values, either on the 'high' O/H or 'low' O/H branch. The double valued nature of diagnostics such as R23 is driven by the balance between temperature and cooling within gas. At low metallicities, the electron temperature is high, meaning that cooling proceeds via collisionally excited lines such as [O III]λ5007 and therefore strong-line diagnostics such as R23 scale with O/H in this regime. However, as the temperature of the gas cools towards higher metallicities, the excitation of collisionally excited lines becomes inefficient, and cooling proceeds instead through infrared lines such as [O III]$\lambda 88\mu$m. This causes a corresponding decrease in the R23 ratio relative to the metallicity. In the intermediate metallicity regime where these two branches meet, breaking the degeneracy of double valued diagnostics can become difficult, leading to large uncertainties. Additional uncertainty is introduced to the R23 and O32 diagnostics by the extinction correction, which is vital due to the large wavelength separation between the [O III]λ5007 and [O II]$\lambda\lambda$3727,29 emission lines.

Many indicators, such as N2 and O3N2, rely on measurement of the [N II]λ6584 emission line to trace the metallicity (Pettini & Pagel, 2004). N2 in particular is widely used, as it uses only the [N II]λ6584 and Hα emission lines, which are very close in wavelength and can therefore be readily observed in a single wavelength band. This proximity not only means that no extinction correction is required, but also means that this index is readily accessible at high redshift, where the simultaneous measurement of multiple rest-frame optical emission lines has been achieved by only a few surveys (see Section 1.5 for further details). Furthermore, these diagnostics have only a single value across the metallicity range of typical H II regions, meaning that they are useful as single diagnostics or when used to break degeneracies in other diagnostics. However, diagnostics based on nitrogen, when used to trace the metallicity, are reliant on the underlying correlation between O/H and the nitrogen-to-oxygen ratio (N/O), which is discussed in further detail in Section 1.4.4. Although the N/O–O/H relationship is tight towards high metallicities, at low metallicities there is a large scatter in N/O at a

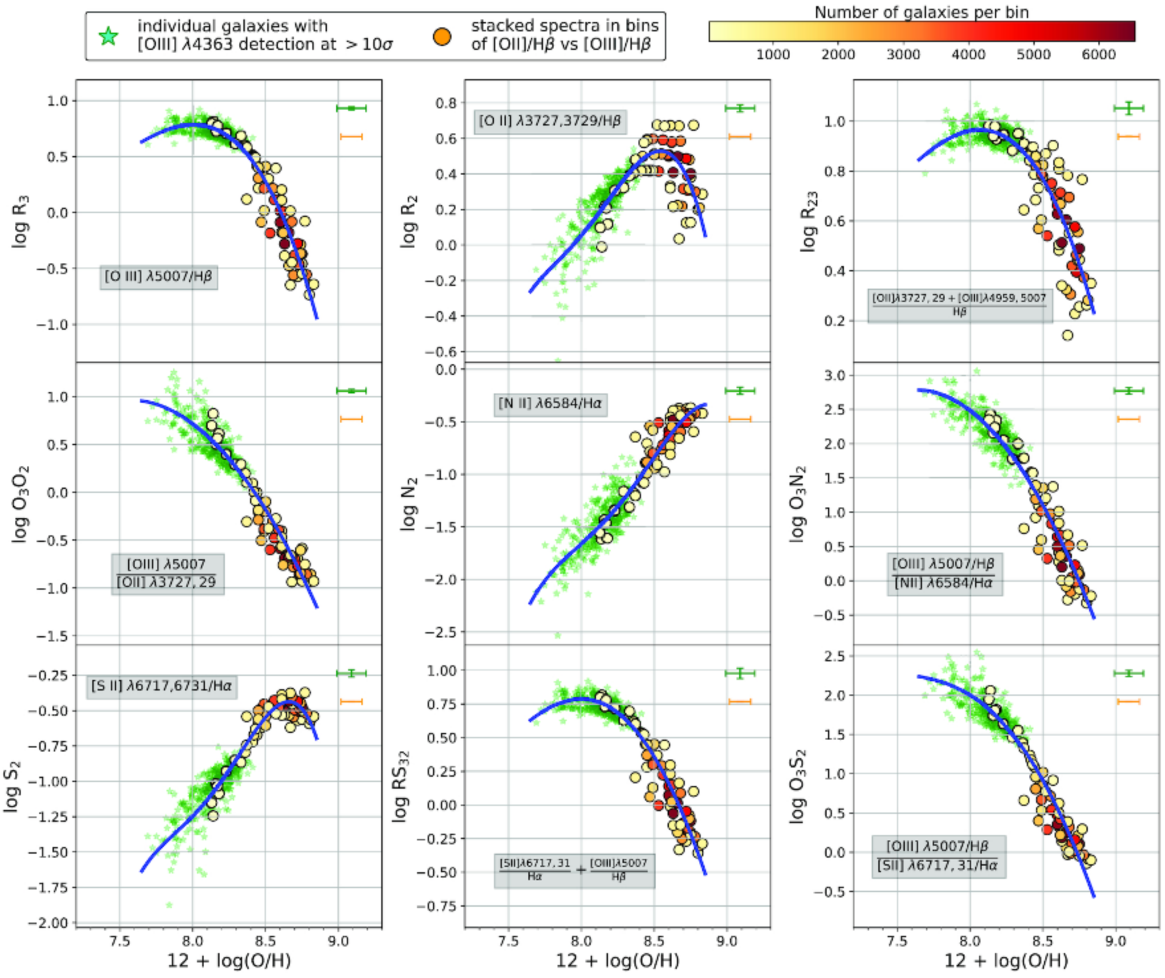

Fig. 1.8 A set of strong-line metallicity diagnostics calibrated from T$_e$-based measurements of oxygen abundance in a combined sample of individual galaxies (green stars) and stacked spectra (circular points, colour-coded by the number of galaxies per stack). Credit: Curti et al. (2020a).

fixed O/H that can introduce uncertainties into the metallicity determination. Furthermore, the cosmic evolution of this relationship is poorly constrained, with studies of galaxies at $z \sim 2$ finding N2 values that are systematically greater than those observed in local galaxies (Steidel et al., 2014; Shapley et al., 2015; Kashino et al., 2017; Strom et al., 2017). This brings into question the reliability of nitrogen based metallicity indicators at low metallicities and high redshifts.

Strong line calibrations: N/O

The N2O2 and N2S2 diagnostics both act as tracers of the abundance of nitrogen (N/H) relative to the abundance of α-elements (α/H) (Pérez-Montero & Contini, 2009). Whilst these particular diagnostics have previously been employed as metallicity diagnostics, they are much more directly tracers of (N/α), meaning the conversion to an estimate for O/H will always rely on the assumption of an underlying N/O–O/H correlation. For example, Dopita et al. (2016) presented a metallicity calibration relying solely on a combination of the N2 and N2S2 emission line ratios. This calibration is advantageous for determining metallicities at high-redshift as it requires observations in only one wavelength band, and is therefore free from uncertainties introduced via flux calibrations or extinction corrections. However, since both N2 and N2S2 are sensitive to the abundance of nitrogen, this calibration is strongly dependent on the underlying calibration between N/O and O/H, with the authors adopting an N/O–O/H relation calibrated using a combination of H II regions and local stars. This calibration is in fair agreement with that observed at intermediate redshifts (Pérez-Montero et al., 2013), however observations of higher-redshift galaxies have demonstrated a large scatter in N/O at a fixed metallicity (Strom et al., 2018). As such, the use of nitrogen-sensitive metallicity calibrations such as those presented in Dopita et al. (2016) may lead to systematic over-estimations of the metallicity in high-redshift galaxies that show an enhancement in N/O. Throughout this thesis, we therefore focus on nitrogen-sensitive line ratios, such as N2O2 and N2S2, as being diagnostics of the N/O ratio rather than O/H.

Similar to N2, the N2S2 diagnostic is advantageous due to the small wavelength separation between the [N II]λ6584 and [S II]$\lambda\lambda$6716,32 emission lines that enables observations in only a single wavelength band and also provides an index that does not rely on an extinction correction. For this reason, many existing works that study the N/O ratio at high redshift rely on the N2S2 diagnostic (Pérez-Montero et al., 2013; Steidel et al., 2014; Masters et al., 2016; Kashino et al., 2017). In contrast, the N2O2 ratio is made up of emission lines, [N II]λ6584 and [O II]$\lambda\lambda$3727,29, that have a large separation in wavelength. This makes it more difficult to determine than N2S2 as simultaneous observations over a wide range of wavelengths are required. Furthermore, an extinction correction is vital to the use of this diagnostic, increasing uncertainties and necessitating the detection of additional emission lines such as Hα and Hβ. Nevertheless, N2O2 is a robust tracer of N/O as the [N II]λ6584 and [O II]$\lambda\lambda$3727,29 emission lines have similar ionisation potentials, hence their ratio has little dependence on the ionisation parameter. By contrast, [S II]$\lambda\lambda$6716,32 has a lower ionisation potential, meaning N2S2 is more sensitive to changes in the ionisation parameter. As such, N2S2 traces N/O only under the assumption that [S II]$\lambda\lambda$6716,32 does not suffer large deviations from [O II]$\lambda\lambda$3727,29.

However, those studies that have been able to measure N2O2 at $z \sim 2$ (Strom et al. 2017, 2018), have suggested that an offset may exist between the N/O values derived from N2O2 relative to N2S2 at high redshifts. The cause of this offset is unknown. Strom et al. (2018)

suggested the offset may be caused by local SDSS galaxies having enhanced [S II] values due to contributions to nebular spectra from diffuse ionised gas (DIG), however Mannucci et al. (2021) found no evidence of DIG contamination in local galaxies. Alternative drivers of the offset, such as different stellar sources of sulphur relative to oxygen (see Section 1.3) or differences in the ionisation conditions of H II regions, are considered in more detail within this thesis.

Impact of calibration sample

Empirical calibrations of chemical abundances can be biased depending on differences between the sample that they are applied to and the underlying sample that has been used to create the calibration. Fundamentally, strong line calibrations are most reliable when they are applied to the same category of objects that have been used for their calibration. However, when considering high-redshift objects, the lack of auroral line detections currently available at high redshift means that direct metallicity calibrations are not yet attainable for these samples. Nevertheless, recent work by Sanders et al. (2021) investigated the reliability of several locally calibrated metallicity diagnostics when applied to high-redshift samples, including the calibrations of Curti et al. (2020a) (shown in Figure 1.8) based on local galaxies, as well as other calibrations such as those from Bian et al. (2018), which are based on samples of local high-redshift analogues chosen to have similar ionisation conditions to those expected at high-z. Both of these calibrations are found to show good agreement with the measurements of high redshift galaxies for oxygen-based metallicity diagnostics (O32, R23, R3, R2). However, it should be noted that this does not imply that all calibrations based on local galaxies perform well at high-redshift. As noted by Sanders et al. (2020), the Curti et al. (2020a) calibrations are unique in that the sample is biased towards individual galaxies in which the [O III]λ4363 can be detected. The calibrations are therefore similar to those of Bian et al. (2018) in that, at low metallicities, they are based upon extreme $z \sim 0$ galaxies with high excitations and specific star formation rates that represent conditions more similar to what we expect at $z \sim 2$.

1.4.3 Metallicity scaling-relations

Mass-metallicity relation

Within local star forming galaxies, a tight correlation is observed to exist between the gas-phase metallicity and the stellar mass (mass-metallicity relation, or MZR) (Tremonti et al., 2004). As shown in the left hand panel of Figure 1.9, this relationship is extremely

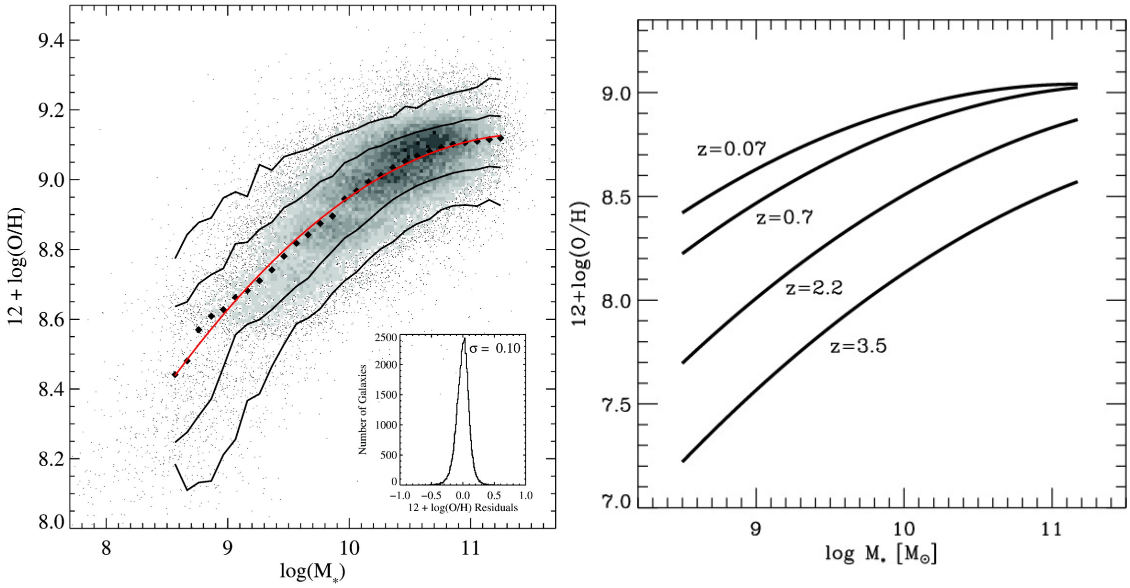

(a) (b)

Fig. 1.9 Relationship between stellar mass and gas-phase metallicity, (a) for a sample of galaxies in the local Universe and (b) for star forming galaxies across different cosmic epochs. Credit: (a) Tremonti et al. (2004) and (b) Maiolino et al. (2008).

tight, with a scatter typically on the order of ∼0.1 dex, and extends over several orders of magnitude in stellar mass. In general, the MZR extends across a wide range of stellar masses, increasing with metallicity up to $M_\star \sim 10^{10}$ $M_\odot$, above which the relationship flattens, although ultimately the shape and normalisation of the MZR are dependent on the choice of metallicity diagnostic. The increase in metallicity towards high stellar masses may imply that more massive galaxies represent more chemically evolved systems, and may also be more capable at retaining more metals they produce due to their deeper gravitational potentials. In contrast, metals within low mass systems with smaller potential wells may be driven out of the galaxies by galaxy-wide winds driven by AGN or supernovae. Similarly, low mass galaxies may be in an earlier stage of their evolution and may be rich in metal-poor gas that is yet to be used to fuel star formation.

The MZR has also been observed to exist up to z ∼3, albeit with clear signs of evolution. In particular, the normalisation of the MZR is found to decrease monotonically at a given stellar mass towards earlier times. As shown in the right-hand panel of Figure 1.9, the result is that high redshift galaxies tend to be less metal-rich than their low redshift counterparts. This evolution is often explained by differences in the gas content of galaxies across cosmic time. High-z galaxies are predicted to be more gas-rich than those seen locally, and are also expected to have increased levels of star formation that correspond to more efficient outflows that are effective at removing metals from the galaxy (Sanders et al., 2021).

Fundamental metallicity relation

Extending beyond two dimensions, the scatter in the MZR has also been shown to correlate with different galaxy properties. As shown in the left-hand panel of Figure 1.10, an anti-correlation exists where the star formation rate increases as the gas-phase metallicity decreases at a fixed stellar mass. By accounting for the scatter in the MZR using the star formation rate, it is possible to define three dimensional surfaces in metallicity, stellar mass and SFR that show a smaller scatter than the MZR alone. As demonstrated in the right-hand panel of Figure 1.10, several works have suggested that this three dimensional relationship holds out to $z \sim 3$, with the lower metallicity of high-z galaxies at a fixed stellar mass expected as a consequence of their higher star formation rates (Mannucci et al., 2010; Curti et al., 2020a; Sanders et al., 2021). In this way, the redshift evolution of the MZR represents a 2D projection of the three dimensional relationship between metallicity, stellar mass and SFR. Due to this redshift invariance, this relationship is often referred to as the fundamental metallicity relation (FMR). The reduced scatter around the FMR, estimated to be as small as 0.05 dex, suggests that the chemical evolution of galaxies is a smooth, secular process that is consistent across cosmic time, with the same physical processes governing the relationship between metallicity, stellar mass and SFR at high and low redshifts. Galaxies are believed to 'surf' along this three dimensional surface, driven by accretion of fresh gas diluting the metallicity and fuelling fresh star formation, which can drive outflows that push metals out of a galaxy whilst enriching the galaxy with new metals over time.

1.4.4 N/O scaling-relations

N/O versus stellar mass

The abundance of nitrogen can be used in addition to, and in conjunction with, the gas-phase metallicity in order to gain further insights into galaxy evolution. As discussed in Section 1.3, oxygen is primarily a product of massive stars and traces the chemical abundance by virtue of being the most common heavy element in the ISM relative to hydrogen. In contrast, nitrogen has a much more complex production history. It can be both a primary or secondary nucleosynthetic product, depending on the metallicity of the galaxy in which it resides. Furthermore, nitrogen is expected to be predominantly produced by low- and intermediate-mass stars, which have longer lifetimes than their low mass counterparts, meaning that

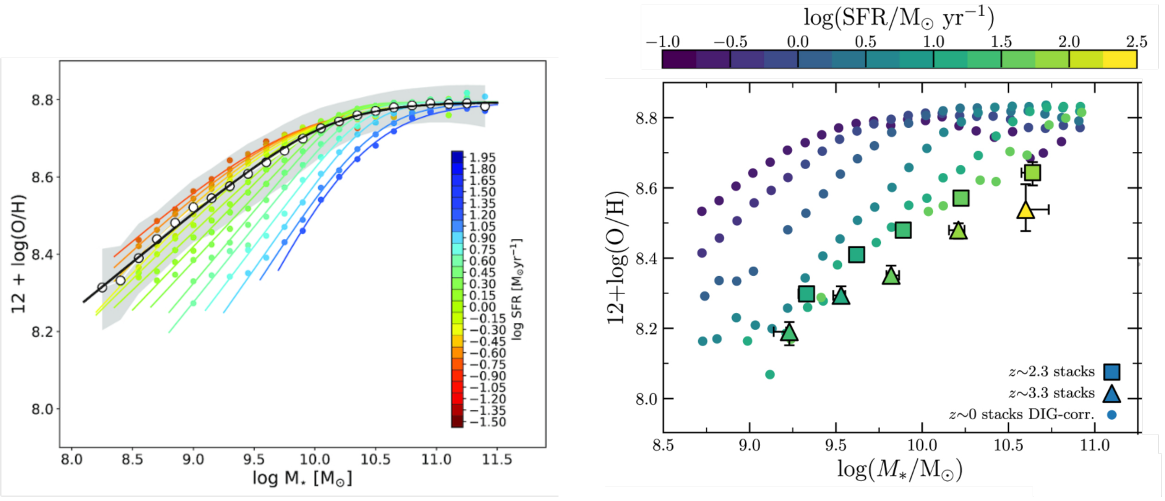

(a) (b)

Fig. 1.10 Secondary dependence of the scatter in the MZR on SFR shown for a sample of galaxies in the local Universe in (a) 2D and (b) 3D, including measurements of galaxies at high redshift. Adapted from (a) Curti et al. (2020a) and (b) Sanders et al. (2021).

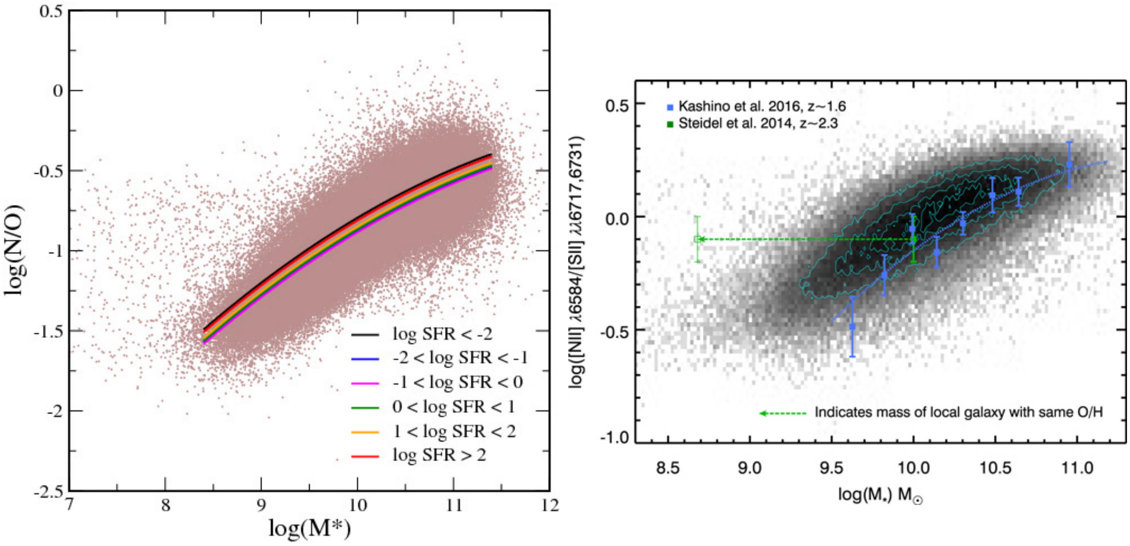

(a) (b)

Fig. 1.11 Relationship between N/O and stellar mass for galaxies in the local Universe. Comparisons are made to: (a) tracks of constant star formation rate, and (b) measurements of high-redshift galaxies. Credit: (a) Pérez-Montero et al. (2013) and (b) Masters et al. (2016).

following an episode of star formation the release of nitrogen into the ISM will be delayed relative to oxygen. Therefore, the N/O ratio acts as a time-sensitive probe of the recent chemical enrichment within a galaxy. Within this section, we outline the scaling relations of the N/O ratio with other galaxy properties, highlighting how these can be used to gain an insight into galaxy evolution.

Firstly, in an analogy to the scaling relations discussed in Section 1.4.3 for the gas-phase metallicity, it can be insightful to consider the N/O abundance of galaxies relative to the stellar mass. Indeed, as shown in Figure 1.11, a correlation between N/O and stellar mass is found to exist in nearby galaxies, with more massive galaxies being more enriched in nitrogen relative to oxygen. Just as the gas-phase metallicity of high-mass galaxies may mean these galaxies represent a more mature stage of chemical enrichment compared to low-mass galaxies, the same logic can apply to the N/O ratio. More massive, evolved systems may have existed for longer times, allowing sufficient enrichment of the ISM by LIMS and allowing several generations of stars to form from increasingly enriched gas, boosting the production of nitrogen at the expense of oxygen. As shown in the left-hand panel of Figure 1.11, Pérez-Montero et al. (2013) investigated whether a secondary dependence on the SFR, as exists for the MZR, also exists in the N/O–$M_\star$ plane. The authors found only a very mild dependence on star formation rate, suggesting N/O responds differently to O/H in relation to the physical processes of galaxy formation that govern the FMR.

The lack of a secondary dependence on the SFR may also suggest that the N/O–$M_\star$ relation is redshift-invariant, which has been suggested by several authors (Andrews & Martini, 2013; Masters et al., 2016). In this scenario, due to the redshift evolution of the MZR from $z \sim 2$ to the present day, we would also expect significant evolution in the relationship between N/O and O/H, as high mass galaxies that show a decrease in O/H would still maintain high N/O values. The right-hand panel of Figure 1.11 is an example of local N/O abundances compared to those found for local galaxies. The relationship between N/O and stellar mass is still observed to exist, with a very mild offset to lower N/O at a fixed stellar mass for galaxies at $z \sim 2$ relative to those observed locally. This modest evolution is suggested to be a consequence of age. Galaxies at a given stellar mass at $z \sim 2$ may be younger than those of an equivalent mass in the present day, and have therefore undergone less latent enrichment of nitrogen into the ISM.

The results summarised above rely on the use of the N2S2 diagnostic to probe the N/O ratio. As highlighted in Section 1.4.2, the use of this diagnostic as a tracer of N/O at high redshift may be misleading. Indeed, work that has adopted the N2O2 diagnostic instead has suggested a more prominent evolution in the N/O–$M_\star$ plane (Strom et al., 2017). Further work is undertaken within this thesis to determine whether the N/O–$M_\star$ relationship is truly redshift invariant.

N/O versus O/H

Multiple studies have investigated the N/O–O/H relation in nearby galaxies (Andrews & Martini, 2013; Pérez-Montero & Contini, 2009; Pérez-Montero et al., 2013). As usual, differences in absolute parameterisations of this relationship vary depending on the samples studied and the choice of corresponding abundance diagnostics. Nevertheless, the qualitative form of the relationship remains consistent.

At high metallicities above 12+log(O/H)>8.5, the region in which most local galaxies lie, the relationship is a simple, positive correlation. This is driven by the underlying secondary production of nitrogen within stars. As galaxies become more rich in oxygen, they produce more nitrogen as a consequence of the CNO cycle. However, in order to predict the value of the slope in high-metallicity regime, models have invoked different physical processes. Vincenzo et al. (2016b) demonstrated that differential outflows, driven by winds that preferentially expel oxygen from the galaxy relative to nitrogen, can be used to explain the local trend of the N/O–O/H relationship. Alternatively, more recent work by Vincenzo & Kobayashi (2018) suggests that the trend observed for local galaxies can be reproduced by hydrodynamical simulations so long as the most massive stars, with $M_\star > 25\ M_\odot$, end their lives as failed supernovae, meaning that they enrich the ISM only with those elements that are synthesised in the outermost shells of the star (H, He, C, N), with all remaining elements falling into the remnant black hole.

At low metallicities, the N/O ratio remains constant, showing little variation with O/H. Within this region, the underlying nitrogen production is expected to be dominated by primary nucleosynthetic processes. However, uncertainties do remain regarding the stellar source of nitrogen within this region. Early work by Matteucci (1986) suggested primary production of nitrogen in massive stars could dominate the production at low metallicities. Similarly, Chiappini et al. (2005) suggested the low-metallicity plateau can be reproduced by invoking high levels of stellar rotation in massive stars. Variable levels of stellar rotational velocities could then be invoked to explain the scatter in N/O in the primary regime. However, the authors note that AGB stars are also capable of producing large amounts of primary nitrogen, and more recent models are able to reproduce the low-metallicity plateau without invoking stellar rotation, with primary nitrogen production instead resulting from AGB stars. The scatter in N/O would then be dependent on the galaxy formation time and star formation history of the galaxy (Vincenzo & Kobayashi, 2018). The models of Vincenzo et al. (2016b), shown in the left-hand panel of Figure 1.12, further suggest that scatter of N/O at low O/H

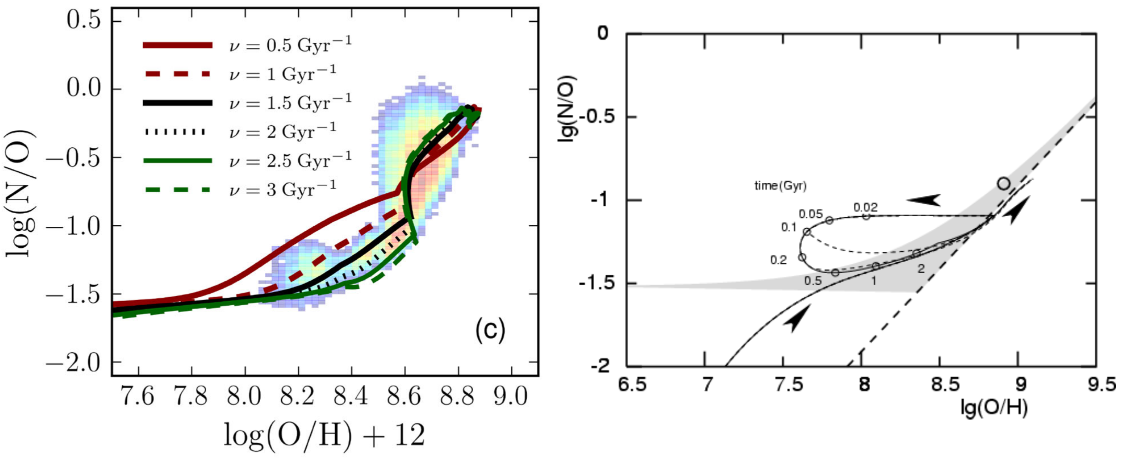

(a) (b)

Fig. 1.12 Relationship between N/O and O/H for galaxies in the local Universe alongside chemical evolution models. (a) Tracks indicate individual galactic chemical evolution tracks modelled assuming a range of different star formation efficiencies. (b) Models showing the deviation from the average N/O–O/H relation driven by the accretion of fresh gas. Credit: (a) Vincenzo et al. (2016b) and (b) Köppen & Hensler (2005).

can be explained by variations in the star formation efficiency of the galaxy, with galaxies that are less efficient at forming stars taking a long time to enrich their ISM in oxygen, therefore allowing the delayed enrichment of nitrogen at lower metallicities. The high scatter in N/O has not only been observed locally, but also at $z \sim 2$ (Strom et al., 2018). The driver of this scatter remains uncertain, but there are recent suggestions that $z \sim 2$ galaxies are old enough to have seen substantial enrichment from LIMS, meaning the scatter could be driven by variable levels of contribution to nitrogen enrichment from these stars (Strom et al., 2022).

It has also been suggested that the N/O–O/H plane can be used to investigate the impact of gas inflows onto a galaxy. In theory, if a galaxy is diluted with pure-pristine hydrogen gas, it will cause a decrease in the observed O/H. However, since no oxygen or nitrogen is introduced, the N/O ratio should remain constant. This would drag the galaxy away from the well defined N/O–O/H relation, towards the top left region of the plane. In line with the interpretation of the FMR, freshly accreted gas would be expected to fuel fresh star formation. Indeed, observations have shown that local galaxies with low metallicities and high N/O ratios have elevated levels of star formation in line with this theory (Andrews & Martini, 2013). Once this star formation begins to re-enhance the ISM with oxygen, the galaxy would begin to loop around, rejoining the main N/O–O/H relationship, as demonstrated by models from Köppen & Hensler (2005) in the right-hand panel of Figure 1.12 (and similarly by Belfiore et al. (2015) for individual, spatially resolved local galaxies). The exact timescales for the deviation from the average N/O–O/H relationship are strongly dependent on the properties of the modelled accretion, including the mass of infalling gas, the star formation prescriptions and the duration of the accretion event, with Köppen & Hensler (2005) finding long accretion episodes associated to timescales of $\sim$1 Gyr are necessary to reproduce excursions towards lower N/O values. If dilution from pristine gas is expected to play an important role in the evolution of galaxies as pertains to the FMR, then signatures of the accretion events should be visible in this plane.

1.5 Integral field spectroscopy of galaxies

The advent of large surveys utilising integral field spectroscopy (IFS) has allowed the spatial mapping of nebular regions in galaxies on scales that were not previously attainable, providing new observations about the distribution of star formation and metals within galaxies that can be used to gain further insights into the formation and evolution of galaxies across cosmic time.

Over the past decade, several IFS surveys including SAMI (Croom et al., 2012), CALIFA (Sánchez et al., 2014) and MaNGA (Bundy et al., 2015) have assembled spatially resolved observations for thousands of local galaxies. Further samples of resolved galaxies at higher redshifts have also been made attainable through the development of near-infrared IFS instruments that enable detection of the rest-frame optical nebular emission lines. Large telescopes such as the VLT have been equipped with instruments like KMOS (Sharples et al., 2013) and SINFONI (Eisenhauer et al., 2003) that have been utilised to determine resolved properties of galaxies out to $z \sim 2$ (Troncoso et al., 2014; Wuyts et al., 2016; Förster Schreiber et al., 2018). However, near-infrared IFS surveys are not straightforward. Ground-based observations in the infrared are subject to strong background emission, driven by atmospheric thermal emission and bright OH sky lines that affect the sensitivity of the observations and make measurements challenging. Furthermore, observations can be complicated by the deep atmospheric absorption bands that mean spectral coverage is often discontinuous. When observations are taken across several different bands, care must be taken to ensure reliable flux corrections within each band, and similarly on a spatially resolved scale additional efforts must be made to align images.

1.5.1 Gravitational lensing

Gravitational lensing is a profound result of Einstein's theory of general relativity. Massive objects distort spacetime, causing curved geometries that cause the path of light to bend as it travels. Therefore, astronomical objects such as galaxy clusters, which have massive gravitational potentials, can distort the light from distant galaxies that lie behind them along the same line of sight. Since these galaxies emit light in all directions, the lensing effect can cause many paths of light to converge onto us, the observer, creating an image of the source galaxy that appears brighter and larger than the source. Furthermore, when the light follows multiple paths this can also produce multiple images of the same galaxy, and can smear and elongate the image into a blur or ring. In the context of observing high redshift galaxies, gravitational lensing can provide an increased sensitivity and resolution, allowing the observer to capture fainter, more distant objects than is conventionally possible. Several IFS surveys of galaxies at high-redshift now employ gravitational lensing in order to enhance their observations (Mason et al., 2017; Girard, M. et al., 2018).

1.5.2 Resolved abundance gradients

Metallicity gradients

The spatial distribution of metals within galaxies can be used to gain further insight into their formation and evolution. IFS surveys such as CALIFA have found that metallicity gradients in local galaxies tend to be negative, flattening at large radii. This is broadly believed to be consistent with an inside-out growth scenario of galaxy evolution, in which central bulges form first and are therefore more chemically evolved at a later time, with the level of local metal enrichment driven by the local star formation history (Sánchez et al., 2014). Belfiore et al. (2017) built on this work using MaNGA to show that metallicity gradients of star forming galaxies have a strong dependence on the stellar mass of the galaxy, as shown in the left-hand panel of Figure 1.13. For low-mass galaxies, the metallicity gradient is close to flat, whilst gradients become increasingly steep with increasing stellar mass (Poetrodjojo et al., 2018). IFS surveys also find evidence of a flattening of the O/H gradient in the most central regions of local galaxies, which may be a consequence of the most massive, central regions of galaxies being chemically mature, and therefore saturating in metallicity (Zinchenko et al., 2016).

At high redshift, it is much harder to measure metallicity gradients in the outer regions of galaxies due to the low surface brightness driving low S/N of emission lines. As such, for most high-z studies gradients are only marginally resolved. Improvements to resolution can be made by using gravitational lensing to magnify objects, however this comes at a cost of additional uncertainties introduced by the lens modelling that is required to properly determine the spatial distribution of the galaxy. Since spectral coverage of near-infrared IFS surveys are often discontinuous, it is common for studies of high-z objects to rely on

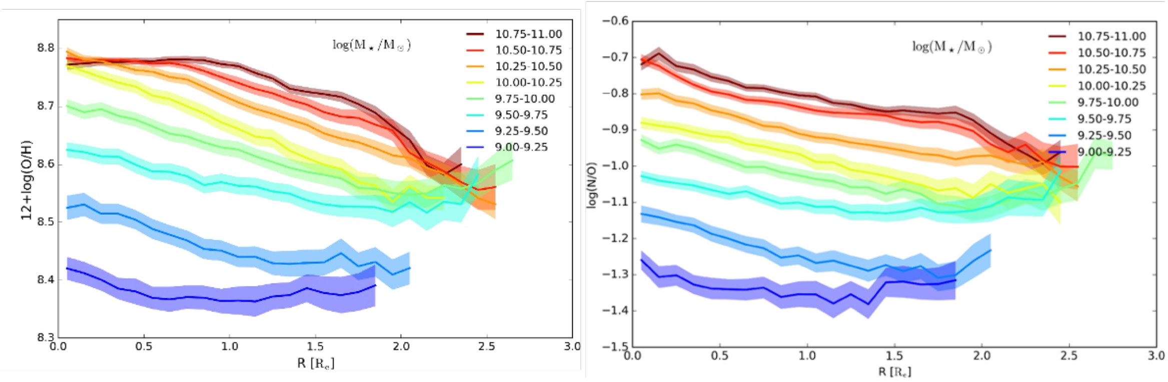

Fig. 1.13 Average gradients in O/H (left) and N/O (right) for local star forming galaxies, split into several bins of stellar mass. For both O/H and N/O, more massive galaxies are characterised by steeper abundance gradients. Credit: Belfiore et al. (2017).

single line diagnostics to trace metallicity, such as N2 (Wuyts et al., 2016; Förster Schreiber et al., 2018). As discussed in Section 1.4.2, the use of only a single diagnostic can lead to the introduction of uncertainties in the metallicity determination. This is particularly the case for nitrogen-based diagnostics that rely on an assumption of an underlying N/O–O/H relationship, which is currently poorly constrained observationally at high-z. Nevertheless, Wuyts et al. (2016) and Förster Schreiber et al. (2018) both find metallicity gradients at $z \sim 2$ that are flatter than those observed locally. Within the context of an inside-out growth model for galaxies, flatter metallicity gradients at earlier times could be indicative of enhanced feedback within galaxies effectively mixing metals within the ISM. However, unlike in local galaxies, no clear dependence of the O/H gradient on stellar mass has been observed at high redshift (Stott et al., 2014; Wuyts et al., 2016).

At higher redshifts still ($z \sim 3$), inverted gradients are found, meaning the metallicity is lower in the centre of the galaxies than in the outskirts. Cresci et al. (2010) noted that the metallicity dilution in the centre of the galaxy is also associated with an enhancement in the central star formation rate. This gradient could therefore be an effect of the inflow of metal-poor gas toward the centre of galaxies, diluting the metallicity and fuelling new star formation (Troncoso et al., 2014). A similar effect has been observed at $z \sim 1$, where inflows drive metallicity dilution in the central region of the galaxy whilst boosting the sSFR. (Stott et al., 2014)

N/O gradients

In local galaxies and H II regions, the N/O gradient is observed to behave similarly to the O/H gradient, with gradients that are generally negative (Berg et al., 2013, 2015; Rogers et al., 2021). As highlighted in the right-hand panel of Figure 1.13, Belfiore et al. (2017) found that N/O gradients steepen with stellar mass and flatten towards the outer region of the galaxy, similar to metallicity. However, unlike O/H, N/O is not observed to flatten in the central regions of galaxies. Whilst the central regions of massive galaxies may have reached a metallicity equilibrium, N/O may still be increasing due to the delayed production of nitrogen relative to oxygen. However, individual galaxies can show a wide variation in N/O gradients, with Pérez-Montero et al. (2016) suggesting that between 4-10% of nearby star forming galaxies have gradients in N/O that are flat or inverted. Indeed, observations of the Milky Way find a flat N/O gradient that may suggest nitrogen production within the Galaxy is dominated by primary processes (Esteban & García-Rojas, 2018). As of yet, little to no literature exists on N/O abundance gradients in high redshift galaxies. This is in part due to the difficulty in observing several rest-frame optical emission lines simultaneously at high-redshift, particularly on a spatially resolved basis, meaning diagnostics such as N2O2 have previously been unattainable in this context.

1.6 Motivation and aims for the thesis

It is clear that gas-phase chemical abundances are a key property to consider in the context of understanding the mechanisms that drive the growth and evolution of galaxies across cosmic time. Within this thesis we investigate the evolution of the chemical abundances in galaxies, utilising large samples of local galaxies from SDSS and MaNGA, and extending to higher redshifts using data obtained in the framework of the KLEVER survey, introduced in Chapter 2.

In Chapter 3 we analyse the scaling relations of N/O with many other galaxy properties including gas-phase metallicity, stellar mass and star formation rate, on a galaxy-integrated basis. We compare observations of the local scaling relations to those observed in high redshift galaxies at $z \sim 2$ to investigate how the physical properties of galaxies may evolve across cosmic time. We then discuss our results in the context of our current understandings of the evolution of scaling relations, before providing a comparison to chemical evolution models. In Chapter 4 we extend our analysis to the spatially resolved scale, taking advantage of the broad wavelength coverage of the KLEVER survey to investigate the spatial variation of N/O in galaxies at high redshift, and presenting some of the first ever measurements of N/O gradients at $z \sim 2$. We compare our observations to those found locally, and interpret these results in the context of inside-out growth models of galaxies and potential bulge growth within galaxies. Finally, we discuss the different results that are obtained when using either N2S2 or N2O2 to derive the N/O abundance gradients, highlighting the need for future observations with improved signal-to-noise and spatial resolution to investigate this discrepancy further. In Chapter 5 we highlight the properties of galaxies that are offset from the local N/O–O/H relation. We then investigate the role that gas accretion may play in driving offsets from the local N/O–O/H relationship using a simple gas-mixing model. We study whether this model is able to reproduce both the expected magnitude and direction of the observed offset, before discussing how further improvements to our simple model may be required to better interpret the observed trends. Finally, in Chapter 6 we summarise the main conclusions of this thesis, before discussing prospects for future work.

Chapter 2

The KLEVER survey

2.1 Introduction

2.1.1 IFS surveys at high redshift

As introduced in Section 1.5, over the past decade great progress has been made in obtaining spatially resolved observations for large samples of local galaxies. Whilst similar programmes have been undertaken towards higher redshifts, they have not been without their own limitations. Many of the IFS observations that exist at $z \sim 2$ have been limited to only a single wavelength band, motivated by the expensive integration times necessary to capture spectra at high redshift using ground based spectroscopy. As a consequence, many IFS studies have focused on exploiting observations in the single band where Hα is redshifted to investigate the kinematics of high-redshift galaxies, e.g. KMOS^{3D} (Wisnioski et al., 2015), KROSS (Stott et al., 2016), KLASS (Mason et al., 2017) or study the impact of AGN, e.g. KASHz (Harrison et al., 2016). Without the simultaneous detection of several rest-frame optical emission lines across multiple wavelength bands, it is difficult to determine galaxy properties such as the chemical abundances on a resolved scale. Efforts have been made that make use of the few emission lines that are detected by single-band IFS surveys (Wuyts et al., 2016; Förster Schreiber et al., 2018), however metallicities determined using only a single diagnostic are subject to dependencies on other physical quantities such as ionisation parameter, the hardness of the ionising field (in the case, for instance, of N2) and the N/O abundance.

Moving away from IFS surveys, recently large samples of galaxies at $z \sim 2$ have been obtained with detections of the full range of rest-optical emission lines, from [O II]$\lambda\lambda$3727,29 up to [S II]$\lambda\lambda$6716,32. In particular, surveys using the MOSFIRE instrument on the Keck telescope such as KBSS (Steidel et al., 2014) and MOSDEF (Shapley et al., 2015) have produced numerous insights into the physical properties of the galaxy population at $z \sim 2$. These surveys find that galaxies at $z \sim 2$ are offset to larger values of N2 and O3 in the [N II] BPT diagram compared to their local counterparts (Steidel et al., 2014; Shapley et al., 2015; Kashino et al., 2017; Strom et al., 2017). The predominant cause of this offset is believed to be a hardening of the ionising radiation field at high-z (Steidel et al., 2014, 2016; Strom et al., 2017), driven by highly super solar oxygen-to-iron ratios that are expected for gas with enrichment that is dominated by the products of core-collapse supernovae (Steidel et al. 2016; Topping et al. 2020a, 2020b; Cullen et al. 2021). Moreover, the nebular properties of high redshift galaxies differ further from those seen locally with higher electron densities, higher ionisation parameters and enhanced N/O values at a fixed O/H (Masters et al. 2014; Shapley et al. 2015; Strom et al. 2017).

Whilst these surveys have provided progress in observing large samples of galaxies at high redshift, the lack of IFS capabilities means that they cannot provide resolved emission line maps of galaxies, as such the spatial variation of physical parameters cannot be probed in the same way as they have been for galaxy-integrated spectra. Surveys using MOSFIRE also have additional uncertainties introduced to line ratios caused by the necessary correction for slit losses within each atmospheric band. Within this Chapter, we introduce the Kmos LEnsed Velocity and Emission line Review (KLEVER) survey, an ESO Large Programme (197.A-0717, PI: Michele Cirasuolo) intended to provide spatially resolved maps of several rest-frame optical emission lines of high-redshift galaxies, enabling the spatial mapping of chemical abundances at $z \sim 2$.

2.1.2 KMOS instrument

This thesis makes extensive use of data collected using the K-band Multi-Object Spectrograph (KMOS, Sharples et al. 2013), a second-generation instrument installed at the Naysmith focus of the 8.2 m Unit telescope 1 (UT1) on the Very Large Telescope (VLT). KMOS is a near-infrared integral field spectrograph with a total of five gratings/filters (IZ, YJ, H, K, HK), providing wavelength coverage from 0.778–2.471 μm. In particular, the work within this thesis makes use of the YJ-, H- and K-band gratings/filters, which yield spectral resolutions of $R = \lambda/\Delta\lambda = 3582$, 4045 and 4227 over the spectral ranges of 1.016–1.353, 1.445–1.859 and 1.934–2.473 μm, respectively.

As a multi-object spectrograph, KMOS has 24 individual telescopic pick-off arms, each made up of a pick-off mirror and associated relay optics, as shown in Figure 2.1. These arms can operate simultaneously within a circular patrol field with a 7.2 arcminute diameter. Each pick-off arm feeds an individual Integral-Field Unit (IFU) with a field of view of 2.8 × 2.8 arcseconds and a default pixel scale of 0.2 × 0.2 arcseconds. Light collected from

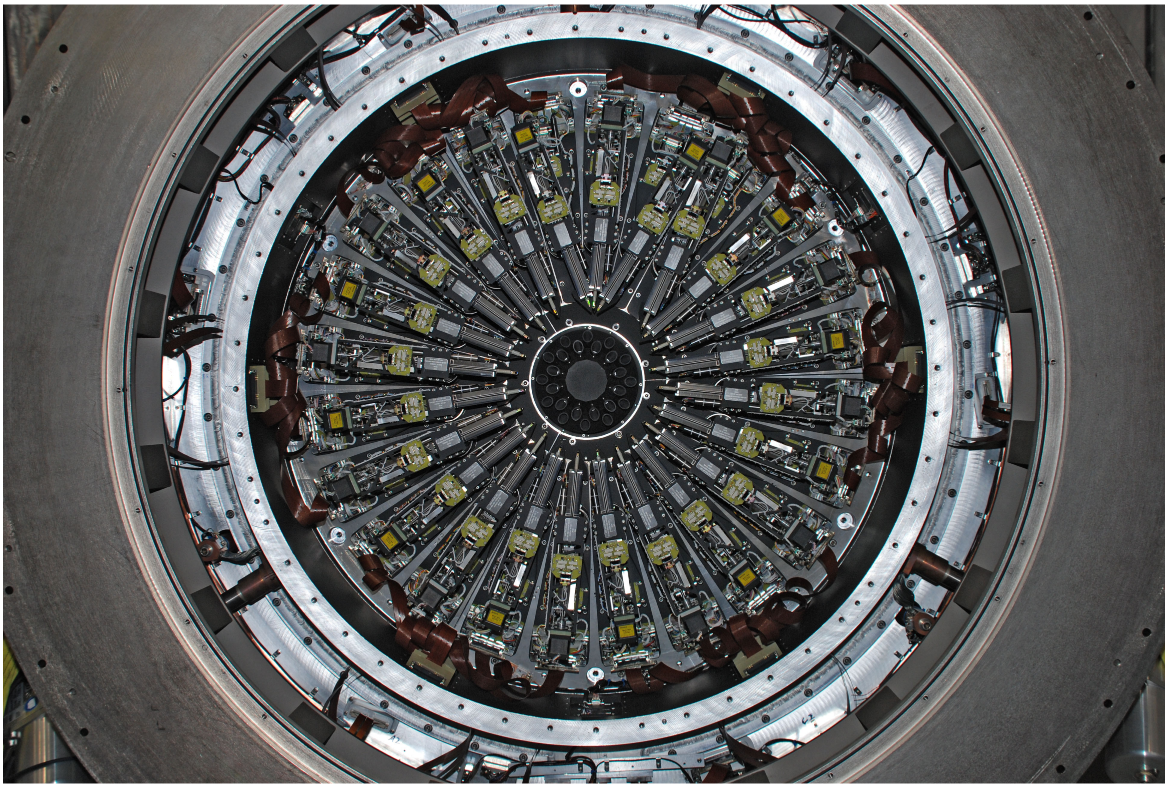

Fig. 2.1 Image of the KMOS instrument showcasing the 24 configurable arms that can be used to target multiple objects simultaneously. Credit: ESO.

each IFU is thereby sliced into 14 identical slices, each made up of 14 spatial pixels. KMOS is comprised of three independent modules, each made up of a spectrograph and a Hawaii 2RG HgCdTe detector. To feed light into each module, the 24 IFUs are divided into three groups, each made up of 8 IFUs. The slices from these 8 IFUs are aligned into a single pseudo-longslit before being fed into the spectrograph, which disperses the light onto the detector. The raw data obtained from each detector then consists of 8×14 sets of standard 2-dimensional slit spectra, arranged next to one other on the detector and separated by a few blank pixels.

2.2 KLEVER survey: observations and data

2.2.1 Sample selection

The key aim of the KLEVER survey is to obtain simultaneous detections of several rest-frame optical emission lines for multiple galaxies at $z\sim2$, requiring observations to be taken across the YJ-, H- and K- band filters. The multiplexing capabilities of KMOS aid in the accumulation of large samples of galaxies at high redshift, however large integration times of at least a few hours per source in each band remain necessary due to the decrease in surface brightness of emission lines with increasing redshift, which scales as $(1+z)^{-4}$. To mitigate this issue, KLEVER takes advantage of existing K-band observations obtained in the context of the KMOS^{3D} survey (Wisnioski et al., 2015), which observed galaxies identified as being star-forming from the 3D-HST Treasury Survey (Brammer et al., 2012; Skelton et al., 2014). The KLEVER survey is therefore, in part, composed of a sub-sample of galaxies from both the KMOS^{3D} and 3D-HST surveys that have confirmed detections of the Hα emission line. In this way, targets within the KLEVER sample are Hα-selected, in contrast to existing high redshift surveys such as KBSS which are rest-UV selected. Selection of targets in the rest-UV may bias the underlying sample towards less massive, dust-free galaxies in which the UV-emission is brightest. By instead adopting a Hα-selection for targets, the KLEVER survey is free from these biases.

The remaining galaxies in the KLEVER sample are gravitationally lensed galaxies that lie within cluster fields from the CLASH (Postman et al. 2012) and Frontier Fields (Lotz et al. 2017) programs. In particular, lensed galaxies behind the RXJ2248.7-4431 (also known as AS1063), MACSJ0416.1-2403, MACS J1149.5+2223 and MS2137-2353 clusters were targeted. The addition of lensed objects benefits the KLEVER survey in two key ways: the magnification caused by gravitational lensing improves the spatial resolution of the targeted objects, whilst the enhanced flux sensitivity allows us to probe fainter high-redshift galaxies with lower stellar masses and star formation rates. Lensed targets were selected using spectroscopic redshift estimates from a range of sources including the CLASH-VLT survey (Rosati et al. 2014, Balestra et al. 2016), the Grism Lens-Amplified Survey from Space (GLASS, Treu et al. 2015) and VLT/MUSE spectroscopic observations of MACS J1149.5+2223 (Grillo et al. 2016). Combining the lensed and un-lensed sources, a total sample of 213 high redshift star-forming galaxies have been targeted by the KLEVER survey, with the observations described in the next section.

2.2.2 Observing strategy

KLEVER observations were taken during ESO observing periods P95-P102. A total of 132 bright, un-lensed star-forming galaxies were selected from the KMOS^{3D} survey. These galaxies are observed in the well-studied southern CANDELS (Grogin et al. 2011; Koekemoer et al. 2011) fields COSMOS, GOODS-S and UDS, ensuring excellent ancillary photometric coverage of the targets from HST as part of the CANDELS project. The majority of the targeted galaxies lie in the redshift range $z \in [2, 2.6]$ where deep K-band observations (typically a minimum of 8 hours on source) from the KMOS^{3D} survey enable robust detections of the

Type	Redshift Range	Number of galaxies	YJ-band	H-band	K-band
Un-lensed	[2, 2.6]	98	[O II]	[O III] + Hβ	Hα + [N II] + [S II]
	"	11	-	[O III] + Hβ	Hα + [N II] + [S II]
	"	5	[O II]	-	Hα + [N II] + [S II]
	[1.1, 1.7]	9	[O III] + Hβ	Hα + [N II] + [S II]	-
	"	9	-	Hα + [N II] + [S II]	-
Lensed	[2, 3.45]	33	[O II]	[O III] + Hβ	Hα + [N II] + [S II]
	[1.1, 1.7]	47	[O III] + Hβ	Hα + [N II] + [S II]	[S III]
	0.88	1	Hα + [N II] + [S II]	[S III]	-

Table 2.1 A breakdown of the observations for the full KLEVER sample. The total sample is a combination of 132 un-lensed and 81 lensed objects. The table shows which rest-frame optical emission lines are detectable in each band for objects within a given redshift range, with all redshifts confirmed by spectroscopic detections. A '-' denotes that no observations were taken in a given band.

Hα, [N II]λ6584 and [S II]$\lambda\lambda$6716,32 emission lines. In order to ensure all data within the KLEVER sample has been reduced using the same procedures, the raw K-band observations from KMOS^{3D} were re-reduced following the methodology outlined in Section 2.2.3. These observations were then supplemented with additional KLEVER observations in the YJ- and H- bands, with a typical integration time of 4-6 hours on source for each band. For those sources for which supplementary observations were made in both the YJ- and H-bands we can obtain detections of rest-frame optical emission lines from [O II]$\lambda\lambda$3727,29 up to [S II]$\lambda\lambda$6716,32. Full details of how many galaxies were observed in each band, and the corresponding emission lines that can then be observed, are shown in Table 2.1.

Unlike the un-lensed galaxies, which required supplemental observations in only two wavelength bands, observations across all three of the K-, H- and YJ-bands were necessary for the lensed galaxies. However, due to the enhanced flux sensitivity caused by gravitational lensing, shorter integration times were required for the lensed galaxies than the un-lensed, with typical on source exposure times of 11 hours in total (5 hours in the K-band and 3 hours each in both the H- and YJ-bands). We targeted lensed galaxies behind the clusters RXJ2248.7-4431 (also known as AS1063), MACSJ0416.1-2403 and MACS J1149.5+2223. As detailed in Table 2.1, 33 of the lensed targets lie in the redshift range $z \in [2, 3.45]$, where detections from [O II]$\lambda\lambda$3727,29 up to [S II]$\lambda\lambda$6716,32 allow a direct comparison to be made with the majority of the un-lensed KLEVER objects. However, 47 of the remaining lensed targets fall in the redshift range $z \in [1.1, 1.7]$, for which we can no longer detect the [O II]$\lambda\lambda$3727,29 doublet in the YJ-band, and instead gain access to the [S III]$\lambda\lambda$9068, 9530 doublet in the K-band. A further lensed target lies on its own at a spectroscopic redshift of z=0.88, allowing access to only the Hα, [N II]λ6584, [S II]$\lambda\lambda$6716,32 and [S III]$\lambda\lambda$9068, 9530 doublet emission lines.

The selection of targets for each pointing was achieved using the KARMA tool (Wegner & Muschielok, 2008). Within each pointing a maximum of 21 IFUs were allocated to targeted galaxies, with the remaining 3 IFUs assigned to nearby bright stars. The observations of these three stars, one for each detector within KMOS, allowed for precise monitoring of the evolution of the seeing conditions and shift of the telescope over the course of the observation. The utilisation of these stars in the reduction of the data is discussed more in Section 2.2.3. All individual science exposures had a duration of 300s, with an object-sky-object (OSO) nodding strategy adopted to benefit sky subtraction. A dither pattern was specified so that for each observation the target object is slightly moved around the field of view the within each IFU. This dithering strategy is adopted so that the same spectral features fall on different parts of the detector, hence minimising the effect of detector artefacts once the individual exposures are combined. Alternating dithers of 0.1 and 0.2 arcseconds, smaller than the default 0.2×0.2 arcsecond sampling, were performed for increased spatial sampling of the PSF.

2.2.3 Data reduction

The raw KMOS observations were reduced using the pipeline provided by ESO (v2.6.6) and implemented within the EsoReflex workflow environment (Freudling et al., 2013). An example of a raw detector image produced from a KMOS science exposure is shown in Figure 2.2. For a single detector, light from 8 individual IFUs, each split into 14 slitlets which themselves are made up of 14 spatial pixels, is arranged along the horizontal axis. Vertically, light within each slitlet is dispersed into 2048 wavelength channels. Emission within the raw image is dominated by OH skylines, emitted by OH molecules in the upper atmosphere of the Earth. Although each OH skyline is emitted at a certain wavelength, the emission can be seen to curve along the y-axis of the detector image, an effect caused by variations in the path length travelled by photons as they approach the detectors through the optics of the KMOS instrument. In this section I outline the main steps within the data reduction pipeline undertaken to convert the raw observations into calibrated, science-ready datacubes.

Dark frame correction

Thermal electrons can leak onto the detector pixels, in some cases causing some pixels to appear ‘hot’ even when the instrument is not exposed to a light source. These false counts could contaminate any science observations, and must therefore be removed. To achieve this, dark frame exposures are taken when the instrument is not illuminated by any light source. Several dark exposures are combined to produce a master dark frame, within which any

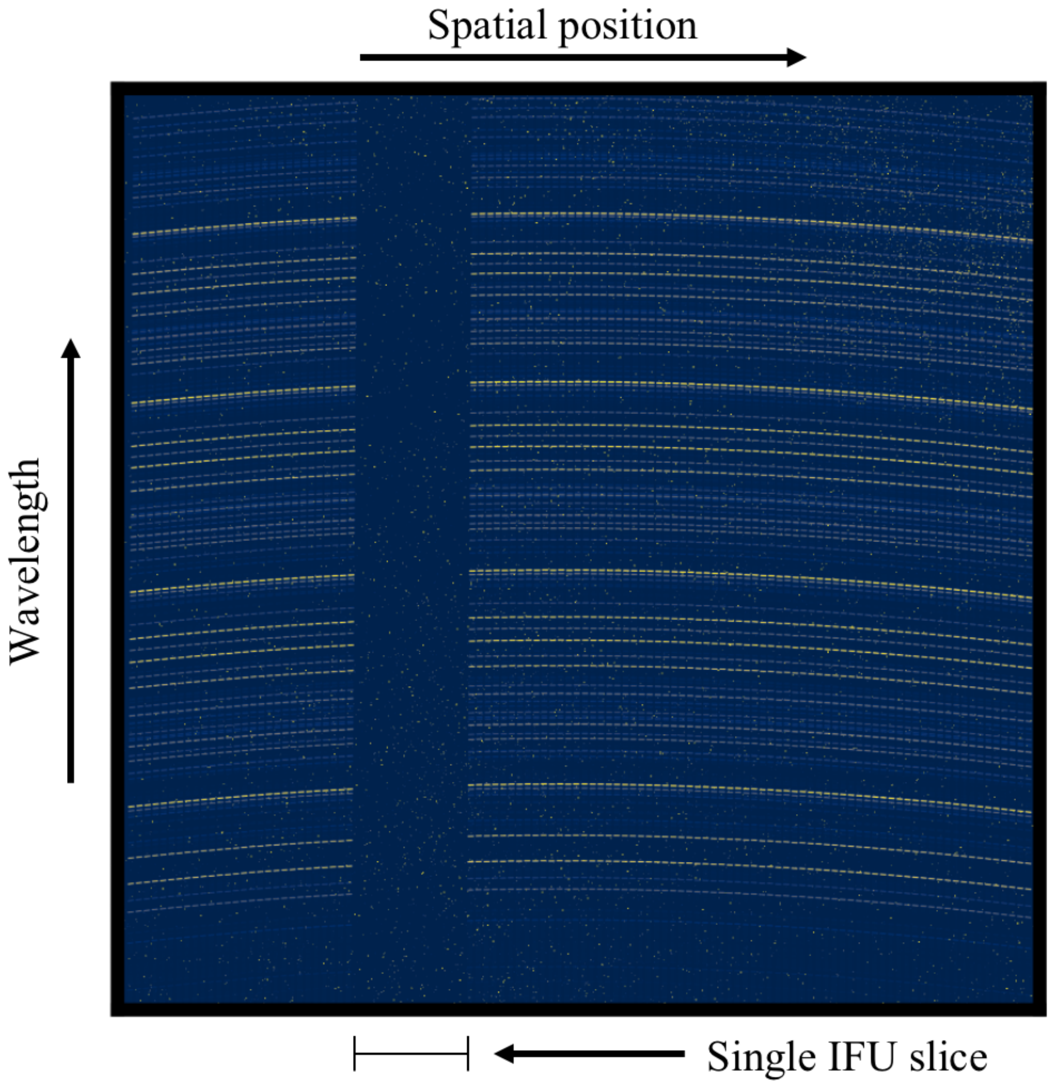

Fig. 2.2 An example of a raw KMOS science exposure in the H-band for a single detector. Horizontally, 8 IFU slices are each divided into 14 slitlets made up of 14 spatial pixels. Vertically, light within each slitlet is dispersed into 2048 wavelength channels. Prominent horizontal arcs caused by OH skylines can be seen to dominate the image, with additional hot pixels scattered about. For this exposure, the third IFU was inactive.

pixels with unphysically large count values can be identified and masked. The ‘bad’ pixel mask is then propagated throughout the rest of the data pipeline.

Flatfielding

Across the detector, different pixels may have different sensitivities to light, also as a function of wavelength. As with the dark field, having pixels that produce different responses to the same light source may introduce spatial biases into the final datacubes. Such inhomogeneous responses therefore obviously need to be corrected. To highlight the different responses of the pixels, the detector is uniformly illuminated using 2 internal lamps mounted within the KMOS instrument. These exposures produce a map of the normalised brightness across the detector which can then be used to produce a master flatfield frame to account for variations in pixel sensitivity. The desired result of these corrections is that an input uniform signal onto the detector produces a uniform output (hence a flat-field).

As the Earth rotates on its axis, the telescope must also rotate in order to track targets across the sky. In doing so, the mapping of light that passes through the optics of the instrument onto the spatial and spectral pixels of the detector can change, an issue referred to as ‘spectral flexure’. It is therefore necessary to create a master flatfield frame at a number of different rotator angles in order to match the mapping of observations taken at different rotator angles. Flatfield lamp exposures are taken at 6 different rotator angles at 60 degree intervals between 0 and 300 degrees. Science exposures are then matched to the nearest applicable rotator angle when flatfield corrections are applied.

At this stage, the x and y positions of each illuminated pixel are also calibrated in terms of sky coordinates. For each IFU, each slitlet is assigned a value depending on the offset from the centre of the field of view, measured in milliarcseconds, ranging from -1500 to +1500. This process is then repeated for each of the 14 spatial pixels within each slitlet, meaning that each illuminated pixel on the detector can be mapped back onto the 2D source plane. In addition to the flatfielding, an illumination correction was implemented at this stage. While the flatfielding step takes into account the detector’s pixel-to-pixel response variations, the illumination correction accounts for the detector not being uniformally illuminated by the lamps during the flatfield exposures. A normalised spatial image of the lamp illumination (at all rotator angles) is constructed for this purpose.

Wavelength calibration

Just as the horizontal detector pixels were mapped into spatial coordinates in the previous step of the reduction, so too must the vertical pixels be mapped into calibrated wavelength values. To achieve this, neon and argon arclamps, that emit light with precisely known wavelength values, are measured as reference frames for the wavelength. On the detector, the position of the arc lines are measured and matched to the list of known neon and argon emission wavelengths. This produces a mapping of spectral pixels onto known wavelength values, creating a wavelength solution for the entire detector. As with the flatfielding, this process must be repeated for each rotator angle to account for any instrument flexure.

Flux calibration and PSF determination

The incidence of light onto the detector is measured as electron counts, which must be converted into units of radiation flux. Therefore, analogous to the wavelength calibration, observations of reference stars with precisely known magnitudes are required. The magnitude, m, of a star is given by

$$m = -2.5\log(F_{\lambda}/F_{\lambda,0}), \tag{2.1}$$

where F_{λ} is the flux at a wavelength of λ and $F_{\lambda,0}$ is the corresponding zeropoint flux. A 'standard star' is observed by one IFU within each module, with short typical exposure times of ~2.5 seconds. Since different objects are observed at different airmasses the standard star exposures must be taken at a similar time to the science observations. Using the master frames from the reduction steps described above, a datacube for the standard star is constructed that is then collapsed over the wavelength dimension, creating a spatial image of the star that provides an estimate of the PSF of the observations. Since KMOS is mounted on a ground-based telescope, any light received must first pass through the the atmosphere as well as the telescope optics. This means results from KMOS are seeing-limited, with a PSF that causes a weighted average of the observed galaxy physical properties, spread out across a seeing disk. Whilst seeing conditions can vary between observations, overall the KLEVER sample have an average PSF of 0.5–0.6 arcseconds (FWHM).

A one dimensional stellar spectrum is extracted from the datacube of the standard star, which is then fit with an atmospheric model using the molecfit tool (Smette, A. et al., 2015; Kausch, W. et al., 2015). The ratio of the atmospheric model compared to the observations of the standard star can then be taken to generate a telluric spectrum that can be used to account for atmospheric absorption features in the scientific spectra. The zeropoint for flux calibration can then be derived by dividing the stellar spectrum by the telluric spectrum and comparing the observed flux to the known magnitude using Equation 2.1. Additional checks on the flux calibration of the KLEVER sample are discussed in Section 2.2.5.

Sky subtraction

The final step in the reduction of the raw science exposures is the sky subtraction, which is necessary in order to remove all signals not associated to the targeted objects. The adoption of an object-sky-object (OSO) nodding pattern means that each object exposure has a corresponding sky exposure, targeting a nearby empty region of sky, that can be subtracted from the science exposure. To improve the sky subtraction, we implemented the advanced sky subtraction method SKYTWEAK from Davies (2007). Within this method, the spectrum from each spaxel within a sky exposure (taken from an object-sky pair) is divided into segments. Each segment contains a set of OH emission lines that result from a particular vibrational transition and scale together in amplitude. A constant scaling factor is then applied to each set of OH lines in order to recover an amplitude that best matches the observations of OH lines in the corresponding object frame, leading to a reduction of the sky line residuals after sky subtraction.

2.2.4 Stacking procedure and cube reconstruction

The steps described above result in a flux calibrated, sky subtracted datacube for all of the 300s science exposures in each of the KMOS IFUs. These individual exposures must then be combined in order to achieve the long integration times necessary to detect rest-frame optical emission lines. The dithered positions must obviously be re-aligned before combining them. In principle this can be done by taking the dither offsets commanded to the telescope. However, over course of a single observing block (OB), the telescope can drift from its initial position due to inaccuracy of pointings and instrument flexures, causing shifts in the position of the target between different exposures relative to the nominal positions. To detect and correct for these shifts, one IFU within each module (each detector) was designated to observe a bright control star. The centroid position of this control star is measured for each exposure, with the shift between each exposure over the course of an OB recorded. The measured stellar shifts were then applied to all of the science exposures taken by all other IFUs within that same module. This methodology was applied for combining both individual exposures within a single OB, as well as when combining observations between different OBs.

The final datacubes were then created using a three-sigma clipped average over all exposures, excluding those with large seeing values (>0.8″) or unusually large shifts in the measured centroid position of the corresponding star. These datacubes contain 2 main extensions: the first containing the measured flux, and the second containing the associated noise. Finally, all datacubes were reconstructed onto a 0.1×0.1 arcsec pixel scale, which is smaller than the native sampling on the detector but allows for better sampling of the PSF exploiting sub-pixels dithers.

2.2.5 Verifying the flux calibration

The flux calibration of the final KLEVER datacubes is reliant on the quality of the flux calibration within the underlying science exposures that make up each cube. Furthermore, the flux calibration is of particular importance to the KLEVER survey since we rely on observations of emission lines that are spread across three distinct observing bands. If the flux correction in one of these bands is wrong, then it could lead to unphysical values when calculating line ratios comprised of emission lines from different bands, e.g. Hα/Hβ. For this reason, an additional check on the accuracy of the flux calibration was carried out using the bright control stars that were observed within each OB. For each control star, in each filter, a spatial image was produced by collapsing over the wavelength axis in order to observe the continuum emission. An aperture of radius $0.8''$ was centred on the image, and the total flux within the aperture was extracted. This total flux estimate was used to cross-check the estimated magnitude of the star against the corresponding magnitude provided by the 2MASS stellar catalogue (Skrutskie et al. 2006).

The results of this comparison are shown in Figure 2.3. As can be seen, the majority of KLEVER observations reproduce stellar magnitudes that are in agreement with the magnitude estimates and errors provided by 2MASS, suggesting a good degree of accuracy in the flux calibration for the full KLEVER sample.

2.3 Initial analysis

2.3.1 Spectral fitting routine

In order to identify emission lines within any spectra extracted from the KLEVER datacubes in a consistent way, it was necessary to build a spectral fitting routine. The routine was built using the least-square minimisation method from the python routine LMFIT (Newville et al. 2016). A straight line was used to define the local continuum, with the slope and normalisation allowed to vary as free parameters. Fitting of a proper stellar continuum is not required as the observed continuum is too faint and the equivalent widths of the detected emission lines are large. All emission lines within a given band were simultaneously fit with single Gaussian profile components that were linked in velocity and line width. The tying of the velocity and line widths is necessary to improve the fit to the data, and is a reasonable assumption to make as the emission is expected to originate from similar nebular regions

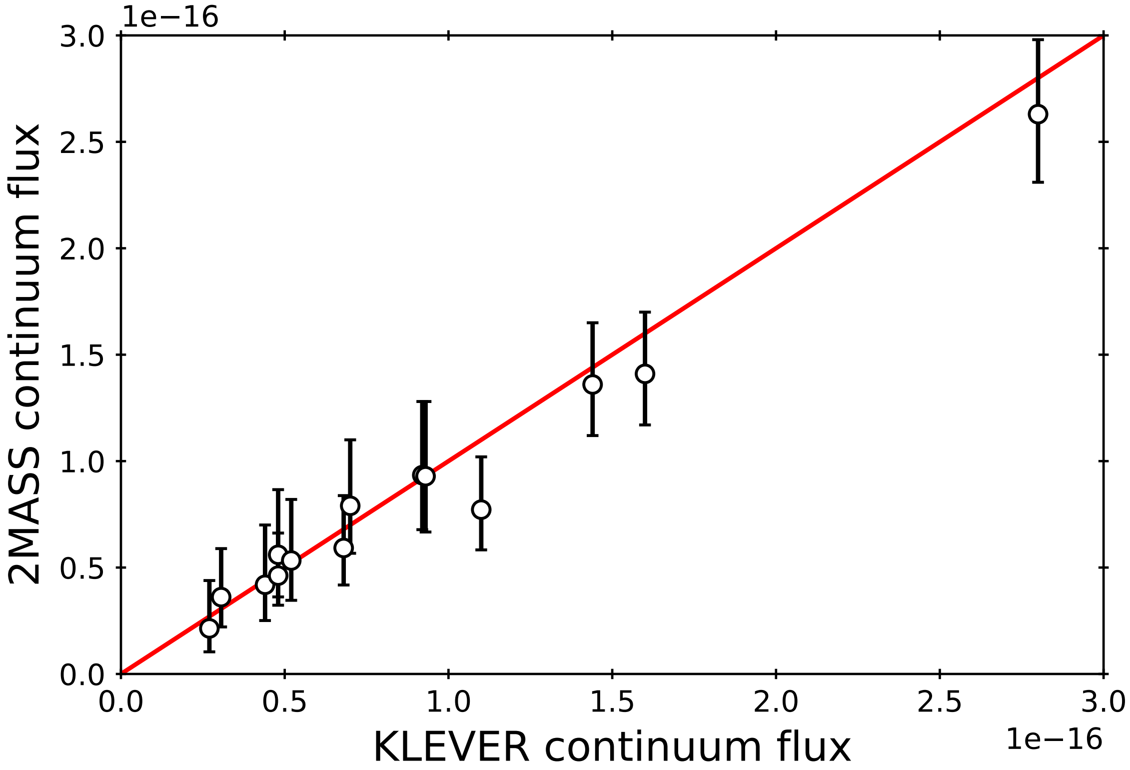

Fig. 2.3 Comparison of stellar fluxes obtained by KLEVER to those obtained from 2MASS in units of erg/s/cm^2/angstrom. The red line shows the 1:1 relation. KLEVER observations generally follow the 1:1 trend, suggesting a good degree of accuracy in the flux calibration.

with similar kinematics. However, velocities and line widths between different observing bands were not tied due to the different resolving powers within KMOS (3582, 4045 and 4227 in the centre of the YJ-, $H-$ and K-bands, respectively).

The amplitudes of several emission lines were also constrained to physical values. The [O II] and [S II] emission line doublets both have ratios that are dependent on the density of the emitting gas, and were allowed to vary between $0.35 <$ [O II]λ3729/[O II]λ3727 $<$ 1.50 and $0.44 <$ [S II]λ6716/[S II]λ6732 < 1.45, respectively (Osterbrock & Ferland 2006). Similarly, the [N II]λ6584/[N II]λ6548 and [O III]λ5007/[O III]λ4958 emission line ratios are both constrained to values of 3 by atomic physics. Each fit was inverse weighted by a corresponding noise spectrum. To minimise contamination from OH emission lines, the spectra were entirely masked at the positions of the brightest of these lines, as identified using the catalogue presented in Rousselot et al. (2000). The noise near each emission line was estimated by taking the root mean square of the flux in two continuum regions either side of the emission line. To determine errors on the flux, velocity and line width values, we repeated the fit 100 times, perturbing the modelled flux values in each wavelength channel by a random number drawn from a Gaussian profile distribution, the width of which was defined by the noise value in the corresponding channel of the noise extension within the datacube. A 2.5-sigma clipping was applied to all of the resulting distributions to remove poor fits to the perturbed data. For each parameter, the estimates for the lower and upper errors were taken to be the 16th and 84th percentiles of the distribution, respectively.

2.3.2 Galaxy-integrated spectra

To measure the global properties of the KLEVER galaxies, galaxy-integrated spectra were extracted from the reduced datacubes using a circular aperture with a diameter of $1.3''$. The choice of size for the aperture is arbitrary. A larger aperture will ensure more of the galaxy is sampled spatially, making the integrated-flux estimates more representative of the total flux within the galaxy, however it will also increase the noise introduced to the spectra, potentially making it harder to detect faint emission lines. Our choice of size, sampling a physical scale of $\sim$11 kpc from $z \in [1.4, 2.2]$, was found to be the best compromise between these two factors. In each band, we created a continuum image of each galaxy by collapsing over the full wavelength range whilst masking strong OH emission lines, with wavelengths identified using the Rousselot et al. (2000) catalogue. The centre of the continuum emission in all images was determined through fitting with an elliptical 2D Gaussian profile, and the pseudo-aperture was centred on this location. In cases where no continuum was detected, an image was made by collapsing around the strongest emission line within that band (typically [O II], [O III], Hα or [S III]), with the centre being determined using the same procedure as

Emission Line	(a)	(b)	(c)	(d)
[O II]$\lambda\lambda$3727,29 S/N	14.7	17.6	18.3	9.7
Hβ S/N	7.1	12.0	5.8	5.8
[O III]λ5007 S/N	41.2	34.1	9.5	8.4
Hα S/N	32.1	44.7	21.7	43.4
[N II]λ6584 S/N	5.8	6.6	3.0	10.8
[S II]$\lambda\lambda$6716,32 S/N	2.4, 2.2	5.4, 2.4	2.7, 0.7	8.5, 8.4

Table 2.2 The signal-to-noise of all of the major emission lines fit in the integrated spectra of our KLEVER sample for the four galaxies presented in Figure 2.5, where (a) = CLASHVLTJ114934_222459, (b) = extra_COS4_06750, (c) = GS3_24364 and (d) = U4_36568 . Note that the S/N presented for the [O II]$\lambda\lambda$3727,29 doublet represents the flux measured for the total doublet as the individual emission lines are often blended due to their small wavelength separation, whereas for the [S II]$\lambda\lambda$6716,32 emission doublet we report the S/N on the individual lines within the doublet.

earlier. Examples of the aperture placement for a galaxy where the continuum is detected and another for which there is no detected continuum are given in Figure 2.4. If neither continuum nor strong emission line images could be created, then the aperture was placed at the centre of the datacube. The aperture was then used to extract two spectra from each datacube: an integrated flux spectrum from the first extension, and an associated noise spectrum from the second extension. Galaxy-integrated spectra were extracted and subsequently fit with the spectral fitting routine for all galaxies within the KLEVER sample.

In Fig 2.5 we present examples of the integrated emission spectra for 4 KLEVER galaxies in the K-, H- and YJ-bands. Integrated noise spectra are shown in cyan, whilst best-fit models (determined using the spectral fitting code discussed in Section 2.3.1) are shown in red. Three of the galaxies are un-lensed, taken from the COSMOS, GOODS-S and UDS fields, with the fourth galaxy being lensed by the MACS J1149.5+2223 cluster. Peaks in the integrated noise spectra are seen to correspond with regions that are contaminated by strong OH sky lines. It can be seen that even when there are OH sky lines very close to nebular emission lines, the weighting of the best-fit procedure by the noise spectrum means contamination by the sky lines is well avoided. The signal-to-noise for all of the major nebular emission lines probed by KLEVER measured for the four galaxies presented in Figure 2.5 are given in Table 2.2.

2.3.3 Spatially binned emission maps

One of the key advantages of the KLEVER survey over existing IFS surveys at $z \sim 2$ is the ability to spatially resolve emission lines within galaxies. Therefore, in addition to the

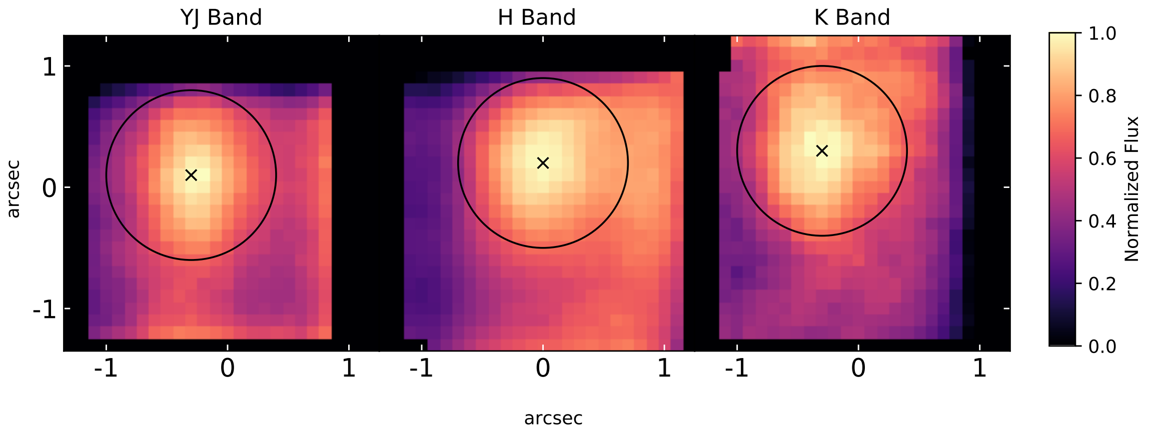

(a) Normalized continuum fluxes in all 3 bands for the lensed object CLASHVLTJ114934_222459.

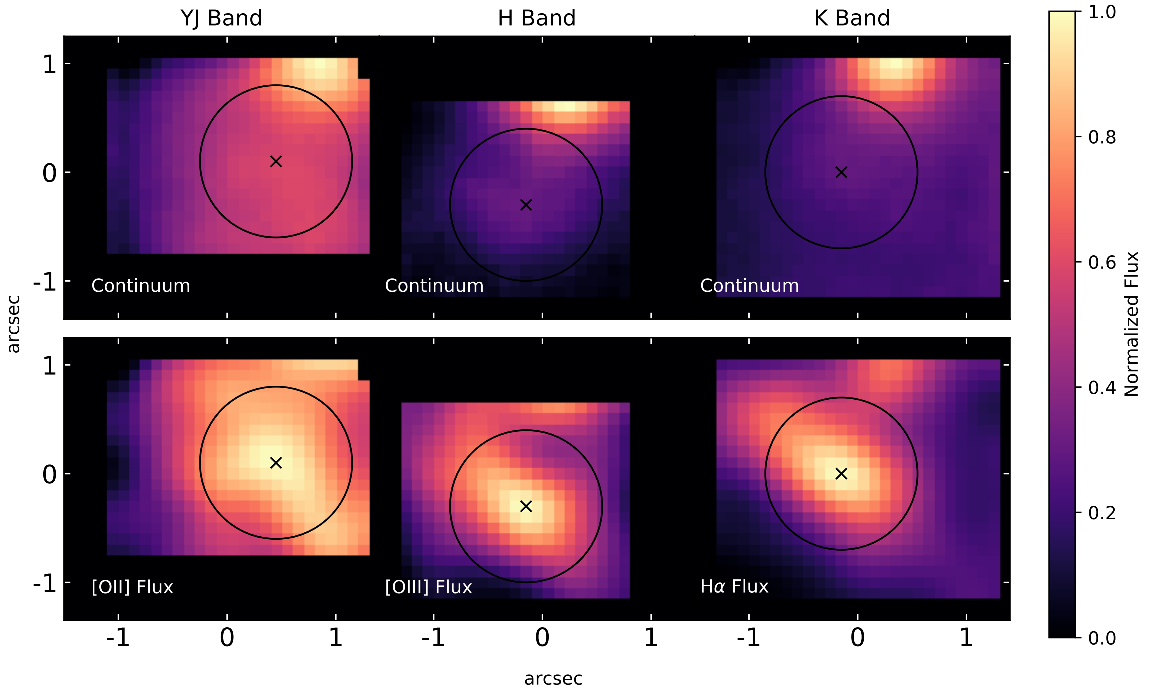

(b) Normalized continuum and emission line fluxes in all 3 bands for GS3_24364.

Fig. 2.4 Examples of the aperture placement used to extract the integrated flux spectra for the KLEVER sample. The origin of the coordinate system in each panel is the centre of the original datacube, which the aperture may be offset from if the observed galaxy is not located in the middle of the datacube. The black cross shows where the aperture was placed to extract the integrated spectra, whilst the black circle shows the region encompassed by the aperture.(a) Galaxy for which the continuum flux is detected in each band when collapsing over the full wavelength range whilst masking both emission lines and strong OH lines. (b) Galaxy for which the continuum is not clearly detected due to contamination by a nearby source. In this case, the aperture was centred on the peak of the strongest emission line in each band, shown in the bottom row.

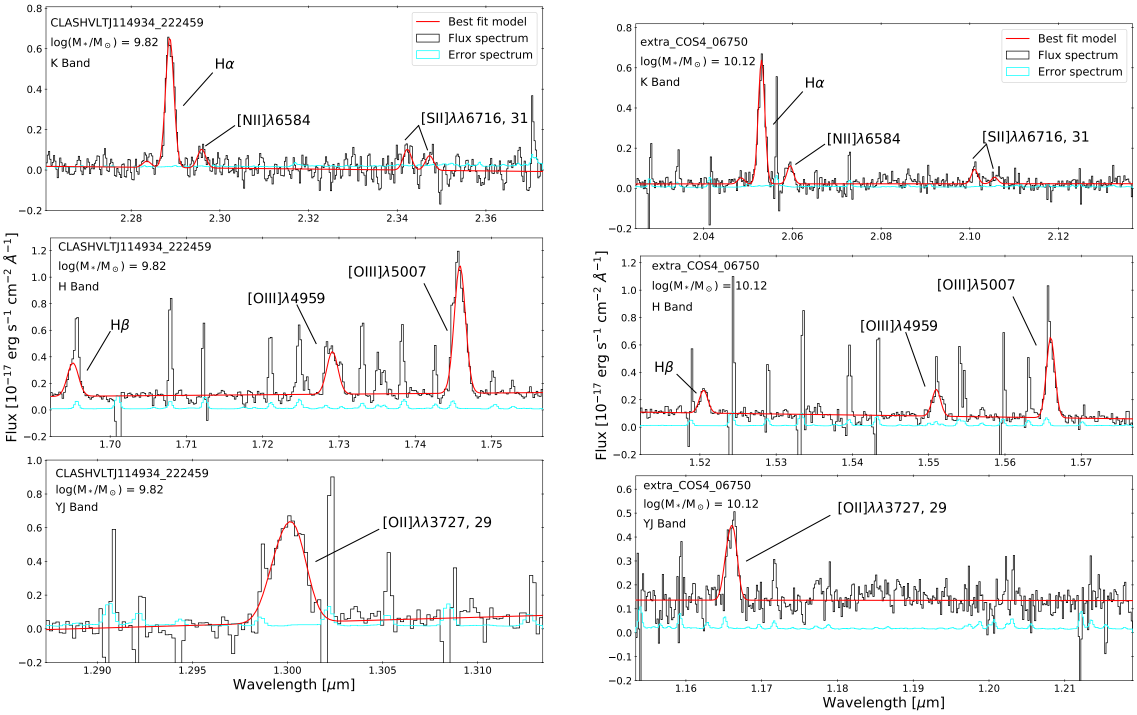

(a) CLASHVLTJ114934_222459, lensed galaxy at z ∼2.49.

(b) extra_COS4_06750, galaxy at z ∼2.13.

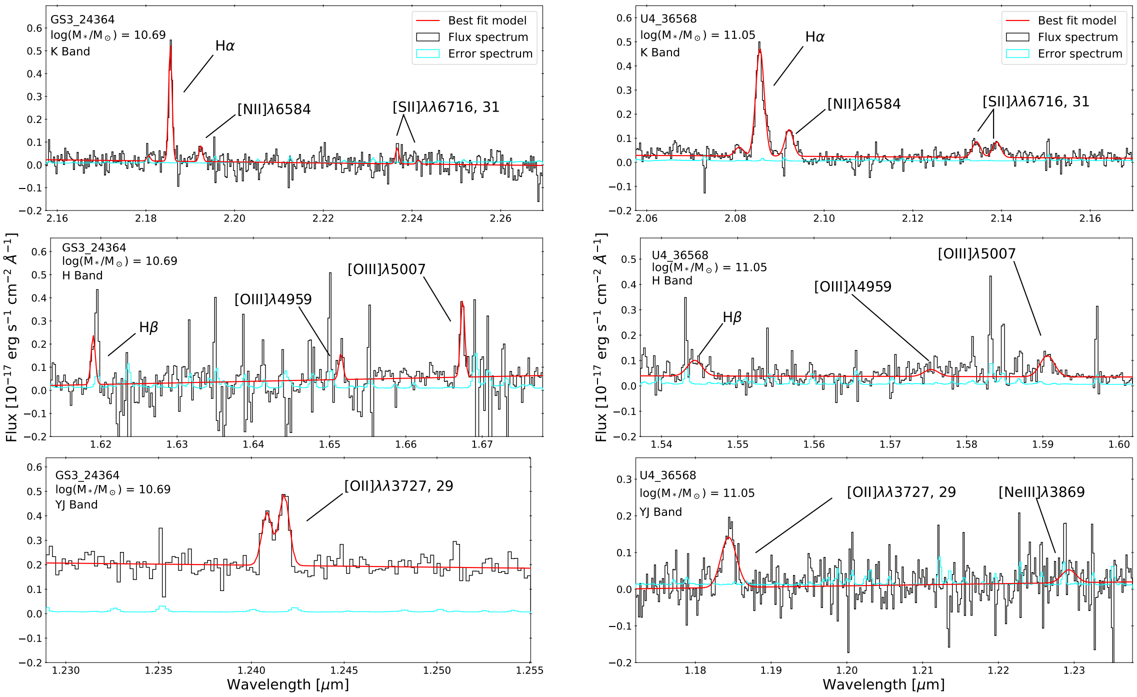

(c) GS3_24364, galaxy at z ∼2.33.

(d) U4_36568, galaxy at z ∼2.18.

Fig. 2.5 Integrated spectra for 4 KLEVER galaxies in the K, H- and YJ-bands. The best-fit to the emission lines are shown as red lines, with the cyan lines showing the integrated error spectra.

galaxy-integrated emission line fluxes outlined in the previous section, spatially resolved emission line maps were produced for all galaxies. The methodology for identifying emission lines is the same as that which was applied to the galaxy-integrated spectra, but applied to the spectra extracted from each spaxel on the 0.1×0.1 arcsecond pixel scale of the KLEVER datacubes. However, as previously noted observations with KMOS are seeing-limited, with the KLEVER observations having a typical PSF-FWHM of 0.5–0.6 arcsec. Therefore, using the fully spatially resolved emission line maps, the FWHM of the seeing is sampled by up to 6 individual points.

In order to address this oversampling, we re-bin the original KLEVER datacubes onto a larger spatial scale, extracting spectra by summing all spaxels within 0.3×0.3 arcsec bins. We centre these spatial bins on the centre of the galaxy within each band as determined using the methodology explained in Section 2.3.2. At this new scale the PSF-FWHM is sampled by roughly two data points. The spatial bins therefore have extracted fluxes that are much less contaminated by fluxes from neighbouring bins than the individual spaxels, therefore better sampling the data and providing more independent estimates for the emission line fluxes in different regions of the galaxy. An example of the flux maps obtained for a KLEVER galaxy in both the original 0.1×0.1 arcsec and the spatially binned 0.3×0.3 arcsec regimes is shown in Figure 2.6.

2.3.4 Stellar masses and SFRs

Within the KLEVER survey, all star formation rates are measured from the dust-corrected Hα emission line luminosity, using the conversion factor between Hα and SFR from Kennicutt & Evans (2012), and normalised to a Chabrier (2003) IMF.

Galaxy-integrated masses

The combination of lensed and un-lensed galaxies means galaxies in the total KLEVER sample span a broad range of stellar masses ($10^8 < \mathrm{M}_\star/\mathrm{M}_\odot < 10^{11.5}$) and star formation rates ($5 < \mathrm{SFR}\ [\mathrm{M}_\odot/\mathrm{yr}] < 300$). As demonstrated in Figure 2.7, the KLEVER survey samples galaxies on, above and below the main sequence of star formation at $z \sim 2$ (Noeske et al. 2007). The determination of the stellar mass estimates is outlined below.

For the un-lensed KLEVER galaxies, derived parameters such as stellar mass were accessed through the KMOS^{3D} data release[1] (Wisnioski et al., 2019). The stellar mass estimates for these galaxies were derived following Wuyts et al. (2011), wherein the FAST (Kriek et al. 2009) code was used to fit the optical to 8 μm SEDs with Bruzual & Charlot

---

[1] https://www.mpe.mpg.de/ir/KMOS3D/data

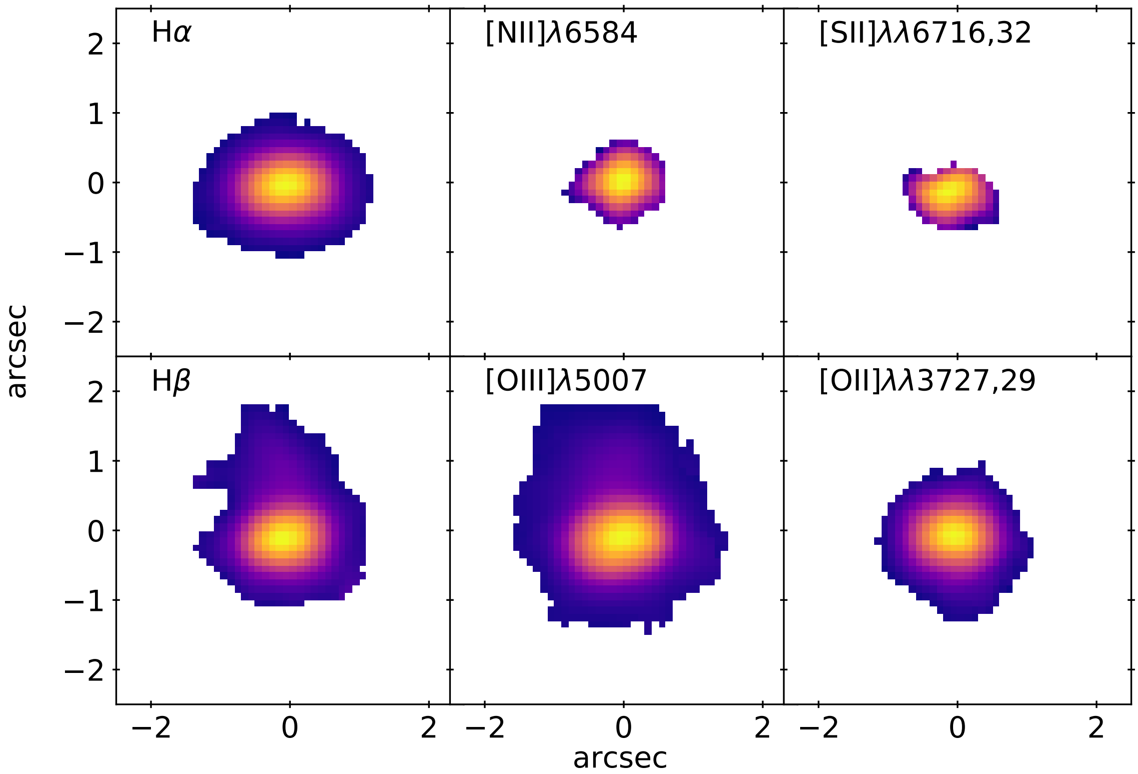

(a) Emission line maps produced from the KLEVER datacubes using a 0.1 × 0.1 arcsecond pixel scale.

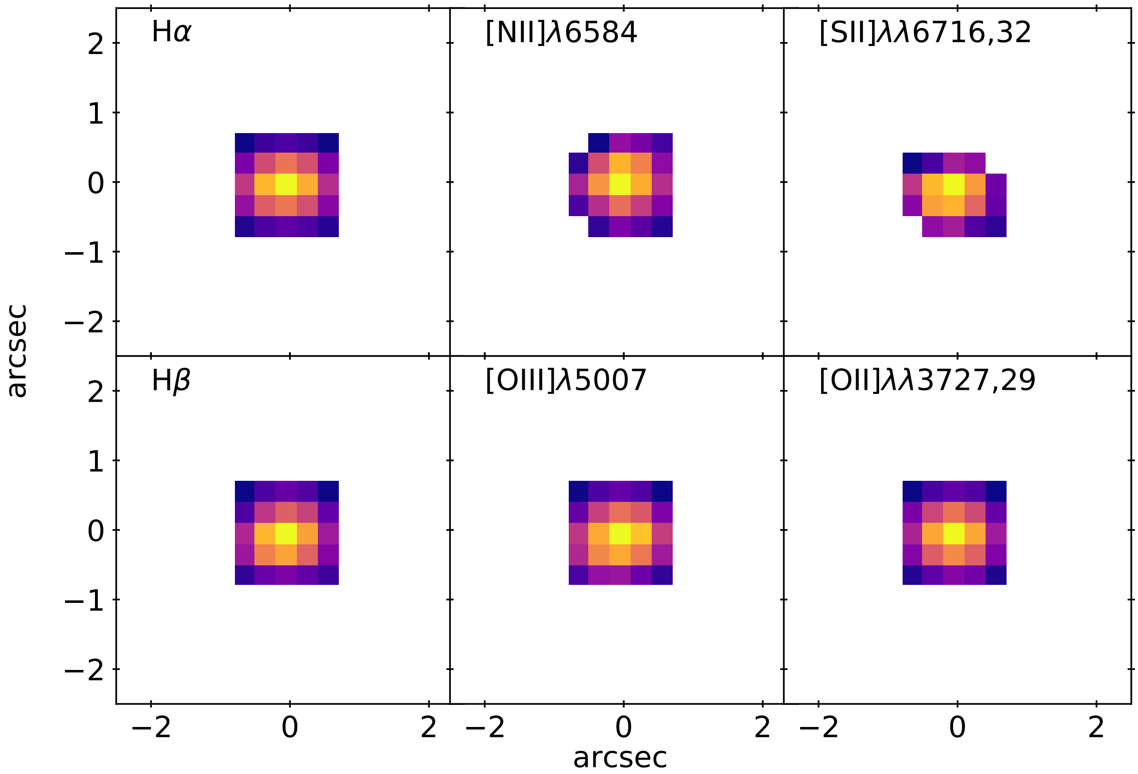

(b) Emission line maps re-binned onto a 0.3 × 0.3 arcsec pixel scale.

Fig. 2.6 Examples of resolved KLEVER emission line maps in two binning regimes.

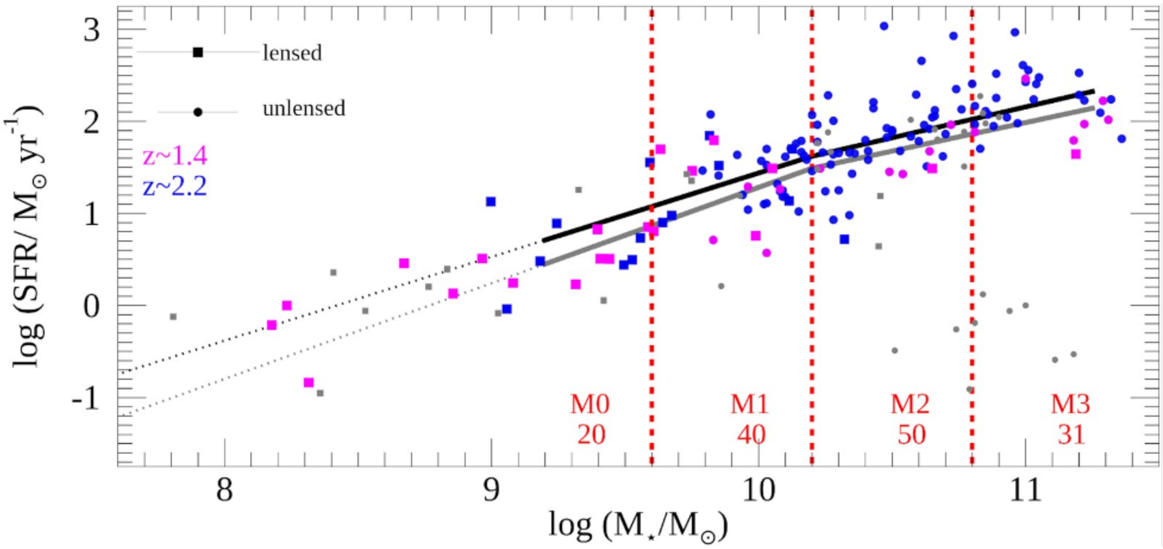

Fig. 2.7 Comparison of KLEVER galaxies to the star-forming main sequence, as determined at high redshift. Credit: Concas et al. (2022).

(2003) (BC03) models assuming solar metallicity, a Calzetti et al. (2000) reddening law, and either constant or exponentially declining star formation histories.

For the lensed KLEVER galaxies, stellar masses were estimated following a similar procedure to that adopted in Curti et al. (2020b). We used the high-z extension of the MAGPHYS code (Da Cunha et al. 2015) to fit the SEDs for our galaxies, using data from deep Frontier Field *HST* images[2] (Lotz et al. 2017) in three optical bands (F435W, F606W, F814W) and four near-IR bands (F105W, F125W, F140W, F160W), plus additional 3.6μm and 4.5μm IRAC data acquired by Spitzer (Castellano et al. 2016; Di Criscienzo et al. 2017; Bradač et al. 2019). MAGPHYS uses BC03 stellar population synthesis and adopts the two-component model of Charlot & Fall (2000) to describe the attenuation of stellar emission at ultraviolet, optical, and near-infrared wavelengths. A Chabrier (2003) IMF is assumed throughout, with the final estimates for the lensed galaxies also being corrected for magnification by considering the median magnification factor for each source taken from the multiple publicly available lensing models of the Frontier Fields[3] (e.g. Zitrin et al. 2013; Caminha et al. 2017; Jauzac et al. 2016). The methods used to build the public models of the Frontier Fields have been tested and validated with image simulations by Meneghetti et al. (2017).

We investigated the systematic differences in stellar mass estimates between the lensed and un-lensed galaxy samples by calculating stellar masses for a sub-sample of GOODS-S

---

[2] https://irsa.ipac.caltech.edu/data/SPITZER/Frontier/

[3] https:archive.stsci.edu/prepds/frontier/lensmodels/

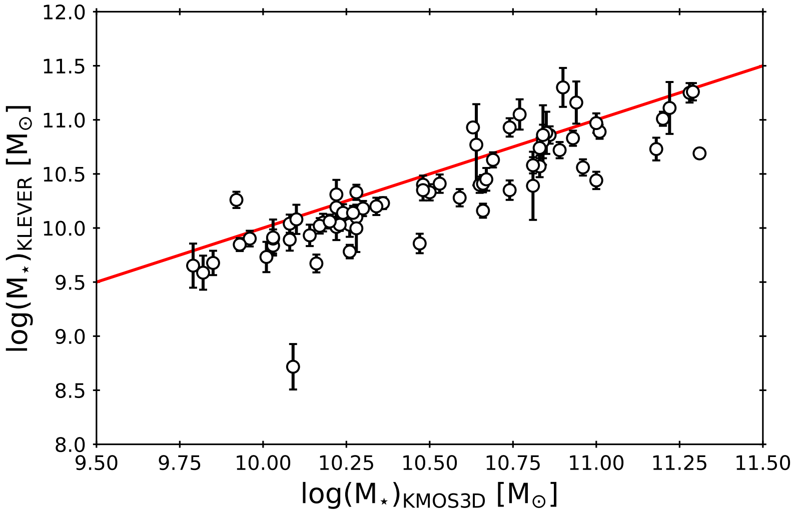

Fig. 2.8 Comparison of the different stellar mass estimates obtained from KLEVER and KMOS^{3D} for a sub-sample of galaxies from GOODS-S. KLEVER mass estimates were obtained using the same methodology that was applied to the lensed KLEVER sample. The 1:1 relation is shown as a solid line.

galaxies using the method applied to our lensed galaxy sample. As shown in Figure 2.8, stellar masses estimated using our method tend to show good agreement with those from KMOS^{3D}, although there is a small systematic offset towards stellar masses that are lower by 0.1 dex compared to KMOS^{3D} estimates. In the context of the work undertaken within this thesis, these systematics are negligible.

Stellar mass maps

Stellar mass maps for galaxies in the KLEVER sample were inferred from resolved SED modelling (see Wuyts et al. (2012); Lang et al. (2014) for further details). In brief, pixels are assigned to objects using the SExtractor (Bertin & Arnouts, 1996) segmentation map that was produced for H_{160} band observations from HST imaging. Following the technique from Cappellari & Copin (2003), pixels within the segmentation map were then Voronoi binned to ensure a minimum S/N level of 10 for each bin. SEDs were extracted from each Voronoi bin and fit using the FAST (Kriek et al. 2009) stellar fitting code, adopting stellar population synthesis models from Bruzual & Charlot (2003) assuming a solar metallicity, a Chabrier (2003) IMF and a Calzetti et al. (2000) reddening law. The resulting Voronoi binned stellar mass images are then pixelized by distributing the stellar mass within each bin over its constituent pixels according to the H-band fluxes of those pixels assuming a constant mass-to-light ratio.

Chapter 3

The cosmic evolution of galaxy-integrated N/O scaling relations

This chapter is adapted from 'The KLEVER survey: nitrogen abundances at $z \sim 2$ and probing the existence of a fundamental nitrogen relation', Connor Hayden-Pawson, Mirko Curti, Roberto Maiolino, Michele Cirasuolo, Francesco Belfiore, Michele Cappellari, Alice Concas, Giovanni Cresci, Fergus Cullen, Chiaki Kobayashi, Filippo Mannucci, Alessandro Marconi, Massimo Meneghetti, Amata Mercurio, Yingjie Peng, Mark Swinbank, Fiorenzo Vincenzo, 2022, MNRAS, 512, Issue 2, 2867-2889.

As introduced in Section 1.4, the relative abundances of metals within the ISM can act as diagnostics for investigating many of the processes that drive galaxy evolution (see Maiolino & Mannucci, 2019, for a review). Within this chapter, we focus on galaxy-integrated abundance ratios of oxygen-to-hydrogen (the gas-phase metallicity, O/H) and nitrogen-to-oxygen (nitrogen abundance, N/O). The gas-phase metallicity is sensitive to the chemical enrichment history of the galaxy through past and current star formation, as well as inflows and outflows of gas driven by phenomena such as pristine gas accretion and supernovae feedback, respectively. Similarly, the nitrogen-to-oxygen abundance acts as a time-sensitive probe of the chemical enrichment history of a galaxy due to the delayed production of nitrogen (formed predominantly in long-lived, low mass stars) relative to oxygen (formed in massive, short-lived stars).

Particular insights can be gained through comparisons of chemical abundances with other galactic properties for large samples of galaxies, many of which are now well established from $z \sim 0$ up to the peak of cosmic star formation at $z \sim 2$. Within the context of the mass-metallicity relation, more massive systems are found to be more chemically enriched (Tremonti et al., 2004). This can be interpreted as massive galaxies representing a more advanced stage of chemical evolution, or as a consequence of massive systems retaining more metals due to their deeper gravitational potentials (Kobayashi et al. 2007; Somerville & Davé 2015). The mass-metallicity relation has been observed to already be in place for galaxy samples out to $z \sim 3$ (Erb et al. 2006; Maiolino et al. 2008; Mannucci et al. 2009; Troncoso et al. 2014; Sanders et al. 2018), although its normalisation is found to decrease with redshift, as a possible consequence of the combined effect of more prominent gas inflows and stronger gas outflows (Sanders et al. 2021). The scatter in the mass-metallicity relation has also been shown to be partly ascribed to a secondary dependence of the metallicity on the star formation rate, with several authors finding evidence of a Fundamental Metallicity Relation between M_*, O/H and SFR that is redshift invariant out to $z \sim 3$ (Mannucci et al. 2010; Andrews & Martini 2013; Cresci et al. 2019; Curti et al. 2020a; Sanders et al. 2021).

Similar scaling relations have been observed for the N/O ratio, which also found to positively correlate with stellar mass (Pérez-Montero & Contini 2009; Pérez-Montero et al. 2013; Andrews & Martini 2013). As for the metallicity, this may be a consequence of higher mass galaxies being more evolved, hence having higher N/O ratios. The mass–N/O relation has also been observed up to $z \sim 2$, albeit with an evolution that is poorly constrained. Studies using N2O2 to trace N/O (Strom et al., 2017) find a greater deficit in N/O at a fixed $M_\star$ than those that use N2S2 (Masters et al., 2016; Kashino et al., 2017). Just as the mass-metallicity relation was found to have a secondary dependence on SFR, authors such as Pérez-Montero et al. (2013) have studied the variation of star formation rate within the mass–N/O plane. However, unlike for the mass-metallicity relation, they find no evidence of a strong secondary dependence on the SFR. This result is interesting within itself as whilst O/H is sensitive to the inflow of pristine/metal-poor gas onto a galaxy, diluting the metallicity, N/O is insensitive to this phenomenon (Köppen & Hensler 2005; Belfiore et al. 2015; Kashino et al. 2016). If confirmed, the lack of SFR dependency in the mass–N/O plane would suggest that the fundamental metallicity relation is driven mainly by dilution caused by infalls of pristine gas.

The N/O–O/H relation has also been extensively studied for nearby galaxies and HII regions by several authors (Shields et al. 1991; Vila-Costas & Edmunds 1993; Van Zee et al. 1998; Henry & Worthey 1999; Pérez-Montero et al. 2016; Pérez-Montero et al. 2013; Pilyugin et al. 2012; Andrews & Martini 2013). Though these studies tend to differ quantitatively depending on the choice of calibrations for deriving chemical abundances, they all agree qualitatively on the nature of the N/O–O/H relation. At low metallicities, N/O tends not vary with O/H, and instead maintains a constant value around $\log(\mathrm{N/O}) \simeq -1.5$, whilst towards higher metallicities the N/O ratio begins to increase rapidly with O/H. Towards higher redshifts, several works have also highlighted an increased N/O ratio at a fixed O/H compared to local galaxies (Masters et al. 2014; Shapley et al. 2015; Strom et al. 2017). Masters et al.

(2016) suggested that this enrichment may be an effect of the mass–N/O relation evolving more slowly than the MZR, supported by observations of studies that utilise N2S2 to trace N/O (e.g. Pérez-Montero et al. 2013, Kashino et al. 2017). However, this hypothesis is in contrast with the stronger evolution of the mass–N/O relation suggested by Strom et al. (2017), determined instead using N2O2. If the M_*–N/O and M_*–O/H relations do indeed evolve at a similar pace, then it would suggest that the N/O–O/H relation is approximately redshift-invariant, as supported by simulations (Vincenzo & Kobayashi, 2018).

In this chapter we review the scaling relations between several galaxy properties (N/O, O/H, M_* and SFR) as measured on a galaxy-integrated basis. In particular, we investigate the evolution of these scaling relations with redshift, with the ultimate goal of shedding light on the galaxy evolutionary processes that drive such relations. In Section 3.1, we introduce the local and high-redshift galaxy samples used to observe the scaling relations. In Sections 3.2 and 3.3 we describe how chemical abundances were determined. Finally, we present the key scaling relations and discuss the extent of their cosmic evolution in Sections 3.4 and 3.5.

3.1 Data

3.1.1 SDSS sample

To study the scaling relations in local galaxies we draw data from the seventh data release (DR7) of the Sloan Digital Sky Survey (Abazajian et al. 2009). The emission line fluxes and stellar mass estimates for galaxies in this data release are obtained from the MPA/JHU catalogue[1].

Selection criteria

We required all galaxies to be star-forming, as determined by their position on the [N II]-BPT diagram (Baldwin et al., 1981), adopting the classification scheme from Kauffmann et al. (2003b) to remove potential AGN. Following Curti et al. (2020a), the photometric flags from the DR7 sample were cross-matched with those from the DR12 sample to remove galaxies that were poorly deblended, as well as those with mass correction factors lower than 1, i.e. where the stellar mass derived from the total photometry is lower than the stellar mass derived from the photometry within the SDSS fibre. To ensure the [O II]$\lambda\lambda$3727,29 emission line doublet falls within the wavelength coverage of the SDSS spectrograph, a minimum redshift threshold of $z > 0.03$ was imposed. This allows us to exploit the same

---

[1] http://www.mpa-garching.mpg.de/SDSS/DR7/

suite of rest-frame optical emission lines in both the local and high-redshift galaxy samples presented in this chapter. Following Mannucci et al. (2010) we adopt a high threshold on the signal-to-noise ratio of the Hα emission line only (SNR>15) in order to reduce any potential biases in the determination of the metallicities and nitrogen abundances that may be caused by imposing SNR thresholds on weaker optical emission lines such as [N II]. Taken together, the above criteria yield a sample of 127,322 galaxies. However, a small number of galaxies in this sample were found to have anomalously low nitrogen abundances as calculated using the [O II]$\lambda\lambda$3727,29 emission line doublet. Imposing a threshold of SNR>2 on the [O II]$\lambda\lambda$3727,29 emission line doublet is sufficient to remove these spurious galaxies, creating a final analysed sample of 126,385 local star forming galaxies.

Stellar masses and extinction correction

The stellar masses for the SDSS sample are provided by the MPA/JHU catalogue and have been derived from fits to the photometry, with estimates following Kauffmann et al. (2003a) and aperture corrections to the total stellar mass following the prescription of Salim et al. (2007). All mass estimates were normalised to a Chabrier (2003) IMF. The final SDSS sample considered within this chapter spans a range of $8 < \log(\mathrm{M}_\star/\mathrm{M}_\odot) < 11.5$ in stellar mass, with a median value of $\log(\mathrm{M}_\star/\mathrm{M}_\odot) = 10$. In order to derive quantities such as metallicity, star formation rate and nitrogen abundance, the optical emission line fluxes must first be corrected for extinction. The Balmer decrement was used to calculate E(B-V)$_{gas}$, assuming case B recombination (Hα/Hβ=2.87) and a Calzetti et al. (2000) extinction curve. We note that using instead the attenuation curve from Cardelli et al. (1989) does not change the quantitative or qualitative results of our analysis.

Star formation rates

Star formation rates were measured from the dust-corrected Hα emission line luminosity, using the conversion factor between Hα and SFR from Kennicutt & Evans (2012). These were then normalised to a Chabrier (2003) IMF in order to align with the stellar mass estimates. Due to the low redshift cut of $z > 0.03$ imposed during sample selection, some galaxies may be included where only the central $\sim$ 1.6 kpc falls within the SDSS fibre, meaning only the inner-most regions of the galaxy are sampled. As such, estimating the star formation rate from the flux within the fibre may lead to systematic underestimations of the total SFR within the galaxy. To obtain estimates for the total star formation rate for our local galaxies, aperture corrections provided by the MPA/JHU catalogue were applied. These corrections build on the work of Salim et al. (2007), where aperture-corrected Hα fluxes from Brinchmann et al. (2004) were shown to be in good agreement with UV-based SFR estimates, with an average offset of just 0.06 dex and no correlation between the residuals and the level of aperture correction applied. Richards et al. (2016) also showed that aperture corrected SFR estimates are accurate to within 0.2 dex for large samples of galaxies. The analysis within this chapter compares SDSS galaxies to KLEVER galaxies for which spectra have been extracted from a circular aperture of diameter $1.3''$ (as discussed in Section 2.3.2). At $z \sim 2.2$, this corresponds to a physical distance of roughly 11 kpc. As such, the majority of the Hα flux is contained within the circular aperture for KLEVER galaxies, meaning any SFR estimates from Hα will be representative of total SFR values. Therefore, we present only the results using total SFR estimates for the SDSS sample and not the fibre estimates, allowing a more direct comparison between our high and low redshift samples.

3.1.2 KLEVER sample

Selection criteria

To investigate scaling relations at $z \sim 2$ we draw from the KLEVER sample, introduced in Chapter 2. Here, we explain the sample criteria applied to the KLEVER galaxies. Emission line fluxes for all KLEVER galaxies were obtained following the spectral fitting procedures outlined in Section 2.3.1. To classify an emission line as a detection we set thresholds on both the SNR and the percentage error on the flux measurement. We require the strongest line observed in a given band (Hα, [O III], [O II], [S III]) to have a SNR>3 and a percentage error on the flux of less than 33%. For the weaker lines within each band, which are tied to the detection of the strongest line by the spectral fitting routine, we reduce these requirements to a SNR>2 and percentage error of less than 50%. For the full sample, we obtain a detection rate of 88% for Hα, 62% for [N II]λ6584, 45% for [S II]λ6717 and 38% for [S II]λ6731. We note that the lower detection rate for the [S II] emission line doublet is partly driven by these lines falling primarily at the far end of the K-band, where rising thermal emission causes increased noise in the near-infrared spectra. [O III]λ5007 is detected for 60% of the sample, and Hβ in 52%. Within the 129 galaxies for which the [O II]$\lambda\lambda$3727,29 doublet can be observed, we obtain a detection rate of 72%, whilst for the galaxies at $z \approx 1.4$, we detect [S III]λ9530 in 45% of objects.

The analysis within this chapter relies on the simultaneous detection of several rest frame optical emission lines needed to derive chemical abundances. As such, we include only KLEVER galaxies for which the [O II], Hβ, [O III], Hα and [N II] emission lines have all been detected. This ensures N2O2 can be detected in order to estimate N/O for all of the high-redshift objects, which is important due to issues which impact the use of the N2S2 as a diagnostic for N/O at high redshift that are discussed further in Section 3.3. However, this criterion limits the range of redshifts probed by removing all KLEVER galaxies at $z \sim 1.4$, for which the [O II] falls below the YJ-band, meaning the remaining galaxies all lie at $z \sim 2$. From a possible 131 galaxies that could be selected by these criteria, 46 met the detection thresholds. We remove 6 galaxies from that were identified as potential AGN based off of their position on the [N II]-BPT diagram using the classification from Kauffmann et al. (2003b). To ensure a clean sample at $z \sim 2$ we also removed 3 KLEVER galaxies that have spuriously large Balmer decrements, potentially caused by strong OH emission lines near the Hβ line corrupting the fit to the data. The final sample of KLEVER galaxies analysed within this chapter then consists of 37 galaxies, 6 of which are lensed, spanning a range of $10^{9.5} < \mathrm{M}_{\star}/\mathrm{M}_{\odot} < 10^{11.5}$ in stellar mass.

Extinction correction and error propagation

All emission lines were corrected for extinction using the Balmer decrement, adopting the same methodology applied to the SDSS galaxies. Since the errors introduced by the extinction correction can be significant at high-redshift, owing to the low S/N of Hβ detections, we explicitly propagate errors from the correction into the final errors on any line ratios using the following method. First, we perturb the Hα and Hβ fluxes within their respective uncertainties. We then calculate a Balmer decrement value from these perturbed fluxes, before using the perturbed Balmer decrement ratio to derive the extinction corrected fluxes. In cases where a perturbed Balmer decrement value falls below the intrinsic case B value of 2.87, we do not correct apply any extinction correction. The fluxes are used to calculate any relevant extinction-corrected line ratios. We repeat this process 1000 times and take the errors on the extinction-corrected line ratio estimate to be the 16th and 84th percentiles of the resulting distribution. To get a final error estimate for the corrected ratio, these extinction errors are summed in quadrature with the error on the line ratio propagated from the uncorrected line flux measurements. We note that the error from the uncorrected line fluxes is still dominant over the error introduced from the extinction correction.

3.2 Metallicity determination

As discussed in Section 1.4.2, gas-phase metallicities can be determined using strong-line diagnostics that are calibrated through measurements of the temperature-sensitive ratio of auroral and nebular emission lines. It has been well documented that the HII regions within high-redshift star-forming galaxies have different physical properties to those found locally (e.g., Kewley et al. 2013; Steidel et al. 2014; Shapley et al. 2015, 2019; Sanders et al. 2016a; Kashino et al. 2017; Strom et al. 2017), which may cause metallicity diagnostics calibrated on samples of local galaxies and HII regions to yield biased metallicity estimates when applied to high-redshift galaxies. Efforts have been made to calibrate metallicity diagnostics at high redshifts, but detections of the essential auroral lines have been possible for just a handful of galaxies at high-redshift, allowing only preliminary calibrations of strong-line diagnostics to be made (Sanders et al. 2016b, 2020). Whilst these results give us an early insight into how the calibrations of certain diagnostics may evolve with redshift, the limited sample size and extreme nature of the galaxies sampled means that they may not be representative of the full galaxy population at high redshift. As such, we must await new facilities like JWST or the MOONS spectrograph on the VLT (Cirasuolo et al. 2020; Maiolino et al. 2020) before we can obtain robust metallicity diagnostics calibrated using direct temperatures at high redshifts. Until then we can only make informed decisions on our choice of metallicity indicators and diagnostics in the knowledge of their own potential biases.

Of particular concern are those diagnostics which include nitrogen. The N2 line ratio is commonly used to determine metallicities in galaxies at high-redshift as the close proximity of the Hα and [N II] lines means that the ratio is insensitive to dust extinction and observations in only one band are required. However, the N2 ratio has been found to overestimate the metallicities of high redshift galaxies (Liu et al. 2008, Newman et al. 2014). N2 is known to correlate with the N/O ratio, as discussed in Pérez-Montero & Contini (2009), meaning the discrepancy at high redshifts may be explained by elevated N/O at a fixed O/H (Masters et al. 2014, 2016; Shapley et al. 2015), whilst an increase in the hardness of the ionising spectrum at a fixed N/O and O/H has also been suggested as a cause of elevated N2 ratios (Steidel et al. 2016; Strom et al. 2017). Indeed, the assumed relation between N/O and O/H is itself important when using strong-line metallicity diagnostics, as those involving nitrogen rely on N/O varying similarly as a function of O/H for both the calibration sample and the sample that the calibration is being applied to. Whilst several studies have found the N/O–O/H relation to be qualitatively similar, systematic differences between the exact parameterisations of this relationship exist depending on the methods and calibrations adopted. The nature of the N/O–O/H relation at high redshift is also not robustly determined, and although there are suggestions from both observations (Strom et al., 2017, 2018) and simulations (Vincenzo & Kobayashi 2018) that the relationship may be redshift invariant, the large scatter of N/O at a given O/H observed in high-redshift galaxies could mean that applying local calibrations may not be appropriate.

To avoid some of these issues, it may be more appropriate to use strong-line calibrations based only on alpha-elements, such as oxygen, at high redshift. Studies such as Shapley et al. (2015) have shown that high redshift galaxies are not offset from local galaxies in oxygen-based diagnostics diagrams, such as R23 v O32. However diagnostic diagrams such as these may be more sensitive to the ionisation conditions within the galaxy, as opposed to the metallicity (see Strom et al. 2018). Recently, Sanders et al. (2020) compared metallicity diagnostics calibrated on local galaxies, HII regions and high-z analogues to a sample of high redshift galaxies for which direct temperature metallicity calibrations were possible. They found that the O32 diagnostic, which has the advantage of being monotonic across the range of metallicities probed, has a scatter for high redshift galaxies at a fixed O/H that is similar to that of local galaxy samples. Furthermore, the calibrations based on local galaxy samples from Curti et al. (2017, 2020a) as well as those from local high-redshift analogues (Bian et al. 2018) are in good agreement with the median values of the high redshift sample for several oxygen-based line ratios (R3, R2, R23, and O32). As such, within this chapter we adopt the metallicity diagnostics provided in Curti et al. (2020a), which have been calibrated for application in the metallicity range $12 + \log(\mathrm{O/H}) \in [7.6, 8.9]$. We use only the R3, R2, R23, and O32 diagnostics, and exclude any diagnostics which make use of nitrogen emission lines. This is particularly important as we derive both metallicity and nitrogen abundance (see Section 3.3.1) using strong-line diagnostics. It is therefore essential that we do not rely on the same nitrogen emission lines for the determination of both of these quantities in order to avoid introducing artificial correlations between them. Combinations of different diagnostics are used simultaneously to constrain the metallicity and break the degeneracies that can occur when using only a single diagnostic. The final metallicities and associated uncertainties were calculated using a simultaneous chi-squared minimisation over all available line ratios, as described in Curti et al. (2020b).

For the SDSS galaxies, no aperture-correction is applied to the metallicity as done for the SFR. The galaxy-integrated metallicity for SDSS galaxies is therefore assumed to be similar to that of the central region probed by the SDSS fibre. However, resolved observations of nearby galaxies have found that galaxies with higher masses tend to have steeper metallicity (as well as N/O) gradients (Belfiore et al., 2017; Schaefer et al., 2020). Therefore, the estimates of metallicity (and subsequently N/O) for the SDSS sample may be biased towards larger values, particularly for high mass galaxies. However, by comparing fibre-based SFR estimates to our aperture-corrected SFR estimates, we estimate that 75% of our SDSS sample have fibre covering fractions greater than 20%, above which abundances from central regions are expected to agree well with integrated values (Kewley et al. 2005).

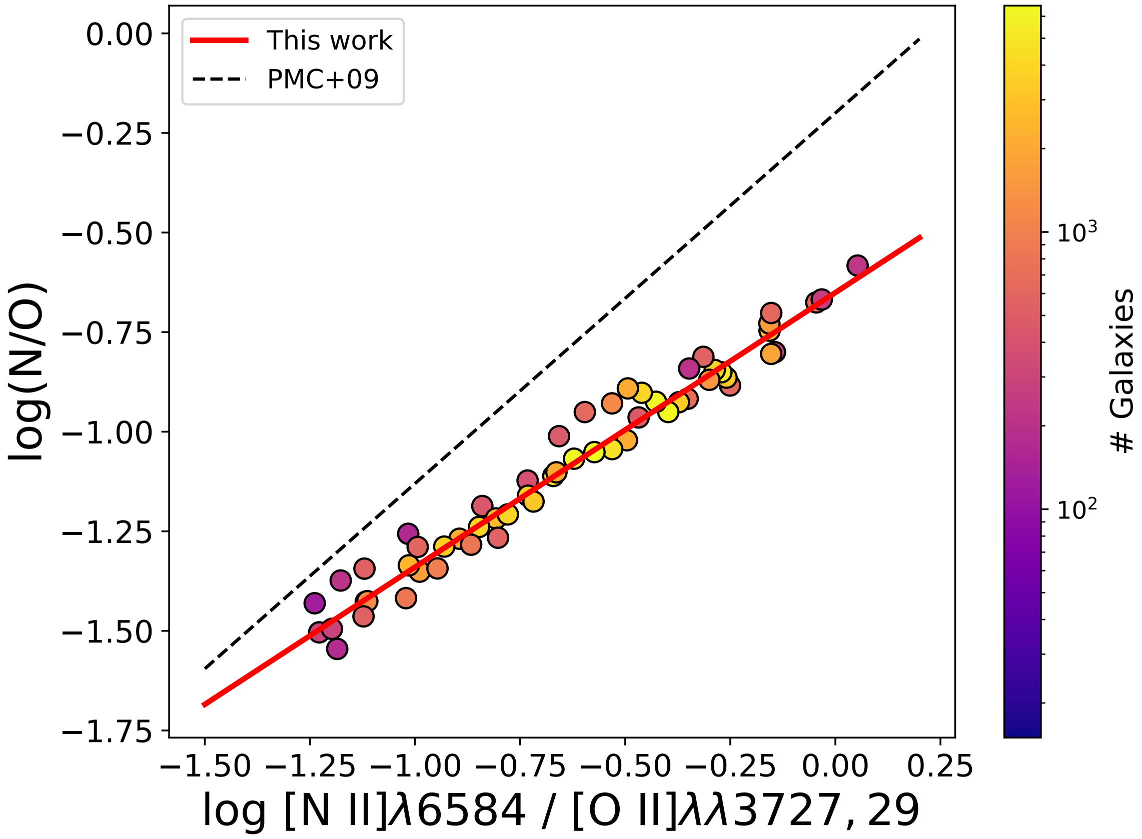

Fig. 3.1 The N/O abundance as a function of N2O2, as measured via detection of auroral lines in stacked spectra of SDSS galaxies (Curti et al. 2017). The red line represents the linear fit to the data for the new N/O calibration provided by Equation 3.1. Each point is colour-coded according to the number of galaxies within each stack, whilst the dashed black line shows, for reference, the log(N2O2) vs log(N/O) calibration presented by PMC09.

3.3 N/O determination

3.3.1 N/O diagnostics

When comparing metallicities to nitrogen abundances, it is important to ensure that they have both been estimated in a self-consistent method to allow direct comparisons between the two. As such, we adopt strong-line diagnostics for the N/O ratio that have been been calibrated using the same sample as the metallicity diagnostics discussed in the previous section. We therefore introduce new calibrations for N/O based on the 'direct', electron-temperature method for abundance determination applied to the sample of stacked SDSS galaxy spectra described in Curti et al. (2017, 2020a).

This calibration relies primarily on the assumption that, given the similar ionisation potentials of N and O, the total N/O abundance can be estimated from the ratio of the individual ionic abundances, e.g. the relative single-ionised species (N/O $\simeq$ N^+/O^+, Garnett 1990, Vila-Costas & Edmunds 1993). In more detail, for each of the stacked spectra in the Curti et al. (2017) sample (corresponding to different bins in the [O II]$\lambda\lambda$3727, 29/Hβ vs [O III]λ5007/Hβ diagram) we derive the electron temperature of the 'low-ionisation' region (characterised, indeed, by the presence of single-ionised oxygen and nitrogen species) from the auroral-to-nebular [O II]$\lambda\lambda$7320, 30/[O II]$\lambda\lambda$3727, 29 line ratio. We use such temperatures to compute the abundance of O^+ and N^+ from the [O II]$\lambda\lambda$3727, 29/Hβ and [N II]λ6584/Hβ ratio, respectively, exploiting the PyNeb package from Luridiana et al. (2015). The electron density is constrained independently, for each spectrum, from the [S II]λ6717/[S II]λ6731 diagnostic ratio. We note here that we adopt the same electron temperature based on the O^+ auroral-to-nebular line ratio to derive both O^+ and N^+ ionic abundances. In fact, although some evidence exists that t_2[N II] and t_2[O II] might differ when measured in individual HII regions (with t_2[O II] higher, on average, than t_2[N II], as potentially driven by the contribution to the [O II]$\lambda\lambda$7320, 30 auroral line flux from dielectronic recombination), the two temperatures are found to be consistent within their uncertainties in our stacked spectra (see Fig. 4 of Curti et al. 2017), as also reported in different studies (see e.g., Esteban et al. 2009; Pilyugin et al. 2009; Berg et al. 2015,2020). Therefore, we prefer to self-consistently model the low-ionisation zone with only one temperature (we choose t_2[O II] over t_2[N II] because it is measured with higher signal-to-noise and in more stacked spectra, and because it has been used to infer the global oxygen abundance as well) rather than introducing systematics by adopting two different temperatures for the two ionic species. Finally, the N/O abundance in our stacks is assumed to be traced by the N^+/O^+ abundance, and this is calibrated against different strong line ratios in a similar fashion as done for the full oxygen abundance calibrations.

Figure 3.1 shows the relationship between the T_e-based N/O abundance inferred for each stacked spectrum as a function of the [N II]/[O II] line ratio, with color-coding indicating the number of galaxies used in each stacked spectrum. The red line is a linear fit to the data, providing the following calibration

$$\log(\mathrm{N/O}) = (0.69 \times \log(\mathrm{N2O2})) - 0.65, \tag{3.1}$$

with the black dashed line showing the calibration from Pérez-Montero & Contini (2009) (hereafter PMC09) as a reference. Similar to the calibration presented in Strom et al. (2017) that used a calibration sample of extragalactic HII regions from Pilyugin et al. (2012), we find that the PMC09 calibration may provide N/O estimates that are ~0.3 dex larger than our

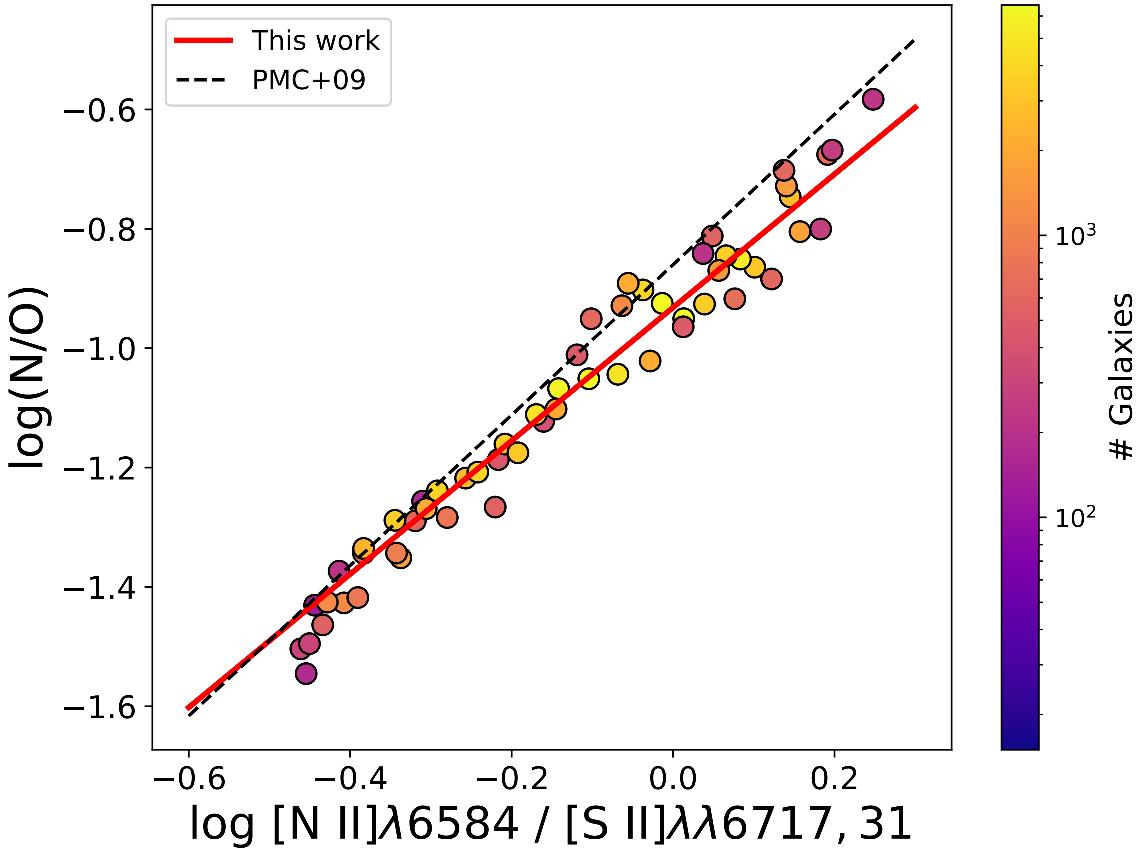

Fig. 3.2 The N/O abundance as a function of N2S2, as measured via detection of auroral lines in stacked spectra of SDSS galaxies (Curti et al. 2017). The red line represents the linear fit to the data for the new N/O calibration provided by Equation 3.2. Each point is colour-coded according to the number of galaxies within each stack, whilst the dashed black line shows, for reference, the log(N2S2) vs log(N/O) calibration presented by PMC09.

own calibration at high N2O2 values. The main cause of the discrepancy between the PMC09 calibration and our own is the different calibration samples. The PMC09 sample is mostly made up of H II galaxies that have low metallicities, with N2O2 values that are typically below -0.75. These galaxies dominate the linear best-fit to the data, and the smaller number of Giant Extragalactic H II Regions that populate the high N2O2 region of the PMC09 sample tend to fall below this best-fit calibration line. By contrast, our stacked SDSS galaxy sample is homogeneous and extends up to N2O2 values greater than 0, providing a best-fit calibration that better represents galaxies with high N/O values. Indeed, the Giant Extragalactic H II Regions that populate the high N2O2 end of the PMC09 sample are well represented by our own calibration.

N/O abundance is also often traced using the N2S2 diagnostic, first introduced in Sabbadin et al. (1977). The clear advantage of this diagnostic over N2O2 is that the proximity of the [N II] and [S II] emission lines means no correction for extinction is required and observations in only a single band are needed to obtain simultaneous detections. Figure 3.2 shows the relationship between the T_e-based N/O abundance inferred for each stacked spectrum from Curti et al. (2017) as a function of the [N II]/[S II] line ratio, with colour-coding indicating the number of galaxies used in each stacked spectrum. The red line is a linear fit to the data, providing the following calibration

$$\log(\mathrm{N/O}) = (1.12 \times \log(\mathrm{N2S2})) - 0.93. \tag{3.2}$$

3.3.2 Discrepancies between N2O2 and N2S2

SFR dependence within SDSS galaxies

As can be seen in Figures 3.1 and 3.2, both N2O2 and N2S2 display tight correlations with the N/O ratio. This is driven by the fact that both oxygen and sulphur are α-elements, meaning N2O2 and N2S2 both trace the N/α ratio. However, differences between these ratios can arise due to the unique chemical enrichment histories and physical properties of both oxygen and sulphur respectively. Here, we investigate whether the differences that arise when using either N2O2 or N2S2 as an N/O diagnostic are correlated with other galaxy properties. We estimate the N/O ratio from both N2O2 (Equation 3.1) and N2S2 (Equation 3.2) for our full SDSS sample. The results are shown as grey contours in Figure 3.3. Overlaid on these contours, we plot tracks of constant star formation rate taken in 0.2 dex wide SFR bins. A clear trend emerges where those galaxies with higher star formation rates have an N/O ratio estimated from N2S2 that is systematically greater than that estimated using N2O2. Similarly, galaxies with lower star formation rates are offset to lower N2S2 values at a fixed N2O2. The difference in N/O as estimated using N2S2 at a fixed N2O2 can vary by more than 0.2 dex depending on the star formation rate, with this effect roughly constant across the full range of N/O values probed by the SDSS sample.

Differences in the N/O estimates from N2S2 relative to N2O2 could be driven by a breakdown in the underlying assumption that $N^+/S^+ \simeq N^+/O^+$. The abundances of O^+ and S^+ are strongly dependent on the ionisation conditions within a given galaxy. Models of H II regions suggest that O^+ has a very similar ionisation structure to N^+, whilst S^+ differs in that it is mostly emitted by the outer shell of the H II region, with doubly-ionised species such as S^{++} dominating the inner regions (Levesque et al. 2010; Mannucci et al. 2021). As the star formation within a galaxy increases, the number of H II regions within the galaxy

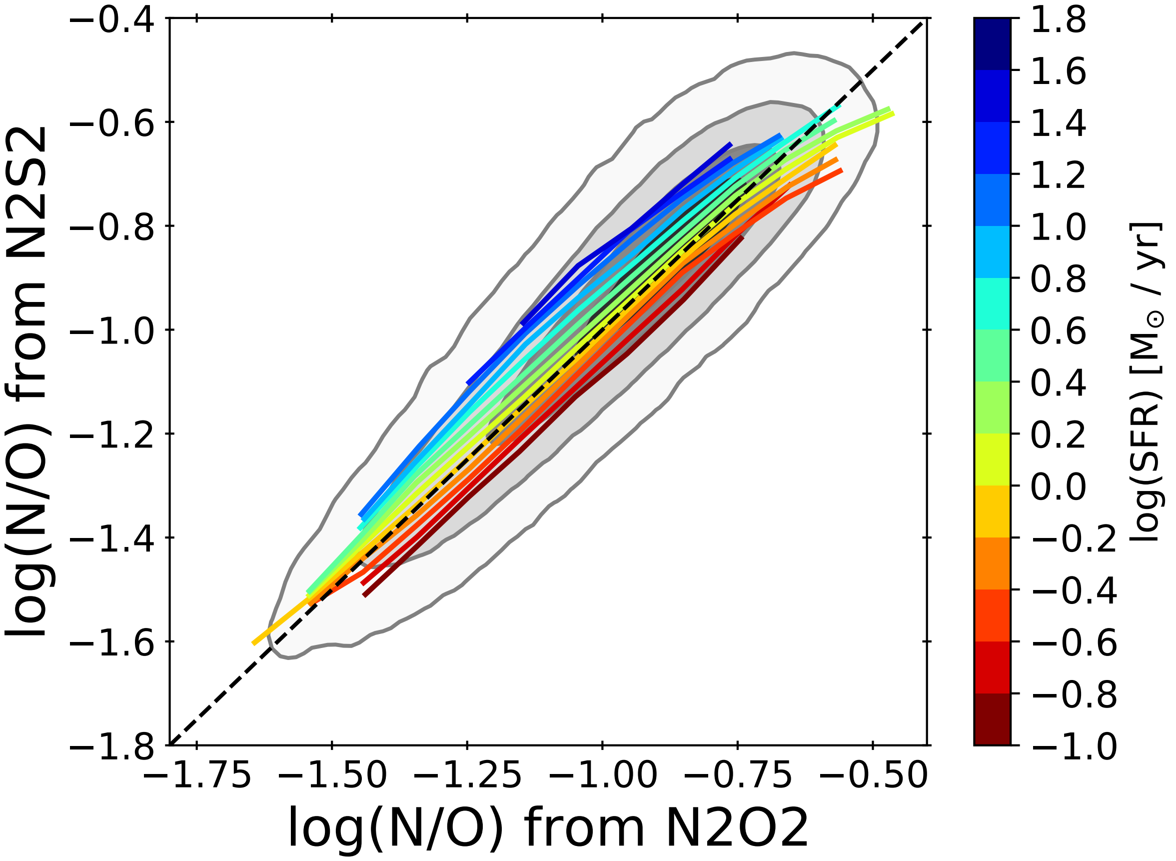

Fig. 3.3 N/O derived from both N2O2 and N2S2 for galaxies in our SDSS sample, with contours showing the regions encompassing 30%, 60% and 90% of the total sample. The coloured lines show how the relationship between N2S2 and N2O2 varies as a function of star formation rate. At a fixed N2O2, more star forming galaxies have systematically larger values of N2S2, causing a discrepancy in the estimation of N/O.

will grow, and these regions may merge. As such, the integrated spectrum of the ionised gas within the galaxy (as observed through an aperture in the case of SDSS) will begin to be dominated by more central HII regions, leading to a decrease in observed S^+, and hence an increase in N2S2. Meanwhile the similar ionisation structures of N^+ and O^+ mean N2O2 is relatively unaffected.

This effect could be particularly significant for high-redshift star forming galaxies, which tend to resemble large HII regions. High levels of star formation at $z \sim 2$ have been associated with a change in the physical conditions of the ionised ISM towards high redshift, with observations of harder ionising radiation fields (Steidel et al., 2014; Strom et al., 2017) and higher ionisation parameters (Kewley et al., 2013; Steidel et al., 2014; Kewley et al., 2015) that may be driven by an increase in specific star formation rate (Kaasinen et al., 2018). Indeed, Strom et al. (2018) found that both high-redshift galaxies and local HII regions were offset from the trend between N2O2 and N2S2 seen in local galaxies. They proposed that the integrated light spectrum of local galaxies may include contributions from DIG in addition to emission from HII regions. Galaxies that have a larger contribution from DIG would be expected to have enhanced flux contribution to the [S II] doublet, which would depress N2S2 at a fixed N2O2. However, recent work by Mannucci et al. (2021) suggests that SDSS galaxies do not have a significant contribution from DIG, and that instead aperture effects on the spectroscopy of nearby HII regions are largely responsible for the observed differences. Indeed, when large enough apertures are used on local HII regions, the observed line ratios are the same as in SDSS galaxies. In Figure 3.4 we plot N/O values derived from N2O2 and N2S2 for SDSS galaxies (shown as grey contours), local H II regions taken from Pilyugin et al. (2012) (shown as orange squares) and KLEVER galaxies for which N2S2 and N2O2 were both detected in the galaxy-integrated spectrum, shown as magenta diamonds. In addition, we overlay the SDSS contours with tracks of constant sSFR taken in 0.2 dex wide sSFR bins. Consistent with the results of Strom et al. (2018), we find galaxies at $z \sim 2$ are offset to larger N2S2 values than local galaxies, and are instead more comparable to local H II regions.

Considering the tracks of constant sSFR in Figure 3.4, the low sSFR tracks all lie on the 1:1 relationship between N2O2 and N2S2 across the full range of N/O values. In contrast, the tracks with high sSFR (>-0.04 /Gyr), which are biased towards low values of N/O, begin to show an offset towards higher N2S2 values. In Figure 3.5 we plot the difference in N/O estimated from N2O2 and N2O2 (ΔN/O) for KLEVER galaxies as a function of specific star formation rate. We find the galaxies with the highest sSFR values are the most offset. To estimate the significance of this trend, we performed a linear least-squares regression, finding a line of best fit (shown in red) with a Pearson correlation coefficient of $r = 0.64$ and a

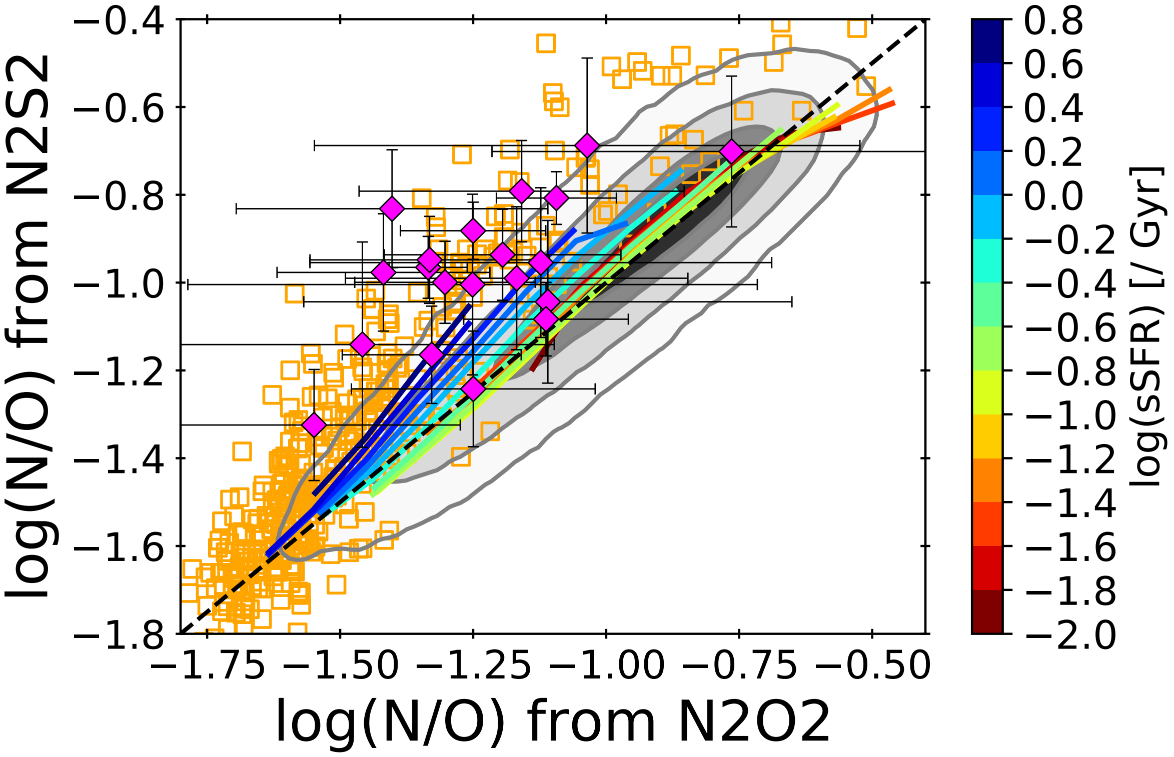

Fig. 3.4 N/O derived from both N2O2 and N2S2 for galaxies in our SDSS sample, with contours showing the regions encompassing 30%, 60% and 90% of the total sample. The coloured lines show how the relationship between N2S2 and N2O2 varies as a function of sSFR. The orange squares show the location of local HII regions, taken from Pilyugin et al. (2012). The magenta diamonds represent KLEVER galaxies, with accompanying errorbars.

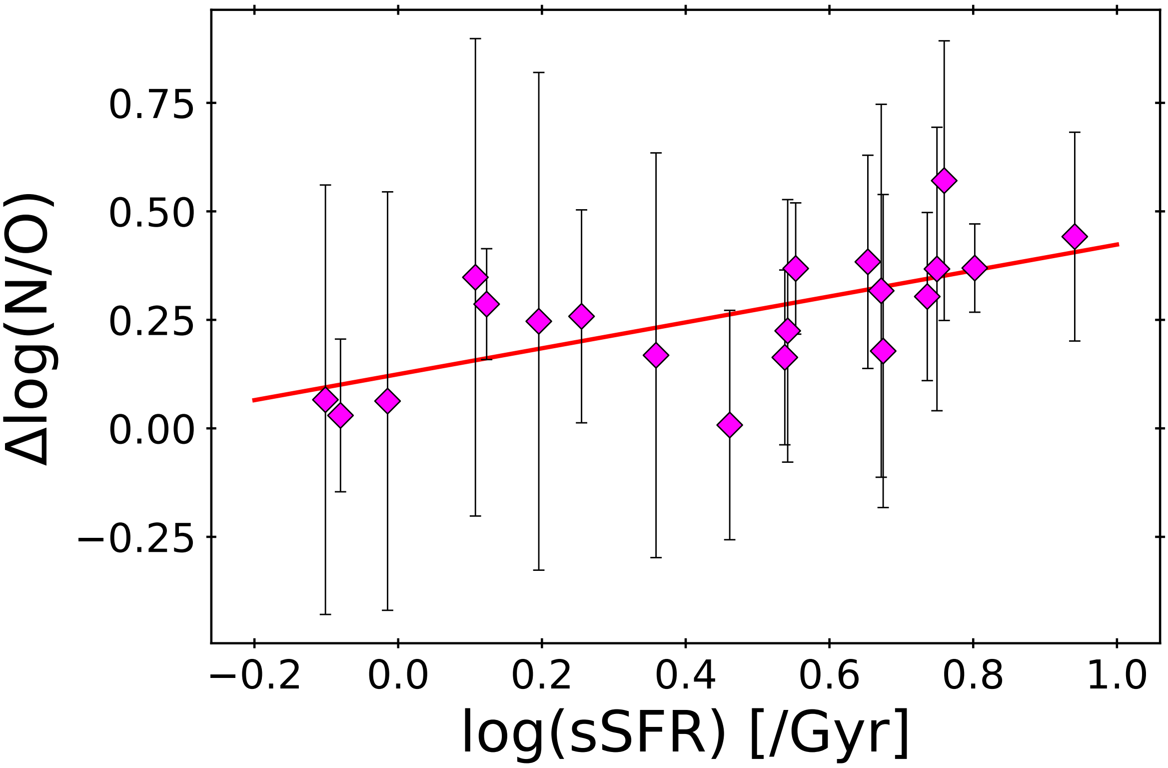

Fig. 3.5 The difference in N/O estimated from N2S2 and N2O2 diagnostics as a function of the specific star formation rate for KLEVER galaxies. A linear regression between these two variables, shown as a red line, finds a significant positive correlation with a Pearson correlation coefficient of r =0.64 and a p-value=0.002.

p-value=0.002, suggesting a statistically significant strong positive correlation exists between these two variables. This result is consistent with our interpretation in which the light from highly star forming galaxies is dominated by the more central zones of H II regions, causing S^+ to decrease relative to O^+.

Due to the caveats discussed above, we caution the use of the N2S2 diagnostic to trace N/O, particularly for high-z galaxies and H II regions wherein [S II] emission from the outer ionised regions may not be properly represented in integrated spectra because of low S/N or small extraction apertures, respectively. We therefore adopt only the N2O2 diagnostic to trace N/O throughout this chapter.

3.4 N/O scaling relations

3.4.1 N/O–O/H relation

Trend in SDSS galaxies

We investigate the distribution of our SDSS galaxy sample in the 12 + log(O/H) vs log(N/O) plane, shown as grey contours in Figure 3.6. The contours show the regions encompassing 30%, 60%, 90% and 99% of the total sample respectively. The white circles show the median nitrogen abundances taken in 0.05 dex bins of metallicity, with the errorbars representative of the standard deviations in N/O within each bin. The trend of N/O steeply rising at high metallicities and flattening at low metallicities has been observed commonly in several other studies in the past (Vila-Costas & Edmunds 1993; Van Zee et al. 1998; Henry & Worthey 1999; Pérez-Montero & Contini 2009; Pilyugin et al. 2012; Andrews & Martini 2013). We choose the following functional form for parameterising the median N/O–O/H relation:

$$\log(\mathrm{N/O}) = \log(\mathrm{N/O})_0 + \gamma/\beta * \log\left(1 + \left(\frac{(\mathrm{O/H})}{(\mathrm{O/H})_0}\right)^{\beta}\right). \tag{3.3}$$

In this equation, log(N/O)$_0$ represents the value of the nitrogen abundance plateau, where nitrogen production is considered primary and does not increase strongly with metallicity. At a metallicity of $\log(\mathrm{O/H}) > \log(\mathrm{O/H})_0$, the function is a simple power law of index γ, representing the region where secondary nitrogen production now dominates and N/O abundance increases strongly with metallicity. The sharpness of transition between the primary and secondary regimes is controlled by the β parameter, with a smaller value of β corresponding to a broader transition. A least-squares fit was performed to fit this model to the median binned data using the LMFIT package (Newville et al., 2016), with the fit being weighted by the standard error calculated using the dispersion in log(N/O) and number of objects within each bin. The best-fit parameter values and standard errors provided by LMFIT are given in Table 3.1.

The best-fit to the SDSS data is shown as a solid red line in Figure 3.6. We obtain a value for the low-metallicity plateau, of $\log(\mathrm{N/O})_0 \approx -1.5$, which is in good quantitative agreement with empirical estimates from other studies of HII regions in nearby galaxies (Vila-Costas & Edmunds 1993; Van Zee et al. 1998; Henry & Worthey 1999; Pérez-Montero & Contini 2009; Pilyugin et al. 2012; Andrews & Martini 2013). The vertical dot-dashed line in Figure 3.6 shows the "transition" metallicity above which secondary nitrogen production dominates, found to be 12+log(O/H)$_0$ = 8.534±0.011, in good agreement with the value estimated in Van Zee et al. (1998) and Andrews & Martini (2013). Other studies such as Shields et al. (1991)

Table 3.1 The values of the best-fit parameters of the median N/O–O/H relation for the SDSS galaxy sample, fit using Eq. 3.3. Note that 12+log(O/H)$_0$ = 8.534 corresponds to a value of (O/H)$_0$ = 3.4 $\times 10^{-4}$.

log(N/O)$_0$	12+log(O/H)$_0$	γ	β
-1.491 ± 0.017	8.534 ± 0.011	2.69 ± 0.11	3.6 ± 0.3

and Henry & Worthey (1999) suggest a transition metallicity lower by roughly 0.2 dex, at 12+log(O/H) = 8.3, whilst a polynomial fit to the Pilyugin et al. (2012) presented in Steidel et al. (2014) suggests a lower transition metallicity still at 12+log(O/H) = 8.2. One reason for the discrepancy in transition metallicities is the differences in parameterisation of the relationship between N/O and O/H. Some works have suggested a sharp transition between primary and secondary nitrogen production (e.g. Charlot & Longhetti 2001; Andrews & Martini 2013), whilst others present a more gradual transition between the two regimes (e.g. Van Zee et al. 1998; Pilyugin et al. 2012). We show that a smooth transition is a more physical representation of the relationship, as the onset of significant secondary nitrogen production within different galaxies will vary dependent on their star formation and chemical enrichment histories. Nonetheless, the main cause of the varying estimations of transition metallicity values is the use of different calibrations and diagnostics to estimate the metallicity, as discussed in Section 1.4.2.

Overall, we find that the relationship between N/O and O/H for our local sample has a scatter of just 0.08 dex for individual galaxies about the best-fit, comparable to that of the mass-metallicity relation (Curti et al. 2020a). The overwhelming majority of our local galaxies (91%) fall into the regime where secondary N production dominates (12+log(O/H)>8.538) and N/O is strongly correlated with O/H with a Spearman's rank correlation coefficient of 0.9. If we consider the remaining 9% of the sample that have 12+log(O/H)<8.538, the correlation between N/O and O/H is significantly weakened, with the Spearman's rank coefficient of just 0.47 when only these galaxies are considered. This manifests in the increased scatter of the relationship at low metallicities, where the standard deviation of individual galaxies about the best-fit increases to 0.1 dex.

Trend in KLEVER galaxies

The distribution of our high-redshift sample in the N/O–O/H plane can be seen in Figure 3.6. KLEVER galaxies are typically found at lower metallicities, with a median metallicity of 12+log(O/H) = 8.46 compared to the SDSS median of 12+log(O/H) = 8.72, which is expected from the evolution of the mass-metallicity relation at high redshift and by the fact that the

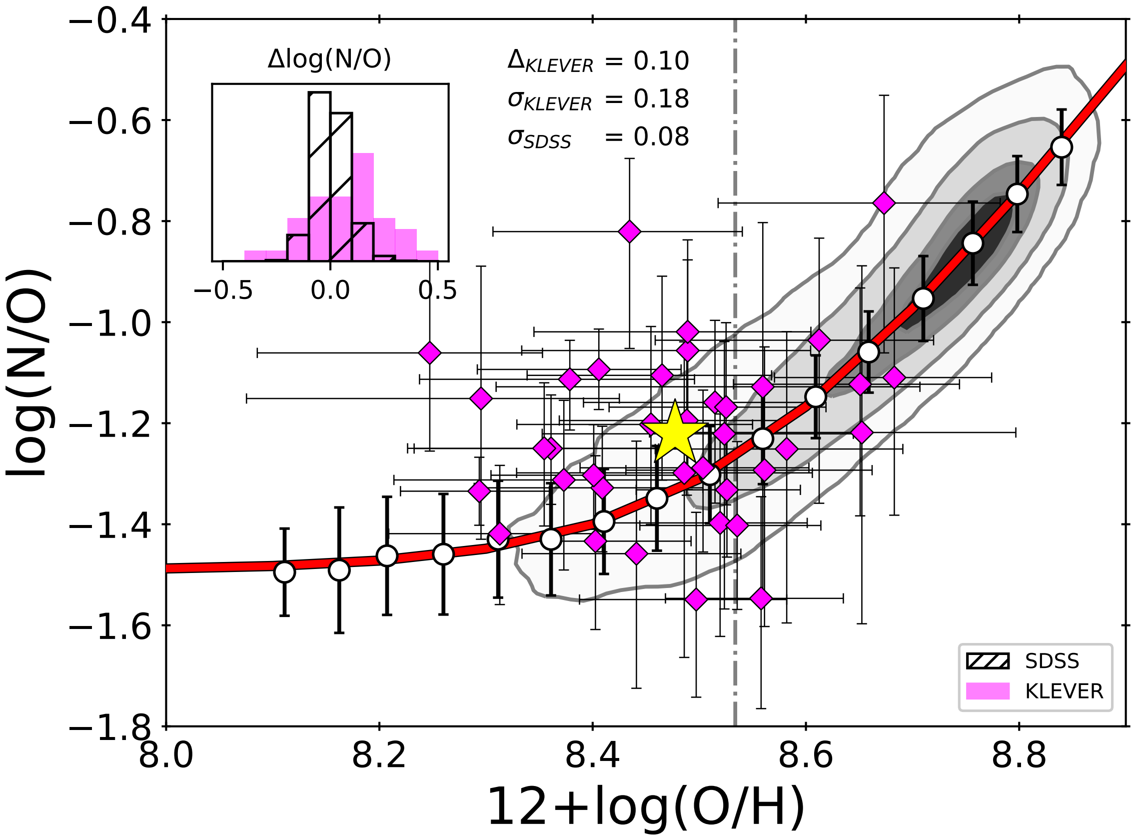

Fig. 3.6 The nitrogen abundance as a function of the gas-phase metallicity for the SDSS and KLEVER galaxy samples. The grey contours show the regions encompassing 30%, 60%, 90% and 99% of the local SDSS sample. The white points show the median binned SDSS data with corresponding standard deviations, with the solid red curve representing the best fit to the data using Eq. 3.3. The black dash-dotted line represents the transition metallicity at 12+log(O/H) = 8.534. The KLEVER galaxies are shown in magenta with corresponding errorbars, with the average position of the KLEVER galaxies shown as a yellow star. The histogram in the top left shows the deviations of the SDSS sample and the KLEVER sample from the best-fit line to the local data. KLEVER galaxies have a large scatter, yet on average show a mild enrichment in N/O of 0.1 dex when compared to SDSS galaxies.

KLEVER galaxies are more highly star-forming and therefore, according to the FMR, are expected to have lower metallicity. It is more interesting to investigate whether KLEVER galaxies at high redshift deviate from the N/O–O/H relation of local galaxies, as traced by the SDSS relation. The distribution of KLEVER galaxies appears more dispersed than the distribution of local galaxies. This is shown more clearly in the inset histogram in Figure 3.6 which shows the distribution of the deviations from the local best fit both for the SDSS galaxies and for the KLEVER galaxies. The dispersion of the KLEVER galaxies around the local relation is 0.18 dex, while the dispersion from SDSS galaxies is only 0.08 (although it increases to 0.10 at lower metallicities).

The large scatter of high redshift galaxies in the N/O–O/H plane has also been reported in Strom et al. (2018), where the distribution of high-z galaxies was found to be well matched to the contours of local extra-galactic HII regions from Pilyugin et al. (2012). If the large scatter of high-redshift galaxies in this plane is physically motivated, then it may indicate that the processes regulating the chemical enrichment of galaxies at high redshift are subject to a more varied range of phenomena that occur on different timescales (given the timescale sensitivity of N/O) with respect to local galaxies. We perform a simple test to examine how much of the dispersion observed in our KLEVER sample is due to the uncertainties in the measurement of metallicities and nitrogen abundances. We assume that the KLEVER galaxies fall on the best fit (red) line to the SDSS data, before perturbing both the nitrogen abundance and metallicity randomly within their measured errors. We then calculate the dispersion of the perturbed KLEVER sample relative to the local best fit, as done for the true KLEVER sample. We repeat this 1,000 times, finding that the mean dispersion of the perturbed KLEVER data is 0.2 dex. We do not include the intrinsic scatter in this test, but note that its inclusion would act to broaden the perturbed sample. The dispersion of 0.2 dex is comparable to the magnitude of the observed scatter, 0.18 dex, suggesting that the larger dispersion in KLEVER galaxies compared to the SDSS sample is expected due to the uncertainties in the estimation of N/O and O/H for our high-z sample.

In Figure 3.6 we also show the average position of KLEVER galaxies in the N/O–O/H plane at log(N/O) = -1.22 and 12+log(O/H) = 8.46. Our high-redshift KLEVER galaxies tend towards larger N/O values at a fixed O/H compared to local galaxies, with an average offset of 0.1 dex in log(N/O). The standard error on the mean log(N/O) value is 0.03 dex, suggesting that the offset of 0.1 dex is significant. However, the large scatter of individual objects remains, and even with the slight offset of KLEVER galaxies to larger N/O values, the majority of the KLEVER sample still lie within the 99% density contours of the SDSS sample, suggesting no strong evolution of the N/O–O/H relation. Our observed offset is smaller than that presented in Masters et al. (2014) (M14), who report an average log(N/O)

$= -0.99$ for a stacked sample of 26 high redshift galaxies. The difference in the absolute values of the nitrogen abundances between M14 and the results presented within this chapter are primarily driven by the choice of different calibrations for N/O. Indeed, if we adopt the calibration provided by Thurston et al. (1996) which uses photoionisation codes to estimate the N/O ratio from strong emission lines, as in M14, our average N/O value increases to log(N/O) ~ -1.1. M14 also report 0.4 dex enhancement in N/O at a fixed O/H, much larger than our own estimated enhancement. However, several factors make a direct comparison of the reported enhancements difficult, including the choice of different metallicity diagnostics and different local samples to compare to, e.g. whilst we use SDSS galaxies, M14 uses local HII regions from Van Zee et al. (1998). It is therefore more straightforward to compare between samples using line ratios, such as N2O2, directly. Shapley et al. (2015) find that $z \sim$2 galaxies are offset to larger values of log(N2O2) by 0.24 dex when compared to SDSS galaxies near log(R3)$\sim$0.5. If we perform a similar analysis, we find that our KLEVER galaxies show a similar enhancement of 0.2 dex in log(N2O2). Similarly, Steidel et al. (2016) present a composite spectrum of high-redshift galaxies from the Keck Baryonic Structure Survey (KBSS) with log(N2O2) $= -1$, which is 0.17 dex lower than the KLEVER average of log(N2O2) $= -0.83$. However, the KBSS composite spectrum has log(O3N2) = 1.64, whereas for our KLEVER sample we find an average log(O3N2) = 1.06, where log(O3N2) $\equiv$ log(R3) $-$ log(N2). The difference in sample selection between KBSS and KLEVER means that the difference in O3N2, and hence N2O2, is expected. Whilst KLEVER galaxies are Hα selected, the KBSS sample differs in that it is rest-UV selected, meaning it may be biased against more massive galaxies, hence probing lower metallicities on average than our sample. The KBSS sample also requires slit-loss corrections in order to compare emission lines between different bands (such as Hα and Hβ). These corrections have a median uncertainty of 8%, introducing an additional source of error that is not present for the KLEVER sample. Our average values for N2O2 are in good agreement with the KBSS sample when compared in the log(O3N2) v log(N2O2) plane as presented in Strom et al. (2017). This suggests the level of nitrogen enrichment in our KLEVER sample is comparable to that of other high-redshift samples found in literature.

3.4.2 Evolution of the N/O–M$_\star$ relation

Trend in SDSS galaxies

Nitrogen abundance is also known to correlate with the stellar mass of galaxies, with higher stellar masses having greater N/O ratios (Pérez-Montero & Contini 2009). It has been argued by Andrews & Martini (2013) that this relation may be tighter than the N/O–O/H relation, however we note that their analysis relies on SDSS galaxies that have been stacked using stellar mass, a choice of binning which will artificially reduce the scatter in the N/O–$M_\star$ plane.

An advantage of studying N/O against stellar mass rather than metallicity is that it provides a more "closed box" diagnostic for the chemical enrichment within a galaxy. This is because N/O and stellar mass are generally invariant to gas inflows and outflows, as opposed to the metallicity which depends more strongly on these processes. Masters et al. (2016) argued that an enhanced N/O at fixed O/H could be a symptom of high-z galaxies having higher stellar masses than local galaxies at a fixed O/H due to the redshift evolution of the mass-metallicity relation. If there is no strong evolution in the relationship between stellar mass and N/O, then this would cause high-z galaxies to naturally have larger N/O values than their local counterparts. Mild evolution of the $M_\star$–N/O relation has been found when using the N2S2 diagnostic to determine N/O, with high-z galaxies tending towards lower N/O out to $z \sim 0.4$ (Pérez-Montero et al. 2013) in a way expected if N/O tracks O/H. Similarly, Masters et al. (2016) brought together data from Kashino et al. (2017) and Steidel et al. (2014) to show a mild evolution of N/O to values that are ∼0.1 dex lower at a fixed stellar mass out to $z \sim 1.6$. Yet, as already discussed in Section 3.3.1, determining the N/O abundance by using the N2S2 is affected by issues plaguing this diagnostic. However, works that instead use the N2O2 diagnostic to determine N/O such as Strom et al. (2017) find a more significant evolution in the stellar mass–N/O relation, with N/O values up to 0.5 dex lower at a fixed stellar mass.

We have investigated these aspects in the SDSS and KLEVER samples in a homogeneous and consistent way, making use of our revised N/O calibration. The trends between stellar mass and N/O for our SDSS and KLEVER samples are shown in Figure 3.7. In order to parametrise a best fit to the local relation, we adopt an ‘S-shaped’ function that accounts for a low log(N/O) plateau at low stellar masses, $\log(\mathrm{N/O})_0$, as observed in Andrews & Martini (2013), as well as a second log(N/O) plateau at high stellar masses, $\log(\mathrm{N/O})_1$, to account for a flattening of the relation as observed in Pérez-Montero & Contini (2009). The function is then defined as

$$\log(\mathrm{N/O}) = \log(\mathrm{N/O})_1 - \frac{[\log(\mathrm{N/O})_1 - \log(\mathrm{N/O})_0]}{\left[1 + (M_*/M_0)^k\right]}, \tag{3.4}$$

where k defines the steepness of the transition between the low and high N/O plateaus and M_0 is the stellar mass about which the gradient of the function begins to decrease. Similar to our method for the N/O–O/H relation, we fit this function by binning in 0.25 dex wide intervals of stellar mass, taking the median nitrogen abundance and calculating the standard deviation within each bin (shown as white circles in Figure 3.7). We then performed a least-squared

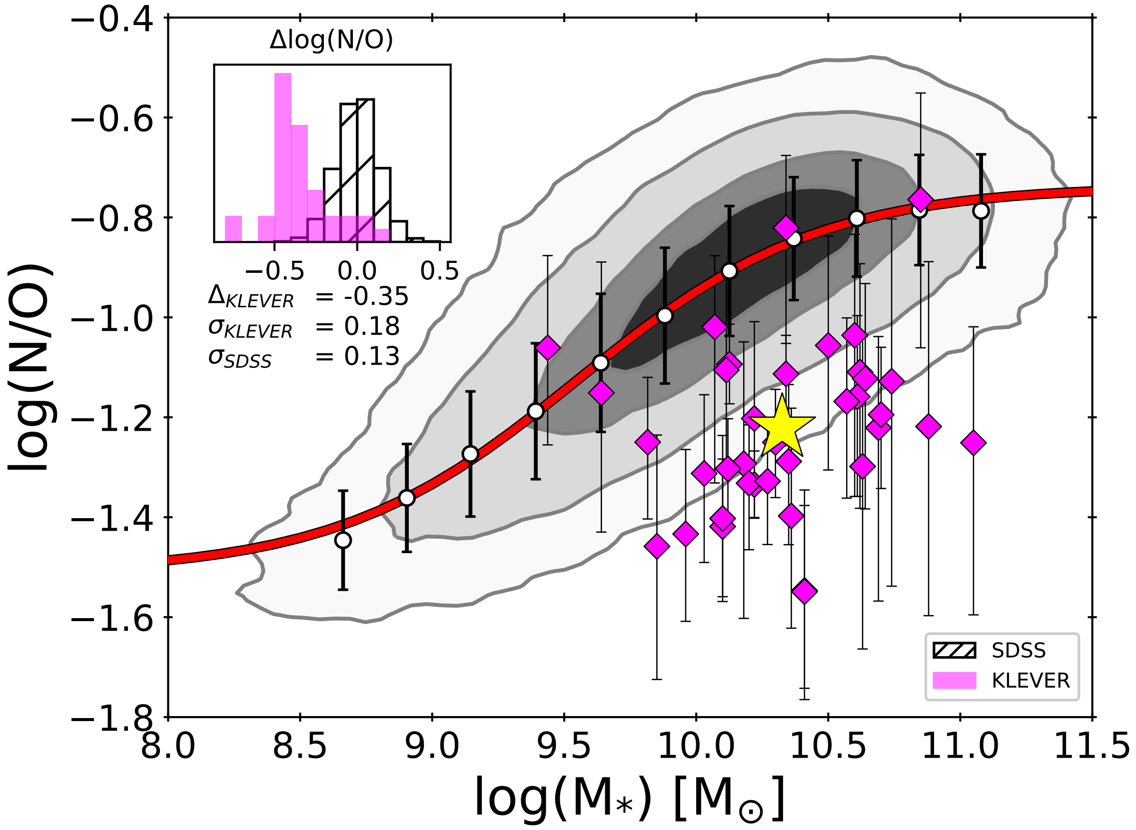

Fig. 3.7 The nitrogen abundance as a function of the stellar mass for the SDSS and KLEVER galaxy samples. The grey contours show the regions encompassing 30%, 60%, 90% and 99% of the total SDSS sample. The white points show the median binned SDSS data with corresponding standard deviations, with the solid red curve representing the best fit to the data using Equation 3.4. The magenta points are the KLEVER galaxies with corresponding errorbars, with the average position of the KLEVER galaxies shown as a yellow star. The histogram in the top left shows the deviations from the best fit in log(N/O) for both the KLEVER and SDSS samples. KLEVER galaxies have an average depletion in N/O of 0.35 dex compared to SDSS galaxies, suggesting significant redshift evolution in the stellar mass–N/O relation.

Table 3.2 The values of the best-fit parameters of the median N/O-stellar mass relation for the SDSS galaxy sample, fit using Eq. 3.4.

$\log(\mathrm{N/O})_0$	$\log(\mathrm{N/O})_1$	k	$\log(\mathrm{M}_0/\mathrm{M}_\odot)$
-1.51 ± 0.04	-0.737 ± 0.015	0.95 ± 0.08	9.55 ± 0.05

regression to fit Equation 3.4 to the median-binned data, including only bins containing at least 25 galaxies and weighting by the standard error calculated from the standard deviation in N/O and the number of objects within each bin. The best fit parameters are reported in Table 3.2. The resulting fit is shown as a solid red curve in Figure 3.7, and appears visually to be a good parametrisation of our binned SDSS data. Whilst we do not probe many galaxies below a stellar mass of $\log(\mathrm{M}/\mathrm{M}_\odot) = 8.9$, the proposed end of the low N/O plateau found in Andrews & Martini (2013), we find that the value of the plateau is in good agreement with the value found earlier in the N/O–O/H plane at $\log(\mathrm{N/O}) \sim -1.5$. At the high mass end the relationship is found to flatten at a value of $\log(\mathrm{N/O}) \sim -0.74$, which could be interpreted in the context of the flattening of the mass-metallicity relation at high stellar masses (Tremonti et al. 2004). When O/H is no longer increasing with stellar mass, the strong dependency of N/O on O/H means a flattening in O/H with stellar mass will be reflected in N/O. For our SDSS galaxy sample the relationship between N/O and stellar mass is less tight than the N/O–O/H relation, with a scatter of 0.13 dex in N/O about the median relation for individual galaxies.

Trend for KLEVER galaxies

The KLEVER galaxies are shown in the stellar mass–N/O plane in Figure 3.7, along with the SDSS comparison sample. The positive correlation between stellar mass and N/O is still recovered at $z \sim 2$, with a Spearman's rank correlation coefficient of 0.31 and p = 0.06, although the correlation is less strong than that found in the SDSS sample, where the Spearman's rank correlation coefficient is 0.74. Our high-redshift galaxies clearly occupy a different region of the N/O-stellar mass plane than the local SDSS galaxies, with roughly half of the KLEVER sample falling below the 99% density contours of the local sample. We find that, on average, KLEVER galaxies fall 0.35 dex below the local best-fit relation. This suggests a significant evolution in the relationship between stellar mass and N/O between $z \sim 0$ and $z \sim 2$. Our results are in agreement with those from Strom et al. (2017), who find that KBSS galaxies at $z \sim 2.3$ are $\sim$0.32 dex lower in N/O at a fixed stellar mass. The strong evolution of the stellar mass–N/O relation is comparable to the evolution of the mass-metallicity relation, where studies have observed a change in O/H of -0.26 dex at a fixed stellar mass for galaxies at $z \sim 2$ compared to local samples (Sanders et al. 2021). Such similar evolution of the mass-metallicity relation and the stellar mass–N/O relation could suggest that the N/O–O/H plane is approximately redshift-invariant.

In contrast with our result, Pérez-Montero et al. (2013) and Masters et al. (2016) found the mass–N/O relation to be redshift invariant or subject to a more modest redshift evolution. Beyond the different redshifts probed, $z \sim$0.4 for Pérez-Montero et al. (2013) and $z \sim$1.6 in Masters et al. (2016), the main reason for the difference with our result is their choice of N2S2 as a diagnostic, rather than N2O2. As highlighted in Figure 12 of Strom et al. (2018), there is an offset in the relationship between N2O2 and N2S2 between local galaxies and high-redshift galaxies, which behave more like HII regions. This offset will mean that using N2S2 to directly trace the nitrogen abundance without using an appropriate conversion to N/O, as done in Masters et al. (2016) and Kashino et al. (2017), will lead to N/O being underestimated in local galaxies with respect to high-redshift samples, making any evolution in the stellar mass–N/O plane less apparent. The use of N2S2 as a diagnostic for the nitrogen abundance and the physical interpretation of evolution in the stellar mass–N/O plane are discussed further in Section 3.5.2.

3.5 Fundamental scaling relations

3.5.1 Fundamental metallicity relation (FMR)

SDSS ($z \sim$0)

Several works have investigated the secondary dependence of the mass-metallicity relation on star formation rate, finding that the relationship between these three variables may also be redshift invariant out to $z \sim 3$ (Mannucci et al. 2010; Andrews & Martini 2013; Cresci et al. 2019; Curti et al. 2020a; Sanders et al. 2021). Two 2D representations of the local relationship between $M_\star$–O/H–SFR are shown in Figure 3.8. In the left-hand panel, the contours and shaded regions show the density of SDSS galaxies in the mass-metallicity plane, while coloured lines show the trend of SDSS galaxies in 0.2 dex wide bins of SFR. For each bin, we take the median O/H in 0.25 dex wide intervals of stellar mass, plotting all bins containing at least 25 objects. The average MZR for the full SDSS sample is shown as a black line, with points of median O/H across the range of stellar masses probed shown as white circles. The majority of the scatter below the average mass-metallicity relation can be explained by variations in star formation rate, with the individual SFR tracks extending out to the 99% density contours of the SDSS sample. The correlation between $M_\star$–O/H–SFR is often understood in the context of gas inflows, where infalling pristine gas dilutes the

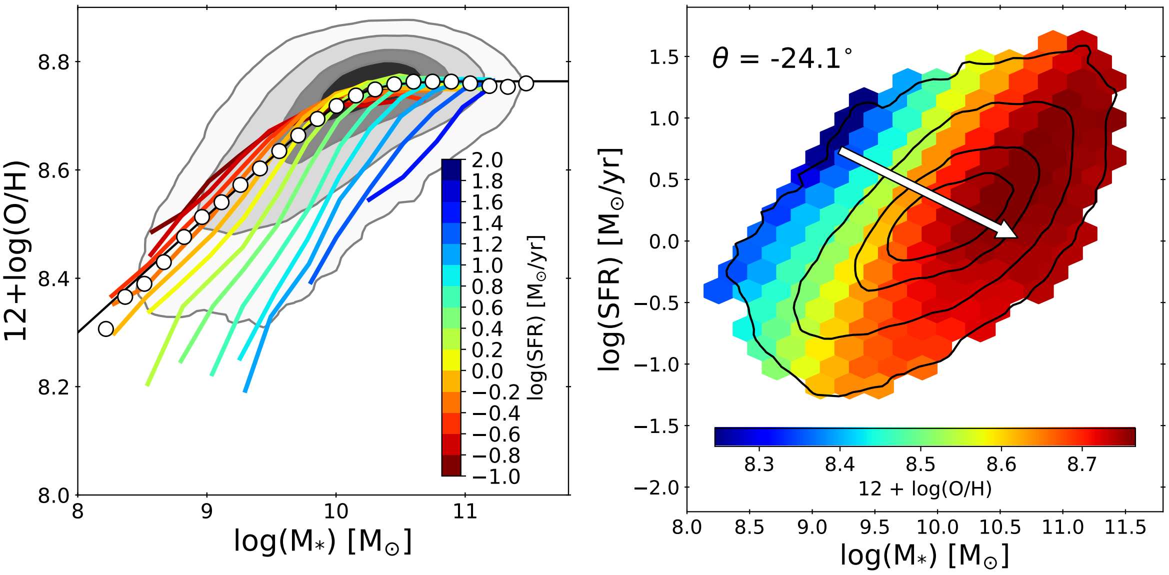

Fig. 3.8 Two representations of the SFR dependence of the MZR in local galaxies. The contours show the regions encompassing 30%, 60%, 90% and 99% of the sample. **Left**: The SDSS data has been binned into 0.2 dex wide bins of SFR. For each SFR bin, the median metallicity is measured in 0.25 dex wide bins of stellar mass, and all bins containing at least 25 objects are plotted. The median bins for the total sample are shown as white circles, with average MZR for the total sample is plotted as a black line. **Right**: the SDSS data has been spatially binned, with all bins containing at least 25 objects being shown, and the colour representing the average metallicity within each bin. The white arrow shows the direction in which metallicity is most efficiently increased for the total sample, derived using partial correlation coefficients as described in Section 3.5.1. The angle of -24.1° highlights that the correlation between O/H and stellar mass is more than twice as strong as the anti-correlation between O/H and SFR.

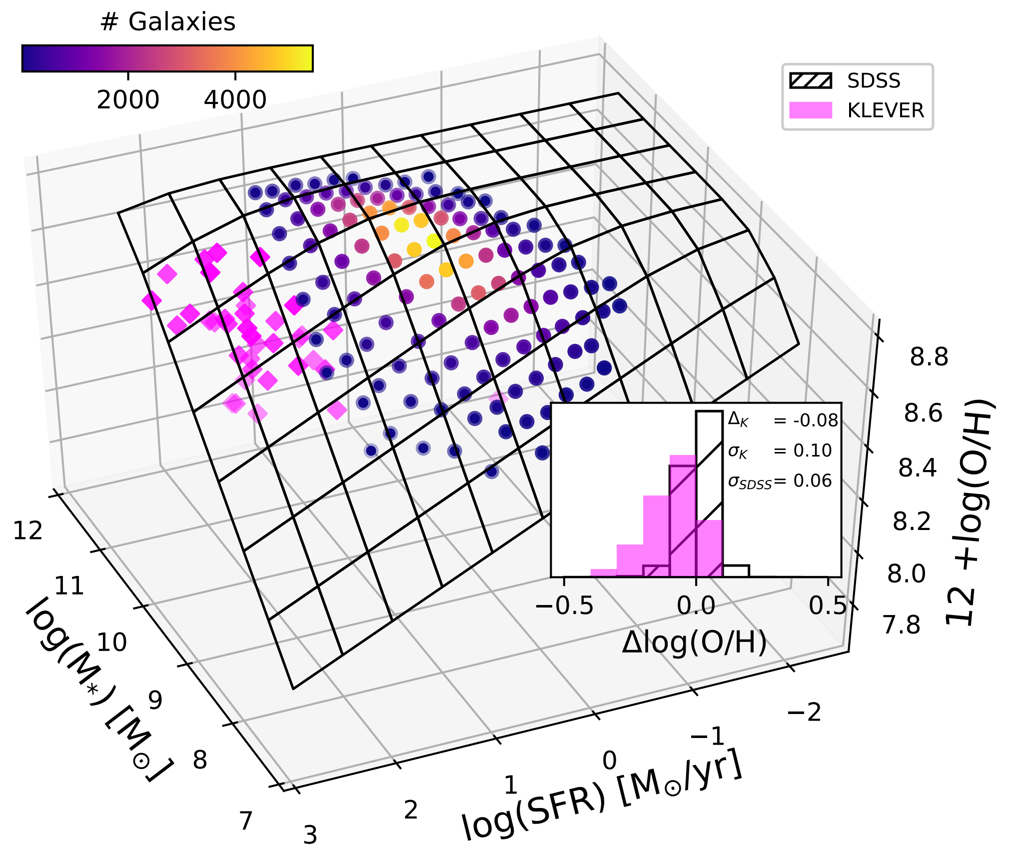

Fig. 3.9 The 3D FMR showing the relationship between $M_\star$–O/H–SFR. The grid shows the relationship derived from the binned SDSS sample, shown as circles, with the colourbar showing the number of galaxies within each $M_\star$–SFR bin. KLEVER galaxies are shown in magenta, and the difference in the scatter of individual galaxies about the FMR for both SDSS and KLEVER galaxies is shown in the histogram. The average offset of KLEVER galaxies from the FMR is just 0.08 dex, which suggests that KLEVER galaxies lie on the FMR within uncertainties.

metallicity whilst fostering star formation at a specific stellar mass (Davé et al. 2011). In this scenario, the secondary anti-correlation between metallicity and SFR should be a byproduct of a more fundamental relation between metallicity and gas content (Bothwell et al. 2013, 2016a, 2016b), although with lower statistics. Other factors may also play a role in causing the fundamental metallicity relation, such as metal-loaded outflows, gas recycling through galactic fountains, or variations in the IMF (Tremonti et al. 2004; Köppen et al. 2007;Davé et al. 2011; Sanders et al. 2021).

In Figure 3.8, we also show an alternative but equivalent representation of the relationship between $M_\star$–O/H-SFR. Here, we spatially bin the SDSS sample in the stellar mass–SFR plane, displaying all bins that contain at least 25 objects, with the colour representing the average metallicity within each bin. The white arrow shows the direction of the metallicity gradient in the stellar mass–SFR plane, as calculated using partial correlation coefficients (PCCs). Partial correlation coefficients quantify the strength of correlation between two variables, A and B, when keeping a third variable, C, fixed. This is defined by

$$\rho_{AB,C} = \frac{\rho_{AB} - \rho_{AC} \cdot \rho_{BC}}{\sqrt{1 - \rho_{AC}^2}\sqrt{1 - \rho_{BC}^2}}, \tag{3.5}$$

where ρ_{AB} represents the Spearman's rank correlation coefficient between variables A and B. Following Bluck et al. (2020), we can then take the PCC between O/H and $M_{\star}$ fixing SFR and the PCC between O/H and SFR fixing $M_{\star}$, and treat them as two components of a vector in order to determine the direction in which we must move on the mass–SFR plane to maximise the change in O/H. This direction is given by

$$\theta = \arctan\left(\frac{\rho_{Yz,X}}{\rho_{Xz,Y}}\right), \tag{3.6}$$

where θ is measured from the horizontal, X and Y are the variables on the respective x and y axes, and z is the third variable being investigated. If the anti-correlation between O/H and star formation rate is equally as strong as the correlation between O/H and stellar mass, we would find that $\theta = -45°$. Instead, we determine that the angle that maximises the change in O/H on the stellar mass–SFR plane is $\theta = -24.1°$. This result highlights that the correlation between O/H and stellar mass is stronger than the anti-correlation between O/H and SFR, which has a secondary but significant role in regulating the O/H. We note that the fundamental metallicity relation found by Mannucci et al. (2010), in which the SFR accounts for about 1/3 of the metallicity variation would have implied an angle of -30° for the gradient arrow. Our results suggest a similar dependency, although the finding that the gradient arrow is flatter indicates that the SFR has a somewhat lesser role in regulating the metallicity. The difference between the result expected from Mannucci et al. (2010) and our own may be driven in part by the use of different metallicity diagnostics.

KLEVER (z ~2.2)

As larger samples of high-redshift galaxies have been assembled, several authors have studied whether the local fundamental metallicity relation still holds at high-redshift. Some works have shown that high-redshift galaxies often fall below the FMR relative to their expected position for a given stellar mass and SFR (Cullen et al. 2014; Troncoso et al. 2014; Sanders et al. 2015, 2018), although this offset is often small and of the order ~ 0.1 dex. Such an offset is well within the predictive errors of locally calibrated FMR planes, especially when considering the potential evolution of metallicity diagnostics at high-z (discussed in Section 3.2). Indeed, recent work by Sanders et al. (2021) found that using a metallicity calibration from Bian et al. (2018) for objects at $z > 2$ yields metallicity estimates that are 0.05-0.1 dex larger than those made using locally calibrated diagnostics, effectively cancelling any offset.

We investigate whether our KLEVER galaxies fall on the fundamental metallicity relation using the parameterisation provided in Curti et al. (2020a), adopting total-SFR estimates for SDSS galaxies. The local FMR is shown as a 3D plane in Figure 3.9, with the locations of the KLEVER points shown in magenta. The inset in the same figure shows the distribution of galaxies around the FMR, both for SDSS local galaxies and for the KLEVER galaxies at $z \sim 2.2$. As can be seen, the average deviation of the O/H for KLEVER galaxies from that estimated using the stellar mass and SFR is just 0.08 dex. This offset is possibly due to our use of locally calibrated metallicity diagnostics, but nevertheless falls well within the uncertainties associated to metallicity predictions made using the FMR that are of the order $\sim$0.15 dex, as shown in Figure 11 of Curti et al. (2020a). KLEVER galaxies also probe a region of the FMR that is not populated by local galaxies, therefore any prediction of their metallicity using the parametrised form of the FMR relies on its extrapolation. As such, we conclude that, to the level of accuracy granted by the present observations, KLEVER galaxies are consistent with evolutionary scenario depicted by the FMR, suggesting that the processes governing the baryonic growth of galaxies operate in the same manner at $z \sim 2$ as they do locally.

3.5.2 Fundamental nitrogen relation (FNR)

SDSS ($z \sim 0$)

Analogous to the FMR defining the relationship between $M_\star$–O/H–SFR, we can replace O/H with N/O to probe the potential existence of a Fundamental Nitrogen Relation (FNR). N/O is not sensitive to many of the physical processes that O/H is, such as pristine gas inflows[2], and instead is sensitive to the enrichment timescales within the galaxy due to the delayed production of nitrogen relative to oxygen. This makes the relationship between $M_\star$–N/O–

---

[2] We do note that N/O may be sensitive to inflows that are rich in oxygen, but do not contain much nitrogen. Such a scenario is compatible with the re-accretion of enriched gas that was expelled from a galaxy early in its evolution, before N enrichment could begin, and would have the effect of decreasing the N/O ratio as long as the inflowing gas mass is large compared to the gas mass within the galaxy. This dilution scenario will be explored in more detail in Chapter 5.

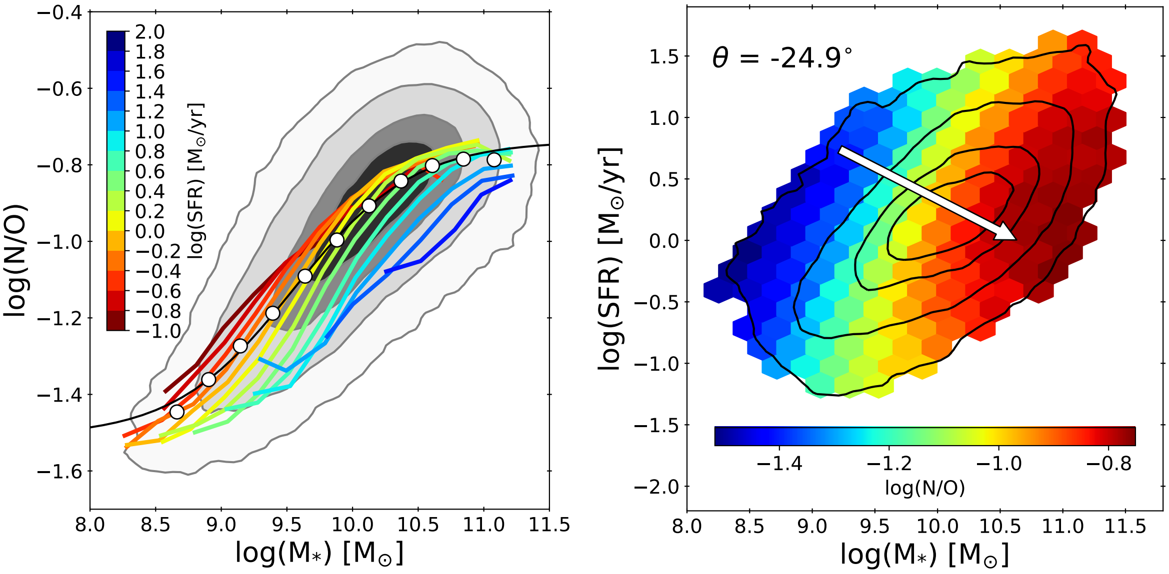

Fig. 3.10 Two representations of the SFR dependence in the stellar mass–N/O plane for local galaxies. The contours show the regions encompassing 30%, 60%, 90% and 99% of the sample. **Left**: The SDSS data has been binned into 0.2 dex wide bins of SFR. For each SFR bin, the median N/O is measured in 0.25 dex wide bins of stellar mass, and all bins containing at least 25 objects are plotted. The median bins for the total sample are shown as white circles, with average stellar mass–N/O relation for the total sample is plotted as a black line. **Right**: the SDSS data has been spatially binned, with all bins containing at least 25 objects being shown, and the colour representing the average nitrogen abundance within each bin. The white arrow shows the direction in which nitrogen abundance is most efficiently increased for the total sample, derived using partial correlation coefficients as described in Section 3.5.1. The angle of −24.9° is extremely similar to the angle of −24.1° derived for the fundamental metallicity relation, highlighting the similarity of the $M_\star$–SFR–O/H and $M_\star$–SFR–N/O relations.

SFR a powerful probe of galaxy evolution in regards to quantities relating to enrichment timescales, such as galaxy age and star formation efficiency.

We begin by investigating the relationship between $M_\star$–N/O–SFR in the 2D stellar mass–N/O plane for local galaxies, following the analysis presented in Section 3.5.1. The results can be seen in Figure 3.10 which is analogous to Fig. 3.8, where now O/H is replaced with N/O. The N/O ratio depends not only on stellar mass, but also on SFR (at fixed $M_\star$): indeed, an anti-correlation exists between N/O and SFR, at fixed stellar mass, similar to the anti-correlation between O/H and SFR found in the fundamental metallicity relation. The similarities between the anti-correlations of N/O and O/H with SFR are well highlighted by considering the partial correlation coefficient vectors on the right-hand side of Figures 3.8 and 3.10. The direction to maximise the N/O variation in the stellar mass–SFR plane is $\theta = -24.9^\circ$ below the horizontal, which is fully consistent with the value of $\theta = -24.1^\circ$ found in the FMR.

We note that if the secondary dependence of O/H on SFR was due to accretion of pristine gas (diluting O/H and fostering SFR), then this should not translate into a secondary dependence of N/O on SFR, as N/O is not sensitive to accretion of pristine (H) gas. The finding that N/O has essentially the same dependence on SFR as O/H suggests that the accretion of pristine gas is not the only origin of the O/H–SFR anti-correlation. An alternative explanation could be that the accreting gas is metal poor, although not pristine, and slightly enriched by primary nitrogen (i.e. $\log(\mathrm{N/O}) \sim -1.5$). This scenario will be investigated in more detail in Chapter 5. Age and star formation history effects, which are linked to the current level of SFR, are also likely to play an additional important role in explaining both relations.

However, we also note that there are differences in the amount of scatter that can be explained by the SFR in these two planes. Unlike in the mass-metallicity relation, the star formation rate tracks in the stellar mass–N/O plane do not extend below the 90% density contours of the local sample. Furthermore, the scatter above the average stellar mass–N/O relation is much larger than that above the MZR, meaning a fundamental nitrogen relation constructed from the SFR tracks will not improve the scatter in N/O as dramatically as the fundamental metallicity relation is able to for O/H.

The relationship between $M_\star$–N/O–SFR has previously been investigated by Pérez-Montero et al. (2013), who found no strong dependence on SFR in the stellar mass–N/O plane, suggesting that the relationship between O/H and SFR is driven primarily by inflows of metal poor-gas, which N/O is insensitive to. Once again, our results are different mainly due to Pérez-Montero et al. (2013) using the N2S2 diagnostic to derive N/O, whilst we use N2O2, with the differences between this diagnostics highlighted earlier in Section 3.3.1. Indeed, if we adopt the N2S2 diagnostic for the sample in this chapter and re-plot the correlation between stellar mass and N/O, we do not identify any dependence on SFR in the stellar mass–N/O plane, aligning our results with those of Pérez-Montero et al. (2013). We note that the dependence on SFR, when using N2O2 as a proper diagnostic, is not unique to our own calibrations, and remains if the calibrations from PMC09 are used instead. This further highlights how the choice of diagnostic for N/O can impact the results.

Given the dependence on SFR that we observe in the stellar mass–N/O plane when adopting the N2O2 diagnostic, we suggest that the fundamental metallicity relation is not purely driven by the accretion of pristine gas, but must also be partially driven by varied chemical enrichment timescales.

To test whether the relationship that we observe between $M_\star$–N/O–SFR evolves with redshift, we aim to define a relationship in the 3D plane between these variables, following a similar approach as for the fundamental metallicity relation in Curti et al. (2020a). We fit the SFR tracks from the left-hand panel of Figure 3.10 with the functional form of the stellar mass–N/O relation from Equation 3.4 using a least-square minimisation. We fit only those SFR tracks with at least 8 data points, each of which contain at least 25 galaxies, to ensure the tracks probe a wide range of stellar masses. However, even with this requirement, not all SFR tracks extend to both the low and high mass regimes where we expect to see plateaus in N/O. As such we set the $\log(\mathrm{N/O})_0$ value to the global value of -1.5 and the $\log(\mathrm{N/O})_1$ value to -0.74 for all SFR tracks. The remaining two parameters, M_0 and k, are allowed to vary freely. There is a linear positive correlation between M_0 and SFR, whilst k shows only a mild non-linear dependence on star formation rate, varying between values of 1 and 1.4. The higher turnover mass (M_0) for more star forming galaxies can be interpreted in the context of age of the galaxy and the star formation efficiency. If we consider SFR to be a tracer of galaxy age then at a fixed stellar mass younger, more star-forming galaxies have had less time for the delayed enrichment of nitrogen relative to oxygen to occur and so have lower N/O ratios. Similarly if we instead consider galaxies at a fixed N/O, the more star forming galaxies tend towards larger stellar masses. In order for these young galaxies to assemble a large stellar mass in a short time, they must be efficient at converting their gas into stars, and thus must have larger star formation efficiencies. Therefore the observed trend could be due to a variation in galaxy age and star formation efficiency.

We obtain the final functional form for our 3D fundamental nitrogen relation by taking Equation 3.4 and allowing M_0 to vary with SFR as $\log(M_0/M_\odot) = m_1 + m_0\log(\mathrm{SFR})$, with k allowed to vary freely. We then use a least-square minimisation to fit this function to the median binned SFR tracks in the stellar mass–N/O plane, with the final parameter values reported in Table 3.3. The resulting 3D representation of the fundamental nitrogen relation

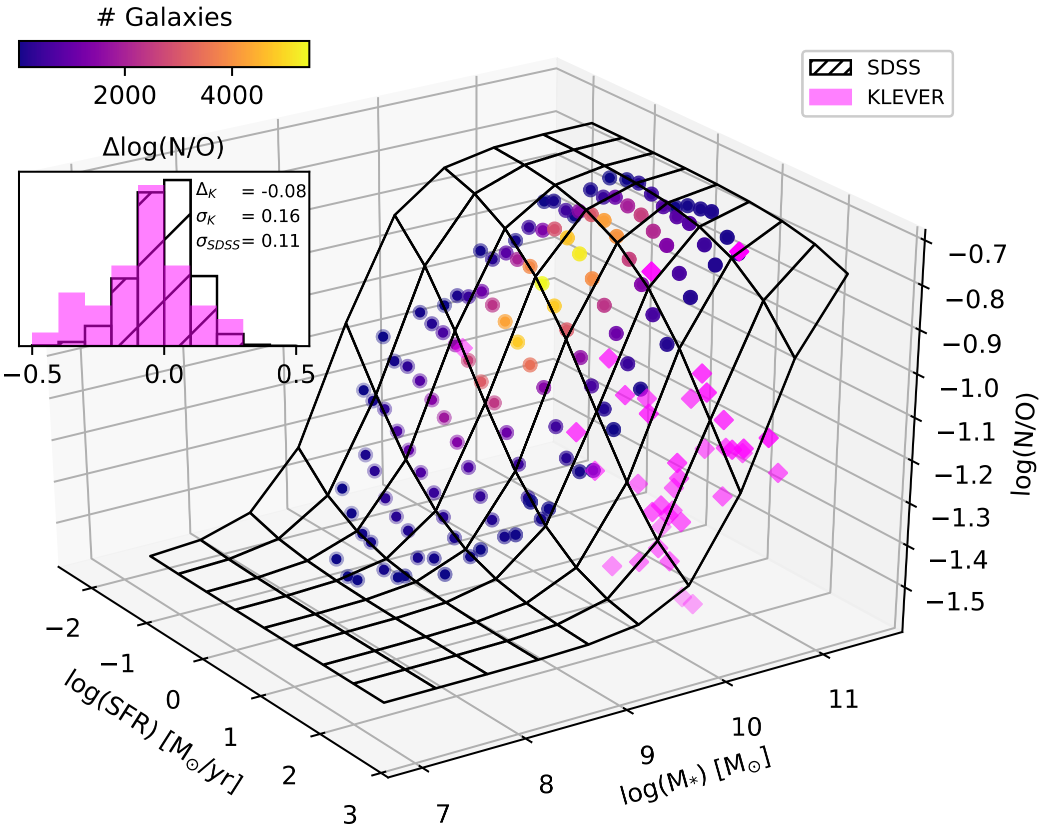

Fig. 3.11 The 3D FNR showing the relationship between $M_\star$–N/O–SFR as derived in this chapter. The grid shows the relationship derived from the binned SDSS sample, shown as circles, with the colourbar showing the number of galaxies within each $M_\star$–SFR bin. KLEVER galaxies are shown in magenta, and the difference in the scatter of individual galaxies about the FNR for both SDSS and KLEVER galaxies is shown in the histogram. Similar to the results presented in Fig 3.9, the average offset of KLEVER galaxies from the FNR is just 0.08 dex, suggesting that KLEVER galaxies lie on the local fundamental nitrogen relation plane.

Table 3.3 The values of the best-fit parameters quantifying the variation of turnover mass with SFR and steepness of the transition from low to high N/O plateaus in our parameterisation of the FNR.

m_1	m_0	k
9.584± 0.004	0.451 ± 0.010	1.324 ± 0.019

can be seen in Figure 3.11. The SDSS points are taken in bins of $M_\star$ and SFR, and are shown as circles with the colour representing the number of galaxies in each bin.

KLEVER (z ~2.2)

The location of KLEVER galaxies on the fundamental nitrogen relation 3D plane is shown in Figure 3.11. The inset histogram shows the distribution of the deviations of SDSS and KLEVER galaxies from the FNR plane. As can be seen, KLEVER galaxies are generally found to be scattered about the fundamental nitrogen relation, meaning that although nitrogen appears to be under-produced in high-z galaxies relative to local ones when compared at a given stellar mass, if we account for the increase in star formation rate then KLEVER galaxies are well described by the local relationship between $M_\star$–N/O–SFR. If we interpret the variation between $M_\star$–N/O–SFR as being driven by time-related quantities such as galaxy age and star formation efficiency, then the high star formation rate values of the KLEVER galaxies, coupled with high stellar masses and low nitrogen abundances, suggests that KLEVER galaxies are chemically young and potentially have higher star formation efficiency than local galaxies (which results in faster oxygen enrichment relative to nitrogen). Furthermore, the apparent redshift invariance of the fundamental nitrogen relation suggests that any variations in $M_\star$, N/O or SFR driven by changes in the age or star formation efficiency occur smoothly between $z \sim 2$ and $z \sim 0$. This interpretation is in agreement with the suggestion from Masters et al. (2016) that a relation between N/O, $M_\star$ and galaxy age may exist, with the dependence on star formation rate acting as a tracer of the evolutionary stage of galaxies in our fundamental nitrogen relation.

3.5.3 The FMR-FNR symbiosis

The existence of a fundamental relationship between $M_\star$, N/O and SFR may be expected given the existence of both the fundamental metallicity relation and the N/O–O/H relation, assuming that these relationships hold for all galaxies. To compare our measured fundamental nitrogen relation to that which we would expect from a combination of the fundamental metallicity relation and the N/O–O/H relationship, we create a ‘model’ FNR. Within our model FNR, for a given stellar mass and star formation rate we calculate the O/H expected from the paramaterisation of the fundamental metallicity relation presented in Curti et al. (2020a), and shown in Figure 3.9. We then convert this expected O/H value into a value of N/O using our median N/O–O/H relation, given by Equation 3.3. The results are shown in Figure 3.12, where in the left hand panel the expected N/O values from the model are plotted against stellar mass in tracks of constant SFR, whilst the right hand panel shows the same plot

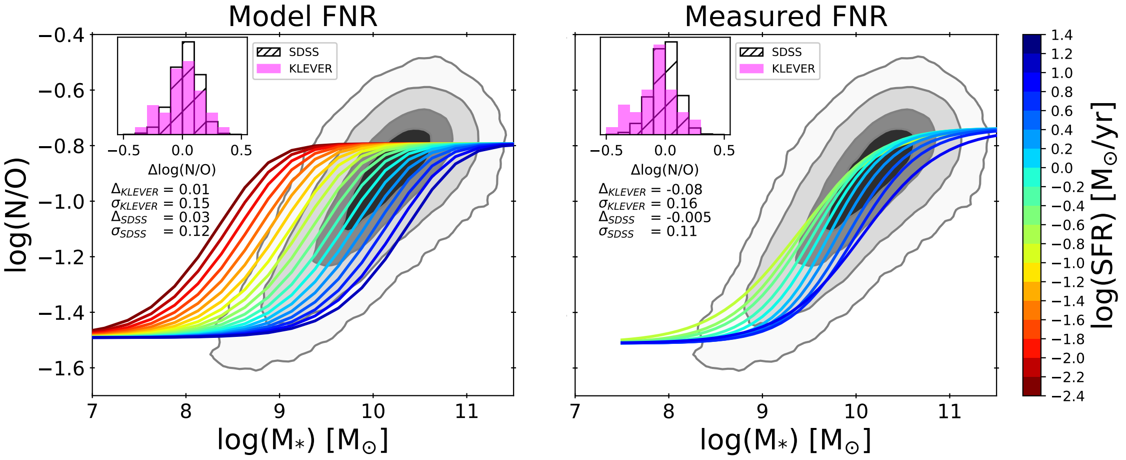

Fig. 3.12 The 2D projection of the fundamental nitrogen relation for both our model (left) and measured (right) relationships. The contours show the regions encompassing 30%, 60%, 90% and 99% of the SDSS sample. The coloured lines show tracks of constant SFR. For both the model and measured FNR, the inset histogram in the top left of each plot shows the difference between the expected and true log(N/O) values for both SDSS and KLEVER galaxies. The median offsets and standard deviations of the SDSS and KLEVER galaxies from both the model and measured FNR are shown below the inset histograms. The similar performance of the model and measured fundamental nitrogen relations suggests that the relationship between $M_\star$–N/O–SFR is driven by a combination of the fundamental metallicity relation and a redshift-invariant N/O–O/H relation.

but with expected N/O values calculated from our measured fundamental nitrogen relation. The inset histogram in the top left of each panel shows the offset between the expected and measured values of log(N/O) for both the SDSS and KLEVER samples.

The similarities between the model and measured FNRs are immediately visible, with the 'S-shaped' form of the star formation rate tracks in the model FNR being naturally reproduced by a combination of the functional forms of the mass-metallicity relation and our N/O–O/H relationship, justifying our choice of Equation 3.4 to parameterise the relationship between N/O and stellar mass. Both the model and measured FNR perform well in accurately predicting the N/O values of both the SDSS and KLEVER samples, with the offset in log(N/O) less than 0.1 dex in all cases. The precision of the model and measured FNRs are also comparable, with the scatters in log(N/O) = 0.12 and 0.11 for the SDSS sample and log(N/O) = 0.15 and 0.16 for the KLEVER sample respectively. The equivalency of our model and measured fundamental nitrogen relations suggest that the fundamental nitrogen relation is primarily driven by the combination of the fundamental metallicity relation with a redshift-invariant N/O–O/H relation. This suggests that evolution of the mass-metallicity relation is driven by processes that are probed not only by O/H, but also by N/O.

3.5.4 The role of galaxy evolutionary stage

To investigate the chemical enrichment history of the KLEVER galaxies further, we recall that the majority of these galaxies were found to lie below a metallicity of 12+log(O/H) $\sim$ 8.5, towards the region of the N/O–O/H plane where the N/O ratio plateaus at log(N/O) ~ -1.5. In Figure 3.13, we plot the stellar mass–N/O relation for only those SDSS galaxies with 12+log(O/H) < 8.5. The contours represent the distribution of the SDSS galaxies, for which we take the average N/O in 0.25 dex intervals of stellar mass and fit a straight line, shown in black. The best fit for the total SDSS sample is shown as a red line. The magenta points show the KLEVER galaxies, and the histogram shows the deviation of SDSS and KLEVER galaxies from the best-fit black line. A linear regression is used for this best-fit as by limiting the sample to only those galaxies with low metallicities, we do not span a wide enough range of stellar masses to probe either the low or high mass plateaus in N/O, leaving only bins that probe the central linear region of the stellar mass–N/O plane. It is clear from this plot that KLEVER galaxies behave similarly to low-metallicity local galaxies in this plane, which suggests that the same mechanisms govern the production of nitrogen in high-z galaxies and low-metallicity local galaxies. Within the SDSS galaxies, a clear dependence on stellar mass is observed, which suggests that even within the low-metallicity galaxies which lie towards the low N/O plateau variable contributions from secondary nitrogen production mechanisms, or delayed nitrogen enrichment, may be present.

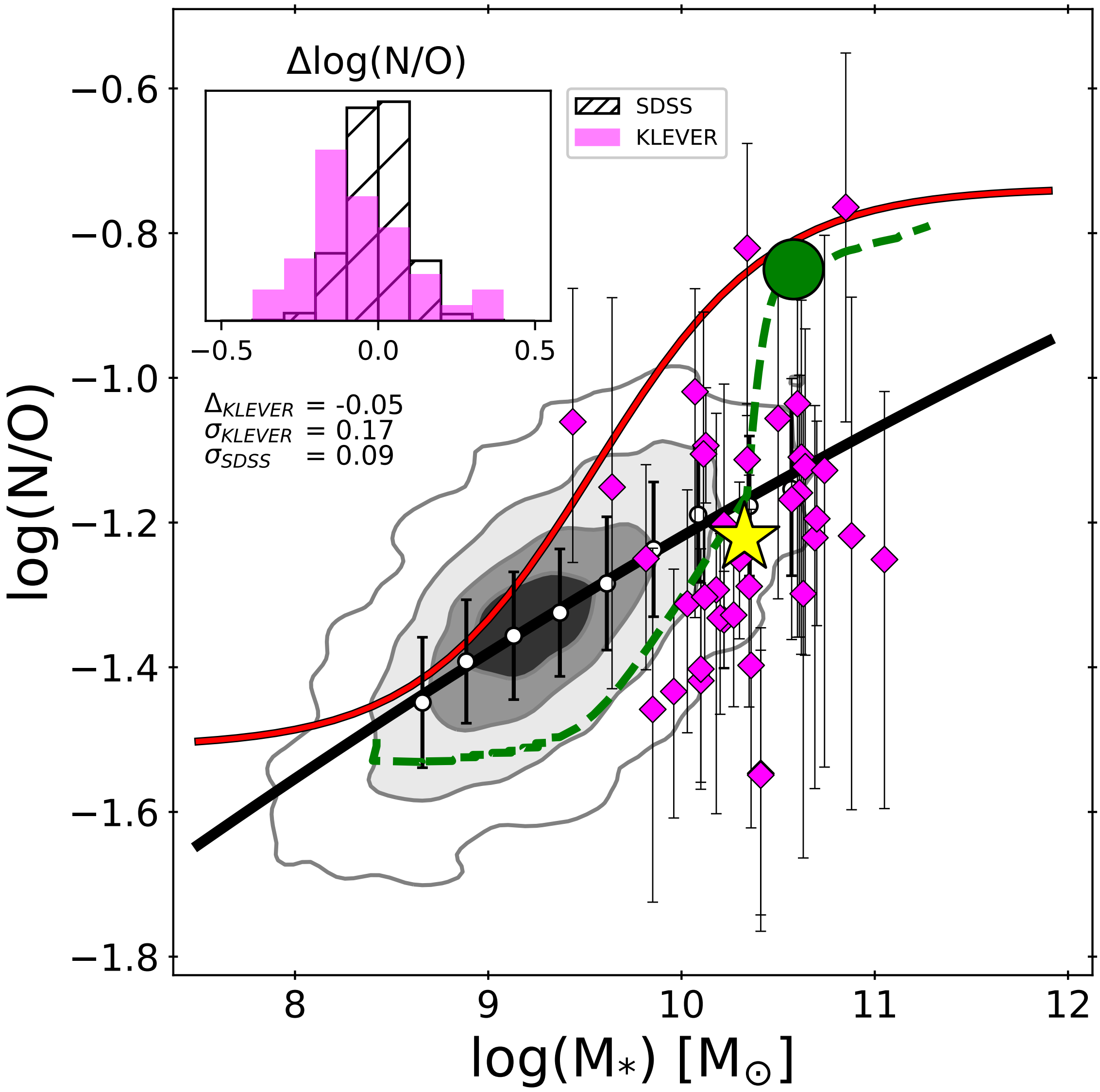

Fig. 3.13 N/O as a function of the stellar mass. The grey contours show the regions encompassing the 30%, 60% 90% contours of the local SDSS galaxies with a gas phase metallicity of 12+log(O/H)<8.534. The magenta points represent individual KLEVER galaxies, with the average position of the KLEVER galaxies shown as a yellow star. The solid red line shows the median N/O–$M_\star$ relation derived for the full SDSS sample, whilst the solid black line shows the best fit to the median N/O–$M_\star$ relation for only SDSS galaxies with 12+log(O/H)<8.534. The histogram in the top left shows the deviation in N/O from the black line for individual low metallicity SDSS galaxies and KLEVER galaxies. The dashed green line shows the evolutionary track for a single galaxy using chemical evolution models with an infall mass $\log(M_{inf}) = 12\ M_\odot$, infall time $\tau_{inf} = 7$ Gyr, mass loading factor $\omega = 1.0$ and star formation efficiency $\nu = 5\ \mathrm{Gyr}^{-1}$ (Vincenzo et al. 2016b). The green circle shows the position of the galaxy at an age of 1 Gyr. The KLEVER galaxies are offset from the local relation by only −0.05 dex when compared to local low-metallicity galaxies, in contrast to the large offset in N/O of −0.32 dex that was found when KLEVER galaxies are compared to the full SDSS sample. This suggests that the production mechanisms for nitrogen in high-redshift galaxies are more similar to low-metallicity local galaxies.

Even without considering the star formation rate, this conclusion is in agreement with our interpretation of the fundamental nitrogen relation. If KLEVER sources are young galaxies with high star formation efficiencies, then they will be able to attain a large stellar mass and metallicity in a short time, with an enrichment history dominated by the products of core-collapse supernovae, in agreement with the results of other works studying high-z galaxies (Steidel et al. 2016; Strom et al. 2018;Shapley et al. 2019; Sanders et al. 2020; Topping et al. 2020a,2020b; Cullen et al. 2021). The delayed enrichment of nitrogen relative to oxygen, mainly caused by low and intermediate mass stars, can then cause the N/O ratio to increase, with N/O increasing to greater values in the more massive, metal-rich galaxies due to a greater impact from secondary nitrogen production in low and intermediate mass stars. To confirm the feasibility of the scenario described above, we plot a galaxy evolutionary track from the chemical evolution models of Vincenzo et al. (2016b) (see also Magrini et al. 2018) in Figure 3.13. We note that the model used assumes a Salpeter (1955) IMF, although we expect that a change to a Chabrier (2003) IMF would have little effect on the shape of the evolutionary track, with a mild change in the normalisation with stellar mass. The evolutionary track is characterised by a large star formation efficiency of 5 Gyr^{-1}, with the track moving horizontally on the plane, increasing stellar mass without enriching N/O, before N/O rapidly begins to increase towards the average relation for the full sample. In Figure 3.13 we highlight where the galaxy would lie on the plane at an age of 1 Gyr. A galaxy on the evolutionary track with log(N/O) $\sim$ -1.2, roughly the median value of the KLEVER sample, would have an age of $\sim$ 0.5 Gyr. This suggests that some of the scatter in N/O values could be attributed to differences in galaxy age (or star formation history), with galaxies with mass-weighted ages that are older having had more time for nitrogen enrichment to occur. More detailed modelling of nitrogen abundances is the topic for future work, however if variation in star formation history of galaxies can explain the scatter of N/O with stellar mass, then it may also be responsible for the large observed scatter in the N/O–O/H plane.

3.6 Summary and conclusions

In this chapter, we have analysed the scaling relations between the nitrogen-over-oxygen (N/O) abundance and various galactic properties including metallicity, stellar mass and star formation rate. We introduced for the first time the full KLEVER sample of high redshift galaxies, and compared a sub-sample of these galaxies to the nitrogen abundance scaling relations found locally. We also introduced new direct-temperature based calibrations of N/O abundance using the N2O2 and N2S2 diagnostics, calibrated using the SDSS stacks presented in Curti et al. (2017). The main findings of the chapter are summarised below.

- KLEVER galaxies have N2O2 values in good agreement with those observed by other authors at this redshift (e.g Shapley et al. 2015; Steidel et al. 2016; Strom et al. 2017). When converted into an estimate of log(N/O) using the new calibrations presented in this chapter, we see a marginal enhancement of 0.1 dex in nitrogen abundance, at a fixed metallicity, for our KLEVER sample relative to local galaxies. Given the large scatter of individual objects in the N/O–O/H plane, particularly towards lower metallicities, this mild offset suggests there is no strong evolution in the N/O–O/H relationship with redshift.

- At a fixed stellar mass, KLEVER galaxies have lower nitrogen abundances than local galaxies by an average 0.35 dex. This finding indicates a strong evolution in the stellar mass–N/O relation, in agreement with Strom et al. (2017). This evolution is primarily driven by the evolution of the mass-metallicity relation, with KLEVER galaxies having lower metallicities than SDSS galaxies when compared at a fixed stellar mass, and hence lower N/O values.

- KLEVER galaxies fall slightly below the Fundamental Metallicity Relation (FMR), as parameterised by Curti et al. (2020a), by an average of $\sim$ 0.1 dex in O/H when using local metallicity calibrations. This offset is within the uncertainties of using the FMR to predict O/H values, particularly when considering that the KLEVER galaxies lie in a region of the FMR extrapolated from the local FMR, suggesting that the equilibrium between gas-phase processes that govern the FMR locally is still in place at $z \sim 2$.

- Similar to the secondary dependence of the mass-metallicity relation on star formation rate, we find a secondary dependence on SFR within the stellar mass–N/O plane. This finding is different to the results found in Pérez-Montero et al. (2013) due to our adoption of N2O2 as a diagnostic for N/O rather than N2S2 (which we have shown to be affected by a dependence on SFR). The finding that N/O has a secondary dependence on SFR similar to O/H, suggests that the FMR is not purely driven by processes that only O/H is sensitive to, such as pristine gas inflows, but also processes that are probed by N/O, such as galaxy age or star formation history, that trace the chemical enrichment histories of galaxies.

- Analogous to the FMR, we use the dependence on SFR within the stellar mass–N/O plane to construct a Fundamental Nitrogen Relation (FNR). We find that the reduced N/O at a fixed stellar mass for high-z galaxies can be accounted for by an increase in star formation rate. This suggests that high redshift galaxies may be young and highly efficient at converting their gas into stars. The apparent fundamentality of the

FNR suggests that processes relating to the chemical enrichment history of galaxies evolve smoothly from $z \sim 2$ to $z \sim 0$. Furthermore, we find that the measured FNR is near-identical to a model FNR, constructed using a combination of the fundamental metallicity relation and a redshift-invariant N/O–O/H relation, suggesting the FNR is a by-product of these relations.

- The trend of N/O with stellar mass for the KLEVER galaxies most closely resembles that of local galaxies with low metallicities, for which variable contributions to nitrogen production from low- and intermediate-mass stars may contribute to the N/O ratio. The location of KLEVER galaxies on this plane is consistent with a scenario in which they are young with high star formation efficiencies, allowing them to attain high stellar masses in a short time before the enhancement due to the secondary production becomes dominant.

Chapter 4

The cosmic evolution of N/O gradients

After an episode of star formation, massive stars will enrich the interstellar medium of a galaxy with oxygen on relatively short timescales ($\sim$ 10 Myr), following their death as Type II supernovae. The abundance of oxygen in the ISM therefore provides a straightforward probe of the evolutionary stage of a galaxy in relation to its recent and historic star formation, and as such is usually adopted as a proxy for the total gas-phase metallicity. As already discussed in the previous chapters and in contrast to oxygen, nitrogen is predominantly released into the ISM by low- and intermediate-mass stars via stellar winds during the asymptotic giant branch phase of their evolution (Vincenzo & Kobayashi, 2018). Since these stars have longer lifetimes than their massive counterparts, the N/O ratio can act as a time-sensitive probe of recent star formation events within a galaxy.

Especially interesting are the spatial variations of chemical abundances across galaxies. Chemical abundance gradients can provide insight into the processes driving galaxy assembly and their timescales, in particular on the interplay of star formation and gas flows on both local and global scales. In the local Universe, chemical abundance gradients within galaxies have been well characterised. Observations of individual HII regions have found that most nearby disc galaxies have negative metallicity and N/O gradients (Vila-Costas & Edmunds, 1992; Oey & Kennicutt, 1993; Zaritsky et al., 1994; Van Zee et al., 1998; Moustakas et al., 2010; Bresolin, 2011; Berg et al., 2013, 2015), with central regions that are more chemically enriched than the outskirts of the galaxy, whilst also finding that chemical element ratios which trace the relative abundance of two α-elements, such as S/O, are generally flat.

These studies have been reinforced by more recent surveys, particularly those that utilise integral field spectroscopy, which have allowed larger samples of galaxies to be assembled, enabling more detailed studies of the slope of the metallicity gradient, and its variation with other galactic properties. Results from the CALIFA survey have observed negative metallicity gradients in local galaxies (Sánchez et al., 2014; Sánchez-Menguiano et al., 2016), consistent with an inside-out growth scenario of galaxies driven by the accelerated accretion of gas towards the centre of galaxies at earlier times (Pichon et al., 2011). Negative gradients in N/O are also observed, albeit with a large scatter in the gradients of individual galaxies that means a non-negligible fraction of objects have either flat or positive gradients in O/H ($\sim$10%) and N/O ($\sim$4%) (Pérez-Montero et al., 2016). Detailed work has also been published regarding abundance gradients of local galaxies using MaNGA data, again finding O/H and N/O gradients that are generally negative (Belfiore et al., 2017; Schaefer et al., 2020). Furthermore, these studies find that gradients in O/H are observed to flatten in the central regions of massive galaxies, whilst no such flattening is seen in N/O. This is consistent with an inside-out growth model in which the central regions have reached a metallicity equilibrium, whilst N/O continues to increase due to the delayed production of nitrogen relative to oxygen. Similarly, the outer regions of massive MaNGA galaxies are observed to have similar O/H values to the central regions of less massive galaxies, but have greater values of N/O. This variation in N/O could be linked to radial gradients in the star formation efficiency, as observed in nearby star forming galaxies (Leroy et al., 2008; Bigiel et al., 2008), with outer regions having lower SFE driving higher N/O values at a fixed O/H (Vincenzo et al., 2016b).

In this chapter we present a study of the O/H and N/O gradients in $z \sim 2$ galaxies based on IFS data from the KLEVER survey. We compare our gradients to those found in local galaxies by applying the same abundance diagnostics used for the KLEVER data to local galaxies taken from the MaNGA survey. Our key aim within the chapter is, for the first time, to observe N/O gradients in high redshift galaxies that may act as a reference point for models of the cosmic evolution of chemical abundance gradients and provide context to the role of gas inflows in galaxy evolution.

4.1 Data

4.1.1 MaNGA sample

To obtain spatially resolved emission line data for local galaxies we draw from the fifteenth data release (DR15) of the Mapping Nearby Galaxies at Apache Point Observatory (MaNGA) survey (Bundy et al., 2015)[1], analysed through the PIPE3D pipeline (Sánchez et al., 2016). Galaxy stellar masses were obtained from the PIPE3D Value Added Catalogue, whilst the NASA-Sloan Atlas provided additional information including galaxy redshift, inclination and the galactocentric distance of each spaxel within a given galaxy.

---

[1] https://www.sdss.org/dr15/manga/manga-data/

For each spaxel, we report an emission line as detected if the signal-to-noise ratio on the line flux is higher than 3. We retain only those spaxels that have detections of each of the Hα, [N II]λ6584, [S II]$\lambda\lambda$6716,32, [O III]λ5007, Hβ and [O II]$\lambda\lambda$3727,29 emission lines. We correct all emission lines for dust attenuation by using the Balmer decrement to calculate E(B-V)$_{gas}$, assuming case B recombination (Hα/Hβ=2.87) and a Cardelli et al. (1989) extinction curve with $R_V = 3.1$. The simultaneous detection of all of these rest-frame optical emission lines allows us to exploit the same suite of chemical abundance diagnostics in both the local and high-redshift galaxy samples presented within this chapter. We required all spaxels to be star-forming, as determined by their position on the [N II]-BPT diagram, adopting the classification scheme from Kauffmann et al. (2003b) to remove regions contaminated by AGN emission. To avoid strong projection effects we include only spaxels from galaxies with an axis ratio $b/a > 0.35$, hence removing any highly inclined galaxies. Altogether, the cuts described above leave us with a sample of 753,058 spaxels taken from 1103 typical star-forming local galaxies.

4.1.2 KLEVER sample

To observe abundance gradients in high redshift galaxies, we draw from the sub-sample of 37 KLEVER galaxies studied in Chapter 3, for which galaxy-integrated N/O abundances could be derived using N2O2. We build on the work of the previous chapter by exploiting the spatially resolved emission maps of KLEVER galaxies. Due to the focus on the spatially resolved properties of galaxies we include only the un-lensed galaxies from the KLEVER survey, as to avoid the uncertainties introduced from deprojecting the lensed sample. This removes 6 of the KLEVER galaxies included in Chapter 3, leaving 31 galaxies taken from the COSMOS, GOODS-S and UDS fields (Grogin et al. 2011; Koekemoer et al. 2011). All galaxies have been determined to be star-forming based on their galaxy-integrated locations on the [N II]-BPT plane, adopting the classification scheme of Kauffmann et al. (2003b) to remove galaxies that may be contaminated by AGN emission. In addition we cross check against X-ray data for galaxies in COSMOS (Marchesi et al., 2016), GOODS-S (Luo et al., 2017) and UDS (Kocevski et al., 2018), ensuring that no AGN are included in our sample by confirming our galaxies have a hard band X-ray luminosity $<10^{42}$ erg/s.

We include only those galaxies for which we are able to spatially map the Hα, [N II], [O III], Hβ and [O II]$\lambda\lambda$3727,29 emission lines. We also include maps of the [S II]$\lambda\lambda$6716,32 doublet when it is detected, but do not require detection of these lines for inclusion in the analysis. An emission line is detected if the S/N>3 (with the noise measured directly from the spectra in the continuum regions near the emission line) and the percentage uncertainty on the flux is less than 50% (where the error on the flux is determined by the spectral fitting routine, detailed in Section 2.3.1).

When necessary, all lines are corrected for dust attenuation by using the Balmer decrement to calculate E(B-V)$_{gas}$, assuming case B recombination (Hα/Hβ=2.87) and a Cardelli et al. (1989) extinction curve with $R_V = 3.1$. As an additional test, we also corrected the KLEVER sample for dust assuming the attenuation curve of Reddy et al. (2015), which is constructed at z$\sim$2. We find that the use of this attenuation curve does not change the qualitative results of our analysis. As done for the galaxy-integrated spectra, we explicitly account for the uncertainty introduced when using reddening-corrected emission lines by perturbing the measured Hα and Hβ fluxes within their respective errors. We then used this perturbed Balmer decrement value to calculate any emission line ratios that depend on reddening-corrected emission line fluxes. This process was repeated 300 times, with the upper and lower errors introduced from the reddening correction taken to be the 16th and 84th percentiles of this distribution respectively. These uncertainties were then summed in quadrature with the error on the line ratio introduced from the errors on the measured line fluxes to produce final upper and lower error estimates for each line ratio.

Our results are obtained using the $0.3'' \times 0.3''$ spatially binned KLEVER data introduced in Section 2.3.3, which better samples the average seeing of the KMOS observations (0.5–0.6$''$). Nevertheless, we include results extracted from the original $0.1'' \times 0.1''$ KLEVER datacubes, which are certainly not independent within the PSF, however we urge that these results are only included to provide a visual aid of the variations of line ratios across galaxies, and we extract no quantitative measurements from these maps. After applying the detection criteria to the emission line maps, we include only galaxies that have at least 3 data points in the spatially binned data for which we can determine the metallicity and the N/O abundance. The determination of chemical abundance is predominantly limited by the detection of the weak Hβ line, which is necessary for extinction corrections. From the 31 galaxies, these cuts leave us with a final sample of 18 galaxies for which we can investigate the spatial variations of N/O at high-redshift. From these 18 galaxies, we resolve a total of 158 spatial bins. Our galaxies span a range of stellar masses from $10 < \log(M_\star/M_\odot) < 11$. As demonstrated in Concas et al. (2022), the majority of KLEVER galaxies fall on the star forming main sequence at $z > 2$ as defined by Whitaker et al. (2014), however the galaxies probed within this work have an median offset of 0.18 dex above this main sequence, suggesting our sample may be biased towards galaxies that have experienced recent bursts of star formation.

4.2 Deriving the abundance gradient

4.2.1 Abundance diagnostics

Metallicity

To determine gas-phase metallicities we utilise the strong-line metallicity diagnostics presented in Curti et al. (2017, 2020a), which have been calibrated for application in the metallicity range $12 + \log(\mathrm{O/H}) \in [7.6, 8.9]$. These works calibrate strong-line diagnostics using a sample of stacked SDSS galaxy spectra via the direct electron temperature method. We follow the same methodology applied to the galaxy-integrated KLEVER data in Chapter 3, wherein we determine the metallicity performing a chi-squared minimisation over multiple oxygen-based emission line diagnostics (R2, R3, O32 and R23) simultaneously. For a further discussion of the advantages as disadvantages of these diagnostics, please refer to Section 3.2. Sanders et al. (2020) found the oxygen-based diagnostics calibrated in Curti et al. (2017) show good agreement with high-redshift electron temperature calibrations, and should therefore not introduce strong biases into our estimation of metallicities for KLEVER galaxies. We exclude any metallicity diagnostics that include the [N II]λ6584 emission line, which we instead use in the determination of the N/O ratio, as to ensure no artificial correlations are introduced due to the use of the line to determine both abundances.

N/O

We determine the N/O abundance within this chapter using both the N2S2 and N2O2 calibrations introduced in the previous Chapter, which are calibrated using the same sample and methodologies as presented in Curti et al. (2017). The N2O2 calibration relies primarily on the assumption that, since nitrogen and oxygen have similar ionisation properties, the total N/O abundance can be estimated from the ratio of the ionic abundances, i.e. $\mathrm{N/O} \simeq \mathrm{N^+/O^+}$ (Garnett, 1990; Vila-Costas & Edmunds, 1993). Similarly, the N2S2 ratio traces N/O by proxy of oxygen and sulphur both being α-elements, with the underlying assumption being that $\mathrm{N/O} \simeq \mathrm{N/S}$. However, given that the gas-phase abundances are traced through line emission from the ionised ISM, the use of N2S2 also assumes that $\mathrm{N^+/S^+} \simeq \mathrm{N^+/O^+}$, which may not necessarily hold, particularly as ionisation conditions within H II regions change across cosmic time (Kewley et al., 2013, 2015; Steidel et al., 2014, 2016; Strom et al., 2017).

As shown in Section 3.3.2, the galaxy-integrated N/O estimated for KLEVER galaxies is offset from local SDSS galaxies, exhibiting enhanced levels of N2S2 relative to N2O2. We investigate whether similar differences exist on a spatially-resolved basis by estimating

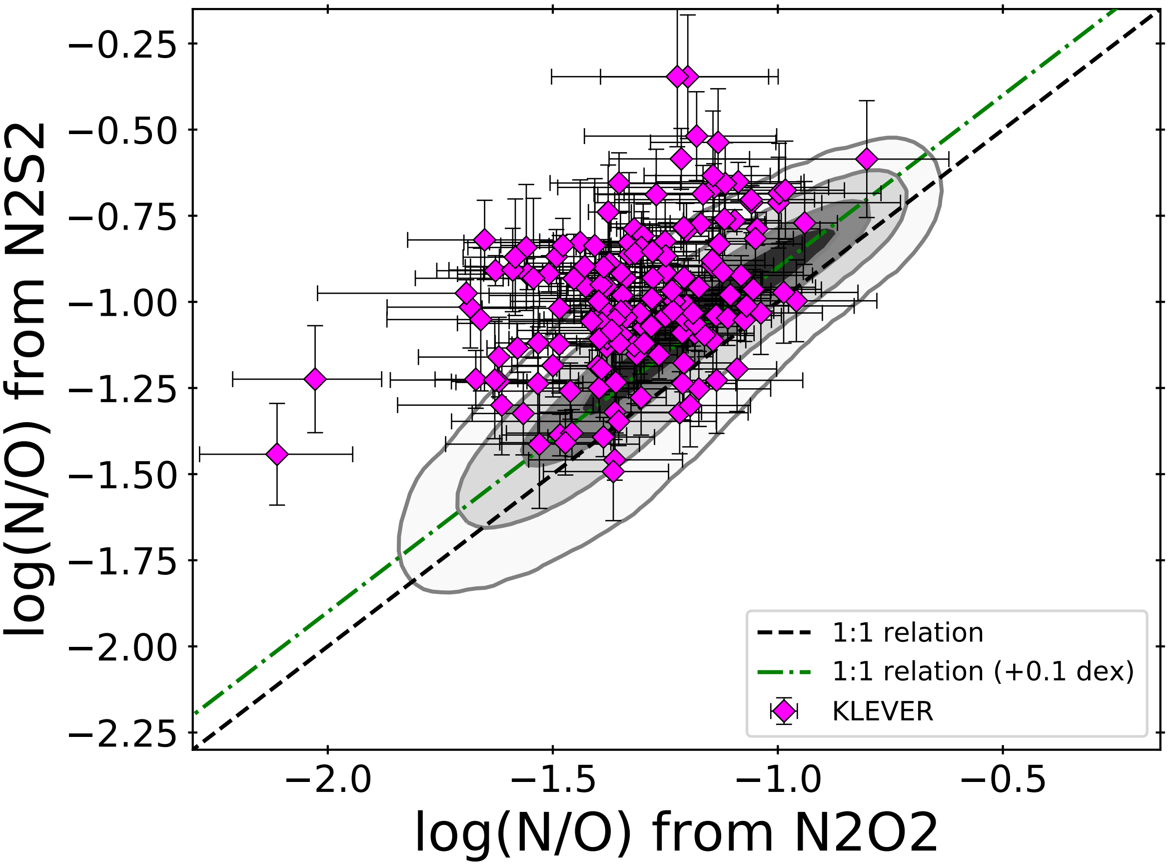

Fig. 4.1 N/O, as derived using both N2O2 and N2S2. Grey contours represent the distribution of MaNGA spaxels, with the contours indicating the regions encompassing 30%, 60% and 90% of the total sample. Spatially resolved KLEVER data is shown in magenta, with accompanying errorbars. Both MaNGA spaxels and KLEVER galaxies fall above the 1:1 relationship, shown as a black dashed lines, indicating that N2S2 is systematically overestimated relative to N2O2 on a spatially resolved basis. The magnitude of this offset for the MaNGA data is roughly 0.1 dex, highlighted by the green dot-dashed line.

N/O from both N2S2 and N2O2 for our full MaNGA and KLEVER samples. The results are shown in Figure 4.1. The MaNGA sample is shown as grey shaded regions, with the contours indicating the regions encompassing 30%, 60% and 90% of the total sample respectively. Spatially binned data from the KLEVER sample is then overlaid in magenta, along with corresponding errorbars. Considering first only the MaNGA data, we can see there is an offset in the average position of MaNGA spaxels from the 1:1 relation between N/O estimated from N2O2 and N2S2, shown as a black dashed line. The majority of spaxels fall above this line, indicating N/O is overestimated when determined using N2S2 compared to N2O2 for the MaNGA sample. Indeed, if we offset the 1:1 relation by 0.1 dex vertically, shown as a green dot-dashed line, we can better trace the average position of the MaNGA spaxels. This suggests that, on a spatially resolved basis, systematic differences in the N/O estimates from N2O2 and N2S2 exist, similar to the trends discussed previously for galaxy-integrated N/O values in Section 3.3.2. This is potentially driven by the MaNGA data resolving smaller spatial scales than SDSS fibres (which were used to calibrate the N/O diagnostics adopted in this work), with the two surveys typically sampling regions of ~ 1.5 kpc and ~ 3–5 kpc, respectively. The spectra extracted from MaNGA spaxels are therefore more likely to be dominated by emission from the central zones of H II regions wherein the ionic fraction of sulphur held in [S II]$\lambda\lambda$6716,32 is low, hence driving higher values of N2S2.

For the spatially binned KLEVER data, we find that the majority of points lie above the average position of the MaNGA galaxies, once again indicating that N2S2 is overestimating N/O relative to N2O2 for galaxies within our sample. We note that Florido et al. (2022) found that the N2S2 diagnostic introduced in Hayden-Pawson et al. (2022) overestimates N/O by an average of 0.16 dex compared to their own calibration that utilises a sample of local H II regions. The difference for the N2O2 is much more negligible, with calibrations from H II regions predicting N/O values that are on average 0.06 dex larger. If we choose to apply the calibrations of Florido et al. (2022) to the KLEVER sample, we find better agreement between N2O2 and N2S2, with the spatial bins more closely scattered around the 1:1 relation. The better agreement with calibrations from H II regions further suggests that the observed offset in N2S2 is driven by the light from galactic regions being dominated by emission from central H II regions.

Nevertheless, we note that the differences between N2O2 and N2S2 described above apply to the magnitude of the N/O abundance. In this chapter, our investigation focuses on the abundance gradient, which is a consideration of the relative change in chemical abundance across the galaxy, making the normalisation of the chemical abundance less important. As such, we use the N/O calibrations introduced in Chapter 3 throughout our analysis to ensure homogeneity in the calibration diagnostics applied to our local and high-z samples, as well as with the metallicity diagnostics from Curti et al. (2017, 2020a).

The major disadvantage of using N2O2 is the necessity for a dust correction that introduces a large uncertainty into the line ratio. This pitfall may be accentuated when determining N2O2 on a spatially resolved scale, as each spatial element may have a different contribution from dust, therefore requiring its own extinction correction. As such, spatially resolved N2O2 measurements will be strongly sensitive to the measured spatial variation in attenuation. Within this chapter we therefore calculate N/O gradients in three different ways. Firstly, we calculate N/O from N2O2 on a fully resolved basis, meaning that the Balmer decrement has been measured within each spatial element and used to estimate the reddening within that region of the galaxy. Secondly, we calculate N/O from N2O2 where the same reddening correction has been applied to all spatial elements within a galaxy by adopting the global, galaxy-integrated value for the Balmer decrement. We denote these two N/O estimates as $\log(\mathrm{N/O})^{\mathrm{R}}_{\mathrm{N2O2}}$ and $\log(\mathrm{N/O})^{\mathrm{G}}_{\mathrm{N2O2}}$ respectively. The latter method is sub-optimal as it does not account for potential spatial variations of the attenuation within galaxies but can be useful in cases where the Hβ line is poorly resolved meaning maps of the local attenuation cannot be obtained. In addition to these two methods, we also determine the N/O gradient using N2S2 to act as an extinction-free measure of the N/α across the galaxy, not forgetting the caveat that $\mathrm{N^+/O^+}$ and $\mathrm{N^+/S^+}$ may not be equivalent in high-z galaxies.

Throughout our analysis, we explicitly account for the errors introduced into N2O2 from the extinction corrections by perturbing the Hα and Hβ lines randomly within their respective errors. We then use these perturbed fluxes to calculate an estimate of the Balmer decrement. This estimate is then used to apply a reddening correction to [N II]λ6584 and [O II]$\lambda\lambda$3727,29 before N2O2 is calculated. This process is repeated 1000 times, with the final N2O2 estimate saved on each repetition. The upper and lower errors on the N2O2 introduced by the extinction correction are then taken to be the 16th and 84th of the resulting distributions. Finally, this error is summed in quadrature with the error on N2O2 associated with the uncertainty in the emission line fluxes of [N II]λ6584 and [O II]$\lambda\lambda$2727,29 to obtain final error estimates for the reddening corrected N2O2.

4.2.2 Measuring the gradient

To determine the radial chemical abundance gradients within a given galaxy, we first calculate the distance of each spatial bin from the centre of each galaxy. We obtain structural parameters such as half-light radii, axis ratios, and position angle estimates for each KLEVER galaxy from van der Wel et al. (2012), wherein GALFIT (Peng et al., 2010) was used to produce single-component Sérsic model fits to H-band near-infrared HST images. Distances of all

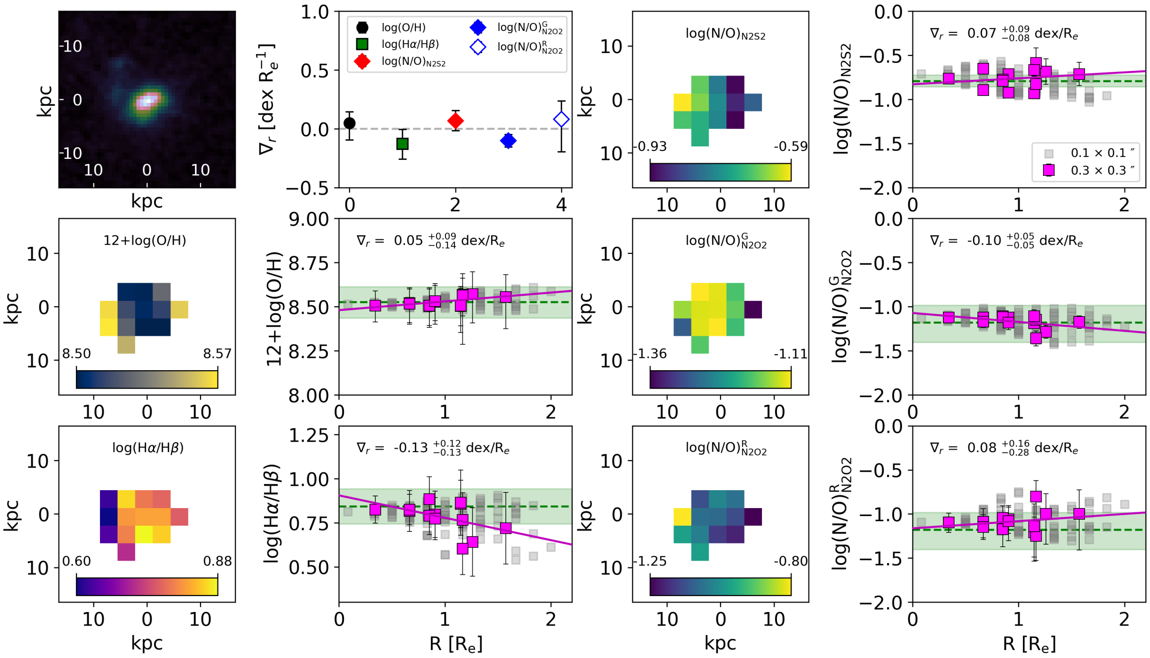

Fig. 4.2 An example of the abundance maps and gradients shown for KLEVER observations of the galaxy COS4_04519. In the top left we show a composite HST image taken from the F125W, F140W and F160W filters. Abundance maps and gradients are plotted for the metallicity, Balmer Decrement and N/O, as derived from N2S2, N2O2 applying a global dust correction and N2O2 applying a resolved dust correction. For all gradients, the original KLEVER data is shown in grey, and the spatially binned data in magenta, with the solid straight line representing the best fit gradient to the spatially binned data. For comparison, we also plot the galaxy-integrated value for each quantity as a dashed green line, with the green shaded area representing the accompanying errors. A comparison of all gradients is shown in the second column of the first row, with the *x*-axis showing a simple indexing of the gradients.

individual spaxels were then derived on a $0.1'' \times 0.1''$pixel scale from the inclination of each galaxy (obtained from the axis ratio b/a), taking into account the measured position angle of the galaxy. The distance of each $0.3'' \times 0.3''$spatial element was then taken to be the mean distance of all spaxels within that element. To account for galaxies becoming more compact towards higher redshifts and provide consistent comparisons of gradients from $z \sim 2$ to the present epoch, we normalise all abundance gradients to the half-light radius.

All gradients were derived by fitting a straight line model to data from each galaxy using an unweighted least-squares linear fit. The errors on the gradient were derived using a Monte Carlo method, wherein all abundances are randomly perturbed within their errors and the gradient is re-fit. This process is repeated 1000 times, and the final lower and upper errors were then taken to be the 16th and 84th percentiles of the resulting gradient distribution.

Figure 4.2 shows an example of the spatially binned abundance maps and corresponding abundance gradients for a typical KLEVER galaxy. We calculate gradients for the metallicity, Balmer decrement, and N/O as derived from the three methods discussed in Section 4.2.1. Spatially binned data is shown in magenta, whilst data from the original KLEVER datacube is shown in grey for comparison. The gradient is shown as a solid magenta line. Galaxy-integrated values for all measured quantities are shown as green dashed lines, with the green shaded area representing the accompanying errors.

4.3 Results

4.3.1 Metallicity gradients

Metallicity gradients for the 18 KLEVER galaxies within our sample are shown as a function of stellar mass in Fig 4.3. Trends in local galaxies are shown in grey using the full MaNGA sample, with the average local metallicity gradient over a range of stellar masses being shown as white circles. KLEVER galaxies are then shown as magenta diamonds. In addition to the individual galaxies, we also plot the average gradients for the KLEVER sample in two distinct bins: one at high mass ($\log(M_\star/M_\odot) >= 10.34$, shown in red) and one at low mass ($\log(M_\star/M_\odot) < 10.34$, shown in green). Data for the KLEVER sample is split roughly evenly between the two mass bins, with the high mass bin containing 10 galaxies with a total of 79 spatial elements, and the low mass bin containing 8 galaxies with a total of 88 spatial elements.

Locally, the majority of metallicity gradients are observed to be negative. However, within the high-z KLEVER sample, we find that metallicity gradients are on average flatter than local galaxies when compared at a fixed stellar mass. This is consistent with previous

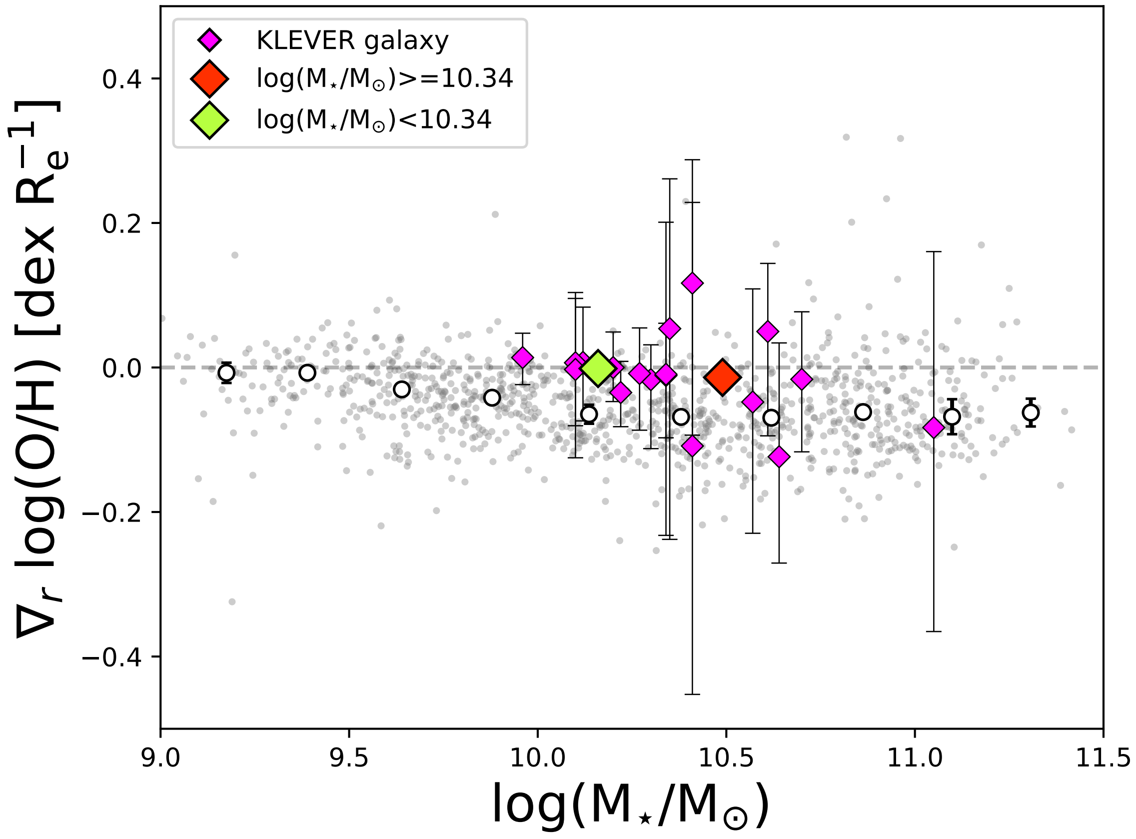

Fig. 4.3 Metallicity gradients as a function of galaxy stellar mass. Individual MaNGA galaxies are shown in grey, with the average gradient in 0.25 dex bins of stellar mass shown in white. The KLEVER gradients are then shown in magenta, with the green and red diamonds representing the average gradients for the low and high mass bins of the KLEVER sample respectively.

results obtained within the framework of the KLEVER survey by Curti et al. (2020b), who found flat metallicity gradients in a sample of 28 lensed galaxies over the redshift range z =1–2.5. This result is in contrast to a pure inside-out growth model for galaxies, which predict steeper metallicity gradients at earlier cosmic times as a consequence of the star formation (and hence the chemical enrichment) beginning sooner in the centre of the galaxy than in the outskirts. However, models are capable of reconciling predictions from inside-out growth models with the observations of flat gradients at high redshift by invoking radial gas flows and feedback processes (e.g. winds and fountains) that expel metals from the central regions and redistribute them to the galaxy outskirts (Gibson et al., 2013; Mott et al., 2013). Radial mixing in addition to inside-out growth is also necessary to reproduce observations of inverted metallicity gradients in galaxies at $z \sim 3$, wherein the local regions of the galaxy are depleted in O/H relative to the outer regions (Cresci et al., 2010; Troncoso et al., 2014). Such inverted gradients are compatible with a scenario in which the central regions of the galaxy are undergoing strong accretion of pristine gas from the cosmic web causing a dilution effect. Taken in combination, these results point to a cosmic evolution of metallicity gradients that start out inverted at $z \sim 3$, become flat by $z \sim 2$ before turning negative by $z \sim 0$.

The trends of the metallicity gradient with the stellar mass have been discussed in detail for local galaxies by Belfiore et al. (2017). In short, metallicity gradients in nearby galaxies are generally negative out to a radius of ∼2 $\mathrm{R_e}$ where most gradients become flat. However, towards lower stellar masses the gradient also becomes flatter. By considering the median gradients of the high- and low- mass KLEVER bins in Figure 4.3, we observe a similar trend wherein the higher mass bin has a more negative gradient. This evolution with stellar mass is very mild, with the median gradient equal to -0.0014 dex/R_e in the low mass bin and -0.014 dex/R_e in the high mass bin. This trend can be seen more clearly in Figure 4.4, wherein we plot the radial profiles of the metallicity in bins of stellar mass for the MaNGA and KLEVER samples. For the KLEVER galaxies, the average metallicity is determined in 0.25 dex wide bins of radius, and only bins which contain at least 3 spatial elements are displayed. It can be seen that the high mass bin only samples out to 1.5 $\mathrm{R_e}$, whilst the lower mass bin samples further out to 2.5 $\mathrm{R_e}$. This is driven by higher mass galaxies being, on average, larger than lower mass galaxies, therefore having higher $\mathrm{R_e}$ values.

It is immediately clear that KLEVER galaxies have much lower metallicities than the MaNGA galaxies. This is a direct consequence of the fundamental metallicity relation, wherein high-redshift galaxies are characterised by higher star formation rates and lower metallicities at a fixed stellar mass compared to local samples (Mannucci et al., 2010; Curti et al., 2020a). Similarly, we observe a distinct difference in the metallicities of our high- and low-mass KLEVER bins, with the higher mass bin characterised by higher metallicities at

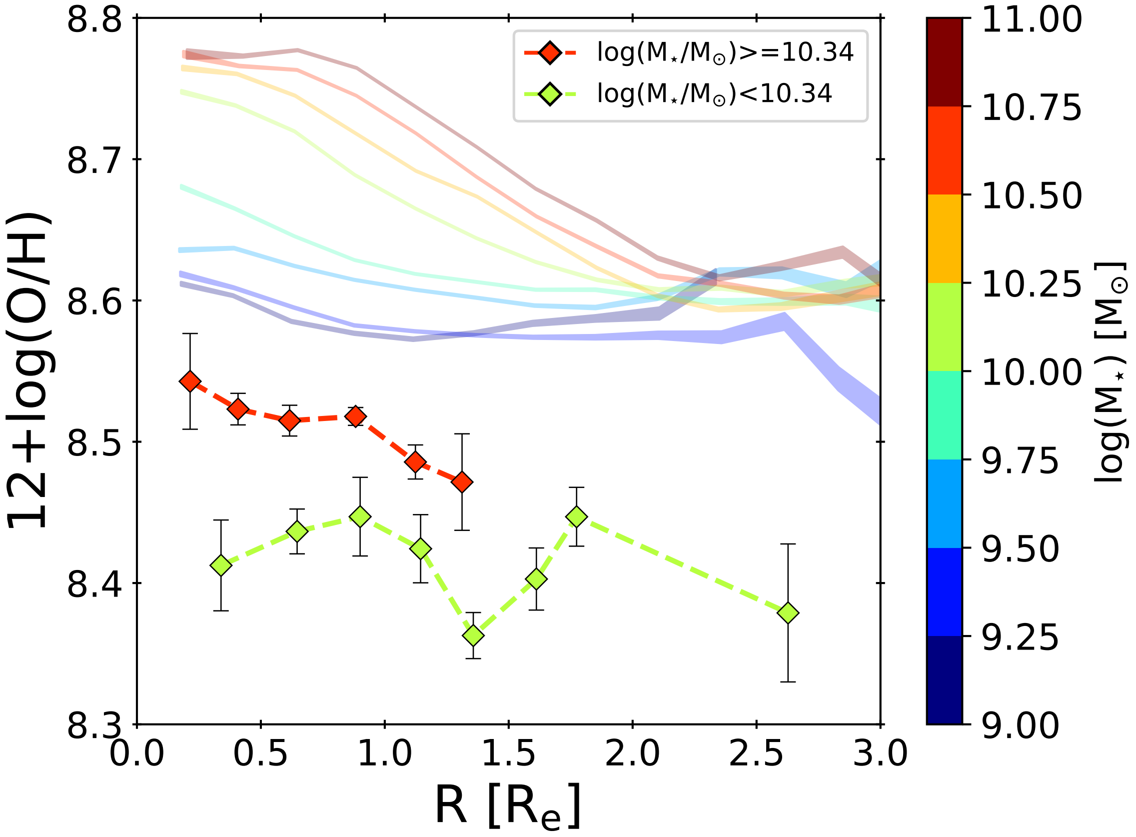

Fig. 4.4 The radial variation of metallicity with galactocentric distance, normalised to the effective radius, for MaNGA and KLEVER galaxies. The MaNGA data is binned in 0.25 dex wide bins of stellar mass and is shown as solid shaded lines. The KLEVER data has similarly been split into a high and low mass bin, with colours matching the equivalent MaNGA mass bin, and is shown as dashed lines, with the average metallicity derived in radial bins of width 0.25 dex.

all radii probed. Again, this result is expected due to the mass-metallicity relation already existing at $z \sim 2$ (Erb et al., 2006; Maiolino et al., 2008; Troncoso et al., 2014; Sanders et al., 2018), with higher mass galaxies being, on average, more chemically evolved than those at lower masses. This clear offset justifies our choice of separating the KLEVER sample into two stellar mass bins. Despite the small sample sizes within each bin, which we acknowledge is a major limitation of our analysis, the difference in the metallicity shows that clear chemical differences exist between the two mass bins.

Besides the offset in the absolute metallicity, differences can also be observed in the radial profile of the two mass bins. The metallicity profile in the high-mass bin appears steeper than the low mass bin across the distance range $0 < \mathrm{R_e} < 1.5$. This is in agreement with the trends observed locally where the metallicity gradient becomes steeper towards higher stellar masses. We also note that in local galaxies, the most central regions (< 0.5 $\mathrm{R_e}$) of higher mass galaxies are observed to have flatter metallicity gradients than lower mass galaxies (Belfiore et al., 2017; Schaefer et al., 2020). This is interpreted at the most central regions of the galaxy being in a chemical equilibrium, wherein metals are well retained, but their production has also slowed due to low gas fractions. We do not observe this trend within the KLEVER sample, which could suggest that the central regions of massive galaxies have not yet reached a chemical equilibrium and are instead still undergoing evolution more akin to lower mass local galaxies. This result is not unexpected, as KLEVER galaxies are observed at relatively low metallicities, and since high gas fractions are expected to be common in galaxies at high redshift, it would be surprising if the central regions were already in a chemical equilibrium. Nevertheless, we note our small sample size and low spatial resolution mean that we cannot conclusively rule-out the possibility of flattening in the central regions.

4.3.2 N/O gradients

Within this section, we present an analysis of N/O gradients within KLEVER galaxies determined in three distinct ways. First we present results of the N/O gradient determined using values of $\log(\mathrm{N/O})^{\mathrm{R}}_{\mathrm{N2O2}}$, wherein each spatial element has had an extinction correction performed using the Balmer decrement measured within that element. We then present the same analysis, instead using $\log(\mathrm{N/O})^{\mathrm{G}}_{\mathrm{N2O2}}$ values, where all spatial elements have had the same extinction correction applied as determined by the galaxy-integrated Balmer decrement, before comparing to the case where N/O is determined from N2S2. These results represent the first measurements of N/O gradients at $z \sim 2$.

$\log(\mathrm{N/O})^{\mathrm{R}}_{\mathrm{N2O2}}$

In Figure 4.5 we present the trends of N/O gradient with stellar mass, using the same format as done for the metallicity gradients in Figure 4.3, including the average gradients for the high- (red) and low- (green) mass KLEVER bins in addition to the individual KLEVER galaxies (shown in magenta). The local MaNGA galaxies are shown in grey, with the average trends with stellar mass shown as white circles. For galaxies in the local Universe, a similar trend to that observed in the metallicity gradients exists, with the majority of N/O gradients being negative. In contrast, the KLEVER galaxies are seen to be flatter than their local counterparts when compared at a fixed stellar mass, with many individual KLEVER galaxies exhibiting inverted N/O gradients. The inversion of the N/O gradients can be observed within each KLEVER mass bin, with a stronger inversion in the more massive, more metal-rich bin.

The stronger inversion in the high mass bin can be clearly seen in Figure 4.6, where the radial profile of the N/O ratio is plotted in several different bins of stellar mass for both MaNGA (solid lines) and KLEVER (dashed lines) galaxies. As with the metallicity, radial trends of N/O have been extensively studied in recent works (Belfiore et al., 2017; Schaefer et al., 2020), with the negative N/O gradients becoming flatter towards lower stellar masses. Unlike the metallicity, no flattening of the N/O is observed in the central regions of local galaxies. This is believed to be a consequence of the delayed production of nitrogen relative to oxygen, meaning that the O/H may have reached an equilibrium, but the N/O is still able to increase. Similarly, beyond 2 $\mathrm{R_e}$ O/H gradients for all stellar mass bins tend to a common value of 12+log(O/H)=8.6, as shown in Figure 4.4. However, no such common N/O value is observed at large radii, with the higher mass bins retaining larger N/O values. This has been interpreted as a consequence of radial mixing of metals within the ISM, with metal-rich gas being pushed from the centre of the galaxy towards the outskirts by star-formation driven winds. As the high metallicity, high-N/O gas from the central regions mixes with lower metallicity gas in the outer regions, the O/H is significantly diluted whilst the N/O remains relatively unaffected (Belfiore et al., 2017). Considering now the KLEVER data, we can see that the high mass bin has larger values of N/O relative to the low mass bin in all but the most central regions of the galaxy. Furthermore, the central regions of both KLEVER bins show a large depletion in N/O relative to local galaxies at a fixed stellar mass, but show a better agreement at a radius of $\sim$1.5 $\mathrm{R_e}$.

In Figure 4.7 we show the relationship between N/O and O/H. Contours show the density distribution of local MaNGA galaxies. The MaNGA data is then split into 0.25 dex wide bins of stellar mass, each of which is then divided into several bins of galactrocentric radius, ranging from 0 to 2 $\mathrm{R_e}$ in 0.25 dex increments. For each radial bin, the median N/O value is then plotted against the median O/H value. At each mass, the values in central (0–0.25 $\mathrm{R_e}$),

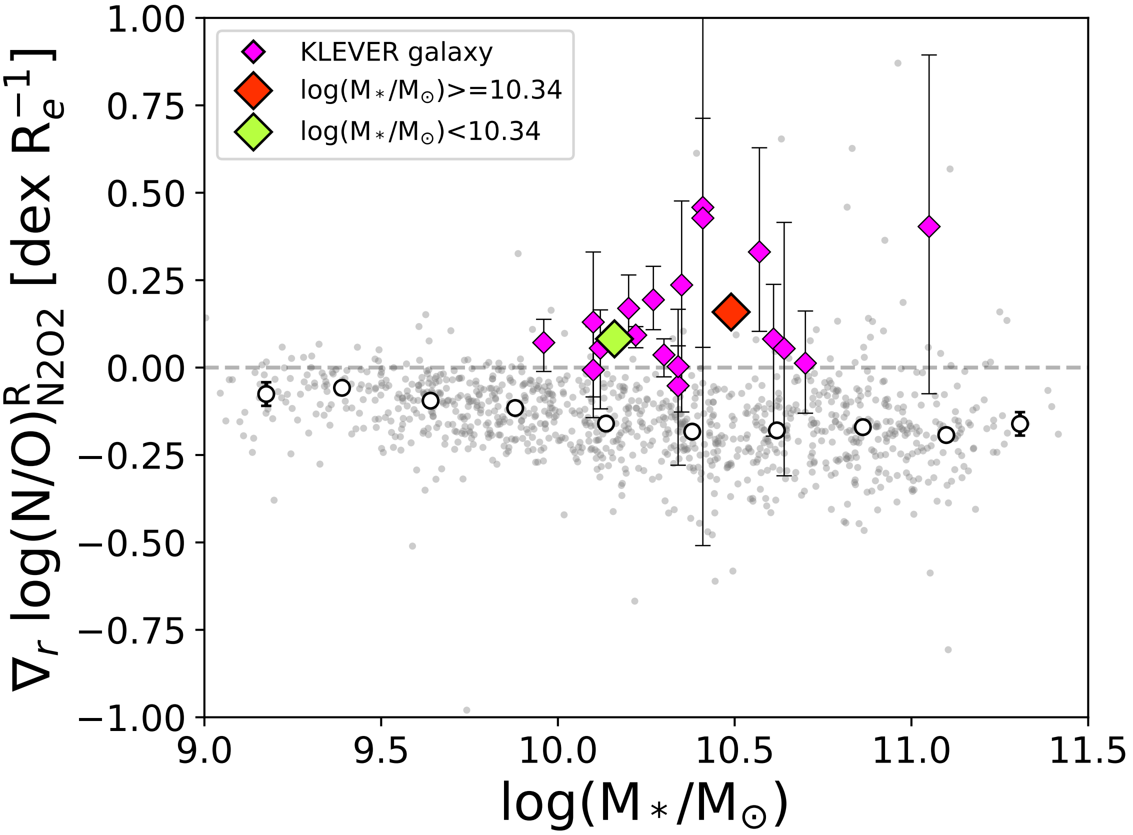

Fig. 4.5 N/O gradients as a function of galaxy stellar mass. Individual MaNGA galaxies are shown in grey, with the average gradient in 0.25 dex bins of stellar mass shown in white. The KLEVER gradients are then shown in magenta, with the green and red diamonds representing the average gradients for the low and high mass bins of the KLEVER sample respectively. N/O values have been determined for KLEVER galaxies via the N2O2 diagnostic, applying a resolved extinction correction using the Balmer decrement measured within each spatial bin.

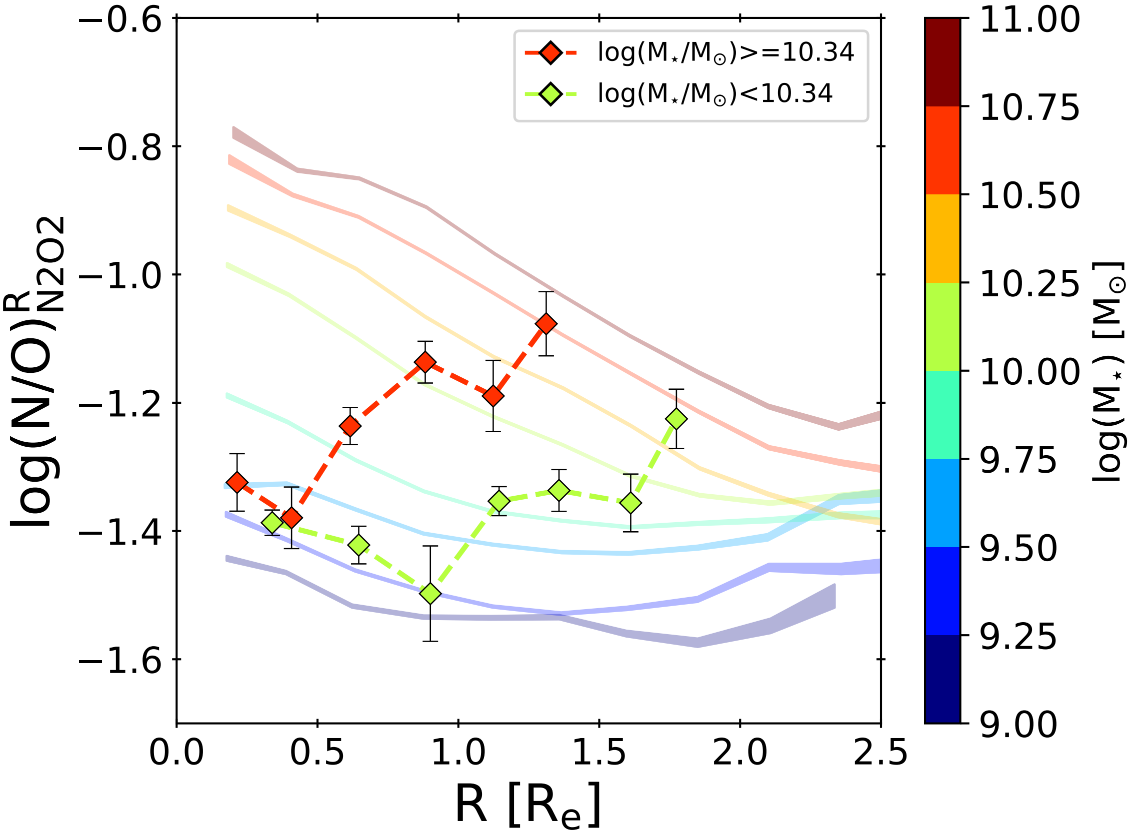

Fig. 4.6 The radial variation of N/O with galactocentric distance, normalised to the effective radius, for MaNGA and KLEVER galaxies. The MaNGA data is binned in 0.25 dex wide bins of stellar mass and is shown as solid shaded lines. The KLEVER data has similarly been split into a high and low mass bin, with colours matching the equivalent MaNGA mass bin, and is shown as dashed lines, with the average N/O derived in radial bins of width 0.25 dex. N/O values have been determined for KLEVER galaxies via the N2O2 diagnostic, applying a resolved extinction correction using the Balmer decrement measured within each spatial bin.

intermediate (1.25–1.5 R_e) and outermost (1.75–2 R_e) regions are shown by circles, squares and stars respectively. For the high-mass KLEVER data, we do not resolve the outermost regions of the galaxy.

The combination of gradients in N/O and O/H leave a clear mark in the N/O–O/H plane. In local galaxies, central regions are enhanced in both N/O and O/H relative to the outer regions, with this trend most evident in high mass galaxies. As such, secondary nitrogen production is evident in local galaxies as the N/O shows a clear dependence on the O/H. However, if we compare to the KLEVER galaxies, no such trend is seen. The high- and low-mass KLEVER bins display similar values of N/O, despite the high-mass bin having a higher metallicity. Moreover, within the high-mass bin, N/O is observed to anti-correlate with O/H due to the combined of negative O/H gradients and inverted N/O gradients. Due to the lack of correlation between metallicity and N/O within the KLEVER sample, it is likely that nitrogen production at $z \sim 2$ is dominated by primary nucleosynthetic processes, with the nitrogen being formed freshly within stars, and therefore showing no dependence on the local oxygen abundance. Further discussion of what physical processes may be driving the inverted N/O gradients will take place in Section 4.4.

$\log(\mathrm{N/O})^{\mathrm{G}}_{\mathrm{N2O2}}$ and $\log(\mathrm{N/O})_{\mathrm{N2S2}}$

In Figure 4.8 we plot the radial gradients for N/O derived from both $\log(\mathrm{N/O})^{\mathrm{G}}_{\mathrm{N2O2}}$ (left panel) and $\log(\mathrm{N/O})_{\mathrm{N2S2}}$ (right panel) as a function of stellar mass. Similar to the results obtained using $\log(\mathrm{N/O})^{\mathrm{R}}_{\mathrm{N2O2}}$, we find that gradients at $z \sim 2$ are flatter than those observed locally when compared at a fixed stellar mass. However, in contrast to the results from $\log(\mathrm{N/O})^{\mathrm{R}}_{\mathrm{N2O2}}$, there is no general trend of inversion in the N/O gradient for either of the KLEVER mass bins. Instead, the trends seen in Figure 4.8 resemble those seen in the metallicity gradients presented in Figure 4.3, where the higher mass bin is associated with more negative gradients. For $\log(\mathrm{N/O})_{\mathrm{N2S2}}$, the low mass KLEVER bin has a median gradient of 0.017 dex/R_e, whilst the high mass bin has a more negative median gradient of -0.047 dex/R_e. Similarly, for $\log(\mathrm{N/O})^{\mathrm{G}}_{\mathrm{N2O2}}$ the low mass KLEVER bin has a median gradient of -0.011 dex/R_e, with a median gradient of $-$ 0.066 dex/R_e for the high mass bin. Not only is the trend with stellar mass similar between these two diagnostics, but the magnitude of the difference in the median gradient between the high and low mass KLEVER bins are comparable (0.064 dex/R_e and 0.055 dex/R_e, respectively), which may suggest that these diagnostics are tracing the same underlying changes in N/O within the KLEVER sample.

In Figure 4.9 we plot the average radial profiles of N/O for the KLEVER and MaNGA samples. It is immediately clear that the $\log(\mathrm{N/O})_{\mathrm{N2S2}}$ values have a much higher normalisation than the $\log(\mathrm{N/O})^{\mathrm{G}}_{\mathrm{N2O2}}$ for KLEVER galaxies. This offset in normalisation is expected

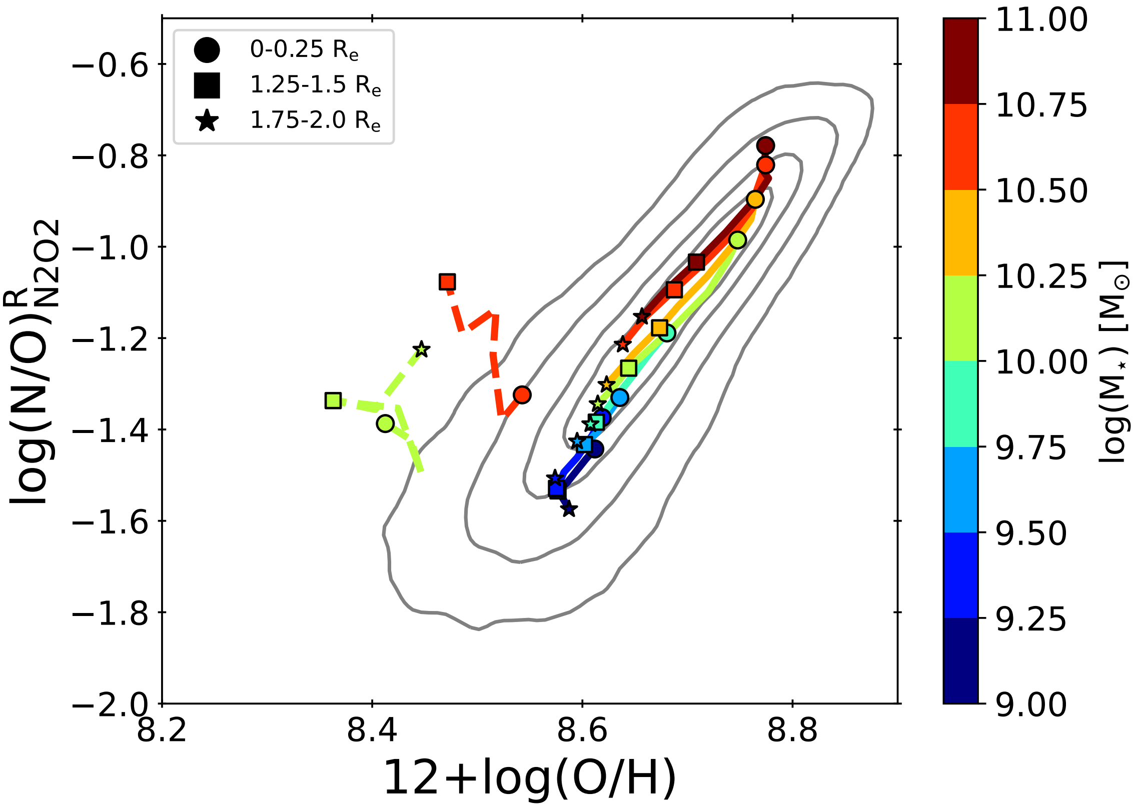

Fig. 4.7 The radial variation of the N/O and O/H within galaxies shown in the N/O–O/H plane. The distribution of MaNGA data is shown by the contours, in addition to solid shaded lines that show the average N/O and O/H in 0.25 dex wide bins of stellar mass. The KLEVER data has similarly been split into a high and low mass bin, with colours matching the equivalent MaNGA mass bin, and is shown as dashed lines. Circles, squares and stars mark the central, intermediate and outer regions of the galaxy as defined in the legend. N/O values have been determined for KLEVER galaxies via the N2O2 diagnostic, applying a resolved extinction correction using the Balmer decrement measured within each spatial bin.

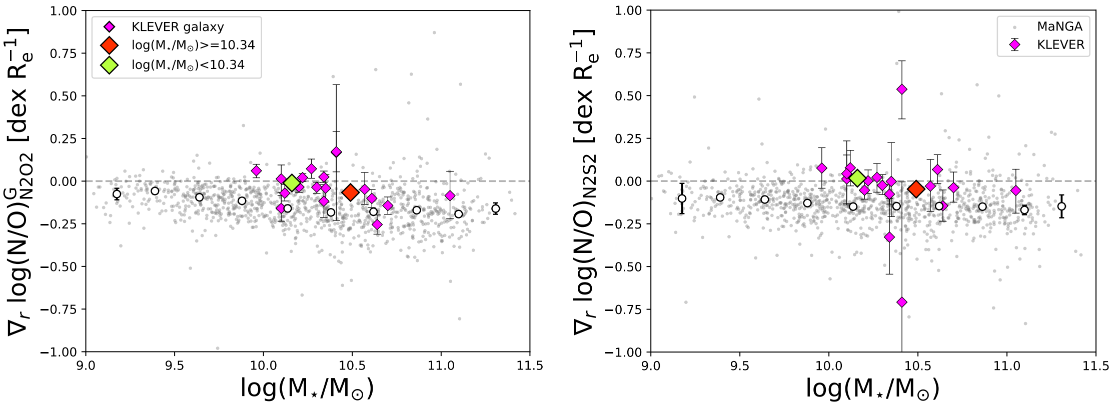

(a) $\log(\mathrm{N/O})^{\mathrm{G}}_{\mathrm{N2O2}}$ (b) $\log(\mathrm{N/O})_{\mathrm{N2S2}}$

Fig. 4.8 N/O gradients as a function of galaxy stellar mass for N/O values derived using (a) $\log(\mathrm{N/O})^{\mathrm{G}}_{\mathrm{N2O2}}$ and (b) $\log(\mathrm{N/O})_{\mathrm{N2S2}}$. Individual MaNGA galaxies are shown in grey, with the average gradient in 0.25 dex bins of stellar mass shown in white. The KLEVER gradients are then shown in magenta, with the green and red diamonds representing the average gradients for the low and high mass bins of the KLEVER sample respectively.

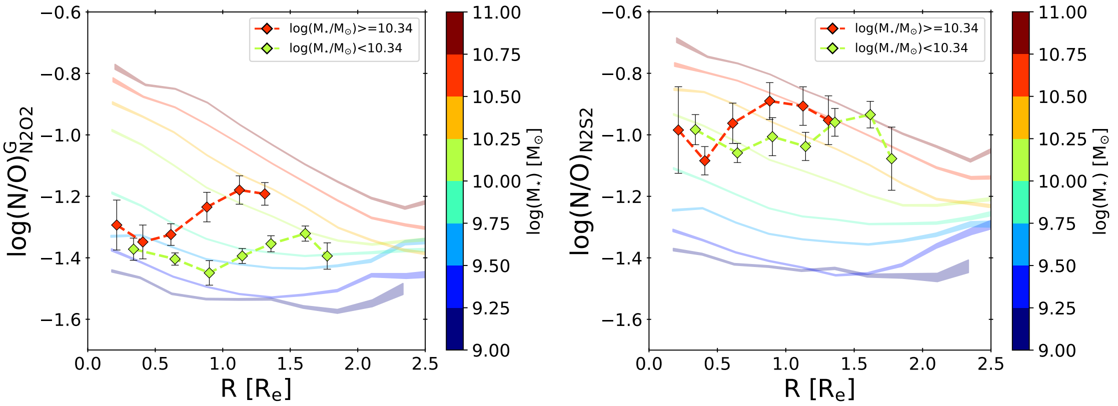

(a) $\log(\mathrm{N/O})^{\mathrm{G}}_{\mathrm{N2O2}}$ (b) $\log(\mathrm{N/O})_{\mathrm{N2S2}}$

Fig. 4.9 The radial variation of N/O with galactocentric distance, normalised to the effective radius for N/O derived from (a) $\log(\mathrm{N/O})^{\mathrm{G}}_{\mathrm{N2O2}}$ and (b) log(N2S2). MaNGA data is binned in 0.25 dex wide bins of stellar mass and is shown as solid shaded lines. The KLEVER data has similarly been split into a high and low mass bin, with colours matching the equivalent MaNGA mass bin, and is shown as dashed lines with the average N/O derived in radial bins of width 0.25 dex.

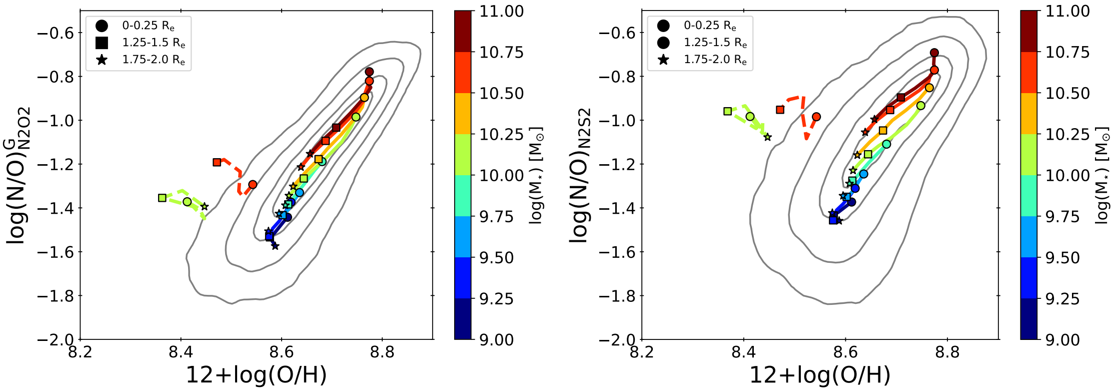

(a) $\log(\mathrm{N/O})^{\mathrm{G}}_{\mathrm{N2O2}}$ (b) $\log(\mathrm{N/O})_{\mathrm{N2S2}}$

Fig. 4.10 The radial variation of the N/O and O/H within galaxies shown in the N/O–O/H plane, with N/O derived from (a) $\log(\mathrm{N/O})^{\mathbf{G}}_{\mathbf{N2O2}}$ and (b) $\log(\mathrm{N/O})_{\mathrm{N2S2}}$. The distribution of MaNGA data is shown by the contours, in addition to solid shaded lines that show the average N/O and O/H in 0.25 dex wide bins of stellar mass. The KLEVER data has similarly been split into a high and low mass bin, with colours matching the equivalent MaNGA mass bin, and is shown as dashed lines. Circles, squares and stars mark the central, intermediate and outer regions of the galaxy as defined in the legend.

given our understanding of the differences between using N2O2 and N2S2 as N/O diagnostics, discussed in more detail in Section 4.2.1. As such, we do not compare the normalisation of the $\log(\mathrm{N/O})_{\mathrm{N2S2}}$ values in the KLEVER data to those in the MaNGA sample. We also note that in the high mass KLEVER bin there appears to be an increase in N/O towards larger galactocentric distances as determined by $\log(\mathrm{N/O})^{\mathrm{G}}_{\mathrm{N2O2}}$, in contrast to the flatter average trend that may be expected from Figure 4.8. This is an effect of averaging over several galaxies at each given radius, with the values within the outermost radial bins being dominated by galaxies with larger N/O values. Notwithstanding this caveat, the radial variation in N/O is shown to be roughly flat across all radii in both of the KLEVER mass bins. Furthermore, the normalisation in N/O is also roughly the same within both KLEVER mass bins. Therefore, although the higher mass KLEVER bin is characterised by a higher metallicity, it is not characterised by a higher N/O ratio. This is similar to the results found for $\log(\mathrm{N/O})^{\mathrm{R}}_{\mathrm{N2O2}}$, and suggests that nitrogen production within all KLEVER galaxies is dominated by primary nucleosynthetic processes that are independent of the galaxy metallicity.

In Figure 4.10 we plot the radial averages of the N/O and O/H ratios for the KLEVER sample for the high- and low-mass KLEVER bins, compared to the same mass-binned trends in local MaNGA galaxies. Combined with the roughly flat O/H gradients, the roughly flat N/O gradients help to form "messy loops" within the N/O–O/H plane, where no strong trend of increasing N/O or O/H with galactocentric radius is seen. This is in stark contrast to

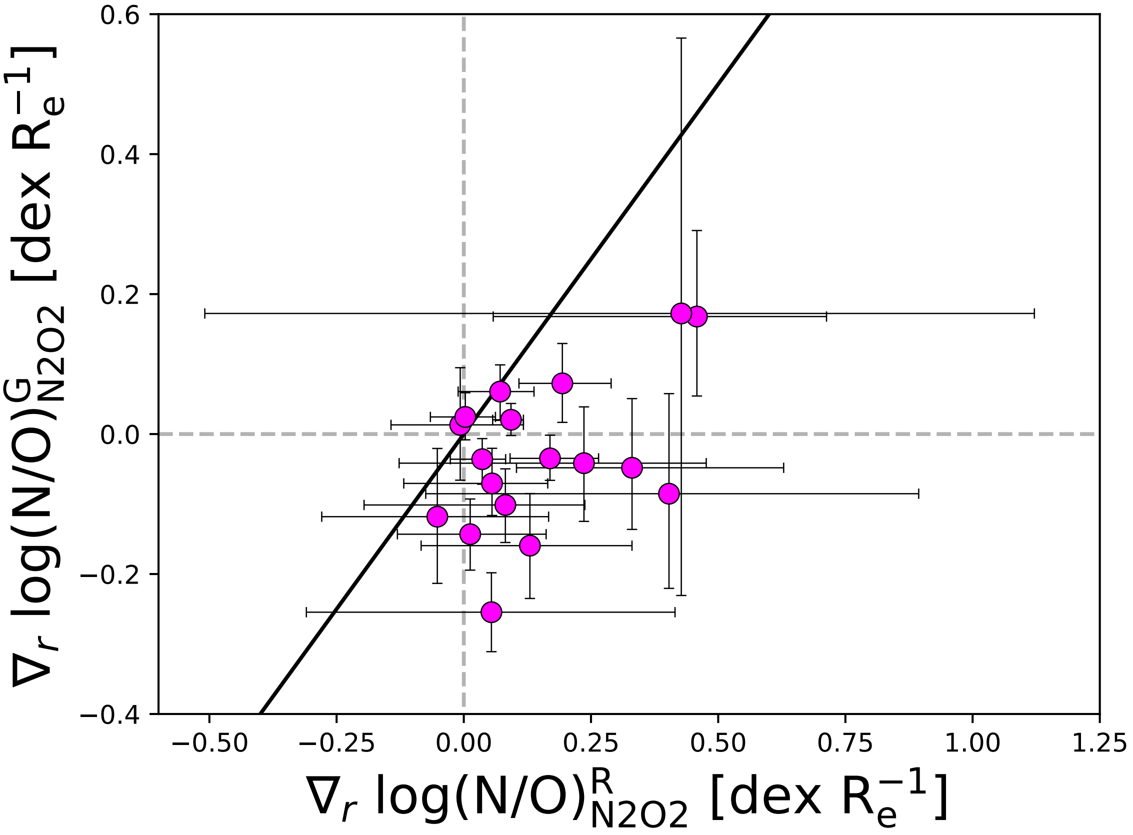

Fig. 4.11 Comparison of the N/O gradients derived from $\log(\mathrm{N/O})^{\mathrm{R}}_{\mathrm{N2O2}}$, wherein each spatial element was extinction corrected using the Balmer decrement measured within that element, and $\log(\mathrm{N/O})^{\mathrm{G}}_{\mathrm{N2O2}}$, wherein the galaxy-integrated extinction correction has been applied to all spatial bins. The black line shows the 1:1 relationship between the gradients.

what is observed within the MaNGA data, wherein for all mass bins there is a clear trend of increasing N/O and O/H towards the galactic centre. These results suggest that much of the order observed in the radial trends of local galaxies is created at later times than z∼2.

4.4 Discussion

4.4.1 Impact of the Balmer decrement

In Figure 4.11 we compare the N/O gradients obtained from $\log(\mathrm{N/O})^{\mathrm{R}}_{\mathrm{N2O2}}$ and $\log(\mathrm{N/O})^{\mathrm{G}}_{\mathrm{N2O2}}$. Despite both of these gradients being derived from the N2O2 diagnostic, a clear difference can be seen with the $\log(\mathrm{N/O})^{\mathrm{R}}_{\mathrm{N2O2}}$ gradients tending to be much more positive. Since the only difference between these two ways of deriving the N/O gradient is the treatment of the underlying extinction correction, this must be a primary reason for the discrepancy. As a

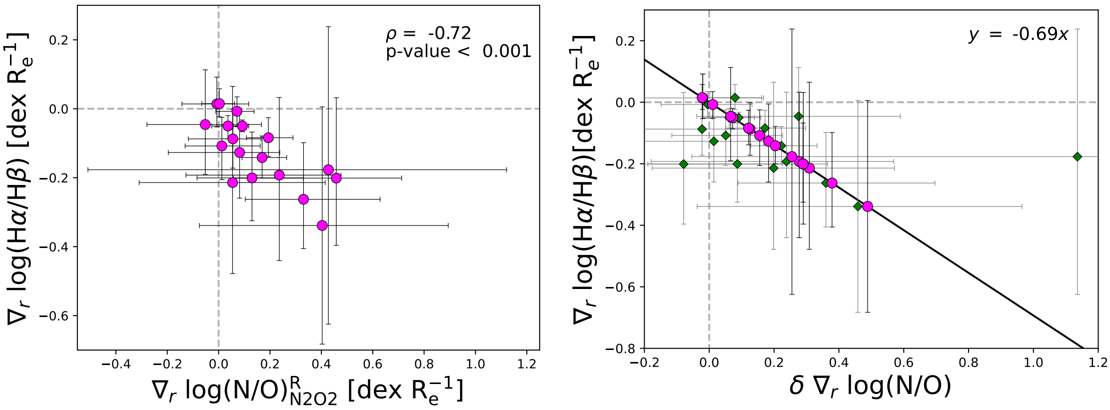

(a) (b)

Fig. 4.12 (a) We show the Balmer decrement gradients against the N/O gradients for the KLEVER sample, wherein N/O has been derived applying an extinction correction to each spatial element based on the Balmer decrement measured within that element. (b) We show the Balmer decrement gradients against the difference between the N/O gradient measured by two different methods. In magenta, we show the difference between gradients derived from $\log(\mathrm{N/O})^{\mathrm{R}}_{\mathrm{N2O2}}$ and $\log(\mathrm{N/O})^{=\mathrm{G}}_{\mathrm{N2O2}}$. In green, we show the difference between gradients derived from $\log(\mathrm{N/O})^{\mathrm{R}}_{\mathrm{N2O2}}$ and $\log(\mathrm{N/O})_{\mathrm{N2S2}}$.

reminder, for $\log(\mathrm{N/O})^{\mathrm{R}}_{\mathrm{N2O2}}$, an extinction correction was applied to each spatial element using the Balmer decrement measured within that element. The extinction is therefore treated as resolved, and is allowed to vary across the galaxy in the same way chemical abundances are allowed to, with each galaxy having its own measured Balmer decrement gradient. In contrast, for $\log(\mathrm{N/O})^{\mathrm{G}}_{\mathrm{N2O2}}$, the galaxy-integrated Balmer decrement was used to calculate the extinction correction, which was then applied to all spatial elements. In effect, this imposes a flat Balmer decrement gradient onto the galaxy, meaning the level of attenuation is assumed to not vary across the galaxy.

We investigate the extent to which Balmer decrement gradients may impact N/O gradients by plotting the $\log(\mathrm{N/O})^{\mathrm{R}}_{\mathrm{N2O2}}$ gradients against the Balmer decrement gradients in the left-hand panel of Figure 4.12. A clear trend emerges where galaxies with more positive N/O gradients have more negative Balmer decrement gradients. This relationship is statistically robust, with a Spearman's rank coefficient of -0.72 and p-value<0.001. The inversion of N2O2 gradients correlating with negative Balmer decrement gradients makes intuitive sense when considering the effect of extinction corrections. When a galaxy has a steep negative gradient in the Balmer decrement, the estimated dust extinction at the centre of the galaxy will be far greater than that estimated near the outskirts. Extinction corrections have a much stronger effect on bluer wavelengths than redder ones, meaning that the [N II]λ6584 emission line is relatively unaffected by the extinction correction, whilst the [O II]$\lambda\lambda$3727,29 emission line flux will be significantly larger if a large correction is applied. The large [O II]$\lambda\lambda$3727,29 fluxes towards the galaxy centre will then have the effect of reducing the N2O2 in these regions compared to the outskirts of the galaxy, causing inverted N2O2, and subsequently N/O, gradients.

The impact of the Balmer decrement correction on the N/O gradient is further highlighted in the right-hand panel of Figure 4.12, where we compare the Balmer decrement gradient to the difference in the N/O gradient derived using different diagnostics, $\delta\ \nabla_r$log(N/O). In magenta we show the difference between the gradients derived from $\log(\mathrm{N/O})^{\mathrm{R}}_{\mathrm{N2O2}}$ and $\log(\mathrm{N/O})^{\mathrm{G}}_{\mathrm{N2O2}}$ gradients, and in green we show the difference between the gradients derived from $\log(\mathrm{N/O})^{\mathrm{R}}_{\mathrm{N2O2}}$ and $\log(\mathrm{N/O})_{\mathrm{N2S2}}$. A clear linear trend can be seen, quantified by $y = -0.69x$, showing that more negative Balmer decrement gradients correspond to more positive N/O gradients. This linear relationship can be used to easily convert between N/O gradients derived using a resolved Balmer decrement and those derived using a flat Balmer decrement. In theory, this relationship could also be used to correct between gradients derived using $\log(\mathrm{N/O})^{\mathrm{R}}_{\mathrm{N2O2}}$ and those derived using $\log(\mathrm{N/O})_{\mathrm{N2S2}}$, since imposing a flat Balmer decrement gradient is equivalent to applying no extinction correction in that it only changes the normalisation of N/O values, not their relative distribution. The majority of the green points in the right-hand panel of Figure 4.12 appear close to the derived linear relationship, and indeed we find a mild negative correlation between the Balmer decrement gradient and the difference between the $\log(\mathrm{N/O})^{\mathrm{R}}_{\mathrm{N2O2}}$ and $\log(\mathrm{N/O})_{\mathrm{N2S2}}$ gradients with a Spearman's rank correlation coefficient of -0.42. However, this relationship is not statistically significant, with a p-value of 0.08, and the errors on the difference between our N/O gradient estimates can be seen to be large. As such, we do not use this linear relationship to reconcile the differences between $\log(\mathrm{N/O})^{\mathrm{R}}_{\mathrm{N2O2}}$ and $\log(\mathrm{N/O})_{\mathrm{N2S2}}$ gradients.

It is worth considering the potential impact of the wavelength dependence of the PSF on the observed gradients within KLEVER galaxies. The diffraction limit of a telescope is defined as $\theta = 1.22\lambda/D$, with D being the diameter of the telescope. Following this equation, light at longer wavelengths will be more scattered than that at shorter wavelengths, meaning the radial profiles of redder emission lines (e.g. Hα and [N II]) will be more extended than those which are bluer (e.g. Hβ and [O II]). For example, in a typical KLEVER galaxy at $z \sim 2$ Hα is observed at $\sim$2.1 μm and Hβ at $\sim$1.5 μm, meaning the diffraction limited scattering of Hα will be $\sim$40% larger than that of Hβ. As such, an intrinsically flat Balmer decrement gradient would be observed to have a positive value. Similarly, the diffraction limited scattering of [N II]λ6584 will be $\sim$75% larger than that of [O II]$\lambda\lambda$3727,29 (typically observed at $\sim$1.2 μm), leading to observed gradients in $\log(\mathrm{N/O})^{\mathrm{G}}_{\mathrm{N2O2}}$ that would be more positive than their intrinsic values. In the context of our results, this would mean that the observed negative Balmer decrement gradients and flat gradients in $\log(\mathrm{N/O})^{\mathrm{G}}_{\mathrm{N2O2}}$ would both intrinsically be more negative. However, KLEVER observations are taken by the VLT without employing any adaptive optics to account for turbulence within the atmosphere. As such, our observations are seeing-limited, meaning the size of the PSF in all observed bands is dominated by atmospheric turbulence rather than the optics of the telescope. We therefore observe no strong wavelength-dependence within the PSF, with the average PSF-FWHM in each of the YJ-, H- and K-bands ranging between 0.5–0.6 arcsec. In this way, our observed gradients are robust against the impact of diffraction by the telescope aperture.

4.4.2 Correlations with the Balmer decrement gradient

In the local Universe, star-forming galaxies tend to have negative Balmer decrement gradients, exhibiting larger extinction values towards their centre than in their outskirts (Boissier et al., 2004), with tight correlations existing between the star formation rate surface density (Σ_{SFR}) and the extinction (Li et al., 2019). Similarly, Reddy et al. (2015) found a correlation between the galaxy-integrated Hα luminosity and Balmer decrement values in $z \sim 2$ galaxies as part of the MOSDEF survey. However, detailed studies of the radial variations of the Balmer decrement with other galaxy properties in local galaxies remain sparse. Even more sparse are studies on Balmer decrement gradients towards high-redshifts. One notable exception is the work of Nelson et al. (2016), wherein Balmer decrement gradients were measured for a sample of 609 galaxies at $z \sim 1.4$. This study found that, on average, galaxies have higher extinction towards their centre. The authors also found a strong dependence on galaxy stellar mass, with more massive galaxies having both greater Balmer decrement values and steeper slopes. These observations correspond to high central star formation rates that account for roughly half of the total star formation rate within the galaxy. As such, these results can be associated with the early formation of dust-rich central bulges within massive galaxies. Within this section, we analyse the trends of the Balmer decrement gradient with other galaxy properties in order to interpret the significance of the negative Balmer decrements measured within the KLEVER sample.

In Figure 4.13 we plot the Balmer decrement gradients against several different properties measured from the KLEVER sample. In the top-left panel, we compare the Balmer decrement gradient to the total galaxy stellar mass. We recover a strong negative correlation, with a Pearson correlation coefficient of -0.66 with more massive galaxies being characterised by more negative Balmer decrement gradients, in agreement with the findings of Nelson et al. (2016). Similarly, in the top-right panel, we compare the Balmer decrement gradient to the gradient in the stellar mass surface density, finding a strong positive correlation

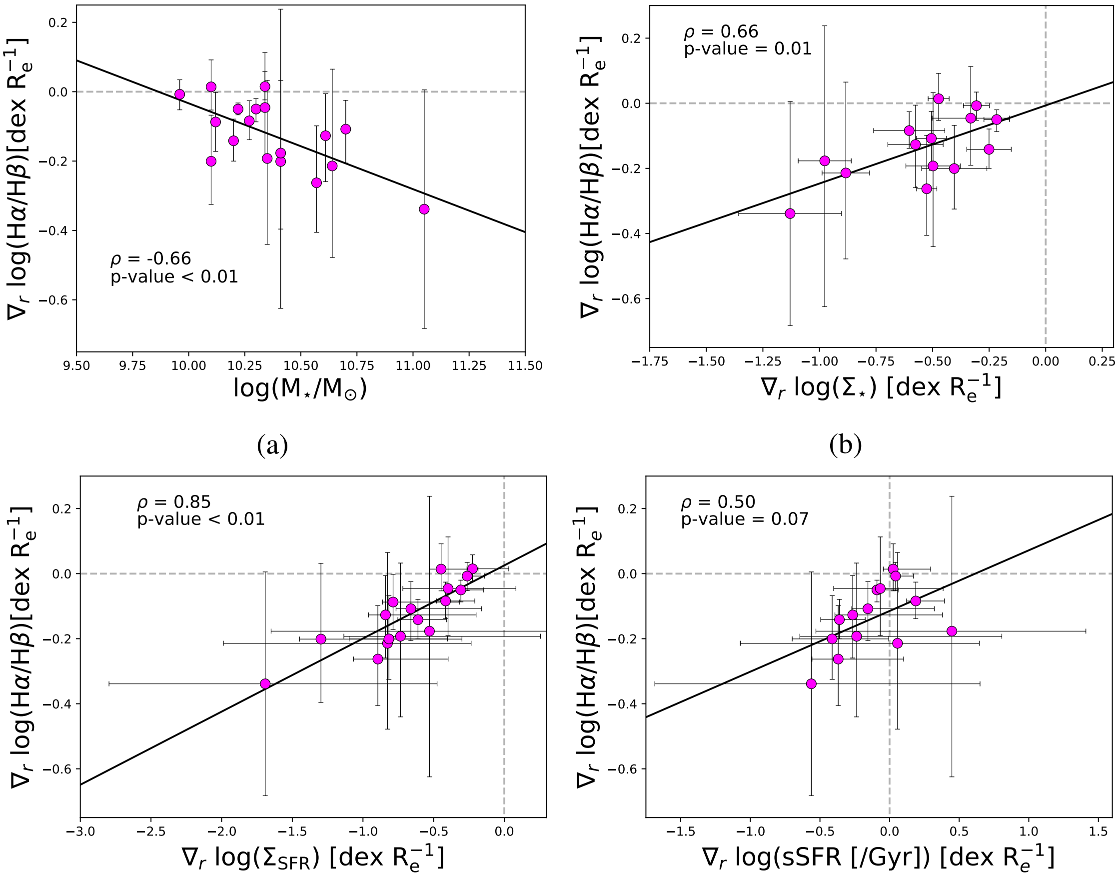

(a) (b)

(c) (d)

Fig. 4.13 Comparison of the measured Balmer decrement gradient to the: (a) galaxy stellar mass, (b) stellar mass surface density gradient, (c) star formation rate surface density gradient, and (d) the specific star formation rate gradient. KLEVER galaxies are shown in magenta, with corresponding errorbars. The solid line shows the linear best-fit between the two variables, with the corresponding Pearson correlation coefficient and p-value for each relationship also displayed.

with a Pearson correlation coefficient of 0.66. This highlights that galaxies with a higher concentration of stellar mass in their centre are also characterised by strongly concentrated central Balmer decrements. In the bottom-left panel, we present a comparison between the Balmer decrement gradient and the gradient in the star formation rate surface density. Once again, a strong positive correlation is recovered, with a Pearson correlation coefficient of 0.85. This tight correlation should be somewhat expected, given the determination of the SFR is dependent on the Hα luminosity, which has been corrected for extinction using the Balmer decrement. Nevertheless, this result highlights that galaxies with more negative Balmer decrement gradients also have more centrally concentrated star formation, a finding that is also in agreement with results found in local galaxies (Li et al., 2019). Finally, in the bottom-right panel, we compare Balmer decrement gradients to the gradients in the specific star formation rate. Although we recover a positive correlation, with a Pearson correlation coefficient of 0.5, the p-value is determined to be 0.07 and we are therefore unable to reject the null hypothesis that there is no correlation between the two variables. Further work with a larger sample size and better S/N should be undertaken at high redshift to better constrain this relationship. Nevertheless, the observed positive correlation may suggest that the central, dustier regions of our high redshift galaxies have also undergone a recent burst of star formation. When taken in combination, these results suggest that more massive galaxies, which have higher concentrations of stellar mass and star formation towards their centres, also have more centrally concentrated dust distributions. These results are consistent with the findings of Nelson et al. (2016) for galaxies at $z \sim 1.4$, suggesting that the central regions of massive galaxies at $z \sim 2$ may be undergoing in-situ bulge construction.

Unlike our own work, in which we consider gradients within individual galaxies, the results of Nelson et al. (2016) rely on stacks of galaxies taken from HST grism data. These stacks are normalised using the F140W flux, hence biasing the stacks towards galaxies with high Hα and Hβ equivalent widths. If galaxies with high equivalent widths have low amounts dust attenuation, then these stacks may underestimate the true dust attenuation within high-redshift galaxies. In this way the stacking methodology may contribute to the lack of dust attenuation observed beyond the central $\sim$1 kpc in the Nelson et al. (2016) stacks relative to the KLEVER sample. Similarly, the use of grism data means the Hα fluxes may be contaminated by [N II] emission, which could bias estimates of the Balmer decrement. However, Nelson et al. (2016) account for such contamination and conclude that their results are unchanged even in the presence of gradients in [N II]/Hα.

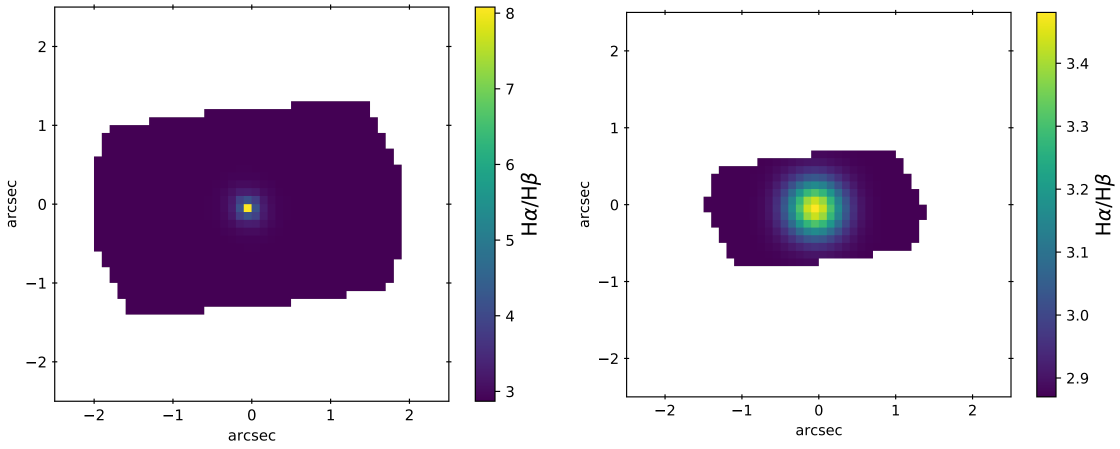

(a) Mock Hα/Hβ 2D profile.

(b) Smoothed Hα/Hβ 2D profile.

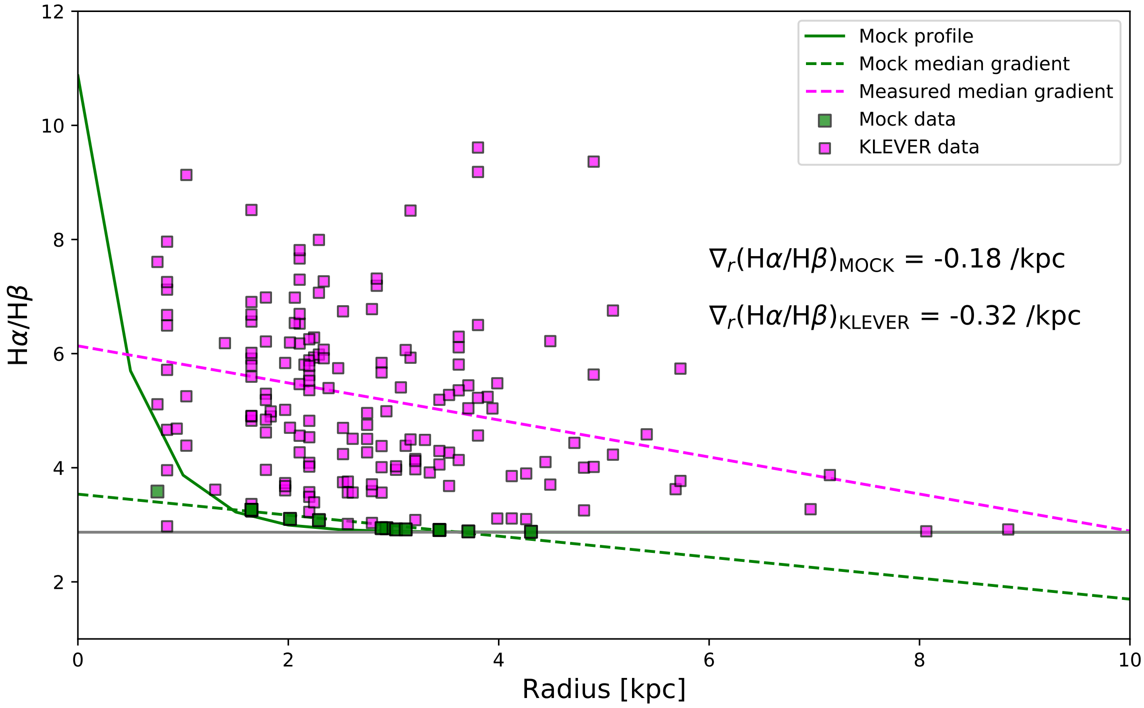

(c) Radial Balmer decrement trends.

Fig. 4.14 A comparison of the observed KLEVER Balmer decrements to what would be expected from the average Balmer decrement profile of massive galaxies at $z\sim$1.4. (a) The image of the Balmer decrement profile for massive galaxies created using the profile from Nelson et al. (2016). (b) The Balmer decrement image from (a), smoothed by the PSF-FWHM of KLEVER observations. (c) The radial profile of the Balmer decrement for measured KLEVER values (shown in magenta) and the expected values for a profile equivalent to that observed at $z\sim$1.4 (shown in green). Average Balmer decrement gradients for the KLEVER and mock data are shown as magenta and green dashed lines, respectively.

4.4.3 Comparison to $z\sim$1.4 Balmer decrement gradients

Nelson et al. (2016) found the strong gradients in the Balmer decrement were generally within the central $\sim$1 kpc of massive galaxies, with the average Balmer decrement values for massive galaxies dropping from $\sim$10 to $\sim$2.87 within 2 kpc. In order to test whether a similar gradient could be observed within the KLEVER sample, we used the $z\sim$1.4 Balmer decrement profile for massive galaxies from Nelson et al. (2016) and created a mock image of the Hα/Hβ emission. We projected the Balmer decrement profile onto several different inclinations and position angles taken from our 18 KLEVER galaxies, with the final mock image created by taking the median of all of these projections. The mock image was then smoothed by a 2D Gaussian kernel with a width equivalent to the PSF-FWHM of the KLEVER observations (typically 0.5–0.6 arcsec). The resulting smoothed mock image represents what the $z\sim$1.4 Balmer decrement profile would be observed as in a KMOS observation. In order to facilitate a direct comparison to the spatially binned KLEVER data, the smoothed image was divided into 0.3×0.3 arcsec spatial bins, from which the median Balmer decrement and projected distance are extracted. A straight-line fit was then performed to determine the Balmer decrement gradient, as measured from KLEVER observations, that would be associated to the $z\sim$1.4 Balmer decrement profile.

The results of this analysis are shown in Figure 4.14. The top row shows the mock (left) and smoothed mock (right) images. The bottom row shows the Balmer decrement profiles for the mock data, shown as green squares, as well as for the KLEVER data, shown in magenta. The solid green line shows the original $z\sim$1.4 Balmer decrement profile, whilst the green dashed line shows the Balmer decrement gradient determined by the mock KLEVER observations of this profile. As can be seen, the seeing of the KLEVER observations strongly smooths out the original profile, leading to a shallow Balmer decrement gradient of -0.18 /kpc. Furthermore, the normalisation of the Balmer decrement drops significantly, with central regions that originally have Hα/H$\beta\sim$10 being reduced to Hα/H$\beta\sim$4. This is not consistent with the Balmer decrement values in the KLEVER data, which are observed to be as large as Hα/Hβ =10. Moreover, the large values of Balmer decrement within the KLEVER data can be seen to extend out to beyond 3 kpc. Indeed, the median Balmer decrement gradient within the KLEVER data is -0.32 /kpc, nearly twice as steep as the gradient we would expect from observations of the $z\sim$1.4 profile. The combination of strong negative Balmer decrement gradients within the KLEVER sample and high Balmer decrement values that extend to large radii suggests that galaxies at $z\sim$2 may contain more dust, spread across a larger region than galaxies at $z\sim$1.4. This is in agreement with observations from Tacchella et al. (2018), who found attenuation profiles derived from the UV continuum that

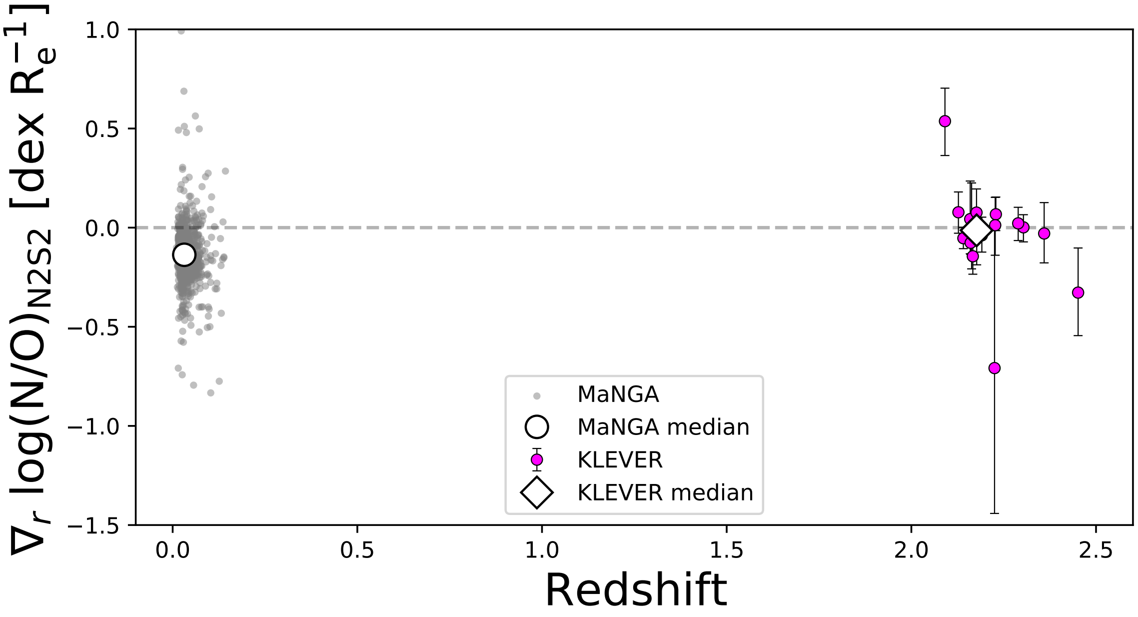

Fig. 4.15 The N/O gradient derived using N2S2 for the MaNGA (grey) and KLEVER (magenta) samples as a function of galaxy redshift. The median gradient for the MaNGA sample is −0.14 dex/R$_e$, shown as a white circle, whilst the median gradient for the KLEVER sample is −0.014 dex/R$_e$, shown as a white diamond.

were typically negative in a sample of 10 galaxies at $z \sim$2, with a significant amount of dust attenuation out to 10 kpc.

4.4.4 Interpretation of flat N/O gradients

Radial mixing

In Figure 4.15 we plot the N/O gradients derived from N2S2 for both the KLEVER and MaNGA samples as a function of redshift. A large variation in the gradients within individual galaxies is observed, both locally and at $z \sim$2, whilst the median MaNGA gradient is −0.14 dex/R$_e$ and the median KLEVER gradient is flatter at −0.014 dex/R$_e$. Many works that predict the evolution of chemical gradients across cosmic time focus on the O/H, with few predictions of the N/O available in literature. Within inside-out growth scenarios, the central regions of galaxies are assembled on shorter timescales than the outer regions. As a consequence, cosmological chemodynamical simulations such as those presented in Vincenzo & Kobayashi (2018) predict more negative gradients in N/O at higher redshifts than those observed locally. The strength of the N/O gradient is also expected to vary as a function of the star formation history of the galaxy, with galaxies that have experienced rapid star formation between z =6 and z =2 predicted to have more negative gradients. These predictions are in contrast to the observations of flat N/O gradients at z ~2 found using $\log(\mathrm{N/O})_{\mathrm{N2S2}}$, as well as $\log(\mathrm{N/O})^{\mathrm{G}}_{\mathrm{N2O2}}$. This difference could be reconciled in the same way as done for the flat O/H gradients at z ~2: invoking enhanced feedback mechanisms that drive radial gas flows, mixing the metals within the ISM across the galaxy (Gibson et al., 2013; Mott et al., 2013). Vincenzo et al. (2016b) suggested that gas outflows with preferential loading factors that expel more oxygen out from a galaxy than nitrogen can be used to explain the high-metallicity slope in the N/O–O/H plane. Such outflows preferentially expel the products of core-collapse supernovae, and would therefore deprive the central regions of oxygen whilst enriching the outskirts, forming negative N/O gradients. This theory is effective at reproducing the negative N/O slopes observed in local galaxies, but is unable to explain the flat gradients observed at z ~2. Instead, our results suggest that any radial mixing of the gas driven by supernovae would not be differential, but would expel oxygen and nitrogen equally.

Primary production in massive stars

The results presented in Section 4.3.2 highlighted that KLEVER galaxies which have higher values of O/H do not show a strong enhancement in their N/O. This suggests that z ~2 galaxies are in an early phase of their chemical evolution, and nitrogen production is still dominated by primary processes that are independent of the metallicity. Within the high-metallicity regime, it is known that nitrogen production is dominated by secondary nucleosynthetic processes taking place within low- and intermediate-mass stars. In contrast, the dominant sources of primary nitrogen remain uncertain, with varying contributions often attributed to massive stars and low- and intermediate-mass stars. Here, we consider the stellar origins of nitrogen within our z ~2 galaxies.

First, we consider the case in which primary nitrogen production is dominated by massive stars. Matteucci (1986) highlighted that primary production of nitrogen from only massive stars was necessary in order to reproduce the observed plateau in N/O at very low metallicities ($12+\log(\mathrm{O/H})<7.5$). Observations of low-metallicity damped Lyman-alpha systems also support the existence of a ‘floor’ in the N/O value at $\log(\mathrm{N/O})\simeq-2.3$ that may reflect the pure-enrichment of nitrogen from massive stars (Spite et al., 2005; Pettini et al., 2008). The N/O and O/H values probed by damped Lyman-alpha systems are much lower than the values observed in local and high-z galaxies, so even if primary nitrogen production from massive stars is evident in these regimes, it is not immediately clear that this would also be the case at higher metallicities when the N/O plateau is closer to $\log(\mathrm{N/O})\simeq-1.5$. However, work investigating the impact of stellar rotation on chemical yields found that nitrogen production can be enhanced in massive stars through rapid rotation (Chiappini et al., 2006), reproducing

N/O values as high as log(N/O)$\simeq -1.5$ even at very low metallicities. Many recent studies have highlighted a strong α-enhancement in galaxies at high-z, which is expected to be a consequence of gas enrichment that is dominated by the products of core-collapse supernovae (Steidel et al. 2016; Topping et al. 2020a, 2020b; Cullen et al. 2021, Strom et al. 2022). If massive stars dominate the enrichment of the ISM at high-z, then it is possible that a significant proportion of the nitrogen within our $z \sim 2$ galaxies is produced within massive stars. This scenario would mean that (within the primary regime) nitrogen and oxygen have the same nucleosynthetic origin, so both oxygen and nitrogen would be released into the ISM from core-collapse supernova. This has two main impacts, both of which are consistent with observations of flat N/O gradients. Firstly, if N and O are released by the same stars, there is no time delay in the enrichment of N relative to O, meaning older, more central regions of the galaxy would be expected to have similar N/O values to the younger, outermost regions. Secondly, any supernova-driven winds would impact both the nitrogen and the oxygen, driving non-differential mixing that could flatten the N/O gradient in the same way as done for the O/H gradient, as discussed earlier within this section.

Primary production in AGB stars

Whilst models support the ability of massive stars to produce significant amounts of primary nitrogen, most work in literature also concedes that similar levels of N/O can be produced by primary nitrogen production within low- and intermediate-mass stars during their AGB phase (Spite et al., 2005; Chiappini et al., 2006; Pettini et al., 2002, 2008). Henry et al. (2000) showed that the log(N/O)$\simeq -1.4$ plateau can be reproduced using nitrogen yields from intermediate mass stars from van den Hoek & Groenewegen (1997). Similarly, the recent models of Vincenzo & Kobayashi (2018) are able to reproduce the low metallicity N/O plateau using primary production in low- and intermediate-mass stars, without invoking any rotational mixing in massive stars. Moreover, a bimodality in the N/O values of damped Lyman-alpha systems has been observed, with higher N/O values, similar to those found in blue compact dwarf galaxies, associated with primary production by LIMS, whilst lower N/O values are associated with primary production from massive rotating stars in young and unevolved systems (Zafar et al., 2014). Henry et al. (2000) suggest that the time delay of nitrogen enriching the ISM relative to oxygen may be as large as 250 Myr. Despite any enrichment time delay, the imprint of nitrogen enrichment from LIMS into the ISM can occur at relatively early times in the chemical evolution of a galaxy, with Chiappini et al. (2006) suggesting that the contribution of AGB stars to the N/O ratio is effective at log(O/H)+12 > 7. Recent work by Strom et al. (2022) studied the scaling relations of stellar mass with multiple tracers of chemical enrichment (O, N, Fe) at high redshift as part of the KBSS survey,

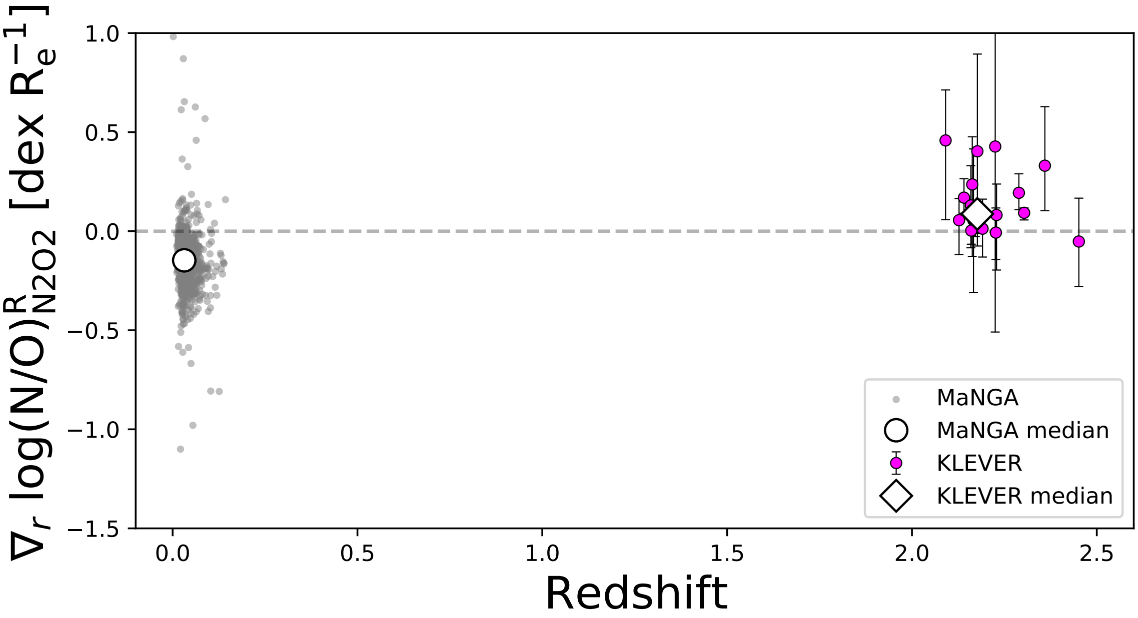

Fig. 4.16 The N/O gradient derived using N2O2 for the MaNGA (grey) and KLEVER (magenta) samples as a function of galaxy redshift. The median gradient for the MaNGA sample is -0.15 dex/R_e, shown as a white circle, whilst the median gradient for the KLEVER sample is 0.087 dex/R_e, shown as a white diamond.

with the results suggesting that by $z \sim 2$ galaxies are already old enough to be substantially enriched by intermediate mass stars. Therefore, it is also possible that intermediate mass stars dominate nitrogen production in our KLEVER galaxies. Due to the time delay of nitrogen relative to oxygen, within an inside-out growth scenario we would expect the N/O gradient to follow the age gradient within the galaxy, hence negative gradients. Once again, to reconcile the inside-out growth scenario with observations it would be necessary to invoke radial gas flows that effectively mix both the nitrogen and the oxygen within galaxies at $z \sim 2$. Alternatively, an increase in oxygen production in the centre of galaxies, perhaps following recent accretion of gas, could counteract any negative N/O gradient, causing a flattening. This concept is discussed further as part of the interpretation of positive N/O gradients (Section 4.4.5).

4.4.5 Interpretation of positive N/O gradients

In Section 4.4.2 we highlighted how the negative Balmer decrement gradients measured in high-mass KLEVER galaxies may be a consequence of in-situ bulge formation within the central regions of galaxies at $z \sim 2$. Similarly, in Section 4.4.1 we discussed how the negative

Balmer decrement gradients correspond to inversions in the measured N2O2 gradients when applying a resolved extinction correction. Within this section, we aim to reconcile the observations of negative Balmer decrements with positive N/O gradients.

The N/O gradients derived from $\log(\mathrm{N/O})^{\mathrm{R}}_{\mathrm{N2O2}}$ are shown as a function of redshift in Figure 4.16. Gradients for the KLEVER sample, shown in magenta, tend to be positive, with a median gradient at $z\sim2$ of 0.087 dex/$\mathrm{R_e}$ (shown as a white diamond). Within the MaNGA sample, shown in grey, positive N/O gradients are uncommon and the median gradient at $z\sim0$ is -0.15 dex/$\mathrm{R_e}$ (shown as a white circle). Whilst interpreting the physical driver of flat N/O gradients in Section 4.4.4, we often drew comparison to the flat gradients that are also observed in O/H. In order to understand the physical origin of inverted N/O gradients, it may be insightful to consider the inverted metallicity gradients that are observed to exist at high redshift. Inverted O/H gradients have been observed at $z\sim3$ (Cresci et al., 2010; Troncoso et al., 2014), and are associated with strong accretion of pristine gas from the cosmic web onto the centre of a galaxy. This accreted hydrogen gas causes a dilution effect, decreasing the O/H in the central regions of a galaxy relative to the outskirts. This fresh gas fuels star formation, which subsequently causes rapid enrichment of the ISM with oxygen. This should act to increase the central O/H, however at early times the rate of infalling primordial gas dominates over the star formation, so the metallicity gradient remains inverted. As time passes, the infall of fresh gas into the central regions decreases, and the chemical enrichment fuelled by the star formation begins to take over, leading to flat O/H gradients by $z\sim2$, and eventually negative gradients by the present day.

This chemical evolutionary framework for the O/H gradient is well studied, with several measurements of metallicities across a range of redshifts allowing comparisons to models (see Curti et al. (2020b), and references therein). Here, we consider the impact this same chemical evolutionary framework may have on the N/O ratio. As with the interpretation of flat gradients in Section 4.4.4, we can consider two specific cases: where primary nitrogen production is dominated by massive stars, and where the production is dominated by LIMS. In the case of primary production from massive stars, the N/O gradient would not change between $z\sim3$ and $z\sim2$ as the O/H gradient does because N/O is unaffected by dilution from pristine gas. Any increase in star formation in the central regions would produce both oxygen and nitrogen, and therefore no change in the N/O ratio would be observed. In contrast, if primary nitrogen production is dominated by LIMS, the boost in central star formation would enrich the ISM with oxygen before the delayed enrichment from nitrogen could occur. This would have a direct impact on the N/O ratio, causing a decrease in N/O for the central, diluted regions of the galaxy. In this way, the accretion of pristine gas to the central regions of galaxies at $z\sim3$ that causes inverted metallicity gradients can also cause inverted N/O gradients. Hereafter, we present a simple schematic detailing how central accretion of pristine gas may impact the N/O and O/H values across cosmic time, with more detailed modelling of this scenario being left to future work.

In Figure 4.17, we show a cartoon diagram of how the N/O and O/H values in central regions of galaxies may be expected to evolve after a large accretion event. We follow the shape of the N/O–O/H loops modelled by Köppen & Hensler (2005) that highlight the expected variation in the N/O–O/H plane when a galaxy undergoes dilution from pristine gas, assuming nitrogen yields from van den Hoek & Groenewegen (1997) wherein LIMS are the dominant source of primary nitrogen (see Figure 1.12b in Section 1). Within our cartoon model, we only consider gas accretion onto the central regions of the galaxy. As such we anchor the position of the outer regions of the galaxy, shown as a star, to a fixed N/O and O/H. We assume the O/H and N/O gradients are both initially flat, meaning the initial position of the central and outer regions of the galaxy in the N/O–O/H plane would be the same. Circles show the potential positions of the central region of the galaxy approximately 0.1 Gyr, 1 Gyr and 2 Gyr after the dilution event, following the timescales for the accretion rate modelled by Köppen & Hensler (2005). Initially, the accretion of pristine hydrogen gas onto central regions decreases the O/H, but has little impact on the N/O. This gas fuels subsequent star formation that then enriches the ISM with oxygen, and N/O begins to decrease. As shown by the yellow circle, the O/H gradient at this stage would be strongly inverted, with a mild inversion in the N/O gradient, matching what may be expected from observations of galaxies at $z \sim 3$ (although no measurements of the N/O gradient currently exist at $z \sim 3$, but are expected to be investigated soon with JWST). Over the next $\sim$1 Gyr, the accretion towards the central regions decreases and the star formation becomes dominant, increasing the O/H ratio. Furthermore, this timescale is long enough for LIMS to enrich the ISM with nitrogen, hence the N/O ratio is no longer decreasing. At this stage, as shown by the green circle, the O/H gradient would be flat, whilst the N/O gradient would now be strongly inverted. This is in agreement with the KLEVER observations at $z \sim 2$. At later times, enrichment of both nitrogen and oxygen continues, leading to negative O/H gradients and flatter N/O gradients (as shown by the purple circle). In this way, the central regions of galaxies may experience an 'N/O pendulum' effect, where the central regions of the galaxy swing from the top-left to the top-right of the N/O–O/H plane across cosmic time.

This is a primitive description of this scenario, and future work applying chemical evolution modelling that accounts for other phenomena such as radial gas flows and changes in the N/O and O/H values within the outer regions of the galaxy should be undertaken. Nevertheless, the cartoon in Figure 4.17 highlights how the positive N/O gradients at $z \sim 2$ may be a consequence of positive O/H gradients at $z \sim 3$. Moreover, the accretion of

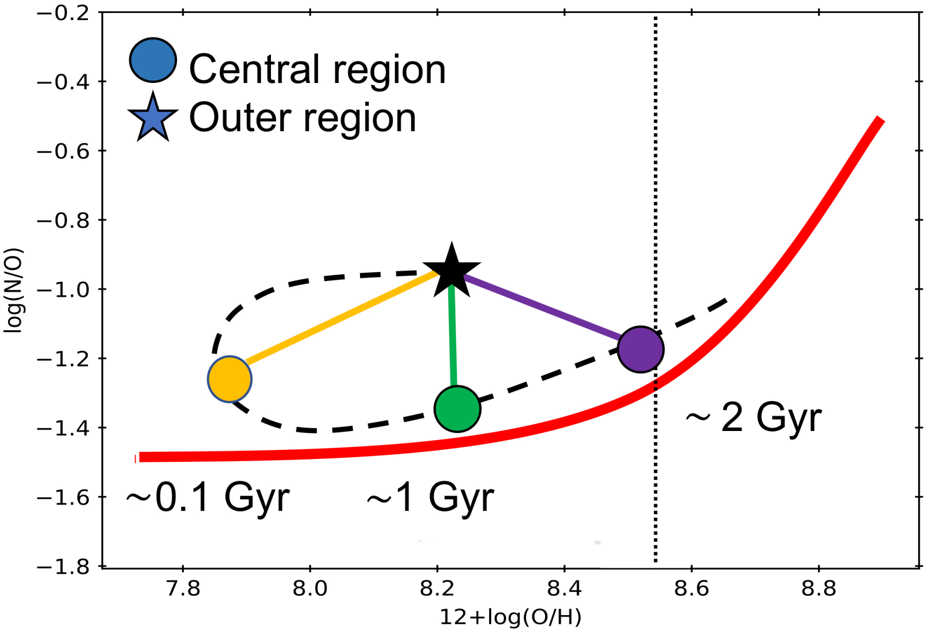

Fig. 4.17 Cartoon diagram showing how the N/O and O/H values may evolve following a dilution event. The red line shows the average local N/O–O/H relation. The black dashed line traces the ‘loop’ in the N/O–O/H plane that is expected following a dilution event, as modelled by Köppen & Hensler (2005). The star represents the outer region of the galaxy, which does not undergo accretion of pristine gas and is assumed to be anchored to its position. We assume N/O and O/H gradients are both initially flat, with the central regions of the galaxy occupying the same position in the N/O–O/H plane as the outer regions. The yellow, green and purple circles then show the potential positions of the central region approximately 0.1 Gyr, 1 Gyr and 2 Gyr after the onset of the accretion event, respectively. Initially, the accretion of pristine gas dilutes the O/H, whilst leaving the N/O unaffected. Subsequent star formation then releases oxygen into the ISM, causing a decrease in N/O, and starts an increase in O/H. Eventually, nitrogen is also released into the ISM, and N/O begins to increase again. This causes a "N/O pendulum effect", where the central region of the galaxy swings from the top left to the top right in the N/O–O/H plane.

gas onto the central regions at $z \sim 2$ may explain why KLEVER galaxies exhibit negative Balmer decrement gradients. This accretion would drive more centrally concentrated star formation, hence more centrally concentrated stellar mass density and subsequently a higher concentration of dust (as traced by $\mathrm{H}\alpha/\mathrm{H}\beta$) within the centre of the galaxy, all of which are trends that we observe within the KLEVER sample. Similarly higher mass galaxies with deeper potential wells may accrete more gas than those at lower masses, which may explain why the higher mass KLEVER bin has steeper Balmer decrement gradients, more positive N/O gradients and more negative O/H gradients. Further observations of the gradients in N2O2 and the Balmer decrement are required across a range of redshifts in order to confirm the validity of this scenario.

In summary, our observations of a combination of flat gradients in O/H, positive gradients in N/O and negative Balmer decrement gradients can be reconciled in the following way. Considering the redshift evolution of the MZR, high-redshift galaxies are expected to have lower metallicities than those seen locally due to a combination of increased metal loss and increased gas fraction (Sanders et al., 2021). As demonstrated in Chapter 3, the existence of a fundamental nitrogen relation suggests that the processes governing the redshift evolution of the MZR must also impact N/O. We can therefore consider the potential impact that gas outflows and inflows may have on the radial distributions of both O/H and N/O in high-z galaxies. If we first consider outflows, these may drive a mixing of the metals throughout a given galaxy, homogenising their distributions. Whilst this scenario is compatible with the flat gradients observed in O/H, it is at odds with the observations of inverted gradients in N/O. Previous work has suggested that outflows may be differential, expelling oxygen preferentially relative to nitrogen (Vincenzo et al., 2016b), however this scenario would act to deplete the central regions of a galaxy in oxygen relative to nitrogen, and would therefore lead to negative N/O gradients. In this way, outflows alone cannot explain our results, and we therefore consider the impact of gas inflows into the central regions of galaxies. Previous work has suggested that the inflow of gas into the central regions of galaxies can dilute the observed O/H, leading to inverted metallicity gradients at $z \sim 3$ (Cresci et al., 2010; Troncoso et al., 2014). Furthermore, models have also been able to reconcile these observations with an inside-out scenario of galaxy growth by invoking strong infalls of primordial gas onto the innermost disk regions of galaxies at early times (Mott et al., 2013). Moreover, such observations are also compatible with the flat O/H gradients observed at $z \sim 2$ (Curti et al., 2020b). Within this framework, the accretion of gas onto the central regions of galaxies would be expected to fuel new star formation and hence the production of new metals, however the subsequent enrichment of the ISM is out-competed by the dilution effect caused by the accretion of gas onto such regions. On timescales of less than $\sim$1 Gyr,

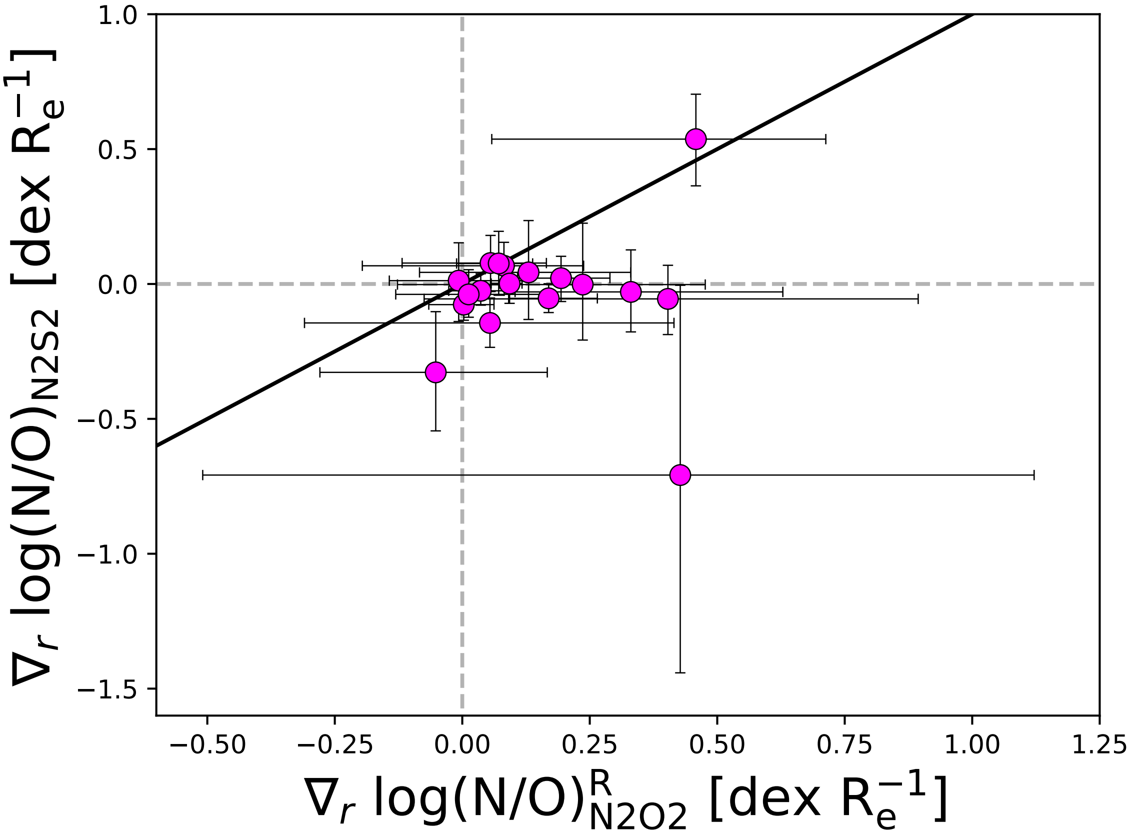

Fig. 4.18 N/O gradients in KLEVER galaxies, shown in magenta, derived from $\log(\mathrm{N/O})_{\mathrm{N2S2}}$ compared to those derived using $\log(\mathrm{N/O})^{\mathrm{R}}_{\mathrm{N2O2}}$. The solid black line shows the 1:1 relation.

the delayed production of nitrogen by LIMS relative to oxygen from massive stars means that centrally concentrated star formation would lead to a decrease in N/O in these regions, driving positive N/O gradients. At the same time, the inside-out growth of galaxies and the centrally concentrated star formation may lead to a higher concentration of dust in the central regions of galaxies, as reflected by negative gradients in the Balmer decrement. In this way, our results can be interpreted as a result of strong accretion of pristine gas into the central regions of galaxies at early times.

4.4.6 The disparity between N2O2 and N2S2 gradients

In Figure 4.18 we show a comparison of KLEVER N/O gradients derived using both $\log(\mathrm{N/O})^{\mathrm{R}}_{\mathrm{N2O2}}$ and $\log(\mathrm{N/O})_{\mathrm{N2S2}}$, with the former being much more positive than the latter. The differences in log(N/O) values derived from N2O2 and N2S2 have been discussed in Section 4.2.1, and are expected to be driven by differences in the ionisation structures of highly star forming regions compared to regions less dominated by star formation. The observed differences between N/O gradients derived using N2O2 and N2S2 may therefore suggest that there are changes in the ionisation structure within different regions of high-redshift galaxies. In particular, the combination of flat N2S2 gradients and positive N2O2 gradients suggest that the [O II]$\lambda\lambda$3727,29 emission line doublet is much more abundant than the [S II]$\lambda\lambda$6716,32 emission line doublet in the central regions of KLEVER galaxies.

To investigate this further, we use CLOUDY models to generate a spherically-symmetric H II region. We input ionisation by a 2 Myr-old simple stellar population, with a density of 10^2cm^{-3}, metallicity [Fe/H]=-0.2 and ionisation parameter log(U)=-3.5. The resulting ionisation structure for a range of elements is shown in Figure 4.19. In the left panel, we show the ionic fractions of different elements as a function of the normalised depth from the emitting cloud. Similar ionisation structures have been presented in previous works (Levesque et al., 2010; Mannucci et al., 2021). Doubly-ionised species such as O^{++} and S^{++} are found to dominate the central regions of the H II cloud relative to their singly-ionised counterparts, which are preferentially emitted in the outer regions. N^+ and O^+ have ionisation structures that show a similar radial dependence, whereas S^+ has a structure that is quite different. In the right hand panel of Figure 4.19 we highlight the impact that the ionisation structure has on the radial variation of N2S2 and N2O2 within individual H II regions. The similar structures of N^+ and O^+ mean that the N2O2 ratio is roughly constant over the entirety of the region, whereas the strong radial variation of S^+ causes the N2S2 value to decrease with radius.

It is important to note that the CLOUDY model represents a single H II region with a single metallicity, stellar population and ionisation parameter. However, any spectrum of galaxy light extracted from an aperture represents a luminosity-weighted average of the emission from an ensemble of all H II regions within that aperture. The spatially binned KLEVER data used throughout this chapter is extracted from 0.3 × 0.3 arcsec apertures, corresponding to a projected physical distance of 2–3 kpc at $z \sim 2$, whilst individual H II regions have typical sizes of 0.01–1 kpc (Cosens et al., 2018), meaning we do not resolve individual H II regions. Nevertheless, strong star formation in the central regions of the galaxy could cause several large H II regions to grow and merge, causing the spectrum extracted from this region to become dominated by the emission from the central regions of H II clouds. As can be seen in Figure 4.19, these central regions are expected to have only a small ionic fraction of sulphur in S^+, leading to larger N/O values estimated from N2S2 at a fixed N2O2. In contrast, the outer regions of the galaxy, where there is less star formation, may have spectra that contain a greater contribution from the outer regions of H II clouds, bringing better agreement between N2O2 and N2S2 derived N/O estimates. This could cause N2S2 to overestimate the N/O value in the central parts of the galaxy relative to N2O2, causing

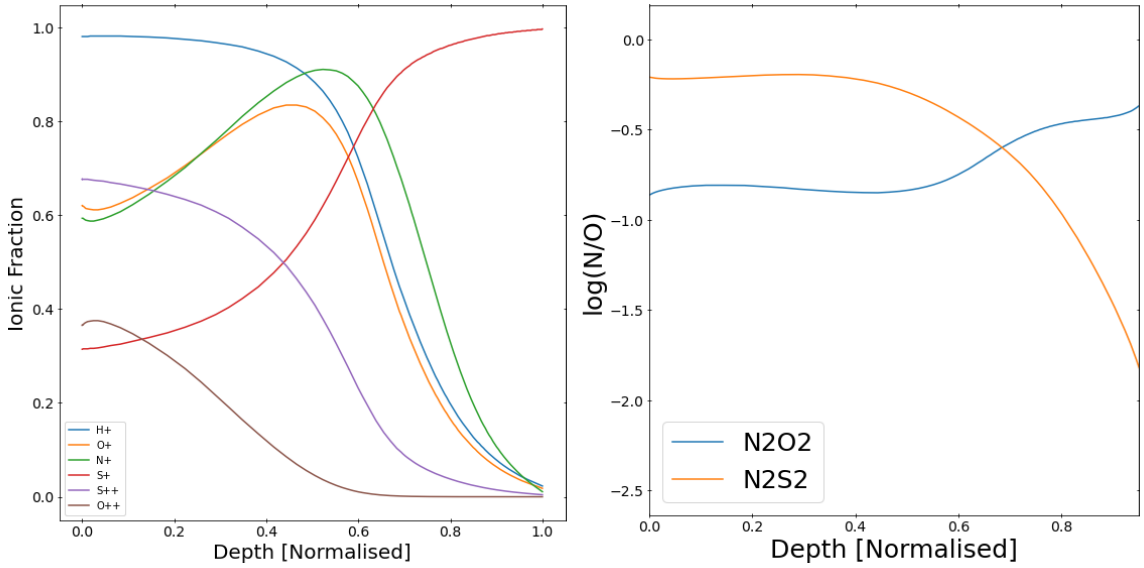

(a) (b)

Fig. 4.19 The expected ionisation structure (a) and emission line flux ratios (b) within a spherically symmetric H II region shown as a function of fractional depth within the emitting cloud. Data is generated using CLOUDY assuming a 2 Myr old simple stellar population, with density 10^2cm^{-3}, metallicity [Fe/H]=$-$0.2 and ionisation parameter log(U)=$-$3.5. N^+ and O^+ tend to have similar ionisation structures, whilst S^+ has a very different structure, leading to differences in the spatial variations of N2O2 relative to N2S2.

positive abundance gradients in N/O to appear flat. In this way, the discrepancy between the N/O gradient estimates from these two diagnostics shown in Figure 4.18 may be driven by variations in the ionisation structures between the central and outer regions of galaxies.

4.5 Summary and conclusions

In this chapter, we have presented the first measurements of N/O gradients for a sample of star-forming galaxies at z ∼2. The main findings of the chapter are summarised below.

- Galaxies at z ∼2 have gradients in N/O that are flatter than local galaxies when compared at a fixed stellar mass. This is contrary to inside-out growth models, which predict steeper N/O at earlier times. We can reconcile this difference by invoking enhanced feedback mechanisms that effectively mix metals within the ISM on galaxy wide scales.
- We observe inverted gradients in N/O when measured using N2O2 and applying a resolved correction for dust attenuation. Positive gradients in N2O2 may be expected

as a consequence of positive metallicity gradients at $z \sim 3$. Accretion of metal poor gas onto the central regions of galaxies at high redshift can trigger star formation, which may rapidly enrich the ISM with oxygen from core-collapse supernovae. If nitrogen production is dominated by low- and intermediate-mass stars, the enrichment of the ISM with nitrogen will be delayed relative to oxygen, leading to a decrease in the central N/O abundance and hence driving positive N/O gradients.

- Negative Balmer decrement gradients are common within high-mass KLEVER galaxies. These galaxies also have higher concentrations of stellar mass and star formation towards their centres, and also have more centrally concentrated dust distributions. These results are consistent with the findings of Nelson et al. (2016) for galaxies at $z \sim 1.4$, suggesting that the central regions of massive galaxies at $z \sim 2$ may be undergoing in-situ bulge construction. In agreement with UV estimates of the attenuation in galaxies at $z \sim 2$ from Tacchella et al. (2018), we observe more extended Balmer decrement profiles than those found at $z \sim 1.4$ by Nelson et al. (2016), suggesting galaxies at $z \sim 2$ have a significant amount of dust attenuation out to large radii.

- When using N2S2 to trace the N/O, or similarly using N2O2 without a resolved attenuation correction, we find gradients that are flat. This finding is in good agreement with previous results for flat gradients in O/H, and taken alone could suggest that N and O have the same nucleosynthetic origin, i.e. both are produced primarily by massive stars at $z \sim 2$. However, we note we are unable to constrain the stellar origin of primary nitrogen at $z \sim 2$, and contributions from low- and intermediate-mass stars may be significant.

- Flatter N/O gradients obtained using N2S2 may be a consequence of the low fraction of S^+ relative to N^+ and O^+ in the central regions of galaxies, which themselves may be dominated by emission from the central parts of H II regions. This could cause N2S2 to overestimate the N/O value in the central parts of the galaxy, causing positive abundance gradients to appear flat.

Chapter 5

Modelling dilution in the local N/O–O/H plane

5.1 Introduction

Throughout this thesis we have encountered the interpretation that differences in the metallicity and N/O values of galaxies can be driven by physical processes relating to gas flows. A long-standing theory within the literature is that infalls of pristine gas will dilute the O/H ratio whilst leaving the N/O ratio unaffected. Previous authors such as Andrews & Martini (2013) have observed galaxies within the local universe that have enhanced SFR and N/O values at low metallicities, suggesting that the subsequent scatter in the N/O–O/H relation may be caused by these galaxies having experienced a large inflow of gas that has lowered the O/H whilst leaving the N/O unaffected. Similarly, Pérez-Montero et al. (2013) suggested that the lack of an observed SFR dependence in the stellar mass–N/O plane, in conjunction with the well-studied SFR dependence in the stellar mass–O/H plane, is caused by accretion events that reduce the O/H and enhance the SFR whilst leaving the N/O unaffected. It was therefore posited that infalls of pristine gas act as the main driver of the fundamental metallicity relation.

However, in Chapter 3 we provided evidence for the existence of an anti-correlation between N/O and SFR that is similar in strength to that observed in O/H. Therefore, processes that are driving the FMR must not impact only the metallicity as previously suggested, but also the N/O ratio. A revision of our current interpretation of gas inflows into galaxies is needed to reconcile theory with our observations. One explanation may be that the accreting gas may not be pristine, but instead be enriched with some level of primary nitrogen (i.e. log(N/O) ~ -1.5), driving a dilution in not only in O/H but also N/O. Similarly, the models of

Köppen & Hensler (2005) highlighted that accretion of pristine gas can initially decrease O/H whilst leaving N/O unaffected, however subsequent star formation acts not only to increase O/H, but also causes an initial decrease in N/O due to the delayed enrichment of the ISM with nitrogen. Several mechanisms other than direct gas accretion are also expected to cause variations in the N/O ratio relative to O/H. Since the enrichment of the ISM with nitrogen is typically delayed by $\sim$100 Myr relative to oxygen, models have suggested that high N/O values at a fixed O/H could be driven by galaxies with lower star formation efficiencies having increased levels of nitrogen enrichment (Mollá et al., 2006; Vincenzo et al., 2016b). Similarly, galactic winds may preferentially expel the products of core-collapse supernovae, such as oxygen, rather than the products of low- and intermediate-mass stars, such as nitrogen, which would drive galaxies towards higher values of N/O and lower values of O/H (van Zee & Haynes, 2006; Vincenzo et al., 2016b). Spatially resolved studies of local galaxies using MaNGA have also demonstrated that galactic fountain scenarios, where metal rich gas is expelled from the central regions of a galaxy and re-accreted onto the outskirts, can explain the scatter in N/O–O/H observed within individual galaxies (Belfiore et al., 2015), with the outer regions of galaxies tending towards higher values of N/O at low metallicities relative to the average N/O–O/H relation (Luo et al., 2021).

Since the FMR is observed to hold out to $z \sim 3$, then evidence for accretion events that supposedly drive the evolution of galaxies should be observable within the local N/O–O/H plane. Within this chapter, we investigate the key trends in the local N/O–O/H plane, highlighting the physical properties of SDSS galaxies that have lower than expected metallicities, as may be expected from a recent accretion event. We undertake preliminary modelling of gas-mixing events in order to investigate the feasibility of gas inflows driving the scatter in the local N/O–O/H plane.

5.2 Data

We investigate the local N/O–O/H relation using data from the seventh data release of SDSS (Abazajian et al. 2009). The emission line fluxes and stellar mass estimates for galaxies in this data release are obtained from the MPA/JHU catalogue[1]. We adopt the same selection criteria applied to galaxies in Section 3.1.1. In brief, all galaxies are defined as star-forming as determined by their position on the [N II]-BPT diagram (Baldwin et al., 1981), adopting the classification scheme from Kauffmann et al. (2003b) to remove potential AGN. A minimum redshift threshold of $z > 0.03$ was imposed to ensure detections of the [O II]$\lambda\lambda$3727,29 emission line doublet. We imposed a detection threshold on Hα S/N $>$

---

[1] http://www.mpa-garching.mpg.de/SDSS/DR7/

15, which essentially acts as a threshold on the SFR and ensures the detection of all other emission lines. Nevertheless, we also impose a lower S/N threshold on all remaining emission lines of S/N > 2. Taken together, these criteria provide a sample of 126,385 local star-forming galaxies.

Stellar mass estimates are provided following the Kauffmann et al. (2003a) approach, with aperture corrections to prescribed by Salim et al. (2007). The Balmer decrement was used to calculate E(B-V)$_{gas}$, assuming case B recombination (Hα/Hβ=2.87) and a Calzetti et al. (2000) extinction curve. Star formation rates were measured from the extinction-corrected Hα luminosity, using the conversion factor between Hα and SFR from Kennicutt & Evans (2012). All stellar mass and SFR estimates were normalised to a Chabrier (2003) IMF. Gas-phase metallicities are calculated using a simultaneous chi-squared minimisation over the R3, R2, R23 and O32 emission line diagnostics, adopting the strong-line calibrations provided by Curti et al. (2020a). N/O abundances are determined using the N2O2 diagnostic, adopting the calibration presented in Section 3.3.1.

5.3 Secondary trends in the N/O–O/H plane

The parameterisation of the local relationship between N/O and O/H within our SDSS sample was introduced in detail in Section 3.4.1. In brief, we observe a bimodal behaviour of SDSS galaxies within the N/O–O/H plane above and below a metallicity of 12+log(O/H)=8.534. Above this metallicity, the relationship between N/O and O/H follows a power law with a slope $= 2.69$. Over 90% of SDSS galaxies fall into this regime, where N/O is strongly correlated with O/H with a small scatter about the average trend of 0.07 dex and a Spearman's rank correlation coefficient of 0.9. This tight relationship is due to the dominant production of nitrogen as a secondary nucleosynthetic element, meaning its yield increases with metallicity. At metallicities lower than 12+log(O/H)=8.534, the SDSS galaxies tend towards a plateau at N/O$=-1.491$, albeit with a scatter of $\sim$0.1 dex. Roughly 10% of our galaxies fall into this regime, where we observe a weaker correlation between N/O and O/H with Spearman's rank coefficient of just 0.47, suggesting nitrogen production is more independent of O/H relative to the high-metallicity regime, consistent with a scenario in which nitrogen is a primary nucleosynthetic product formed freshly from hydrogen and helium within stars. Within this section we present an overview of the trends between N/O, O/H, SFR and stellar mass, with a particular focus on deviations from the average relation in the N/O–O/H plane.

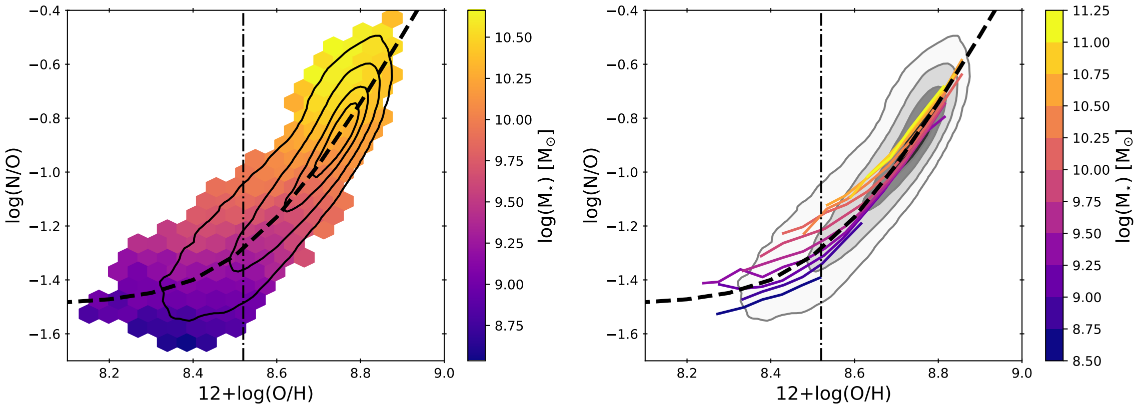

(a) Spatial stellar mass bins.

(b) Trends with constant stellar mass.

Fig. 5.1 The average trends with stellar mass in the N/O–O/H plane for local galaxies. Contours show the distribution of SDSS galaxies, whilst the black dashed line shows the best fit to the N/O–O/H relation, and the dot-dashed vertical line shows the 'transition' metallicity between the primary and secondary regimes at 12+log(O/H)=8.534. In (a), the median stellar mass is shown in hexagonal spatial bins in the N/O–O/H plane, with each bin containing at least 10 galaxies. In (b), we show tracks of constant stellar mass, extracted in 0.25 dex wide increments. Within each track of constant mass, each point on the track shows the median N/O within a 0.05 dex wide metallicity bin. Only points containing at least 25 galaxies are plotted.

5.3.1 Stellar mass

In Figure 5.1 we show the trends with stellar mass in the N/O–O/H plane. In the left-hand panel, we plot the median stellar mass values taken in spatial hexagonal bins within the N/O–O/H plane, displaying only bins containing at least 10 galaxies. This visualisation of the data is useful for identifying which regions of the N/O–O/H plane are most dominated by certain galaxy properties. For example, in Figure 5.1 a clear trend can be seen in that more massive galaxies tend to occupy regions with higher N/O and O/H values. This result is not surprising given our understanding of the mass-metallicity and mass-N/O relations. Galaxies with high stellar masses have naturally undergone lots of historic star formation that has enriched the ISM with metals over time, creating a chemically mature system. Similarly, at high metallicities nitrogen production is dominated by secondary nucleosynthetic processes, resulting in larger values of N/O. One may naively assume from the binning in the left-hand panel of Figure 5.1 that the highest mass galaxies all reside at high N/O and O/H values, above the median local relation, and that as such, an increase in stellar mass at high metallicities would increase the N/O. However, this is not the case. In the right-hand panel, we show tracks of constant stellar mass in the N/O–O/H plane, determined by first binning the data in 0.25 dex wide stellar mass bins, before calculating the median N/O value across 0.05 dex wide bins of O/H. Only those points containing at least 25 galaxies are displayed. With this methodology, it can be see that the average distribution of the highest mass bin actually lies close to the median N/O–O/H relation, following a similar distribution to lower mass galaxies. Therefore, whilst the most massive galaxies tend towards higher values of O/H and N/O and dominate the region above the median relation at high metallicities, an increase in stellar mass at high metallicities does not correspond to an increase in the N/O. Interestingly, at lower metallicities it can be seen that tracks of a higher stellar mass do correspond to higher N/O values. This trend is particularly evident below the transition metallicity of $12+\log(\mathrm{O/H})=8.534$. In this regime, nearly all of the scatter in the distribution of the SDSS galaxies can be well traced by changes in stellar mass.

5.3.2 SFR and sSFR

In Figure 5.2 we present the average trends of star formation rate in the N/O–O/H plane, in the same way as done for the stellar mass previously. In the left hand panel, a strong trend can be observed running perpendicular to the median N/O–O/H relation, with more star forming galaxies being offset above the average relation and those with low star formation rates falling below it. This trend appears most evident below $\log(\mathrm{N/O})\sim-1$, with galaxies that have larger N/O values showing no clear trend with SFR. In the right hand panel, the

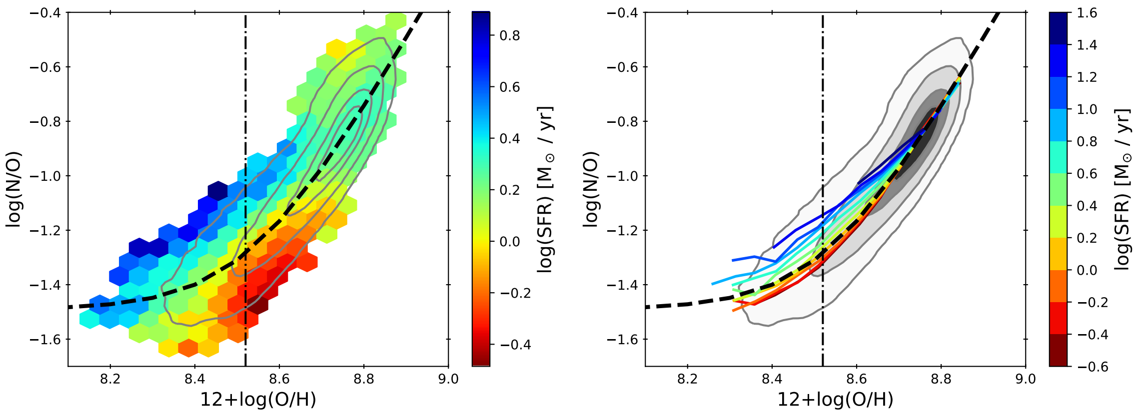

(a) Spatial SFR bins.

(b) Trends with constant SFR.

Fig. 5.2 The average trends with SFR in the N/O–O/H plane for local galaxies. Contours show the distribution of SDSS galaxies, whilst the black dashed line shows the best fit to the N/O–O/H relation, and the dot-dashed vertical line shows the ‘transition’ metallicity between the primary and secondary regimes at 12+log(O/H)=8.534. In (a), the median SFR is shown in hexagonal spatial bins in the N/O–O/H plane, with each bin containing at least 10 galaxies. In (b), we show tracks of constant SFR, extracted in 0.2 dex wide increments. Within each track of constant SFR, each point on the track shows the median N/O within a 0.05 dex wide metallicity bin. Only points containing at least 25 galaxies are plotted.

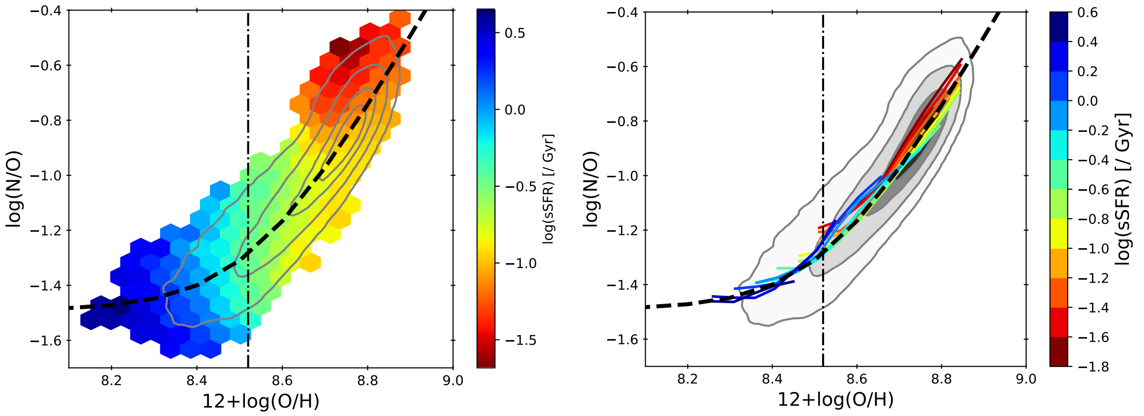

(a) Spatial sSFR bins.

(b) Trends with constant sSFR.

Fig. 5.3 The average trends with sSFR in the N/O–O/H plane for local galaxies. Contours show the distribution of SDSS galaxies, whilst the black dashed line shows the best fit to the N/O–O/H relation, and the dot-dashed vertical line shows the ‘transition’ metallicity between the primary and secondary regimes at 12+log(O/H)=8.534. In (a), the median sSFR is shown in hexagonal spatial bins in the N/O–O/H plane, with each bin containing at least 10 galaxies. In (b), we show tracks of constant sSFR, extracted in 0.2 dex wide increments. Within each track of constant sSFR, each point on the track shows the median N/O within a 0.05 dex wide metallicity bin. Only points containing at least 25 galaxies are plotted.

tracks of constant star formation rate show a similar trend: galaxies with low metallicities and high star formation rates are enhanced in N/O, with this trend getting weaker towards higher metallicities, before reaching the highest metallicities where no trend with the SFR is observed. Indeed, the tracks of constant SFR behave in a qualitatively similar way to the tracks of constant stellar mass shown in the right-hand panel of Figure 5.1. This may be expected given the existence of the star forming main sequence, with higher mass galaxies generally having larger star formation rates. To investigate this further, we repeat our analysis for the specific star formation rate, as shown in Figure 5.3. In the left-hand panel, the spatially binned average sSFR values show a clear trend wherein the highest sSFR have low values of O/H and N/O, whilst those with the lowest sSFR values tend to have the highest O/H and N/O values. In the right-hand panel, the tracks of constant sSFR are shown to all lie upon the median N/O–O/H relation for the full range of the SDSS sample. This indicates that galaxies at a fixed sSFR are scattered evenly about the median N/O–O/H relation, and that a change in sSFR will act to move a galaxy upwards or downwards along this median relation. Furthermore, the lack of correlation between the scatter in the N/O–O/H plane and sSFR at low metallicities suggest that the trends observed for stellar mass (Fig 5.1) and SFR (Fig 5.2) are in fact coupled, since the scatter is removed by accounting for those galaxies with higher stellar masses also having higher star formation rates. In summary, at low metallicities and N/O values, galaxies tend to have enhanced levels of recent star formation, as probed by the sSFR. Within this regime, those galaxies with higher masses and star formation rates will have larger values of N/O at a fixed metallicity.

5.3.3 Deviation from SFMS and MZR

To better contextualise the trends observed in the N/O–O/H plane, it can be useful to study how the deviations of galaxies from the median N/O–O/H sequence correlate with the deviations from other well-known scaling relations of galaxy properties. In Figure 5.4 we repeat our analysis of spatial variations in the N/O–O/H plane for the deviation in SFR from the star-forming main sequence, $\Delta\log(\mathrm{SFR})_{SFMS}$. We parameterise the star forming main sequence within our SDSS sample by calculating the median SFR within 0.15 dex wide stellar mass bins, before fitting the points from all bins containing at least 25 galaxies with a straight line using a least squares minimisation. The resulting relation between SFR and stellar mass is then $\log(\mathrm{SFR}) = 0.53 \times \log(\mathrm{M}_\star) - 5.17$. Our SFMS agrees well with that from (Renzini & Peng, 2015), albeit with a slightly shallower slope and higher normalisation. In the left-hand panel of Figure 5.4 it can be seen that galaxies with the highest rate of star formation relative to the star forming main sequence tend to be in the ‘primary’ regime, with low metallicities and N/O values. In contrast, galaxies in the secondary regime are

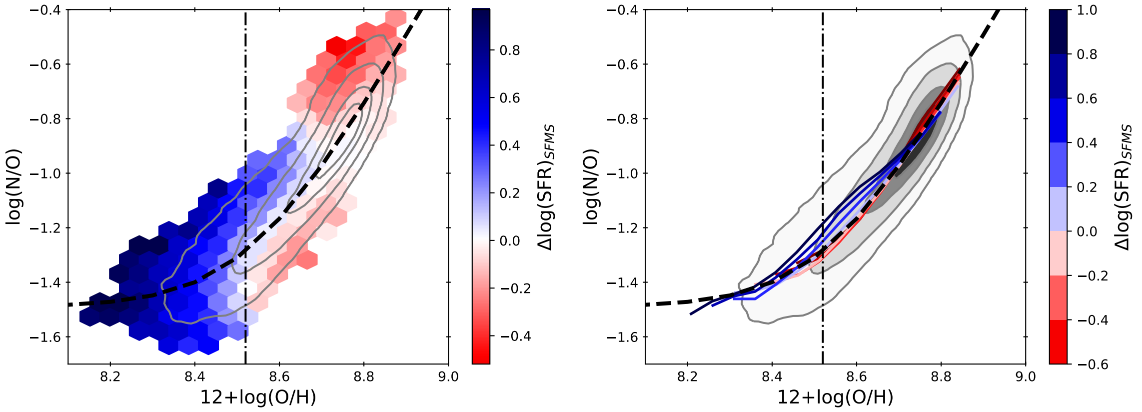

(a) Spatial Δlog(SFR)$_{SFMS}$ bins.

(b) Trends with constant Δlog(SFR)$_{SFMS}$.

Fig. 5.4 The average trends with Δlog(SFR)$_{SFMS}$ in the N/O–O/H plane for local galaxies. Δlog(SFR)$_{SFMS}$ is measured relative to the median relationship between stellar mass and SFR observed within our SDSS sample. Contours show the distribution of SDSS galaxies, whilst the black dashed line shows the best fit to the N/O–O/H relation, and the dot-dashed vertical line shows the 'transition' metallicity between the primary and secondary regimes at 12+log(O/H)=8.534. In (a), the median Δlog(SFR)$_{SFMS}$ is shown in hexagonal spatial bins in the N/O–O/H plane, with each bin containing at least 10 galaxies. In (b), we show tracks of constant Δlog(SFR)$_{SFMS}$, extracted in 0.2 dex wide increments. For a given track, each point shows the median N/O within a 0.05 dex wide metallicity bin. Only points containing at least 25 galaxies are plotted.

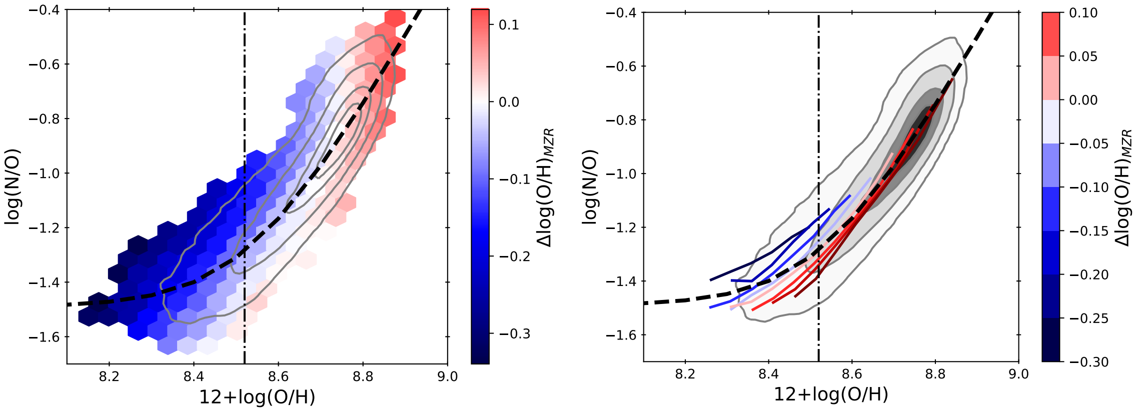

(a) Spatial Δlog(O/H)$_{MZR}$ bins.

(b) Trends with constant Δlog(O/H)$_{MZR}$.

Fig. 5.5 The average trends with Δlog(O/H)$_{MZR}$ in the N/O–O/H plane for local galaxies. Δlog(O/H)$_{MZR}$ is measured relative to the median relationship between mass and metallicity observed within our SDSS sample. Contours show the distribution of SDSS galaxies, whilst the black dashed line shows the best fit to the N/O–O/H relation, and the dot-dashed vertical line shows the 'transition' metallicity between the primary and secondary regimes at 12+log(O/H)=8.534. In (a), the median Δlog(O/H)$_{MZR}$ is shown in hexagonal spatial bins in the N/O–O/H plane, with each bin containing at least 10 galaxies. In (b), we show tracks of constant Δlog(O/H)$_{MZR}$, extracted in 0.2 dex wide increments. For a given track, each point shows the median N/O within a 0.05 dex wide metallicity bin. Only points containing at least 25 galaxies are plotted.

generally within one standard deviation (0.35 dex) of the star forming main sequence. In the right-hand panel, tracks of constant Δlog(SFR)$_{SFMS}$ generally lie on the median N/O–O/H relation, suggesting Δlog(SFR)$_{SFMS}$ is a better predictor of location along the N/O–O/H relation rather than the scatter round it. These results are in agreement with our findings for the sSFR presented in Figure 5.3, suggesting that galaxies experiencing a recent burst of star formation tend towards lower metallicities and N/O values.

In Figure 5.5 we show the spatial variations in the N/O–O/H plane for the deviation of galaxies in metallicity from the local mass-metallicity relation (as parameterised by Curti et al. (2020a)), Δlog(O/H)$_{MZR}$. In the left-hand panel it can be seen that the majority of galaxies in the 'secondary' regime are within one standard deviation (0.07 dex) of the local MZR. In contrast, galaxies in the 'primary' regime tend to have much lower metallicities than predicted by their stellar mass using the MZR. Moreover, considering the right-hand panel of Figure 5.5 it can be seen that the scatter in the 'primary' regime is correlated with the deviation from the MZR, with the most metal-depleted galaxies characterised by an enhancement in N/O at a fixed metallicity.

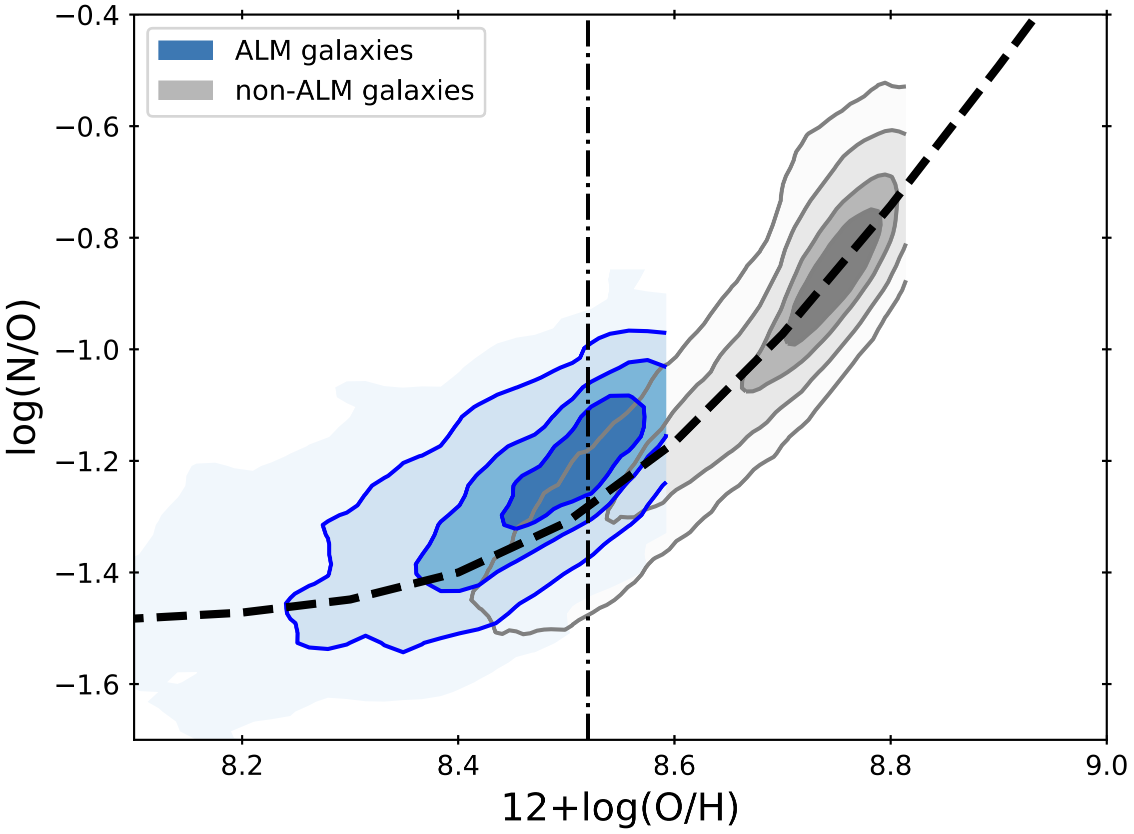

Fig. 5.6 The distribution of SDSS galaxies in the N/O–O/H plane split into those with anomalously low metallicities (ALM) relative to the local MZR, shown in blue, and those that lie on the local MZR, shown in grey. A galaxy is considered to be consistent with the MZR if $|\Delta\log(\mathrm{O/H})|<0.054$ dex, whereas galaxies are defined as ALM if they fall more than 3σ below the MZR, such that $\Delta\log(\mathrm{O/H})<-0.162$ dex.

A similar trend of metal dilution at low O/H and high N/O has been observed on a spatially resolved basis by Luo et al. (2021), who found that spaxels from MaNGA galaxies with metallicities lower than expected from the resolved MZR generally occupied the region above the median N/O–O/H relation. Luo et al. (2021) defined these spaxels, with metallicities more than 3σ below the resolved MZR, as 'anomalously low metallicity' (ALM) regions. We can extend a similar analysis to the SDSS galaxies presented within this chapter, defining ALM galaxies to be those with metallicities that deviate more than 3σ below the MZR in the local Universe. We determine the scatter about the MZR by fitting a Gaussian profile to the positive side of the MZR deviation distribution and assuming a symmetric negative side, finding a best fit $\sigma = 0.054$. We then define galaxies that lie on the MZR as having $|\Delta\log(\mathrm{O/H})|<0.054$ dex in order to ensure a clean selection between our ALM and non-ALM galaxies. The results are shown in Figure 5.6, with the ALM galaxies shown in blue with the contours showing the 30%, 60% and 90% distributions of the galaxies. ALM galaxies can clearly be seen to have systematically larger N/O values than the non-ALM sample when compared at a given metallicity, consistent with the results presented by Luo et al. (2021). The hard upper metallicity cut in the non-ALM sample is driven by the highest metallicity galaxies all falling within 0.054 dex of the local MZR, with a similar effect being seen in the ALM sample where all galaxies above 12+log(O/H)$\sim$8.6 deviate from the local MZR by less than 0.162 dex.

5.4 Gas mixing models

To summarise the key trends observed in the N/O–O/H plane thus far in this chapter: at low metallicities, galaxies tend to have high sSFR values and lie well above the local star forming main sequence, suggesting they have undergone a recent burst of star formation. In addition, galaxies within this region that have enhanced N/O values at a fixed metallicity also display higher stellar masses, higher star formation rates and have lower metallicities than expected from the local MZR. The combination of lower than expected metallicities and high amount of star formation may suggest that these galaxies have undergone recent accretion of gas. Within this section, we investigate the role of the accretion of gas onto a galaxy in the creation of low metallicity, high N/O galaxies.

5.4.1 Dilution vectors

We have already defined ALM galaxies as those with a much lower metallicity than expected from the MZR given their stellar mass. It is therefore useful to consider where these

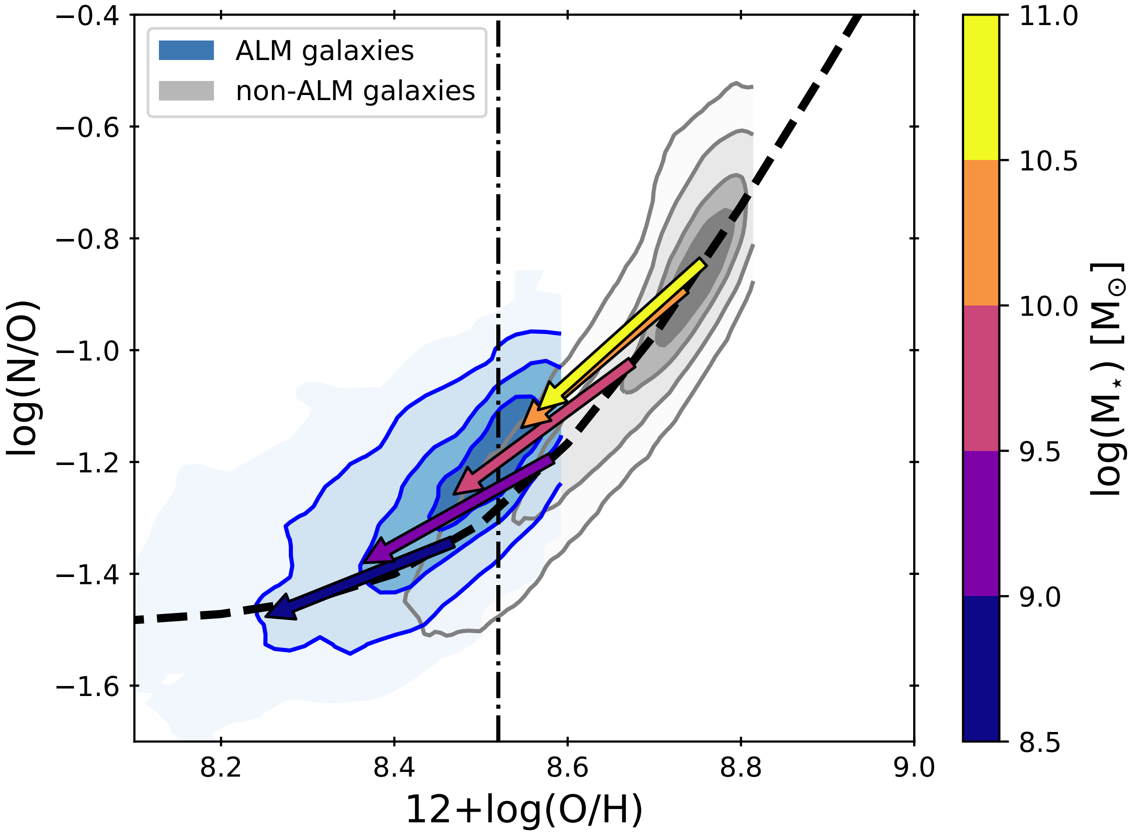

Fig. 5.7 Distribution of ALM and non-ALM galaxies from SDSS in the N/O–O/H plane. The arrows overlaying the contours represent ‘dilution’ vectors, that compare the expected position of a galaxy in the N/O–O/H given its stellar mass to the observed position. The vectors shown are taken as the median of all individual vectors within 0.5 dex increments of stellar mass.

Stellar mass range	[8.5, 9.0]	[9.0, 9.5]	[9.5, 10.0]	[10.0, 10.5]	[10.5, 11.0]
Vector angle	31.7	40.8	48.9	52.9	54.3
Vector magnitude	0.27	0.30	0.33	0.33	0.34

Table 5.1 Values for the angle (measured in degrees anti-clockwise from the horizontal) and magnitude of the dilution vectors calculated in different bins of stellar mass. Bins of higher stellar mass are characterised by steeper dilution vector angles, whilst only a mild trend of increasing vector magnitude is observed.

galaxies are expected to be in the N/O–O/H plane. We take the expected metallicity to be the metallicity a galaxy of a given stellar mass would have if it lay on the median MZR. Similarly, the expected N/O value corresponds to the point on the median N/O–O/H relation where a galaxy would lie given its expected metallicity. For each ALM galaxy we can then define a 'dilution' vector, so-named as it corresponds to a decrease in both the O/H and N/O, by comparing its expected position in the N/O–O/H plane to that which is observed. As highlighted in Figure 5.1, N/O increases with stellar mass within the low metallicity regime. We therefore calculate the median dilution vector in several bins of stellar mass for all ALM galaxies, with the results shown in Figure 5.7. The angle below the horizontal line and magnitude of each vector is given in Table 5.1. The magnitude of the dilution vectors remains roughly constant across all stellar mass bins, showing only a mild increase from 0.27 dex to 0.34 dex towards higher stellar masses, suggesting the size of any potential dilution event is the same across all stellar masses. In contrast, a clear trend in the dilution angle is observed, with more massive galaxies having steeper dilution vectors. This means that any hypothetical dilution event has a larger impact on the N/O ratio at high masses than it does at low masses. Moreover, the highest mass dilution vectors all finish in a location above the median N/O–O/H relation, however in the lowest mass bin the dilution vector does not cause a deviation from the median relation.

5.4.2 Toy dilution model

Simple gas mixing scenario

To quantify the impact of dilution in the N/O–O/H plane we construct a simple gas mixing toy model, following Belfiore et al. (2015). We consider the case where a galaxy with a mass of gas $\mathrm{M}_{\mathrm{gas}}^{\mathrm{G}}$ and a metallicity Z^{G} mixes with a gas cloud that has a low metallicity Z^{C} and a corresponding gas mass $\mathrm{M}_{\mathrm{gas}}^{\mathrm{C}}$. In each case, the abundance of nitrogen relative to oxygen ($\mathrm{N/O}^{\mathrm{G}}$ and $\mathrm{N/O}^{\mathrm{C}}$ for the galaxy and the gas cloud, respectively) can be determined from the median N/O–O/H relation for SDSS galaxies, as parameterised in Section 3.4.1. After mixing of these two objects, the resulting metallicity Z can be parameterised as

$$\mathrm{Z} = \frac{(\mathrm{Z^G} \times \mathrm{m_{gas}}) + \mathrm{Z^C}}{1 + \mathrm{m_{gas}}}, \tag{5.1}$$

where $\mathrm{m_{gas}}$ is the ratio of the gas mass in the galaxy to the gas mass in the cloud. Similarly, the final N/O value can be calculated as

$$\mathrm{N/O} = \frac{(\mathrm{N/O^G} \times \mathrm{m_{gas}} \times \mathrm{z_{gas}}) + \mathrm{N/O^C}}{1 + (\mathrm{m_{gas}} \times \mathrm{z_{gas}})}, \tag{5.2}$$

where $\mathrm{z_{gas}}$ is the ratio of the metallicity in the galaxy to the metallicity in the gas cloud. The additional dependence of the N/O on $\mathrm{z_{gas}}$ is given by the fact that the nitrogen abundance is measured relative to oxygen, rather than hydrogen.

Using Equations 5.1 and 5.2 we can construct basic dilution tracks on the N/O–O/H plane that depend on only three quantities: $\mathrm{m_{gas}}$, $\mathrm{Z^G}$ and $\mathrm{Z^C}$. We construct such models with the aim of identifying which input variables best match the observed dilution vectors at three different stellar mass intervals corresponding to $\log(\mathrm{M_\star/M_\odot}) \in [8.5, 9]$, [9.5, 10] and [10.5, 11], respectively. We choose $\mathrm{Z^G}$ to match the metallicity expected from the MZR within each mass bin, before adopting three different gas cloud metallicities such that $\mathrm{Z^C} = 15\%$, 35% or 55% of $\mathrm{Z^G}$. Finally, we vary $\mathrm{m_{gas}}$ between 1 and 0.01. The resulting models are shown in Figure 5.8. The gas mixing model traces curved lines in the N/O–O/H plane, with a shape that is determined by the metallicity of the gas cloud. Gas clouds with lower metallicities will naturally extend further horizontally. The distance a galaxy moves along one of these dilution lines is determined by the value of $\mathrm{m_{gas}}$, represented as diamonds and annotated with their corresponding values in Figure 5.8. The measured dilution vectors within each mass bin are shown as white arrows. Within each mass bin, the gas mixing model that best matches the direction of the observed dilution vector is one which has a gas cloud metallicity that is 55% of the initial galaxy metallicity. Similarly, the models best-match the magnitude of the observed dilution vector when the gas mass in the galaxy is roughly 10–30% of that gas mass within the diluting cloud.

Comparison to change in gas fraction

We have shown that the direction of the dilution vectors in the N/O–O/H plane can be well approximated by the accretion of metal-rich gas. The magnitude of the dilution vector is also well matched by mixing models wherein the mass of gas within the cloud is 3–10 times larger than that within the galaxy. To test the validity of this prediction, we compare

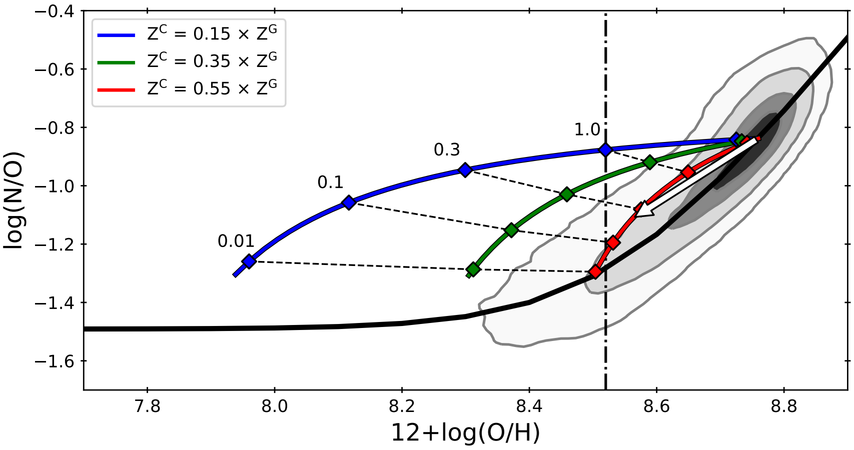

(a) $\log(M_\star/M_\odot) \in [10.5, 11]$

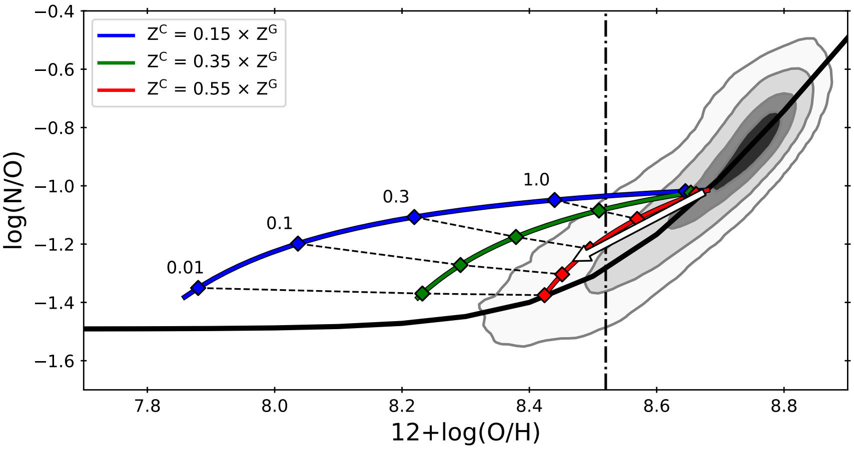

(b) $\log(M_\star/M_\odot) \in [9.5, 10]$

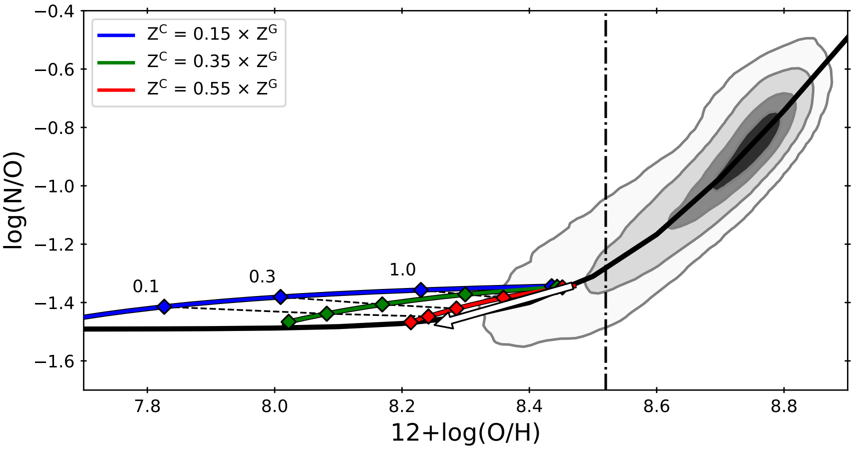

(c) $\log(M_\star/M_\odot) \in [8.5, 9]$

Fig. 5.8 Simple gas mixing model compared to the average dilution vector, shown as a white arrow, for galaxies at a range of different stellar masses. Each coloured line corresponds to a different input Z^C. The diamonds represent the position of the galaxy after the gas mixing has taken place, as determined by m_{gas}, with the black dashed lines connecting points of constant m_{gas} along the different Z^C tracks.

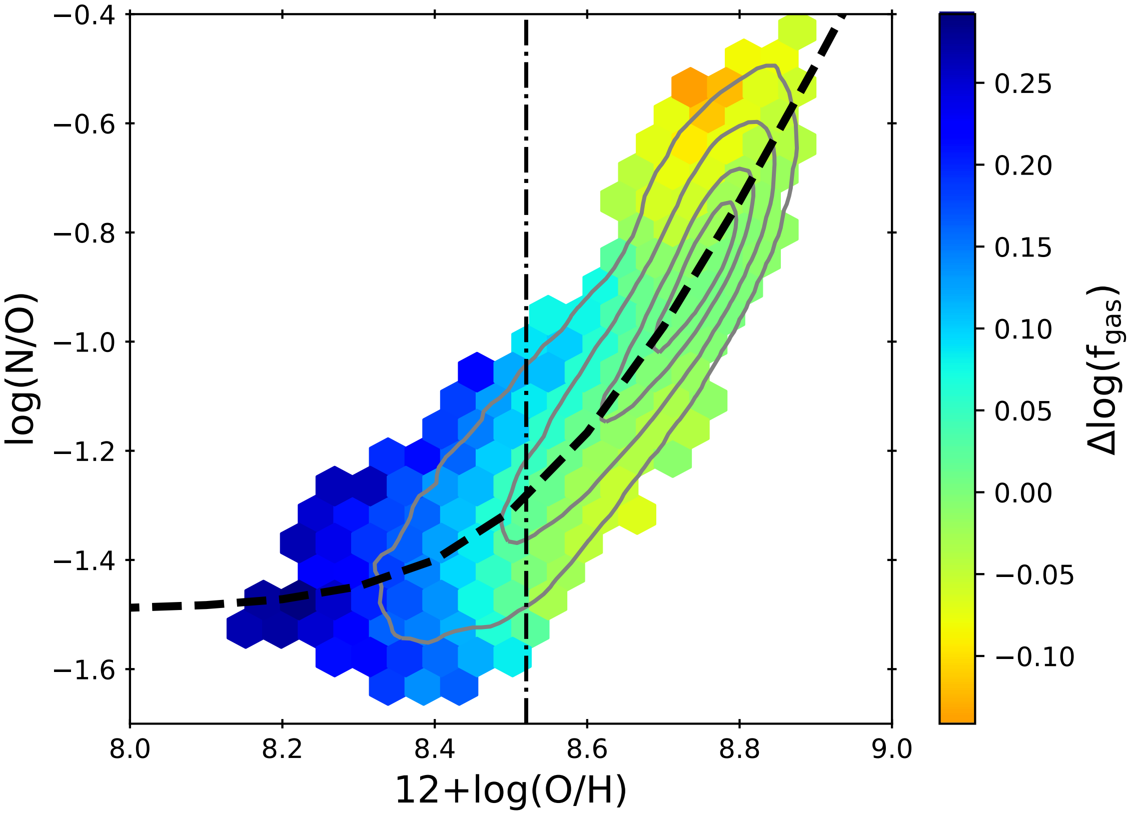

(a) Spatial variation of Δlog(f_{gas})

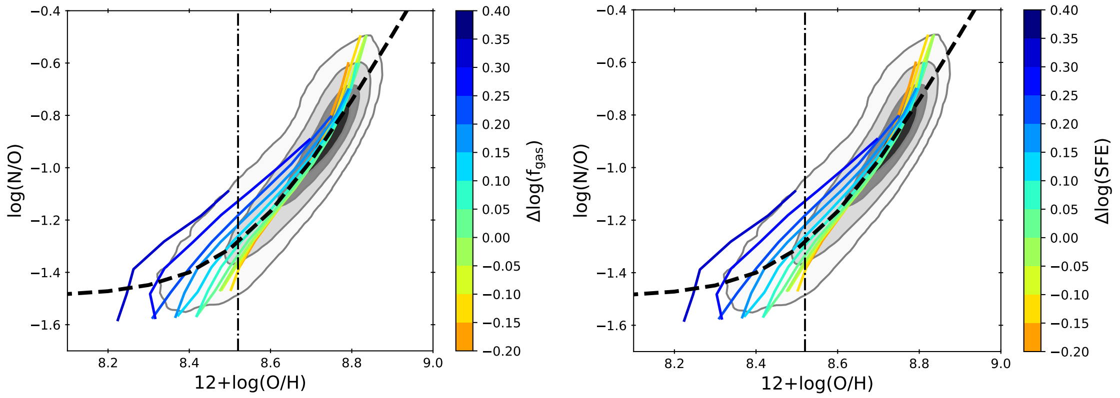

(b) Tracks of constant Δlog(f_{gas}) (c) Tracks of constant Δlog(SFE)

Fig. 5.9 In the top panel, we show the spatial variations of the change in gas fraction (determined via the offset from the local star forming main sequence) for SDSS galaxies, with the median Δlog(f_{gas}) shown for hexagonal bins containing at least 25 objects. In the bottom-left panel, we show tracks of constant Δlog(f_{gas}), split into 0.05 dex wide bins. For each track metallicity values are averaged in 0.1 dex wide bins of log(N/O). Similarly, in the bottom-right panel we show the same distribution converted into an expected change in the star formation efficiency, determined using the scaling relations presented in Piotrowska et al. (2020).

observations of the change in the gas fraction (Δlog($\mathrm{f_{gas}}$), where $\mathrm{f_{gas}}$=$\mathrm{M_{gas}/M_{\star}}$) within the SDSS sample to those expected from the mixing model. The change in gas fraction within each SDSS galaxy was estimated from the deviation from the star forming main sequence, using the correlation between Δlog(SFR)$_{SFMS}$ and Δlog($\mathrm{f_{gas}}$) observed by Piotrowska et al. (2020), wherein galaxies above the star forming main sequence are observed to have higher gas fractions and star formation efficiencies. The spatial variation of Δlog($\mathrm{f_{gas}}$) is presented in Figure 5.9, which naturally follows the distribution of Δlog(SFR)$_{SFMS}$ in Figure 5.4, with galaxies at low metallicities experiencing large increases in their star formation and consequently their gas fraction. In the bottom-left panel, we plot tracks of constant Δlog($\mathrm{f_{gas}}$), within each of which the median metallicity is determined in 0.1 dex wide bins of log(N/O), highlighting that galaxies with the highest N/O values within the low-metallicity regime exhibit the largest increases in gas fraction. Additionally, in the bottom-right panel we plot tracks of Δlog(SFE), again determined using a conversion from Δlog(SFR)$_{SFMS}$ taken from Piotrowska et al. (2020). The tracks are near-identical to those shown for Δlog($\mathrm{f_{gas}}$), which is expected as the results of Piotrowska et al. (2020) show that an increase in star formation relative to the star forming main sequence is strongly correlated to both an increase in gas content and star formation efficiency by an approximately equal amount. The trends with SFE are significant as they suggest that in the low metallicity regime, an increase in N/O corresponds to a relative increase in the star formation efficiency of a galaxy. This is in direct contrast with predictions from chemical evolution models, in which galaxies with lower star formation efficiencies are expected to lie at higher N/O at a fixed O/H due to the delayed production of nitrogen relative to oxygen (Mollá et al., 2006; Vincenzo et al., 2016b).

To facilitate a direct comparison between the mixing models and the observations, we convert the ratio of the gas masses into a change in gas fraction, with the relationship between these two variables defined as Δlog($\mathrm{f_{gas}}$)=log(1+$\mathrm{m_{gas}^{-1}}$). We then re-run the mixing models using a gas cloud metallicity that is 55% of the initial galaxy metallicity in order to match the direction of the observed dilution vectors and varying Δlog($\mathrm{f_{gas}}$) over the range of positive values observed in SDSS, from 0.05 to 0.3 dex. The results are shown in the top panel of Figure 5.10, wherein the coloured lines show tracks of constant Δlog($\mathrm{f_{gas}}$) between the mixing models that begin with galaxies at three different metallicities. It is important to note that by varying the change in gas fraction in the models within the range of observed values, we are unable to reproduce dilution tracks with the same magnitude as the dilution vectors shown in Figure 5.8, for which we would expect changes in the gas fraction as large as Δlog($\mathrm{f_{gas}}$)= 0.64–1 dex. Even so, the Δlog($\mathrm{f_{gas}}$) expected from the models is shown to not match the underlying SDSS observations when the accreting gas cloud has $\mathrm{Z^C} = 0.55 \times \mathrm{Z^G}$. Instead, the underlying SDSS data show changes in gas fraction that are smaller than

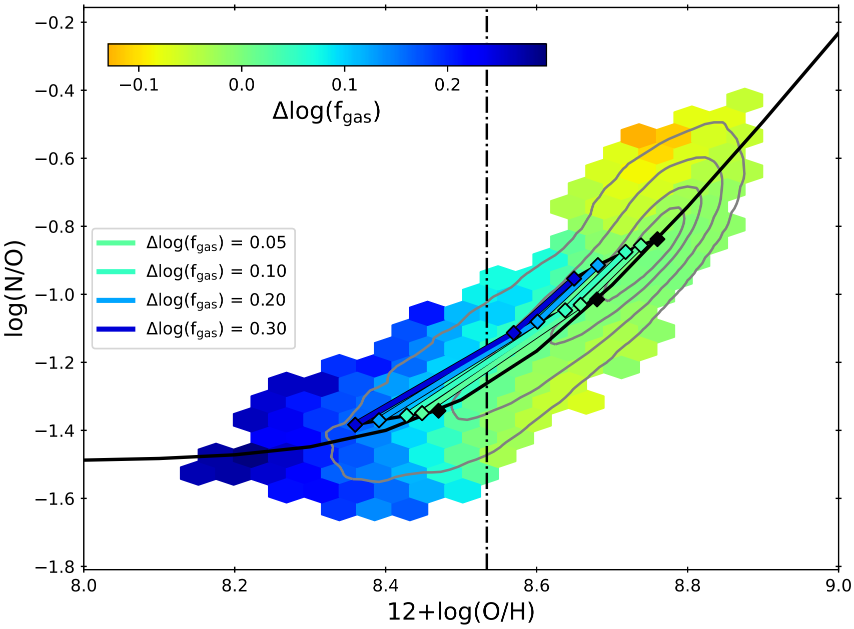

(a) $Z^{C} = 0.55 \times Z^{G}$

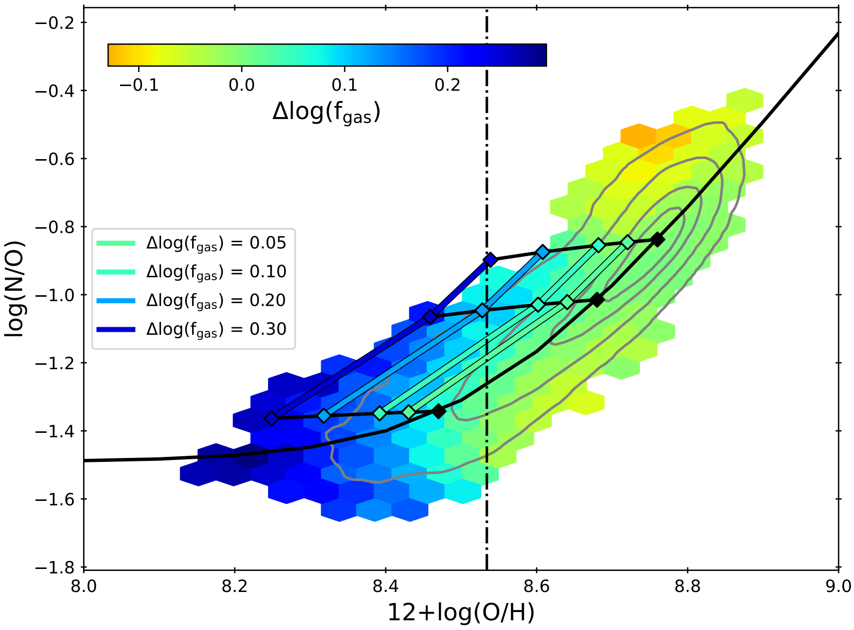

(b) $Z^{C} = 0.2 \times Z^{G}$

Fig. 5.10 Simple gas mixing model comparing the change in gas fraction predicted by the modelled accretion events to those observed within the SDSS data, as determined using the offset from the star forming main sequence utilising the scaling relations from Piotrowska et al. (2020). In the top panel, we show the scenario where the accreting cloud has a metallicity that is 55% of the galaxy metallicity, whilst in the bottom panel we present the modelled dilution tracks when the accreting cloud has a lower metallicity that is 20% of the galaxy metallicity.

those predicted by the model, particularly for the models that have large initial Z^G values. This result shows that although the accretion of metal-rich gas onto a galaxy can explain the direction of the dilution vectors observed within SDSS galaxies, the magnitude of the vector cannot be reconciled with observations, suggesting that dilution from metal-rich gas is not the main driver of scatter in the N/O–O/H plane.

In the bottom panel of Figure 5.10, we show the same tracks of constant $\Delta\log(f_{gas})$ for our mixing model obtained by inputting a lower metallicity for the gas cloud equivalent to $Z^C = 0.2 \times Z^G$. It can clearly be seen that these models better reproduce the underlying trends in $\Delta\log(f_{gas})$ for SDSS galaxies. However, the direction of each of the dilution tracks is approximately horizontal, suggesting minimal change in N/O in contrast to the dilution vectors presented in Figure 5.8. These results suggest that accretion of metal poor gas may better explain the observed scatter in the N/O–O/H plane, however improvements to these models must be made in order to reproduce the observed decrease in N/O. This may be achieved by introducing more complexity into the simple gas mixing models presented here. Following Köppen & Hensler (2005), star formation and subsequent chemical enrichment should be introduced to the models, as the enrichment of the ISM with oxygen on short timescale relative to oxygen may act to reduce the N/O value and bring better agreement between the models and observations. Further processes such as star-formation driven outflows with an SFR-dependent metal loading factor should also be considered.

5.4.3 Summary and conclusions

In this chapter we have presented preliminary work analysing the scatter within the local N/O–O/H plane as defined by SDSS galaxies. In agreement with previous observations of local galaxies Andrews & Martini (2013); Luo et al. (2021), we find evidence of highly star forming, massive galaxies at low metallicities that show enhanced N/O ratios. Following the prescription of Luo et al. (2021), we define these galaxies as having anomalously low metallicities (ALM). We compare the position of these galaxies in the N/O–O/H plane to their expected position, determined via their stellar mass using the mass-metallicity and the N/O–O/H relations. We find that across all stellar masses, ALM galaxies are depleted in both N/O and O/H relative to their expected values. We recover a mild trend where more massive galaxies show a steeper decline in their N/O than those at low metallicities.

In order to investigate whether the dilution in N/O and O/H may be driven by the recent accretion of gas onto a galaxy, we present simple gas mixing models. We find that the direction of the dilution tracks at all stellar masses is consistent with the accretion of metal rich gas with a metallicity equal to 55% of that of the galaxy. Our models also predict that the gas fraction within the galaxy is expected to increase by between 0.64–1 dex. To test whether this is compatible with observations, we determine the change in gas fraction within SDSS galaxies expected from their deviation from the star forming main sequence, as parameterised by Piotrowska et al. (2020). We find that our models are unable to reproduce the observed trends in the SDSS data, with local galaxies exhibiting smaller changes in their gas fraction than those expected from the accretion of gas with metallicity equal to 55% of that of the galaxy. Instead, we find the observed changes in gas fraction are more closely described by the accretion of more metal poor gas, with metallicity equal to 20% of that of the galaxy. However, these models are unable to reproduce the observed decrease in N/O, instead producing dilution tracks that a near-horizontal. We conclude that more detailed modelling is required in order to reconcile observations with predictions. In particular, prescriptions for star formation and subsequent enrichment of the ISM with oxygen on shorter timescale than nitrogen may be able to reproduce the observed decrease in N/O, and should therefore be considered in order to better constrain the impact of dilution events on galaxy N/O and O/H values.

Chapter 6

Conclusions

6.1 Summary

Chemical abundances provide a useful probe of the evolutionary stages of galaxies and can provide insight into the different physical processes that drive galaxy evolution. The advent of several surveys utilising near-infrared integral field spectroscopy has enabled large samples of galaxies to be assembled locally and at high-redshift on spatially resolved scales. In particular, observations at $z \sim 2$ have enabled the chemical abundances of galaxies during the peak of cosmic star formation to be determined, allowing the evolution of chemical abundances across comic time to be investigated.

In this thesis, we have presented an analysis of the N/O ratios observed in high-redshift galaxies on both galaxy-integrated and spatially resolved scales using data from the KLEVER survey. We compared our observations with those in local galaxies in order to place constraints on the chemical evolution of galaxies across cosmic time, interpreting these results in the context of the different physical processes that may drive galaxy evolution. The analyses and key results are outlined below.

How do scaling relations involving N/O abundances evolve across cosmic time?

In Chapter 3 we analyse the galaxy-integrated scaling relations between the N/O abundance and various galactic properties including metallicity, stellar mass and star formation rate. We leverage the statistical power of the SDSS Survey to analyse these trends for a sample of over 100,000 star forming galaxies in the local Universe. In addition, from the KLEVER survey we draw 37 star forming galaxies at $z \sim 2$ for which we simultaneously detect several rest-frame optical emission lines from [O II]$\lambda\lambda$3727,29 up to [S II]$\lambda\lambda$6716,32, enabling us to independently estimate both the gas-phase metallicity and N/O abundances by way of locally calibrated strong-line diagnostics.

We recover a bimodal relationship between N/O and O/H for SDSS galaxies, with N/O increasing strongly with O/H at high metallicity, whilst remaining relatively constant at low metallicity. This is consistent with our understanding of the two dominant nucleosynthetic production mechanisms for nitrogen. At low metallicities, nitrogen is a primary product formed freshly within stars from hydrogen and helium, meaning N/O has no strong dependence on O/H. At higher metallicities, nitrogen becomes a secondary nucleosynthetic product and is formed at the expense of oxygen that was present within a star at its birth, causing N/O to increase with O/H. We find that KLEVER galaxies tend to be scattered about the 'transition' metallicity between the primary and secondary nitrogen regimes, exhibiting a mild increase in log(N/O) of 0.1 dex relative to SDSS galaxies when compared at a fixed metallicity. This suggests that there is no strong evolution in the relationship between N/O and O/H from $z \sim 2$ to the present day.

We observe a more notable difference between local and high-redshift galaxies when we investigate the relationship between N/O and stellar mass. Within the SDSS sample, galaxies with larger stellar masses are characterised by higher N/O ratios. The same trend is observed in the KLEVER sample, however the normalisation of this relationship is much lower at $z \sim 2$ than that observed locally. KLEVER galaxies are observed to have N/O abundances that are lower than local galaxies by an average of 0.35 dex when compared at a fixed stellar mass, indicating a strong evolution in the relationship between stellar mass and N/O. This evolution is primarily driven by the well-studied evolution of the mass-metallicity relation, with KLEVER galaxies having lower metallicities than SDSS galaxies when compared at a fixed stellar mass, and hence lower N/O values. Extending beyond two-dimensional trends, we investigate whether KLEVER galaxies lie on the plane of the fundamental metallicity relation (FMR) that defines the three-dimensional relationship between stellar mass, metallicity and star formation rate. We find that KLEVER galaxies show good agreement with local calibrations of the FMR as parameterised by Curti et al. (2020a), exhibiting a mild offset of just 0.1 dex. This offset is negligible when considering several sources of errors in its estimation, including the use of locally-calibrated diagnostics to determine chemical abundances in high-redshift galaxies and the extrapolation of the local FMR to the high stellar mass, high star formation rate region occupied by KLEVER galaxies. The lack of a strong offset from the FMR suggests that the locally observed equilibrium between gas-phase processes that govern the evolution of galaxies is still in place at $z \sim 2$.

Adopting the methodology used to construct the FMR, we investigate the variation of star formation rate in the local relationship between stellar mass and N/O. We find a strong secondary dependence on SFR, wherein galaxies with higher star formation rates have lower N/O values at a fixed stellar mass. This result is at odds with previous work that established only a mild trend with SFR existed in the stellar mass–N/O plane Pérez-Montero et al. (2013). We determine that this discrepancy is driven by our use of the N2O2 diagnostic to determine the N/O ratio, as opposed to the N2S2 diagnostic that has been adopted by previous authors. These two diagnostics show good agreement to first order, however we find a secondary dependence on SFR exists that causes N2S2 to increase with SFR at a fixed N2O2. The exact cause of this secondary dependence is unclear, however we suggest it may be driven by changes to the ionisation structure within galaxies, triggered by star formation, causing [S II]$\lambda\lambda$6716,32 to decrease relative to [O II]$\lambda\lambda$3727,29. We use partial correlation coefficients to show that N/O has roughly the same dependence on SFR as is observed for O/H. This finding suggests that the FMR must be driven by processes that are not only sensitive to O/H, such as dilution from pristine gas, but also processes that are sensitive to N/O such as metal-rich inflows or variations in star formation efficiency. Continuing the analogy to the FMR, we use our local SDSS sample to construct a three dimensional plane between stellar mass, star formation rate and N/O, which we name the fundamental nitrogen relation (FNR). To test whether this relationship is indeed fundamental we compare to our KLEVER sample, finding the median offset from the expected N/O is just 0.08 dex. This suggests that processes sensitive to the timescales of the chemical enrichment of the ISM in galaxies, probed by N/O, evolve smoothly from $z{\sim}2$ to $z{\sim}0$. Furthermore, we find that the measured FNR is near-identical to a model FNR constructed using a combination of the fundamental metallicity relation and a redshift-invariant N/O-O/H relation, suggesting the FNR is a by-product of these relations.

Finally, we observe that the relationship between N/O and stellar mass observed for KLEVER galaxies is similar to that observed in low-metallicity local galaxies, which may have variable contributions to the N/O abundance from nitrogen production within low- and intermediate-mass stars. We compare to chemical evolution models from Vincenzo et al. (2016b) to show that the location of KLEVER galaxies on the N/O–stellar mass plane is consistent with young ages and high star formation efficiencies, allowing them to attain high stellar masses in a short time before the enhancement due to the secondary nitrogen production becomes dominant.

How does the spatial distribution of N/O abundances within galaxies evolve across cosmic time?

In Chapter 4 we draw upon spatially resolved observations of galaxies from the MaNGA and KLEVER surveys to investigate the gradients in N/O across star forming galaxies at different cosmic times. This chapter presents some of the first ever measurements of N/O gradients observed at $z \sim 2$, as derived from the locally-calibrated strong line diagnostics N2O2 and N2S2. The main finding of our work is that galaxies at $z \sim 2$ generally have gradients in N/O that are flatter than those observed in local galaxies, when compared at a fixed stellar mass. This is contrary to inside-out growth models, which predict steeper N/O gradients at earlier cosmic times. However, inside-out growth models may be able to reconcile this difference by invoking radial mixing of gas or enhanced feedback mechanisms that act to effectively mix the metals within the ISM at $z \sim 2$, producing flatter gradients.

N/O gradients derived using N2O2 are generally positive within the KLEVER sample, suggesting that central regions are depleted in N/O relative to the galactic outskirts. We suggest that positive N/O gradients may be expected as a consequence of the positive metallicity gradients that have been observed at $z \sim 3$. In this scenario, accretion of metal poor gas onto the central regions of galaxies at high redshift initially dilutes the O/H whilst leaving the N/O unaffected. The freshly accreted gas triggers star formation which rapidly enriches the ISM with oxygen from core-collapse supernovae. If nitrogen production is dominated by low- and intermediate-mass stars, the enrichment of the ISM with nitrogen will be delayed relative to oxygen on the order of $\sim$100 Myr. This will cause the N/O ratio in the central regions of the galaxy to decrease, hence causing positive N/O gradients. At later times, further generations of LIMS could then re-enrich the central regions with nitrogen. Further modelling and observations of gradients in high-redshift galaxies are needed to properly constrain this scenario.

We identify that positive N2O2 gradients are strongly correlated to the existence of negative gradients in the Balmer decrement. When a galaxy has a negative Balmer decrement gradient any extinction correction determined from the Balmer decrement values will be larger in the centre of the galaxy than near the outskirts. Since bluer emission lines are more strongly impacted by any extinction correction than redder ones, a large correction will lead to large values of [O II]$\lambda\lambda$3727,29 relative to [N II]λ6584, causing a decrease in the central N2O2 values relative to the outskirts, and hence resulting in a positive N/O decrement. We show that negative Balmer decrement gradients within the KLEVER sample are also correlated with more negative stellar mass surface density gradients and more negative star formation rate gradients. We also observe a mild correlation with more negative sSFR gradients, however a p-value of 0.07 means we cannot rule out the null hypothesis of no correlation, and further work with larger sample sizes is required to verify this relationship. When taken in combination, these results suggest that galaxies with higher concentrations of stellar mass and star formation towards their centres also have more centrally concentrated dust distributions, consistent with the findings of Nelson et al. (2016) for galaxies at $z \sim 1.4$. This may suggest that the central regions of massive galaxies at $z \sim 2$ may be undergoing in-situ bulge formation.

We find discrepancies in the gradients measured using N2S2 relative to those measured using N2O2 within our KLEVER sample. N2S2-derived gradients are generally observed to be flat, in good agreement with the observation of flat gradients in O/H. Taken alone, this result could suggest that both oxygen and nitrogen have the same nucleosynthetic origin at $z \sim 2$, i.e that both are produced via primary processes within massive stars and released into the ISM following their death as core-collapse supernovae. However, we note that large uncertainties persist regarding the extent to which primary nitrogen production is dominated by massive stars relative to low- and intermediate-mass stars (LIMS). Indeed, contributions from LIMS are expected to be significant in galaxies at $z \sim 2$, and we are therefore unable to rigorously constrain the stellar origin of primary nitrogen from our observations.

Finally, as with the discrepancy between N2O2 and N2S2 observed in Chapter 3, we suggest that the difference between N2O2-derived and N2S2-derived N/O gradients may be a consequence of the strong central concentration of star formation in high-z galaxies, causing the spectra extracted from central regions to be dominated by emission from the central zones of H II regions which typically have low fractions of S^+ relative to N^+ and O^+. This could cause N2S2 to overestimate the N/O value in the central parts of the galaxy, causing any positive abundance gradients to appear flat. However, the low spatial resolution of the KLEVER data, coupled the low S/N of the Hβ line, means that the determination of the Balmer decrement gradients within our high-z sample is subject to large uncertainties. As such, the application of a resolved attenuation correction in order derive line ratios such as N2O2 means the resulting N2O2 gradients are highly uncertain, and future work with better spatial resolution and sensitivity should be undertaken to better constrain the existence of a discrepancy between N2O2 and N2S2 gradients.

Can we find evidence for gas dilution in SDSS galaxies?

Gas flows into galaxies are understood to play an important role in the evolution of galaxies across cosmic time, diluting the metallicity within galaxies and providing fuel for subsequent star formation. Many works in literature have suggested that accretion of pristine gas will act to dilute the O/H ratio whilst having no impact on the N/O ratio, causing a scatter in the N/O–O/H relation observed in local galaxies (Pérez-Montero et al., 2013; Andrews &

Martini, 2013). However, as highlighted in Chapters 3 and 4, physical processes that impact the O/H within a galaxy are also expected to have an impact of the N/O ratio. A more detailed understanding of how gas inflows impact the O/H and N/O ratios respectively is therefore required. Within Chapter 5, we investigate the scatter in the local N/O–O/H relation, before comparing to gas mixing models in order to study how accretion of gas may impact N/O and O/H.

We use a sample of SDSS galaxies to study the secondary trends of parameters such as star formation rate and stellar mass in the local N/O–O/H plane to identify the properties of galaxies which are most offset from the average relation. We find that, at low metallicities galaxies that show an enhancement in N/O tend to be more massive and more star-forming. Furthermore, these galaxies are also shown to have much lower metallicities than expected from the local MZR given their stellar mass, which we then define as anomalously low metallicity (ALM galaxies). We measure the strength of the offset from the expected positions of ALM galaxies in both O/H and N/O for a range of stellar masses, finding that in addition to lower O/H values ALM galaxies also show lower N/O values across all stellar mass ranges. The dilution of the N/O is most pronounced in the high mass galaxies, with a weaker dilution in N/O observed at lower masses.

We investigate whether the observed dilution in O/H and N/O can be reproduced by recent accretion events by comparing our observations to simple gas mixing models. We are able to reproduce the observed direction of the dilution at all stellar masses by invoking mixing between a galaxy and a metal-rich gas cloud with a metallicity equal to 55% of that of the galaxy. This could suggest that re-accretion of metal-rich gas that was previously expelled from the galaxy into the CGM could drive the observed scatter in the N/O–O/H plane. However, our models also predict that the gas fraction within the galaxy is expected to increase by between 0.64–1 dex. We compare this to observations of the change in gas fraction that is expected in SDSS galaxies given their offset from the local star forming main sequence, following the relationship defined in Piotrowska et al. (2020). We find our models of metal-rich accretion are unable to reproduce the observed trends, with the models over-predicting the change in gas fraction relative to what is observed within SDSS. If we instead invoke a more metal-poor gas cloud, with metallicity equal to 20% of that of the galaxy, we find better agreement between the change in gas fraction predicted by the model and those observed within the data, however we are unable to reproduce the observed dilution in N/O, with mixing tracks instead being horizontal in the N/O–O/H plane.

We conclude that further modelling beyond our simple gas mixing approximation must be pursued in order to better explain the observed scatter in the N/O–O/H plane. In particular, gas accretion events are associated with an increase in star formation, that will lead to enrichment of the ISM with new metals. Therefore, future models should build on the work presented within this chapter by including prescriptions for star formation and subsequent enrichment of the ISM, as well as star-formation driven outflows with an SFR-dependent metal loading factor. Indeed, if the ISM is enriched with oxygen on shorter timescales than nitrogen, as expected from the former being produced mostly in massive stars and the latter mostly in low- and intermediate- mass stars, then accretion events may cause a decrease in the N/O ratio which would bring better agreement between the metal-poor gas accretion scenario and observations.

6.2 Outlook: a clearer picture of the high redshift Universe

This thesis has made extensive use of data from the KLEVER survey to investigate chemical abundances in galaxies at $z \sim 2$, with our results leaning heavily on the observations of un-lensed galaxies. However, a significant fraction of the KLEVER survey is made up of lensed galaxies. Full lens modelling a de-projection for these galaxies is required in order to enable spatially resolved investigations of the chemical abundances within lensed galaxies to take place. The magnification of lensed galaxies grants better spatial resolution than obtain for the un-lensed KLEVER galaxies. As such, the addition of lensed galaxies to future spatially resolved analysis will help to further constrain observations of chemical abundance gradients at high redshift. The spatially resolved KLEVER data for the full sample can also be used to investigate whether scaling relations that are observed on a galaxy-integrated basis, such as the FMR, are also observed on local scales at high redshift. Future analysis can then investigate the resolved-FMR within KLEVER galaxies, as well as the resolved-FNR, which was recently shown to exist within local galaxies (Schaefer et al., 2022).

Moving beyond KLEVER, the natural extension of much of the work presented within this thesis is to build upon the observations of the chemical properties of galaxies at $z \sim 2$ using the next generation of telescopes. In the near future, the number of galaxies observed at high redshifts will be vastly increased by instruments such as the Multi-Object Optical and Near-infrared Spectrograph (MOONS) on the Very Large Telescope in Chile, which will deliver high-resolution spectroscopic measurements for $\sim 10^5$ galaxies between $z = 1$ and $z = 3$. Such observations will allow a thorough comparisons to be made between scaling relations that are observed in local galaxies and those which are found to exist at higher redshifts. In particular, observations from MOONS will be able to better constrain whether relations such as the FMR and the FNR, as parameterised within this thesis, are truly fundamental, providing key constraints on galaxy evolution. Moreover, MOONS will enable direct T_e-based calibrations of chemical abundance diagnostics within high-redshift galaxy samples, removing the reliance on locally-calibrated diagnostics. Indeed, analysis from the Early Release Observations programme of the James Webb Space Telescope (JWST) have offered a tantalising glimpse of how high-redshift T_e-based calibrations can be used to investigate the evolution of the fundamental metallicity relation out to redshifts as far as $z \sim 8$ (Curti et al., 2022).

Our understanding of the spatially resolved properties of high redshift galaxies will also be completely revolutionised by NIRSPEC on JWST. The unprecedented sensitivity of this instrument will allow both O/H and N/O gradients to be accurately measured at $z > 3$ and up to $z \sim 6$ with excellent spatial resolution. The KLEVER gradient measurements at $z \sim 2$ provided within this thesis therefore provide a valuable benchmark against which future observations can be compared. For example, the larger sample sizes and increased sensitivities provided by NIRSPEC will enable studies to confirm whether N/O gradients are flatter than those observed locally, as expected from the work in this thesis. Furthermore, work can be undertaken to investigate whether the observed discrepancy between N2O2- and N2S2- derived N/O gradients exists in galaxy samples beyond that presented in Chapter 4. Observations of N2O2 gradients beyond $z \sim 2.5$ will provide the first measurements of N/O gradients beyond our KLEVER observations, enabling direct comparisons to be made to the inverted metallicity gradients observed at $z \sim 3$ (Cresci et al., 2010; Troncoso et al., 2014). Such observations will contribute to providing a more comprehensive view of how N/O gradients evolve across cosmic time, which will in turn enable constraints to be placed on the feasibility of the proposed scenarios such as the ‘N/O pendulum effect’ outlined in Chapter 4 as an explanation of the inverted N/O gradients at $z \sim 2$. Similarly, observations will be able to further constrain whether or not negative Balmer decrement gradients are common in massive galaxies at high-redshift, shedding light on how accretion of gas onto the central regions of galaxies may drive the formation of highly star forming, dusty galactic cores.

Finally, improvements in the modelling of N/O ratios in galaxies is a promising area of future work. Current literature is largely devoid of predictions of the cosmic evolution of the N/O gradient, with those that do exist unable to reproduce the current observations at $z \sim 2$ (Vincenzo & Kobayashi, 2018). The application of many existing inside-out growth models that invoke radial gas mixing or enhanced feedback mechanisms to explain flatter metallicity gradients at high redshift should be extended to the N/O ratio in order to ensure consistency between the predictions made for these two chemical abundances. Particular focus should be placed on modelling whether the N/O ratios of observed in high-redshift galaxies are more compatible with primary nitrogen production dominated by massive stars or with production dominated by low- and intermediate-mass stars. The stellar source of nitrogen has a direct impact on the time delay expected in the enrichment of nitrogen relative to oxygen, and is therefore vital for interpretations of N/O values at high redshifts where primary production mechanisms are expected to be dominant. Such models can then be used to ascertain whether inverted N/O gradients at high redshift should be expected as a consequence of inverted metallicity gradients, following the ‘N/O pendulum effect’ presented in Chapter 4. Similarly, improved models can be used to constrain whether high N/O values at low metallicities within the SDSS sample are compatible with gas accretion events, shedding light on the properties of this accreted gas and providing insight into the properties of gas flows that may drive the evolution of galaxies.

Finally, attempts should be made to reconcile the differences in N/O abundances determined by N2S2 relative to N2O2. Ideally, multi-zone models constructed from multiple H II regions with varying physical properties should be constructed in order to assess the impact that enhanced star formation may have on [S II]$\lambda\lambda$6716,32 fluxes relative to [O II]$\lambda\lambda$3727,29 and [N II]λ6584 fluxes when extracted from a given aperture. This work should be undertaken in the context of local galaxies, where the properties of H II regions are well understood and ionisation structures of these regions can be readily modelled. An extension of similar analysis to higher redshifts may prove difficult given the evolving conditions of H II regions, with few existing models that can predict the ionisation structure expected from harder ionising spectra driven by young, α-enhanced stars, as observed at earlier times in the Universe.

References

Abazajian K. N., et al., 2009, ApJS, 182, 543

Andrews B. H., Martini P., 2013, ApJ, 765, 140

Baldwin J. A., Phillips M. M., Terlevich R., 1981, PASP, 93, 5

Balestra I., et al., 2016, ApJS, 224, 33

Belfiore F., et al., 2015, MNRAS, 449, 867

Belfiore F., et al., 2017, MNRAS, 469, 151

Bennett J. S., Sijacki D., 2020, MNRAS, 499, 597

Berg D. A., Skillman E. D., Garnett D. R., Croxall K. V., Marble A. R., Smith J. D., Gordon K., Kennicutt Robert C. J., 2013, ApJ, 775, 128

Berg D. A., Skillman E. D., Croxall K. V., Pogge R. W., Moustakas J., Johnson-Groh M., 2015, ApJ, 806, 16

Berg D. A., Pogge R. W., Skillman E. D., Croxall K. V., Moustakas J., Rogers N. S. J., Sun J., 2020, ApJ, 893, 96

Bertin E., Arnouts S., 1996, A&AS, 117, 393

Bian F., Kewley L. J., Dopita M. A., 2018, ApJ, 859, 175

Bigiel F., Leroy A., Walter F., Brinks E., de Blok W. J. G., Madore B., Thornley M. D., 2008, AJ, 136, 2846

Blitz L., Rosolowsky E., 2006, ApJ, 650, 933

Bluck A. F. L., Maiolino R., Sánchez S. F., Ellison S. L., Thorp M. D., Piotrowska J. M., Teimoorinia H., Bundy K. A., 2020, MNRAS, 492, 96

Boissier S., Boselli A., Buat V., Donas J., Milliard B., 2004, A&A, 424, 465

Bothwell M. S., Maiolino R., Kennicutt R., Cresci G., Mannucci F., Marconi A., Cicone C., 2013, MNRAS, 433, 1425

Bothwell M. S., Maiolino R., Peng Y., Cicone C., Griffith H., Wagg J., 2016a, MNRAS, 455, 1156

Bothwell M. S., Maiolino R., Cicone C., Peng Y., Wagg J., 2016b, A&A, 595, A48

Bradač M., et al., 2019, MNRAS, 489, 99

Brammer G. B., et al., 2012, ApJS, 200, 13

Bresolin F., 2011, ApJ, 729, 56

Brinchmann J., Charlot S., White S. D. M., Tremonti C., Kauffmann G., Heckman T., Brinkmann J., 2004, MNRAS, 351, 1151

Brinchmann J., Kunth D., Durret F., 2008, A&A, 485, 657

Bruzual G., Charlot S., 2003, MNRAS, 344, 1000

Bundy K., et al., 2015, ApJ, 798, 7

Burbidge E. M., Burbidge G. R., Fowler W. A., Hoyle F., 1957, Reviews of Modern Physics, 29, 547

Calzetti D., Armus L., Bohlin R. C., Kinney A. L., Koornneef J., Storchi-Bergmann T., 2000, ApJ, 533, 682

Caminha G. B., et al., 2017, A&A, 600, A90

Cappellari M., Copin Y., 2003, MNRAS, 342, 345

Cardelli J. A., Clayton G. C., Mathis J. S., 1989, ApJ, 345, 245

Castellano M., et al., 2016, A&A, 590, A31

Chabrier G., 2003, PASP, 115, 763

Charlot S., Fall S. M., 2000, ApJ, 539, 718

Charlot S., Longhetti M., 2001, MNRAS, 323, 887

Chiappini C., Matteucci F., Ballero S. K., 2005, A&A, 437, 429

Chiappini C., Hirschi R., Meynet G., Ekström S., Maeder A., Matteucci F., 2006, A&A, 449, L27

Cicone C., et al., 2014, A&A, 562, A21

Cirasuolo M., et al., 2020, The Messenger, 180, 10

Concas A., et al., 2022, MNRAS, 513, 2535

Cosens M., et al., 2018, ApJ, 869, 11

Cresci G., Mannucci F., Maiolino R., Marconi A., Gnerucci A., Magrini L., 2010, Nature, 467, 811

Cresci G., Mannucci F., Curti M., 2019, A&A, 627, A42

Croom S. M., et al., 2012, MNRAS, 421, 872

Cullen F., Cirasuolo M., McLure R. J., Dunlop J. S., Bowler R. A. A., 2014, MNRAS, 440, 2300

Cullen F., et al., 2021, MNRAS, 505, 903

Curti M., Cresci G., Mannucci F., Marconi A., Maiolino R., Esposito S., 2017, MNRAS, 465, 1384

Curti M., Mannucci F., Cresci G., Maiolino R., 2020a, MNRAS, 491, 944

Curti M., et al., 2020b, MNRAS, 492, 821

Curti M., et al., 2022, arXiv e-prints, p. arXiv:2207.12375

Da Cunha E., et al., 2015, ApJ, 806, 110

Davé R., Finlator K., Oppenheimer B. D., 2011, MNRAS, 416, 1354

Davies R. I., 2007, MNRAS, 375, 1099

Dekel A., Zolotov A., Tweed D., Cacciato M., Ceverino D., Primack J. R., 2013, MNRAS, 435, 999

Di Criscienzo M., et al., 2017, A&A, 607, A30

Dopita M. A., Kewley L. J., Sutherland R. S., Nicholls D. C., 2016, Ap&SS, 361, 61

Einstein A., 1916, Annalen der Physik, 354, 769

Eisenhauer F., et al., 2003, in Iye M., Moorwood A. F. M., eds, Society of Photo-Optical Instrumentation Engineers (SPIE) Conference Series Vol. 4841, Instrument Design and Performance for Optical/Infrared Ground-based Telescopes. pp 1548–1561 (`arXiv:astro-ph/0306191`), doi:10.1117/12.459468

Elmegreen B. G., Klessen R. S., Wilson C. D., 2008, ApJ, 681, 365

Erb D. K., Shapley A. E., Pettini M., Steidel C. C., Reddy N. A., Adelberger K. L., 2006, ApJ, 644, 813

Esteban C., García-Rojas J., 2018, MNRAS, 478, 2315

Esteban C., Bresolin F., Peimbert M., García-Rojas J., Peimbert A., Mesa-Delgado A., 2009, ApJ, 700, 654

Fabian A. C., 2012, ARA&A, 50, 455

Ferland G. J., et al., 2013, Rev. Mex. Astron. Astrofis., 49, 137

Florido E., Zurita A., Pérez-Montero E., 2022, MNRAS, 513, 2006

Fluetsch A., et al., 2019, MNRAS, 483, 4586

Förster Schreiber N. M., et al., 2018, ApJS, 238, 21

Freudling W., Romaniello M., Bramich D. M., Ballester P., Forchi V., García-Dabló C. E., Moehler S., Neeser M. J., 2013, A&A, 559, A96

Garnett D. R., 1990, ApJ, 363, 142

Gibson B. K., Pilkington K., Brook C. B., Stinson G. S., Bailin J., 2013, A&A, 554, A47

Girard, M. et al., 2018, A&A, 613, A72

Grillo C., et al., 2016, ApJ, 822, 78

Grogin N. A., et al., 2011, ApJS, 197, 35

Harrison C. M., et al., 2016, MNRAS, 456, 1195

Hayden-Pawson C., et al., 2022, MNRAS, 512, 2867

Henry R. B. C., Worthey G., 1999, PASP, 111, 919

Henry R. B. C., Edmunds M. G., Köppen J., 2000, ApJ, 541, 660

Jauzac M., et al., 2016, MNRAS, 457, 2029

Jeans J. H., 1902, Philosophical Transactions of the Royal Society of London Series A, 199, 1

Kaasinen M., Kewley L., Bian F., Groves B., Kashino D., Silverman J., Kartaltepe J., 2018, MNRAS, 477, 5568

Kashino D., Renzini A., Silverman J. D., Daddi E., 2016, ApJ, 823, L24

Kashino D., et al., 2017, ApJ, 835, 88

Kauffmann G., et al., 2003a, MNRAS, 341, 33

Kauffmann G., et al., 2003b, MNRAS, 346, 1055

Kausch, W. et al., 2015, A&A, 576, A78

Kennicutt Robert C. J., 1998, ApJ, 498, 541

Kennicutt R. C., Evans N. J., 2012, ARA&A, 50, 531

Kewley L. J., Jansen R. A., Geller M. J., 2005, PASP, 117, 227

Kewley L. J., Maier C., Yabe K., Ohta K., Akiyama M., Dopita M. A., Yuan T., 2013, ApJ, 774, L10

Kewley L. J., Zahid H. J., Geller M. J., Dopita M. A., Hwang H. S., Fabricant D., 2015, ApJ, 812, L20

Kobayashi C., Springel V., White S. D. M., 2007, MNRAS, 376, 1465

Kobayashi C., Karakas A. I., Lugaro M., 2020, ApJ, 900, 179

Kocevski D. D., et al., 2018, ApJS, 236, 48

Koekemoer A. M., et al., 2011, ApJS, 197, 36

Köppen J., Hensler G., 2005, A&A, 434, 531

Köppen J., Weidner C., Kroupa P., 2007, MNRAS, 375, 673

Kriek M., van Dokkum P. G., Labbé I., Franx M., Illingworth G. D., Marchesini D., Quadri R. F., 2009, ApJ, 700, 221

Kroupa P., 2001, MNRAS, 322, 231

Kroupa P., Tout C. A., Gilmore G., 1993, MNRAS, 262, 545

Lang P., et al., 2014, ApJ, 788, 11

Leroy A. K., Walter F., Brinks E., Bigiel F., de Blok W. J. G., Madore B., Thornley M. D., 2008, AJ, 136, 2782

Levesque E. M., Kewley L. J., Larson K. L., 2010, AJ, 139, 712

Li H., Wuyts S., Lei H., Lin L., Lam M. I., Boquien M., Andrews B. H., Schneider D. P., 2019, The Astrophysical Journal, 872, 63

Liu X., Shapley A. E., Coil A. L., Brinchmann J., Ma C.-P., 2008, ApJ, 678, 758

Lotz J. M., et al., 2017, ApJ, 837, 97

Luo B., et al., 2017, ApJS, 228, 2

Luo Y., et al., 2021, ApJ, 908, 183

Luridiana V., Morisset C., Shaw R. A., 2015, A&A, 573, A42

Madau P., Dickinson M., 2014, Annual Review of Astronomy and Astrophysics, 52, 415

Magrini L., et al., 2018, A&A, 618, A102

Maiolino R., Mannucci F., 2019, A&ARv, 27, 3

Maiolino R., et al., 2008, A&A, 488, 463

Maiolino R., et al., 2020, The Messenger, 180, 24

Mannucci F., et al., 2009, MNRAS, 398, 1915

Mannucci F., Cresci G., Maiolino R., Marconi A., Gnerucci A., 2010, MNRAS, 408, 2115

Mannucci F., et al., 2021, MNRAS, 508, 1582

Marchesi S., et al., 2016, ApJ, 830, 100

Mason C. A., et al., 2017, ApJ, 838, 14

Masters D., et al., 2014, ApJ, 785, 153

Masters D., Faisst A., Capak P., 2016, ApJ, 828, 18

Matteucci F., 1986, MNRAS, 221, 911

Matteucci F., 2012, Chemical Evolution of Galaxies. Springer Berlin, Heidelberg, doi:10.1007/978-3-642-22491-1

McGaugh S. S., 1991, ApJ, 380, 140

Meneghetti M., et al., 2017, Monthly Notices of the Royal Astronomical Society, 472, 3177–3216

Meynet G., Maeder A., 2002, A&A, 390, 561

Mollá M., Vílchez J. M., Gavilán M., Díaz A. I., 2006, MNRAS, 372, 1069

Mott A., Spitoni E., Matteucci F., 2013, MNRAS, 435, 2918

Moustakas J., Kennicutt Robert C. J., Tremonti C. A., Dale D. A., Smith J.-D. T., Calzetti D., 2010, ApJS, 190, 233

Nagao T., Maiolino R., Marconi A., 2006, A&A, 459, 85

Nelson E. J., et al., 2016, ApJ, 817, L9

Newman S. F., et al., 2014, ApJ, 781, 21

Newville M., Stensitzki T., Allen D. B., Rawlik M., Ingargiola A., Nelson A., 2016, Lmfit: Non-Linear Least-Square Minimization and Curve-Fitting for Python (ascl:1606.014)

Noeske K. G., et al., 2007, ApJ, 660, L43

Nomoto K., Kobayashi C., Tominaga N., 2013, ARA&A, 51, 457

Oey M. S., Kennicutt R. C. J., 1993, ApJ, 411, 137

Osterbrock D. E., Ferland G. J., 2006, Astrophysics of gaseous nebulae and active galactic nuclei. University Science Books

Pagel B. E. J., Edmunds M. G., Blackwell D. E., Chun M. S., Smith G., 1979, MNRAS, 189, 95

Pagel B. E. J., Terlevich R. J., Melnick J., 1986, PASP, 98, 1005

Peng C. Y., Ho L. C., Impey C. D., Rix H.-W., 2010, AJ, 139, 2097

Pérez-Montero E., 2017, PASP, 129, 043001

Pérez-Montero E., Contini T., 2009, MNRAS, 398, 949

Pérez-Montero E., et al., 2013, A&A, 549, A25

Pérez-Montero E., et al., 2016, A&A, 595, A62

Pettini M., Pagel B. E. J., 2004, MNRAS, 348, L59

Pettini M., Ellison S. L., Bergeron J., Petitjean P., 2002, A&A, 391, 21

Pettini M., Zych B. J., Steidel C. C., Chaffee F. H., 2008, MNRAS, 385, 2011

Pichon C., Pogosyan D., Kimm T., Slyz A., Devriendt J., Dubois Y., 2011, MNRAS, 418, 2493

Pilyugin L. S., Mattsson L., Vílchez J. M., Cedrés B., 2009, MNRAS, 398, 485

Pilyugin L. S., Grebel E. K., Mattsson L., 2012, MNRAS, 424, 2316

Piotrowska J. M., Bluck A. F. L., Maiolino R., Concas A., Peng Y., 2020, MNRAS, 492, L6

Planck Collaboration et al., 2020, A&A, 641, A6

Poetrodjojo H., et al., 2018, MNRAS, 479, 5235

Postman M., et al., 2012, ApJS, 199, 25

Reddy N. A., et al., 2015, ApJ, 806, 259

Renzini A., Peng Y.-j., 2015, ApJ, 801, L29

Richards S. N., et al., 2016, MNRAS, 455, 2826

Rogers N. S. J., Skillman E. D., Pogge R. W., Berg D. A., Moustakas J., Croxall K. V., Sun J., 2021, ApJ, 915, 21

Rosati P., et al., 2014, The Messenger, 158, 48

Rousselot P., Lidman C., Cuby J. G., Moreels G., Monnet G., 2000, A&A, 354, 1134

Rubin V. C., Ford W. K. J., Thonnard N., 1978, ApJ, 225, L107

Rubin V. C., Ford W. K. J., Thonnard N., 1980, ApJ, 238, 471

Sabbadin F., Minello S., Bianchini A., 1977, A&A, 60, 147

Salim S., et al., 2007, ApJS, 173, 267

Salpeter E. E., 1955, ApJ, 121, 161

Sánchez-Menguiano L., et al., 2016, A&A, 587, A70

Sánchez S. F., et al., 2014, A&A, 563, A49

Sánchez S. F., et al., 2016, Rev. Mex. Astron. Astrofis., 52, 171

Sanders R. L., et al., 2015, ApJ, 799, 138

Sanders R. L., et al., 2016a, ApJ, 816, 23

Sanders R. L., et al., 2016b, ApJ, 825, L23

Sanders R. L., et al., 2018, ApJ, 858, 99

Sanders R. L., et al., 2020, MNRAS, 491, 1427

Sanders R. L., et al., 2021, ApJ, 914, 19

Sarzi M., Spiniello C., La Barbera F., Krajnović D., van den Bosch R., 2018, MNRAS, 478, 4084

Schaefer A. L., Tremonti C., Belfiore F., Pace Z., Bershady M. A., Andrews B. H., Drory N., 2020, ApJ, 890, L3

Schaefer A. L., et al., 2022, arXiv e-prints, p. arXiv:2203.17026

Schmidt M., 1959, ApJ, 129, 243

Shapley A. E., et al., 2015, ApJ, 801, 88

Shapley A. E., et al., 2019, ApJ, 881, L35

Sharples R., et al., 2013, The Messenger, 151, 21

Shields G. A., Skillman E. D., Kennicutt Robert C. J., 1991, ApJ, 371, 82

Skelton R. E., et al., 2014, ApJS, 214, 24

Skrutskie M. F., et al., 2006, AJ, 131, 1163

Smette, A. et al., 2015, A&A, 576, A77

Somerville R. S., Davé R., 2015, ARA&A, 53, 51

Spite M., et al., 2005, A&A, 430, 655

Steidel C. C., et al., 2014, ApJ, 795, 165

Steidel C. C., Strom A. L., Pettini M., Rudie G. C., Reddy N. A., Trainor R. F., 2016, ApJ, 826, 159

Stott J. P., et al., 2014, MNRAS, 443, 2695

Stott J. P., et al., 2016, MNRAS, 457, 1888

Strom A. L., Steidel C. C., Rudie G. C., Trainor R. F., Pettini M., Reddy N. A., 2017, ApJ, 836, 164

Strom A. L., Steidel C. C., Rudie G. C., Trainor R. F., Pettini M., 2018, ApJ, 868, 117

Strom A. L., Rudie G. C., Steidel C. C., Trainor R. F., 2022, ApJ, 925, 116

Tacchella S., et al., 2018, ApJ, 859, 56

Taylor A. N., Dye S., Broadhurst T. J., Benítez N., van Kampen E., 1998, ApJ, 501, 539

Thurston T. R., Edmunds M. G., Henry R. B. C., 1996, MNRAS, 283, 990

Topping M. W., Shapley A. E., Reddy N. A., Sanders R. L., Coil A. L., Kriek M., Mobasher B., Siana B., 2020a, MNRAS, 495, 4430

Topping M. W., Shapley A. E., Reddy N. A., Sanders R. L., Coil A. L., Kriek M., Mobasher B., Siana B., 2020b, MNRAS, 499, 1652

Tremonti C. A., et al., 2004, ApJ, 613, 898

Treu T., et al., 2015, ApJ, 812, 114

Troncoso P., et al., 2014, A&A, 563, A58

Tumlinson J., Peeples M. S., Werk J. K., 2017, Annual Review of Astronomy and Astrophysics, 55, 389

Van Dokkum P. G., Conroy C., 2010, Nature, 468, 940

Van Zee L., Salzer J. J., Haynes M. P., 1998, ApJ, 497, L1

Ventura P., Di Criscienzo M., Carini R., D'Antona F., 2013, MNRAS, 431, 3642

Vila-Costas M. B., Edmunds M. G., 1992, MNRAS, 259, 121

Vila-Costas M. B., Edmunds M. G., 1993, MNRAS, 265, 199

Vincenzo F., Kobayashi C., 2018, MNRAS, 478, 155

Vincenzo F., Matteucci F., Belfiore F., Maiolino R., 2016a, MNRAS, 455, 4183

Vincenzo F., Belfiore F., Maiolino R., Matteucci F., Ventura P., 2016b, MNRAS, 458, 3466

Wegner M., Muschielok B., 2008, in Bridger A., Radziwill N. M., eds, Society of Photo-Optical Instrumentation Engineers (SPIE) Conference Series Vol. 7019, Advanced Software and Control for Astronomy II. p. 70190T, doi:10.1117/12.787190

Whitaker K. E., van Dokkum P. G., Brammer G., Franx M., 2012, ApJ, 754, L29

Whitaker K. E., et al., 2014, ApJ, 795, 104

Wisnioski E., et al., 2015, ApJ, 799, 209

Wisnioski E., et al., 2019, ApJ, 886, 124

Wuyts S., et al., 2011, ApJ, 742, 96

Wuyts S., et al., 2012, ApJ, 753, 114

Wuyts E., et al., 2016, ApJ, 827, 74

Zafar T., Centurión M., Péroux C., Molaro P., D'Odorico V., Vladilo G., Popping A., 2014, MNRAS, 444, 744

Zaritsky D., Kennicutt Robert C. J., Huchra J. P., 1994, ApJ, 420, 87

Zinchenko I. A., Pilyugin L. S., Grebel E. K., Sánchez S. F., Vílchez J. M., 2016, MNRAS, 462, 2715

Zitrin A., et al., 2013, ApJ, 762, L30

Zwicky F., 1933, Helvetica Physica Acta, 6, 110

van Zee L., Haynes M. P., 2006, ApJ, 636, 214

van den Hoek L. B., Groenewegen M. A. T., 1997, A&AS, 123, 305

van der Wel A., et al., 2012, ApJS, 203, 24